UNIVERSITY OF CALIFORNIA, SAN DIEGO

Chemically Reacting Plumes, Gas Hydrate Dissociation and Dendrite Solidification

A dissertation submitted in partial satisfaction of the requirements for the degree Doctor of Philosophy

in

Engineering Sciences (Mechanical Engineering)

by

Devin Thomas Conroy

Committee in charge:

Professor Stefan G. Llewellyn Smith, Chair
Professor Miriam Kastner
Professor Juan Lasheras
Professor William Reeburgh
Professor James Rottman
Professor Daniel Tartakovsky

2008

The dissertation of Devin Thomas Conroy is approved, and it is acceptable in quality and form for publication on microfilm:

Chair

University of California, San Diego

2008

Dedicated to my family

Even if there is only one possible unified theory, it is just a set of rules and equations. What is it that breathes fire into the equations and makes a universe for them to describe? The usual approach of science of constructing a mathematical model cannot answer the questions of why there should be a universe for the model to describe. Why does the universe go to all the bother of existing?

Stephen W. Hawking

If I have seen further than others, it is by standing upon the shoulders of giants.

Isaac Newton

TABLE OF CONTENTS

LIST OF FIGURES

LIST OF TABLES

ACKNOWLEDGMENTS

Many people helped me during my time at the Univ. of California, San Diego and while words cannot sufficiently express my gratitude I would like to acknowledge them here. First and foremost I would like to thank my wife Alexis who has been very understanding all these years. She is the main reason I started on the path of a graduate student and the reason I am here today. I would also like to thank my family for their patience and support.

I would like to thank my research advisor Stefan Llewellyn Smith, who graciously took me under his wing many years ago. His insight and encouragement were essential to my personal and professional development, which allowed me to understand more than I thought I could. Furthermore I would like to thank Colm Caulfield who co-advised me on my first research project on chemically reacting plumes.

My gratitude is extended to my doctoral committee members for taking time out of their busy schedules to assist me and for their helpful comments on the direction of my research. Finally, I would like to thank my fellow grad students for our academic discussions and for their friendship.

Financial support was generously provided by the National Science Foundation. Chapter 3 has been published in the *Journal of Fluid Mechanics*, 2005, Conroy, D. T., S. G. Llewellyn Smith and C. P. Caulfield (Cambridge University Press). Chapter 4, in part, has been submitted to the *Journal of Fluid Mechanics*, 2008, Conroy, D. T. and S. G. Llewellyn Smith (Cambridge University Press). I was both the primary investigator and lead author of each of the papers described above.

VITA

2002	B.Sc. San Francisco State University (Mechanical Eng.)
2004	M.Sc., U. of California, San Diego (Mechanical Eng.)
2004–2008	Research Assistant, U. California, San Diego
2006	Teaching Assistant, U. California, San Diego
2008	Ph.D., U. California, San Diego (Eng. Sciences)

SELECTED PUBLICATIONS

Conroy, D.T., and Llewellyn Smith, S.G., 2007: Solidification of slender dendrites. *J. Crystal Growth (In preparation)*

Conroy, D.T., and Llewellyn Smith, S.G., 2007: Endothermic and exothermic chemically-reacting plumes. *J. Fluid Mech. (Submitted)*

Conroy, D.T., 2006: Mush-liquid interfaces with cross flow. *In Proc. 2006 Geophysical Fluid Dynamics Summer Study Program, Woods Hole Oceanographic Institution*

Conroy, D.T., and Llewellyn Smith, S.G., 2006: Chemically reacting plumes. *In Proc. Sixth International Symposium on Stratified Flows*

Conroy, D.T., Llewellyn Smith, S.G. and Caulfield, C.P., 2005: Evolution of a chemically reacting plume in a ventilated room. *J. Fluid Mech.*, **537**, 221–253.

FIELDS OF STUDY

Major Field: Fluid mechanics

Plume dynamics with chemistry
Profs. Stefan Llewellyn Smith and Colm Caulfield

Moving boundary problems, two phase flow through porous media and dendrite solidification
Profs. Stefan Llewellyn Smith

ABSTRACT OF THE DISSERTATION

Chemically reacting plumes, gas hydrate dissociation and dendrite solidification

by

Devin Thomas Conroy
Doctor of Philosophy in Engineering Sciences (Mechanical Engineering)
University of California, San Diego, 2008
Professor Stefan Llewellyn Smith, Chair

Chemical transport by natural convection is a common occurrence in environmental and industrial settings, and in many cases a reaction occurs between the source fluid and the fluid entrained by the ambient. This process is particularly important in the case of ventilated spaces, especially when the chemical is hazardous to the occupants. We explore analytically, numerically and experimentally the physics involved when a chemically reacting plume enters a ventilated space in order to determine the species distribution in time. We compare our results to traditional ventilation strategies that rely on well-mixed spaces and discuss the main differences. Furthermore, there are many case in which the chemical reaction is endothermic or exothermic, such as in dilution reactions, pool fires and others. In this case the buoyancy force depends on the heat of reaction as well as the ambient density distribution and we develop a model to take into account this extra source/sink applying methods based on traditional plume models.

This thesis also presents a separate investigation on gas hydrate decomposition in porous media due to an increase in ocean water temperature. The

problem is essentially broken up into two parts, depending on the system conditions in relation to the phase diagram. In the first case the hydrate dissolves at warmer temperatures at a rate that scales with species diffusion. In the second case the hydrate dissociates into water and gas, which requires a special treatment for the two-phase flow through the sediment. Here we determine methane gas flow rates into the ocean from the sea bed as a function of thermal forcing and sediment properties.

Finally, we present a related project on dendrite solidification in supercooled binary liquids (e.g. hydrate and alloys). Slender body theory is applied to a steady state dendrite and solved analytically using the Wiener-Hopf technique. We examine the interface shape as a function of temperature, concentration, and kinetic under-cooling and compare this to the classic similarity solution.

1

Thesis outline and scope

During my graduate career at the University of California – San Diego I have been fortunate to work on various research projects in parallel whereas most dissertations focus on a set of closely related topics. Fortunately all of my projects can be tied together by the fact that they are related to melting/solidification processes in the environment. For example, during the dissociation of gas hydrates under the seafloor, gas will flow into the ocean forming a bubble plume. The collection of bubbles are commonly modeled using turbulent plume theory with a closure relationship that takes into account the collective bubble motion on the plume dynamics. In addition, since the bubbles are dissolving in response to phase disequilibrium, the plume can be considered to be reactive.

Furthermore, the rejection of salt during the solidification of seawater may lead to the formation of salt plumes. The release of dense saline water from these mushy structure may be the dominate mode of convection in the polar regions. For these reasons, this document is separated into two main areas: turbulent plumes and melting/solidification problems and is roughly divided into the following 3 parts:

- Chapters 2-4: Chemically reacting plumes
- Chapters 5-7: Gas hydrate dissociation

- Chapter 8: Dendrite solidification

Chapter 3 examines the effects of chemical reactions on the dynamics of a turbulent plume and their relationship to contaminant removal in occupied spaces. Through a combination of analytical, numerical and experimental techniques, we examine the evolution of species concentrations in a ventilated room with nonlinear reaction rates and compare them to traditional, well-mixed, HVAC systems. Since traditional systems distribute the chemistry uniformly, whereas natural convection stratifies the chemistry, we show that a plume may lead to a more efficient ventilation strategy if the initial fluid in the room is contaminated.

Chapter 4 explores the relationship between buoyancy fluxes and internal heat gains/losses from exothermic and endothermic reactions. These reactions can have important effects on the plume dynamics since the entrainment rate, which scales with the vertical velocity, will be a function of the heat release or absorption. For chemically and density stratified environments, this will have an important effect on the vertical density distribution because the entrainment rate will not necessarily decrease with distance from this source. In traditional models this will not be the case, since the reaction will contribute to the buoyancy of the plume. As a result, the maximum rise height of the plume for exothermic reactions may actually decrease with reaction rate if this occurs in a region of high ambient density.

Chapter 6 investigates melting and dissolution rates of methane gas hydrates in porous media in response to changes in system conditions from phase equilibria. A model is developed based on conservation equations for heat, mass, momentum and species and solved analytically in an infinite domain. We compare two formulations of the problem, corresponding to pure hydrate layers with large hydrate saturations and hydrate layers with variable hydrate saturations. In general, a mushy layer will melt/dissolve more quickly because the system is limited by thermal diffusion rather than mass diffusion as in the pure case.

Chapter 7 extends the model developed in Chapter 6 to hydrate disso-

ciation in which gas and water are released from the phase boundary. The new problem involves a multiphase flow through the sediment, which we solve numerically and analytically for a few limiting cases, such as large latent heat release or weak gravitational forces. We examine the effects of system properties such as temperature and capillary forces on the gas flux through the sediment and total concentration of methane released from the seafloor. Generally, for small Stefan numbers (large temperature scale) and shallow deposits the total amount of gas entering the ocean can be significant, possibly kilograms per year.

In Chapter 8 we solve the steady dendrite problem in which a solid needle-like structure grows into a super-cooled binary fluid using slender body theory. We consider the full interfacial conditions, including curvature, binary, and kinetic under-cooling effects and solve the first-order outer problem using the Wiener-Hopf technique. In the case of a pure liquid we investigate the effect of kinetic under-cooling on the interface displacement and compare these results with the similarity solution. The method is appropriate for slender dendrites and is found to be equivalent to the similarity solution in the small Péclet number limit. In addition, the growth rate can be determined uniquely, provided the thickness of the dendrite is known at some position, rather than the radius of curvature. Furthermore we investigate the effect of component concentrations on the interface position and growth velocity.

I

Chemically reacting plumes

2

Introduction to plumes with chemically reacting species

Many processes in the natural world rely on the transport of heat and material by convection, in which buoyancy forces generated by some mechanism (e.g. solar radiation) drive the motion of a parcel of fluid. The fluid therefore moves in order to minimize its potential energy. In many cases the convection usually has a self similar profile and we can use turbulent plume theory to model the structure of the flow. The simplest approach, starting with the seminal work of Morton et al. (1956), is to consider a set of conservation equations with a constitutive relationship for the turbulent entrainment (expressing the rate at which ambient fluid is incorporated into the plume). This relationship is known as the 'entrainment rate' and is proportional to the center line velocity and thus scales with the turbulent production. Plume theory has been compared successfully with the experiments of Ricou and Spalding (1961) and Turner (1973), and extended to various geophysical and industrial settings such as volcanic eruptions (Woods 1995), bubble plumes (Mcdougal 1978, and Asaeda and Imberger 1993), ventilation (Baines and Turner 1969) and many more. An excellent introduction to plume theory and its applications can be found in Linden (2000).

An interesting application for plume models is to include a chemically-

reacting species that is initially buoyant and reacts with the entrained ambient fluid. In the simplest case the conversion of chemical to thermal energy is small (small heat of reaction) and the chemistry is passively driven (Conroy et al. 2005). In more complicated cases the heat of reaction is sufficiently large and contributes substantially to the plume dynamics, manifesting itself as a buoyancy source. We discuss some applications for these types of models in the following sections.

2.1 Environmental plumes

Plumes are the most common form of large-Reynolds-number convection in the ocean and the atmosphere (Linden 2000). The environment can generally be treated as unbounded (no solid boundaries such as walls), which is naturally stratified in density by either heat or solute. In all cases the entrainment of dense fluid causes the plume to rise to a maximum height. At this height the momentum of the plume changes direction from upward to downward, and provided the momentum of the plume is negative the plume will descend in the form of a fountain before it ultimately spreads out horizontally (Bloomfield and Kerr 2000). A common manifestation is the visually stunning umbrella cloud formed from a volcanic eruption.

2.1.1 Examples

Black smokers

On the ocean floor of the mid-ocean ridges, plumes of hot sulfide-bearing sea water issue into the water column from hydrothermal vents. The water is heated to temperatures near 350°C from beneath the Earth's crust in magma chambers, in which sulfur-bearing materials are dissolved into the high pressure fluid. As the buoyant fluid seeps out of the Earth's crust, a turbulent plume forms and entrains cool, ambient sea water. As the fluid cools a precipitation reaction occurs forming small black particles of metal sulfides causing the plume to resemble

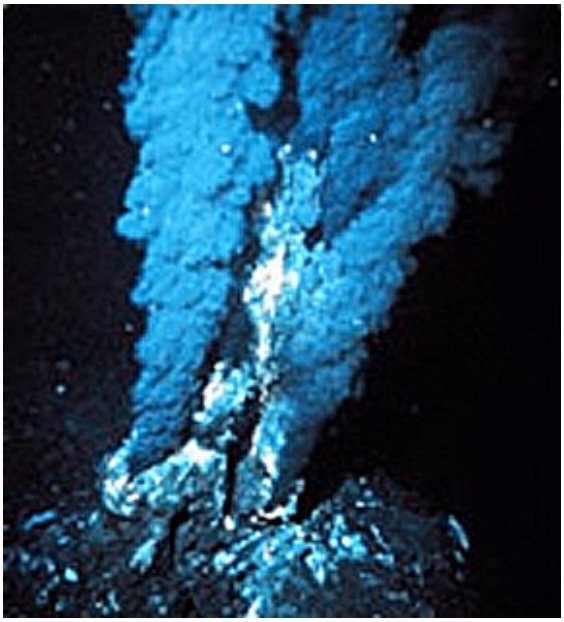

Figure 2.1: Black smoker image from http//:www.rst.gsfc.nasa.gov

black smoke (hence the name "black smoker") as seen in Figure 2.1.

Mid-ocean ridges are deep underwater and essentially devoid of sunlight. However new organisms have been found to thrive on the sulfide-rich seawater using chemosynthesis as a pathway for energy sequestration. These regions support a unique ecosystem critically dependent on the concentrations of the chemicals issuing from the plumes, which is of great interest to researchers in biology and oceanography (Tunnicliffe 1992).

Volcanic eruptions

Similarly to the examples above concerning black smokers, a plume is formed from a volcanic eruption as seen in Figure 2.2 with a spectacular display of ejected ash and molten magma. Initially the material is ejected at high velocities. The extremely large temperatures and thus buoyancy allows the plume to rise as high as 45 km into the stratosphere. The hot fluid is composed of a mixture denser than air and behaves with jet-like characteristics, but as the jet entrains ambient

Figure 2.2: Volcanic eruption image from http//:www.rst.gsfc.nasa.gov

air, the thermal energy of the ash and magma is transferred to the gas and the average density decreases. As the volume increases with height and the density decreases, the jet behaves as a plume and therefore the maximum rise height of the volcanic eruption increases (Huppert 2000).

Generally, the ejected volcanic material has multiphase fluid-like properties with many different chemicals such as carbon dioxide (CO_2), sulfur dioxide (SO_2), carbon monoxide (CO), hydrogen chloride (HCl) and many more. In addition sulfate aerosols from volcanic eruptions can accelerate ozone depleting chemical reactions in the stratosphere as they encounter man made CFC's (Brasseur and Granier 1992).

Chemical fires

Chemically reacting plumes are a common occurrence resulting from the flow that develops above a pool of ignited fuel (i.e. pool fires). Provided the fire is unbounded and the vaporization rate is above a minimum value, a single plume forms with two distinct stages. In the first stage a reacting plume rises above the fuel source in the form of a fire, in which hot, buoyant fuel mixes with entrained ambient air. The highly exothermic reaction increases the buoyancy of the plume

until the initial plume species is completely consumed. At this height the plume behaves as a non-Boussinesq plume without reaction and with a virtual origin correction (Tieszen 2001).

Bubble plumes

Gas that has migrated out of the sediment and entered the water column will rise to the surface due to buoyancy forces in the form of distributed bubble plumes. Motivated by oil well blowouts and reservoir de-stratification many authors have performed laboratory investigations as well as developing mathematical models. Experimental studies by McDougall (1978) have shown that bubble plumes form a double plume configuration, where bubbles stay confined to an inner core and entrained ambient fluid forms an annular plume moving upwards at some slower velocity than the bubbles. Since most ambient environments are stratified, the fluid that forms the outer plume eventually loses momentum and consequently detrains and falls to some neutrally buoyant level. Further, Asaeda and Imberger (1993) found that in addition to the double plume configuration, the detrained fluid forms an annular down-draught that eventually turns into a horizontal intrusion flow.

In deep ocean water, where the hydrate stability zone extends far enough above the sea floor, gas hydrates may nucleate on the bubble surfaces as they rise, forming a crystalline rind. The formation process rejects salt and releases latent heat which acts in concert to modify the water density. In addition, the buoyant core, which is a combination of solid hydrate and gas, will in general have a larger average density. After the coated bubbles leave the hydrate stability zone the hydrate will begin to decompose into water and free gas. Of course the buoyancy forces acting on the plume will be different at various stages and vertical locations of the plume. Zheng et. al. (2002) included hydrate formation in a bubble plume model, using a Lagrangian formulation and in the presence of a cross flow. They modeled the hydrate formation as a kinetic and thermodynamic process with the

assumption that the rind remains spherical and grows with time due to the diffusion of gas across its porous shell.

2.2 Ventilation and plumes in confined spaces

Plumes issuing into a confined space such as a room in an office building are a common occurrence in conjunction with building ventilation where the source of buoyancy comes from sources of heat. These heat sources can originate from people, electronic equipment, air conditioning, smoke, etc. Flows of this type were first studied by Baines and Turner (1969) who considered the flow that develops in an initially homogeneous room a turbulent plume. As it rises the plume entrains ambient fluid, until it eventually reaches the ceiling, spreads horizontally and then descends into the space. As the plume continually entrains ambient fluid the old plume fluid gets re-entrained and the density structure evolves with time as seen in Figure 2.3. This mechanism is known as the "filling box" process and in the case of a single vent, the room fluid will be replaced by plume fluid within a few replacement time scales (the time it takes to fill the room at the source flow rate).

The filling box model of Baines and Turner (1969) only applies provided the aspect ratio of the room is sufficiently large. In this case the mixing that occurs when the plume spreads along the ceiling is confined to a small region and the velocity of the room fluid is only in the vertical direction. Furthermore, this assumption implies that the vertical velocity of the plume is much larger than the downward velocity of the room fluid. This fact was exploited by Germeles (1975) in his numerical algorithm, which essentially decouples the plume dynamics from the room dynamic during each step of the time integration. The plume then sees a quiescent ambient that is determined by tracking a sufficiently large number of fluid layers. This technique can still be used when a reaction is occurring in the room, provided the rate of change of ambient fluid is small compared to the vertical propagation of a parcel of fluid in the plume.

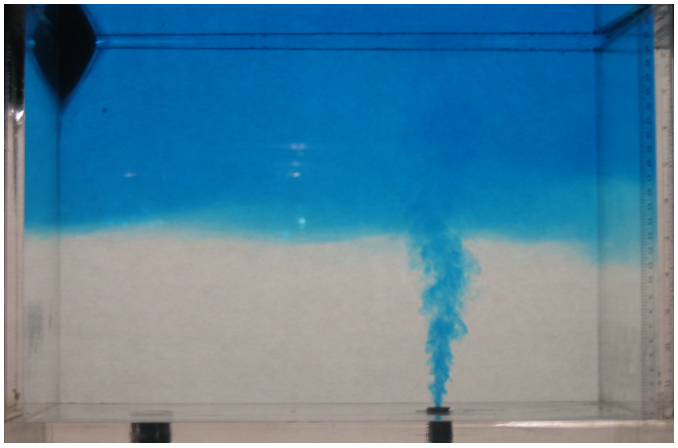

Figure 2.3: A ventilated filling box with a dyed freshwater plume entering a salty, ambient fluid from the bottom and a vent located at the floor. The interface separating the clear and dyed fluid is the first front and it moves downwards at a velocity that is dependent on the plume flow rate and horizontal room area.

2.2.1 Natural Ventilation

Natural ventilation, which models heat sources, such as people or electronic equipment as ideal plumes has recently experienced a considerable amount of research since it is more efficient than traditional HVAC systems in certain geographical regions. Essentially, natural ventilation takes advantage of the density stratification generated from heat sources to transport fluid into and out of the occupied space. Since the space is not well mixed, this strategy has the advantage of conditioning only the occupied zone, which is at the ground level. The generated heat and contaminants flow to the top of the room where they are extracted and fresh, cool air flows in from the floor. A review of natural ventilation has been compiled by Linden et al.(1990) although there is still substantial ongoing research, especially regarding the engineering aspects associated with building design strategies and optimization.

2.2.2 Example

Indoor air quality

Since many people spend a large fraction of their time within enclosed spaces, it is important to control the indoor air quality, especially when there is a continuous release of a hazardous chemical. A hazardous chemical may be carbon monoxide from car exhaust, cigarette smoke flowing in from an open window, or radon contained within the bedrock that enters in from the building foundation. These chemicals may be considered passive, since they advect with the fluid or diffuse, but do not contribute to the momentum of the bulk fluid motion. From the standpoint of indoor air quality it is clearly necessary to understand how these chemicals are transported so as to maintain the occupied zone at tolerable levels.

In addition, there exists the possibility of an accidental release of a hazardous chemical that reacts with the surrounding air, producing a chemical species that is either hazardous or acts to dilute the hazardous reactant. These may include pyrophoric chemicals, such as phosphorus, which react with the water in humid air and become very toxic. These chemicals may be transported in pipelines through buildings for manufacturing processes and may leak, forming a dense fluid that enters the space and falls downward with turbulent plume-like characteristics. In this case it is important to understand the chemical reaction mechanism and how the species are transported through the ventilated room.

3

Chemically reacting plumes in a ventilated filling box

3.1 Abstract

The dynamics of a second order chemical reaction in an enclosed space driven by the mixing produced by a turbulent buoyant plume are studied theoretically, numerically and experimentally. An isolated turbulent buoyant plume source is located in an enclosure with a single external opening. Both the source and the opening are located at the bottom of the enclosure. The enclosure is filled with a fluid of a given density with a fixed initial concentration of a chemical. The source supplies a constant volume flux of fluid of different density containing a different chemical of known and constant concentration.These two chemicals undergo a second order non-reversible reaction, leading to the creation of a third product chemical. For simplicity, we restrict attention to the situation where the reaction process does not affect the density of the fluids involved. Because of the natural constraint of volume conservation, fluid from the enclosure is continually vented. We study the evolution of the various chemical species as they are advected by the developing ventilated filling box process within the room that is driven by the plume dynamics. In particular, we study both the mean and vertical distributions

of the chemical species as a function of time within the room. We compare the results of analogue laboratory experiments with theoretical predictions derived from reduced numerical models, and find excellent agreement. Important parameters for the behavior of the system are associated with the source volume flux and specific momentum flux relative to the source specific buoyancy flux, the ratio of the initial concentrations of the reacting chemical input in the plume and the reacting chemical in the enclosed space, the reaction rate of the chemicals and the aspect ratio of the room. Although the behavior of the system depends on all these parameters in a non-trivial way, in general the concentration within the room of the chemical input at the isolated source passes through three distinct phases. Initially, as the source fluid flows into the room, the mean concentration of the input chemical increases due to the inflow, with some loss due to the reaction with the chemical initially within the room. After a finite time, the layer of fluid contaminated by the inflow reaches the opening to the exterior at the base of the room. During an ensuing intermediate phase, the rate of increase in the concentration of the input chemical then drops non-trivially, due to the extra sink for the input chemical of the outflow through the opening. During this intermediate stage, the concentration of the input chemical continues to rise, but at a rate that is reduced due to the reaction with the fluid in the room. Ultimately, all the fluid (and hence the chemical) that was originally within the room is lost, both through reaction and outflow through the opening, and the room approaches its final steady state, being filled completely with source fluid.

3.2 Introduction

In many industrial settings, pipelines transport pressurized chemicals in the liquid state that would undergo a chemical reaction if exposed to air. If a leak were to occur, the chemical would enter the ambient environment, and under ambient pressure, vaporize and cool, forming a gas, with in general a different

density from the ambient air. Provided the source remains relatively isolated, and the leaking fluid has some initial momentum, which is a plausible scenario, the resulting plume, driven by buoyancy, would inevitably entrain ambient air. This entrainment would have two principal effects. Firstly, it would increase the volume of air that is at least partially contaminated by the released chemical. Secondly, it would allow the released chemical to react with the entrained air. This air, contaminated with both the original chemical and the reaction product, would thus start to fill the space. From a hazard analysis viewpoint, it is clearly important to understand the spatial and temporal evolution of this contamination. For example, such an understanding would allow the identification of the time available to evacuate a building before concentrations of either the released chemical or the product became hazardous. Naturally, similar concerns also arise when the release of the hazardous reacting chemical is intentional, and many of the scientific and theoretical modeling issues are the same.

Furthermore, situations with analogous physical properties occur in geophysics. For example, in oceanography, a few decades ago deep sea hydrothermal vents, (known as "black smokers" because they discharge a black precipitate composed of sulfur bearing material) were discovered at mid-ocean ridges. Hot seawater and sulphites, formed in hot magma chambers below the surface, seep out of the ground as a low density fluid. Although there are significant thermal differences between the vented fluid and the surrounding ambient sea water, there is no vaporization because of the high pressure. The vented buoyant fluid forms a turbulent plume that when mixed with the cold ambient seawater creates a precipitate that can be seen as black smoke. Since these regions are far underwater and essentially devoid of sunlight, new organisms have been found to thrive on the chemically rich seawater using chemosynthesis as an energy source. These regions support a unique ecosystem critically dependent on the concentrations of the chemicals issuing from the plumes, which is of great interest to researchers in biology and oceanography (Tunnicliffe 1992). Due to the local topography, and also to the

ambient stratification of the ocean (see Cardoso & Woods 1993), the plume fluid propagates only a finite distance away from the source, and so there are marked points of similarity with the industrial situation.

The fundamental fluid dynamical aspect of this class of problems is the presence within a finite, though large, restricted area, or "room", (with limited "ventilation" to the exterior) of an isolated source of fluid of both different density and chemical composition from the fluid initially within the room. In the absence of chemical reaction between the source and ambient fluid, such flows have been widely studied, building upon the original seminal contribution of Baines & Turner (1969; henceforth BT69). They considered the flow that develops when an isolated source of buoyancy alone (a so-called "point source plume") issues into an enclosed region. As the plume rises it entrains ambient fluid (in a way that is well modeled by the classic approach of Morton, Taylor & Turner 1956; henceforth MTT56), until ultimately the plume fluid reaches the ceiling of the room, where, provided the aspect ratio of the room is sufficiently small, it spreads out, and forms a "first front" of fluid that has been cycled through the plume. As the plume continues to entrain, the first front moves downward through the room, and the region above the first front fills with fluid that has, at some stage, been entrained into the plume. This filling box mechanism continues for all times if the source has zero volume flux, as the first front only approaches the source height asymptotically.

The evolution of the density distribution within the room can be accurately studied numerically using the numerical algorithm initially proposed by Germeles (1975). Essentially, this algorithm makes a quasi-steady approximation, assuming that the transit time of a fluid parcel within the plume from floor to ceiling is very much faster than the transit time for a fluid parcel within the room from the ceiling to the floor. This assumption is satisfied provided the source is isolated and always occupies a negligibly small fraction of the cross-sectional area of the room at all heights, and so the aspect ratio of the room is sufficiently small. In such a circumstance, the evolution of the plume can be considered to occur in a

quiescent ambient. At any time instant, once the properties (and in particular the volume flux) of the plume are determined at all heights, the evolution of the ambient density distribution in the room can be determined by tracking the motion of a sufficiently large number of layers of ambient fluid. The propagation of each of the interfaces between the layers is determined by requiring that the upflow volume flux in the plume at that height is balanced by a slower downflow of ambient fluid, with the effect that entrainment into the plume causes neighboring interfaces to move closer together. This method, discussed in more detail below, leads to an accurate representation of the evolution of the ambient density distribution within the room.

A particularly important aspect of the point source model that deserves attention is the requirement that the source has finite buoyancy flux yet zero volume flux. This corresponds formally to the requirement that there is no lower bound on the fluid density within the system. Therefore, the density of the layer above the first front continues to decrease without limit, with an asymptotic vertical structure in the density profile, consistent with the assumption that the buoyancy flux in the plume varies linearly with distance from the source (see Worster & Huppert 1983).

Caulfield & Woods (2002; henceforth CW02) generalized this flow to consider the behavior when the source has a nonzero source volume flux. This source volume flux changes the behavior of the system qualitatively in several ways. Firstly, since the source has a constant finite volume flux (and for consistency also a finite source momentum flux), there is a minimum fluid density within the system, corresponding to the density of the fluid issuing from the source. In the limit of long time, the fluid in the room approaches this density asymptotically. Secondly, since there is a finite volume flux into the system, there must be at least one opening to the exterior, or vent, to allow for conservation of volume. Furthermore, the first front arrives at the location of the opening in finite time, and for the particularly straightforward case where the source and the opening are both at the

floor of the room, this implies that the entire room becomes filled in a finite time with fluid that has been cycled through the plume, and contaminated fluid starts to issue from the opening. Since the fluid in the vicinity of the source becomes less dense than the initial ambient fluid, if the source volume flux is constant, the source buoyancy flux decreases. Therefore, as discussed in CW02 in detail, the source starts to behave less and less like a buoyant plume, and more and more like a forced jet. Indeed, asymptotically, as the fluid throughout the room approaches the density of the source fluid, the source ceases to be buoyant, and the flow within the room is driven by a source of momentum alone, enabling the development of an asymptotic analytical model for the evolution of the density within the room which is a slight improvement on that discussed by Worster & Huppert (1983) and BT69.

None of these studies however considered the possibility of chemical reaction between the source fluid and ambient fluid within the room, and so in this Chapter we generalize the previous work to consider the behavior of a system where the source fluid and the fluid initially within the room chemically react. For there to be a possibility of chemical reaction, it is clearly necessary for there to be a finite volume flux of source fluid into the enclosed space, and so there must be at least one vent to conserve fluid volume. As a first attempt to consider this class of problems, we will restrict ourself to flows with vents at a single height, thus avoiding the possibility of the development of different steady states, as can occur when there are two vents at different heights (see Woods, Caulfield & Phillips 2003). Generalizing CW02, we therefore restrict our attention to the simplest case, where the source and a single external opening are at the same location, the floor of the room. Of course, the same model can apply to flows with multiple openings at the same height, provided uni-directional flow occurs through each opening. Furthermore, to gain an understanding of the extent to which the filling box flow itself affects the evolution of the chemically reacting species, we assume that the reaction has no effect on the flow dynamics, i.e. as the different species react they

have no effect on the fluid density, and so play a passive role on the flow dynamics. This problem still exhibits a rich range of flow behaviors, and has the particular attractions that it is a simple generalization of previous studies and that the results of theoretical predictions can be tested experimentally.

The Chapter is therefore organized as follows. In § 3.3, we briefly review the standard plume model due to MTT56, and discuss the generalizations required to model flow within an enclosed space (as discussed in BT69) with a finite volume flux and a single vent (CW02). We add to this model the evolution of passively advected reactive species, one initially in the plume source and the other initially in the enclosed space. We also generate simplified well-mixed models which ignore the plume dynamics, and the associated vertical distribution induced by the plume within the room. Once we have developed these models and identified the critical governing parameters and the important time scales for the flow, in § 3.4, we present the results of time-dependent numerical solutions of this model for various relevant choices of the parameters. We discuss in some detail the inherent assumptions of the model, which place some restrictions on the possible choices of the various flow parameters. In § 3.4, the solution is generated using the method originally proposed by Germeles (1975) appropriately modified to track the dynamically passive concentrations of the various chemical species both within the plume and in the interior of the room. In § 3.5, we discuss the experimental method which we have used to consider the flow under consideration, in particular the chemicals which we have identified to have the appropriate properties. We then compare the results of the experiments with the various theories and numerical models which we have developed to investigate their usefulness, identifying points of agreement and discussing reasons for observed discrepancies. Finally, in § 3.6, we draw some conclusions.

3.3 Model description

A Schematic representation of the flow geometry is shown in figure 3.3. Here a turbulent plume source is located at $z = 0$ in a room of depth H with a single external opening also at $z = 0$. The plume has fixed source radius b_s, source velocity w_s and source density ρ_s, so that the source density concentration $\hat{C}_P(0,t) = 1$ as defined in (3.26). The source fluid also has fixed concentration P_{10} of species one alone. The room is initially filled with fluid of density $\rho_{R0} > \rho_s$ corresponding to room density concentration $\hat{C}_R(z,0) = 0$ as defined in (3.26) and concentration R_{20} of species two alone. As the plume rises and entrains fluid, the plume fluid has concentrations $P_1(z,t)$, $P_2(z,t)$, $P_3(z,t)$ and $\hat{C}_P(z,t)$ of the reacting species one and two, the product species three, and the fluid density respectively. Similarly, as the filling box process modifies the stratification in the room, the room fluid has concentrations $R_1(z,t)$, $R_2(z,t)$, $R_3(z,t)$ and $\hat{C}_R(z,t)$ of the reacting species one and two, the product species three, and the fluid density respectively. Eventually, due to the continual venting (with flux Q_s) of room fluid through the external opening, $R_1 \to P_{10}$, $\hat{C}_R \to 1$, R_2, $R_3 \to 0$, as the room becomes completely filled with source fluid. When we consider well-mixed models, we ignore any distinction between plume fluid and room fluid, and consider well-mixed concentrations W_1, W_2 and W_3 of the three chemical species and concentration $\hat{C}_W$ of the fluid density.

There are three components to the required model: a model for the isolated plume source; a model for the induced flow within the room; and a model for the chemical reactions between the different species. We consider each in turn.

3.3.1 Plume dynamics

We consider an isolated source of fluid of finite extent, supplying fluid of different density and velocity compared to the surrounding environment. We make the Boussinesq assumption, and so suppose that the density differences involved are sufficiently small so that they only affect the buoyancy force. Although the

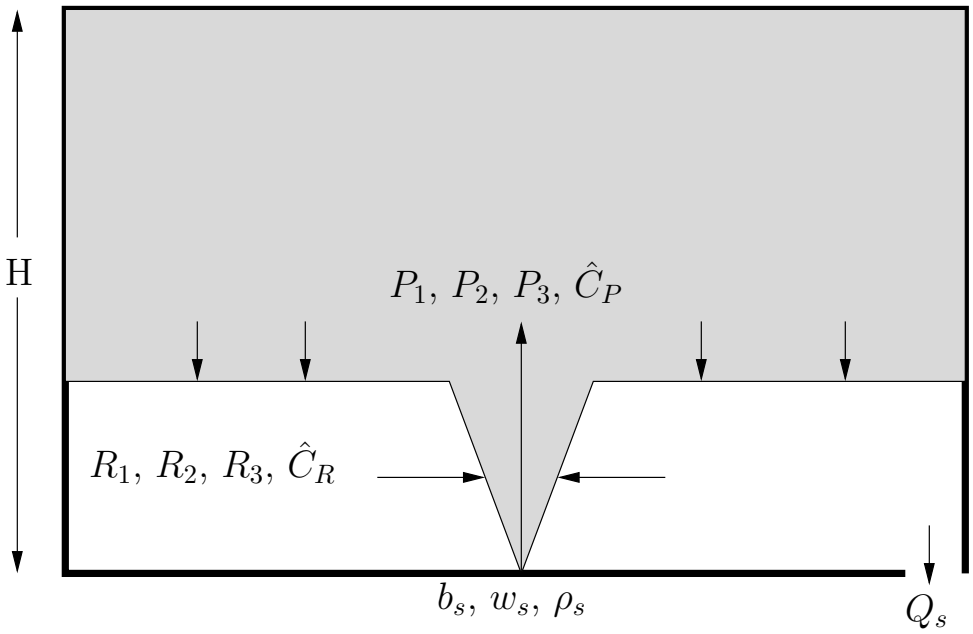

Figure 3.1: Schematic representation of the flow geometry discussed in the text.

dynamics of the ensuing plume are highly turbulent and irregular at sufficiently high Reynolds number, MTT56 demonstrated that the dynamics of the evolving plume can be understood well through consideration of the behavior of three integrated conserved quantities: the volume flux πQ, the specific momentum flux πM and the specific buoyancy flux πB, defined as

$$\pi Q(z,t) = \frac{2\pi}{T_t}\int_{t-T_t/2}^{t+T_t/2}\int_0^\infty r w_P \,\mathrm{d}t\,\mathrm{d}r = \pi \bar{w}_P b^2, \tag{3.1}$$

$$\pi M(z,t) = \frac{2\pi}{T_t}\int_{t-T_t/2}^{t+T_t/2}\int_0^\infty r w_P^2 \,\mathrm{d}t\,\mathrm{d}r = \pi \bar{w}_P^2 b^2, \tag{3.2}$$

$$\begin{aligned}\pi B(z,t) &= \frac{2\pi}{T_t}\int_{t-T_t/2}^{t+T_t/2}\int_0^\infty r w_P g\frac{\rho_R-\rho_P}{\rho_{R0}}\,\mathrm{d}t\,\mathrm{d}r \\ &= \pi g\frac{\rho_R-\bar{\rho}_P}{\rho_{R0}}\bar{w}_P b^2 = \pi g'_P \bar{w}_P b^2.\end{aligned} \tag{3.3}$$

In the equations above $w_P(r,z,t)$ and $\rho_P(r,z,t)$ are the vertical velocity and density profiles in the plume, ρ_R is the ambient density, ρ_{R0} is a reference density, the initial (constant) density in the room, and g'_P is the reduced gravity of the plume relative to the local ambient fluid. Bars denote averages over the plume. The

various fluxes are in general time-dependent, but we take a rolling time average to smooth out turbulent fluctuations over time scales substantially shorter than a characteristic time scale T_t. For simplicity we assume that the flow in the plume has a top hat profile, i.e. the vertical velocity and density take one value inside the plume and another value outside: at all heights and times the plume is defined with a characteristic radius $b(z,t)$. (This makes it clear that consideration of the three fluxes Q, M and B is equivalent to consideration of the three characteristic properties of the plume: its radius b, its velocity w_P and the plume reduced gravity g'_P.) As discussed in MTT56, it is straightforward to derive governing equations for the fluxes within a plume under the assumption that the characteristic entrainment velocity u_e can be related to the vertical velocity w_P at every height within the plume by an universal constant of proportionality, the so-called entrainment constant α, to yield

$$\frac{\partial Q}{\partial z} = 2\alpha M^{1/2}, \tag{3.4}$$

$$\frac{\partial M}{\partial z} = \frac{BQ}{M}, \tag{3.5}$$

$$\frac{\partial B}{\partial z} = \frac{g}{\rho_{R0}}\frac{\partial \rho_R}{\partial z}Q = -N^2 Q, \tag{3.6}$$

where N^2 is the buoyancy frequency.

3.3.2 Room dynamics

The equations discussed above are closed provided source conditions Q_s, M_s and B_0 for volume flux, momentum flux and initial buoyancy flux (or equivalently source radius, velocity and density) are given, and there is some mechanism to determine the ambient density distribution outside the plume. In the circumstance we are considering, namely that of an isolated single plume rising from the bottom ($z = 0$) of an enclosed space with one vent at the same level as the source, the ambient density is coupled to, and determined by, the plume dynamics in a straightforward manner, as discussed in more detail in CW02. We assume that the plume is sufficiently isolated (i.e. $b^2 \ll A_c$ at all heights in the room, where A_c

is the cross-sectional area of the room) for the entrainment into the plume to be essentially horizontal. Therefore, the fluxes evolve as the plume rises in the room in a manner that is well approximated by the equations (3.6).

However, when the plume reaches the ceiling, the upper boundary forces the fluid at the top of the plume to spread out horizontally like a gravity current. As discussed in BT69 and considered in more detail in Hunt, Cooper & Linden (2001) provided the aspect ratio and the source momentum flux are sufficiently small, a filling box flow then develops, and the fluid from the gravity current descends in well organized horizontal layers into the room surrounding the plume when it encounters the side walls. Therefore, the ambient density distribution evolves in a time and depth-dependent manner due to the continual arrival of plume fluid at the ceiling.

This evolving ambient density also affects the plume behavior through entrainment. Indeed, as fluid is entrained into the plume there must be a return flow in the room to conserve mass. BT69 demonstrated that for a confined room if the plume occupies a negligible cross-sectional area (and so $\pi b^2 \ll A_c$ as already assumed) of the room then the return flow is uniform and given by the volume conservation relation

$$w_R A_c \simeq -\pi Q, \tag{3.7}$$

where w_R is the vertical velocity of the ambient fluid in the room. Assuming that the flow is sufficiently high Reynolds number so that the effects of diffusion can be ignored compared to advection in the equation for conservation of mass for the fluid within the room, (3.7) can be used to obtain

$$\frac{\partial \rho_R}{\partial t} = \frac{\pi Q}{A_c} \frac{\partial \rho_R}{\partial z}, \tag{3.8}$$

where we have used the fact that there is no net flow through the room due to the vent and the source both being at the floor of the room. This equation closes the system given an initial density distribution of $\rho_R = \rho_{R0}$ within the room, leading to what is referred to as a "filling box process".

It is important to appreciate that there is an essential quasi-steady approximation at the heart of the filling box process. Although the ambient density distribution in the room is evolving, it is assumed that it varies sufficiently slowly compared to the rising plume so that the plume can be assumed to be passing through a time-independent ambient density in the room. Equivalently to the assumption that the plume is isolated, the filling box process requires that the upward velocity w_P in the plume is always very much greater than the downward velocity in the environment, and so

$$\frac{M}{Q} \gg \frac{\pi Q}{A_c}. \tag{3.9}$$

Characteristic scaling for these quantities can be found by considering for simplicity the well-known "point source" similarity solution, where the source is a source of buoyancy alone with $Q_s = 0 = M_s$. For this situation, the governing equations for flow in an unstratified environment admit a similarity solution

$$Q = \frac{6\alpha}{5}\left(\frac{9\alpha B_0}{10}\right)^{1/3} z^{5/3}; \quad M = \left(\frac{9\alpha B_0}{10}\right)^{2/3} z^{4/3}. \tag{3.10}$$

For this similarity solution, the plume velocity drops monotonically with distance from the source, while the volume flux naturally increases monotonically due to entrainment. Therefore, the most stringent restriction for (3.9) is at the ceiling, when $z = H$, in which case the validity condition becomes a condition on an aspect ratio parameter θ such that

$$\theta = \left(\frac{5}{6\alpha}\right)^2 \frac{A_c}{\pi H^2} \gg 1. \tag{3.11}$$

Therefore, we expect the quasi-steady approximation to be valid provided the aspect ratio of the room is sufficiently small, and hence the parameter θ is sufficiently large.

The source conditions (as noted on figure 3.3) that we choose to use are constant source radius b_s, source velocity w_s, and source density ρ_s, corresponding to constant source volume flux $Q_s = b_s^2 w_s$, source specific momentum flux $M_s =$

$b_s^2 w_s^2$, and initial source buoyancy flux $B_0 = g(\rho_{R0} - \rho_s)Q_s/\rho_{R0}$. As discussed in more detail in CW02, due to the finite source volume flux and the location of the vent, the density of the ambient fluid at the source decreases below ρ_{R0} in finite time, as fluid that has been cycled through the plume reaches the external opening. Therefore, since $\rho_R(0) < \rho_{R0}$, if the source has a flux of constant density fluid, the source buoyancy flux satisfies $B_s = g(\rho_R(0) - \rho_s)Q_s/\rho_{R0} < B_0$, and over time the source will behave less and less as the source of a buoyant plume, and more and more as the source of a forced momentum jet.

3.3.3 Chemistry dynamics

We now generalize the filling box process to allow for the time-dependent chemical reaction of different species. For simplicity, we do not allow the chemically reacting species to affect the flow dynamically. In particular, we assume that any heat of reaction is sufficiently small so that it does not affect the fluid density. This is a valid assumption for the experimental fluids and reactions which we consider in this Chapter. We consider the situation where two distinct species can react to form a third product species through a second order reaction. Therefore, in general, we are interested in the spatial and temporal evolution of these three species both within the plume rising from the isolated source, and in the ambient fluid within the room. We denote the concentration of the three species within the plume as $P_1(z,t)$ and $P_2(z,t)$ for the reactants, and $P_3(z,t)$ for the product, while in the room we denote the equivalent quantities by $R_1(z,t)$, $R_2(z,t)$ and $R_3(z,t)$. The isolated plume source fluid is assumed to contain only species one with concentration P_{10}, while the room initially contains only species two, with concentration R_{20}. Therefore, the boundary and initial conditions are

$$P_2(0,t) = P_3(0,t) = R_1(z,0) = R_3(z,0) = 0;\ P_1(0,t) = P_{10}; R_2(z,0) = R_{20}. \tag{3.12}$$

As ambient fluid is entrained into the plume in a height and time-dependent manner, the concentration P_2 of species two within the plume fluid will increase

from zero initially. Similarly, when the filling box process starts at the ceiling of the room, the concentration R_1 of species one at the ceiling will increase from zero. Once these dynamic effects have taken place, we then assume that a second order non-reversible reaction takes place between the reacting species both in plume fluid rising from the isolated source and in the room. A second-order non-reversible reaction is a reaction of the form

$$P_1 + P_2 \rightarrow P_3, \;\; R_1 + R_2 \rightarrow R_3, \tag{3.13}$$

in which the mutual presence of species one and two is necessary for the reaction and the reaction rate is proportional to the product of the concentrations of the two reacting species (for further details, see e.g. Levine 2002). Then

$$\frac{\mathrm{D}P_1}{\mathrm{D}t} = \frac{\mathrm{D}P_2}{\mathrm{D}t} = -KP_1P_2; \qquad \frac{\mathrm{D}P_3}{\mathrm{D}t} = KP_1P_2; \tag{3.14}$$

$$\frac{\mathrm{D}R_1}{\mathrm{D}t} = \frac{\mathrm{D}R_2}{\mathrm{D}t} = -KR_1R_2; \qquad \frac{\mathrm{D}R_3}{\mathrm{D}t} = KR_1R_2. \tag{3.15}$$

Here, the second order rate constant $K(T, \mu)$ is determined experimentally for a particular reaction and may in general be a function of temperature, T and, in the case of solutions, of ionic strength, μ. $\mathrm{D}/\mathrm{D}t$ is the conventional convective derivative, since the reaction is a Lagrangian process that advects passively with fluid parcels. The potential dependencies on temperature and ionic strength are very important, because if the fluid density within the room is due to temperature or compositional differences (e.g. through varying concentrations of sodium chloride) then we expect the reaction rate to vary with this density. In the room, consistently with the assumptions at the heart of the filling box process, we assume that all motions are homogeneous, and that diffusive processes are insignificant compared to advection. Therefore, there is no vertical mixing, and no vertical reaction between the various species in the room, and so the evolutions of the various concentrations R_1, R_2 and R_3 are determined purely by (3.15).

However, we are also interested in understanding how the various species vary with height within the plume. We consider as an example the flux of species

one in the plume through a particular level within the room, which must satisfy

$$\frac{\partial}{\partial z}[P_1 Q] = 2R_1 \alpha M^{1/2} - \frac{Q^2}{M} K P_1 P_2. \tag{3.16}$$

The first term on the right hand side of (3.16) quantifies the entrainment by the plume of species one from the room fluid (with concentration R_1) while the second term quantifies the loss of species one due to reaction, using the definition of the plume velocity, $w_P = M/Q$. Using the product rule on the left hand side of (3.16) and rearranging, we can then derive an equation for the spatial variation of species one in the rising plume:

$$\frac{\partial P_1}{\partial z} = \frac{2\alpha M^{1/2}}{Q}(R_1 - P_1) - K\frac{Q}{M} P_1 P_2. \tag{3.17}$$

Analagous equations can naturally be derived for the other species within the plume, yielding

$$\frac{\partial P_2}{\partial z} = \frac{2\alpha M^{1/2}}{Q}(R_2 - P_2) - K\frac{Q}{M} P_1 P_2, \tag{3.18}$$

$$\frac{\partial P_3}{\partial z} = \frac{2\alpha M^{1/2}}{Q}(R_3 - P_3) + K\frac{Q}{M} P_1 P_2. \tag{3.19}$$

As in the dynamic filling box process, inherent in this model is a quasi-steady approximation, in that we assume that the room concentration of the various species does not vary appreciably during the vertical propagation of a particular fluid parcel in the plume. Comparing the typical transit time of a fluid parcel, using the velocity estimates at the ceiling derived from the similarity solution (3.10) to the inverse of the reaction rate (scaled with the maximum concentrations of species one and two) yields the condition

$$\left(\frac{5}{6\alpha}\right)\left(\frac{9\alpha B_0}{10}\right)^{1/3} \gg K H^{4/3} \sqrt{R_{20} P_{10}}. \tag{3.20}$$

3.3.4 Well-mixed models

The isolated source within the room inevitably leads to vertical variations in both density and species concentration within the room. However, particularly when the source volume flux is small compared to the volume flux of the

plume when it arrives at the ceiling, (and hence significant entrainment occurs during the plume evolution towards the ceiling) the developing layers can be well-approximated by well-mixed layers (see CW02 for a fuller discussion). Assuming that the room is completely well-mixed leads to simple models for the evolution of the densities and species within the room. The time evolution of the well-mixed density ρ_W within the room must satisfy the equation

$$\frac{d}{dt}(A_c H \rho_W) = \pi \rho_s Q_s - \pi \rho_W Q_s;\ \rho_W(0) = \rho_{R0}, \tag{3.21}$$

since the source continually supplies fluid of density ρ_s with the same volume flux as the well-mixed fluid which leaves through the external opening. Therefore, under this assumption, the well-mixed fluid within the room is predicted to converge exponentially to the density of the source fluid:

$$\frac{\rho_{R0} - \rho_W}{\rho_{R0} - \rho_s} = 1 - \exp\left[\frac{-\pi Q_s}{A_c H} t\right]. \tag{3.22}$$

Similar reduced models can be derived for well-mixed concentrations W_1, W_2 and W_3 for each of the three species. For species one (input at the source) we obtain

$$\frac{d}{dt}(A_c H W_1) = -K A_c H W_1 W_2 + \pi Q_s (P_{10} - W_1);\ W_1(0) = 0 \tag{3.23}$$

since there is initially none of this species in the room, there is a constant flux (with concentration P_{10} by definition) from the source, and there are losses due to reaction with species two and outflow of the well-mixed concentration through the source. Similar equations for W_2 and W_3 are

$$\frac{d}{dt}(A_c H W_2) = -K A_c H W_1 W_2 - \pi Q_s W_2;\ W_2(0) = R_{20}, \tag{3.24}$$

$$\frac{d}{dt}(A_c H W_3) = K A_c H W_1 W_2 - \pi Q_s W_3;\ W_3(0) = 0, \tag{3.25}$$

showing that W_2 decreases from its original value of R_{20} due both to reaction and outflow, while W_3 increases due to reaction provided the other two species are present, but decreases due to outflow. Although these equations do not have

a simple solution, it is clear that as $t \to \infty$, $W_2 \to 0$ and hence $W_3 \to 0$ and $W_1 \to P_{10}$, i.e. the input concentration of species one eventually fills the interior, analogously to the way the room density approaches that of the source fluid. We will be interested in identifying circumstances when these well-mixed models are adequate descriptions of the flow evolution, and also the parameter ranges in which the complexities inherent in the more general filling box description are observable and significant.

3.3.5 Nondimensionalization

We now introduce nondimensional variables (see CW02 for a detailed discussion). The natural length scale to use is the height H of the room. Motivated by the form of the well-mixed density, we scale the density difference from the initial ambient density by the density difference between initial ambient and source fluid, i.e.

$$\hat{z} = \frac{z}{H}, \qquad \hat{C}(z,t) = \frac{\rho - \rho_{R0}}{\rho_s - \rho_{R0}}. \tag{3.26}$$

Therefore, for the plume fluid at the source the fluid density concentration $\hat{C}_P(0,t) = 1$, while initially for the ambient fluid in the room, the fluid density concentration $\hat{C}_r(z,0) = 0$. It is natural to scale the volume flux with its source value Q_s, and the buoyancy flux with its initial value B_0, i.e.

$$\hat{Q}(z,t) = \frac{Q}{Q_s};\ \hat{Q}(0,t) = 1, \tag{3.27}$$

$$\hat{B}(z,t) = \frac{B}{B_0};\ \hat{B}(0,t) = 1 - \hat{C}_R(0,t). \tag{3.28}$$

As observed above, requiring the source density to be constant as in this model, with a nonzero source volume flux, implies that the source buoyancy flux can drop from its initial value as the first front reaches the floor of the room, (and so $\hat{C}_R(0,t) > 0$) which must happen in finite time if the source has nonzero source volume flux and the external opening is at the same height as the source.

From comparison with the point source similarity solution (3.10) discussed above, the source volume flux Q_s can be used to define a so-called "effective

origin" (see Caulfield & Woods 1995, Hunt & Kaye 2001) z_e:

$$Q_s = \frac{6\alpha}{5}\left(\frac{9\alpha B_0}{10}\right)^{1/3} z_e^{5/3}, \tag{3.29}$$

i.e. z_e is the notional location below $z = 0$ of a point source with buoyancy flux B_0 which would have volume Q_s at $z = 0$ given by the similarity solution (3.10). Clearly, this point source would also have a particular momentum flux M_{ss} at $z = 0$ given by the similarity solution, where

$$M_{ss} = \left(\frac{9\alpha B_0}{10}\right)^{2/3} z_e^{4/3}. \tag{3.30}$$

We use this characteristic scale M_{ss} to nondimensionalize the momentum flux, and so

$$\hat{M} = \frac{M}{M_{ss}}; \quad \hat{M}(0,t) = \hat{M}_s. \tag{3.31}$$

If $\hat{M}_s > 1$ the source has an excess of momentum flux above the point source similarity solution, and so it is commonly referred to as a forced plume. This is equivalent to the source either having too small a source radius, or too large a source velocity. Conversely, if $\hat{M}_s < 1$, the source has a deficit of momentum flux, and it is referred to either as a distributed (Caulfield & Woods 1995) or lazy plume (Hunt & Kaye 2001) as this deficit is equivalent either to a large source radius, or a small source velocity. Finally, if $\hat{M}_s = 1$, the plume is said to be in pure plume balance, (see Caulfield & Woods 1995) and the plume follows the similarity solution (3.10) for all time (with z replaced by the offset $z + z_e$).

Since the source volume flux is essential to the flow dynamics, the natural time scale of the fluid flow is the fluid replacement time or turnover time scale t_r, defined as

$$t_r = \frac{A_c H}{\pi Q_s}, \tag{3.32}$$

i.e. the time required by the source to replace completely the fluid within the room in the absence of entrainment, and so we define $\hat{t} = t/t_r$. This is also the characteristic time scale of the well-mixed model, as is clear from (3.22), which

can be written in terms of a well-mixed fluid density concentration $\hat{C}_W$ as

$$\hat{C}_W = 1 - e^{-\hat{t}}. \tag{3.33}$$

However, it is important to appreciate that all the chemical species within the room may not converge to their steady states on the replacement time scale, particularly in situations where the reaction rate is relatively fast, and so reaction plays a dominant effect in determining the time scale for the chemical species, rather than the (finite volume flux) filling box flow dynamics. We discuss this in more detail below, particularly in section 3.4.

For the chemical concentrations, as already noted, the natural scaling is the geometrical mean of the two initial concentrations, and so we nondimensionalize as follows

$$[\hat{R}_1(\hat{z},\hat{t}), \hat{R}_2(\hat{z},\hat{t}), \hat{R}_3(\hat{z},\hat{t})] = \frac{(R_1, R_2, R_3)}{\sqrt{P_{10}R_{20}}}, \tag{3.34}$$

$$[\hat{P}_1(\hat{z},\hat{t}), \hat{P}_2(\hat{z},\hat{t}), \hat{P}_3(\hat{z},\hat{t})] = \frac{(P_1, P_2, P_3)}{\sqrt{P_{10}R_{20}}}, \tag{3.35}$$

with initial and boundary conditions

$$\hat{R}_1(\hat{z},0) = \hat{R}_3(\hat{z},0) = 0; \quad \hat{R}_2(\hat{z},0) = \sqrt{\frac{R_{20}}{P_{10}}} \equiv \phi, \tag{3.36}$$

$$\hat{P}_2(0,\hat{t}) = \hat{P}_3(0,\hat{t}) = 0; \quad \hat{P}_1(0,\hat{t}) = \frac{1}{\phi}. \tag{3.37}$$

with $\hat{R}_1 = R_1/\sqrt{P_{10}R_{20}} \to \sqrt{P_{10}/R_{20}} = 1/\phi$ and $\hat{R}_2 \to 0$ as $\hat{t} \to \infty$. We also use $\sqrt{R_{20}P_{10}}$ and t_r to define a nondimensional reaction rate λ as

$$\lambda = \frac{K\sqrt{R_{20}P_{10}}A_c H}{\pi Q_s}, \tag{3.38}$$

where it is important to remember that, since λ can be a function of temperature and ionic strength, it may depend on the local values of the fluid density, or equivalently fluid density concentration. Using this scaling, the quasi-steady approximation for the reaction (3.20) takes the form (using (3.11) and (3.29))

$$\frac{\theta}{\hat{z}_e^{5/3}\lambda} \gg 1, \tag{3.39}$$

which is clearly related to the quasi-steady approximation condition (3.11) for the validity of the filling box process.

Using these natural scalings, the plume equations may be rewritten as

$$\frac{\partial \hat{Q}}{\partial \hat{z}} = \frac{5}{3\hat{z}_e}\hat{M}^{1/2}, \tag{3.40}$$

$$\frac{\partial \hat{M}}{\partial \hat{z}} = \frac{4}{3\hat{z}_e}\frac{\hat{B}\hat{Q}}{\hat{M}}, \tag{3.41}$$

$$\frac{\partial \hat{B}}{\partial \hat{z}} = -\hat{Q}\frac{\partial \hat{C}_R}{\partial \hat{z}}, \tag{3.42}$$

with the boundary conditions as already noted

$$\hat{Q}(0,t) = 1;\ \hat{M}(0,t) = \hat{M}_s;\ \hat{B}(0,t) = 1 - \hat{C}_R(0,t). \tag{3.43}$$

If the ambient concentration is constant and zero, and $\hat{M}_s = 1$ so that the plume is in pure plume balance, the similarity solution (3.10) takes the form

$$\hat{Q} = \left(\frac{\hat{z}+\hat{z}_e}{\hat{z}_e}\right)^{5/3}; \qquad \hat{M} = \left(\frac{\hat{z}+\hat{z}_e}{\hat{z}_e}\right)^{4/3}. \tag{3.44}$$

The equation for the evolution of the ambient density in the room (3.8) becomes

$$\frac{\partial \hat{C}_R}{\partial \hat{t}} = \hat{Q}\frac{\partial \hat{C}_R}{\partial \hat{z}}; \qquad \hat{C}_R(\hat{z},0) = 0. \tag{3.45}$$

Similarly, the equations for the evolution of the chemical species in the room (3.15) and in the isolated source (3.17)-(3.19) become respectively

$$\frac{D\hat{R}_1}{D\hat{t}} = -\lambda \hat{R}_1 \hat{R}_2, \tag{3.46}$$

$$\frac{D\hat{R}_2}{D\hat{t}} = -\lambda \hat{R}_1 \hat{R}_2, \tag{3.47}$$

$$\frac{D\hat{R}_3}{D\hat{t}} = \lambda \hat{R}_1 \hat{R}_2, \tag{3.48}$$

and

$$\frac{\partial \hat{P}_1}{\partial \hat{z}} = \frac{5}{3\hat{z}_e}\frac{\hat{M}^{1/2}}{\hat{Q}}(\hat{R}_1 - \hat{P}_1) - \frac{\lambda \hat{z}_e^2}{\theta}\frac{\hat{Q}}{\hat{M}}\hat{P}_1\hat{P}_2, \tag{3.49}$$

$$\frac{\partial \hat{P}_2}{\partial \hat{z}} = \frac{5}{3\hat{z}_e}\frac{\hat{M}^{1/2}}{\hat{Q}}(\hat{R}_2 - \hat{P}_2) - \frac{\lambda \hat{z}_e^2}{\theta}\frac{\hat{Q}}{\hat{M}}\hat{P}_1\hat{P}_2, \tag{3.50}$$

$$\frac{\partial \hat{P}_3}{\partial \hat{z}} = \frac{5}{3\hat{z}_e}\frac{\hat{M}^{1/2}}{\hat{Q}}(\hat{R}_3 - \hat{P}_3) + \frac{\lambda \hat{z}_e^2}{\theta}\frac{\hat{Q}}{\hat{M}}\hat{P}_1\hat{P}_2, \tag{3.51}$$

with initial and boundary conditions

$$\hat{P}_1(0,\hat{t}) = \frac{1}{\phi};\ \ \hat{P}_2(0,\hat{t}) = \hat{P}_3(0,\hat{t}) = 0; \tag{3.52}$$

$$\hat{R}_2(\hat{z},0) = \phi;\ \ \hat{R}_1(\hat{z},0) = \hat{R}_3(\hat{z},0) = 0. \tag{3.53}$$

It is apparent by using (3.44) at $\hat{z} = 1$ that the quasi-steady assumption for the chemically reacting species (3.39) corresponds to requiring that the second terms on the right hand side of (3.51) be appropriately small. Finally, the well-mixed equations (3.23)–(3.25) for the various chemical species become

$$\frac{\mathrm{d}\hat{W}_1}{\mathrm{d}\hat{t}} = \frac{1}{\phi} - \hat{W}_1 - \lambda\hat{W}_1\hat{W}_2; \qquad \hat{W}_1(0) = 0, \tag{3.54}$$

$$\frac{\mathrm{d}\hat{W}_2}{\mathrm{d}\hat{t}} = -\hat{W}_2 - \lambda\hat{W}_1\hat{W}_2; \qquad \hat{W}_2(0) = \phi, \tag{3.55}$$

$$\frac{\mathrm{d}\hat{W}_3}{\mathrm{d}\hat{t}} = -\hat{W}_3 + \lambda\hat{W}_1\hat{W}_2; \qquad \hat{W}_3(0) = 0. \tag{3.56}$$

Two particular limiting solutions of these equations are useful for understanding the time scales of the evolution of the reacting species within the flow, particularly in the circumstances which we consider experimentally. Firstly, if $\lambda\hat{W}_2 \ll 1$, which is certainly always true when $\lambda\phi \ll 1$, then, under the further simplifying assumption that the reaction rate is independent of the local density,

$$\hat{W}_{1a} \simeq \frac{1}{\phi}(1 - e^{-\hat{t}}), \tag{3.57}$$

$$\hat{W}_{2a} \simeq \phi \exp\left[-\left(\hat{t} + \frac{\lambda}{\phi}\left[\hat{t} - 1 + e^{-\hat{t}}\right]\right)\right]. \tag{3.58}$$

This corresponds to a situation where the concentration of species two is always very low, and the reaction is pseudo first order, with the concentration of species two limiting the reaction of the input species one. The other limiting case is $\lambda\hat{W}_1 \ll 1$ (definitely the case initially, but true for all time if $\lambda/\phi \ll 1$) then, where once again if we assume that λ is independent of the local density,

$$\hat{W}_{1b} \simeq \frac{1 - \exp\left[-\left(t + \lambda\phi\left[1 - e^{-\hat{t}}\right]\right)\right]}{\phi} - \lambda\left[E_1\left(\lambda\phi e^{-\hat{t}}\right) - E_1\left(\lambda\phi\right)\right]\exp\left[-t + \lambda\phi e^{-\hat{t}}\right], \tag{3.59}$$

$$\hat{W}_{2b} \simeq \phi e^{-\hat{t}}, \tag{3.60}$$

where $E_1(v)$ is the exponential integral, (see Abramowitz & Stegun 1965) defined, for positive v as

$$E_1(v) = \int_v^\infty \frac{e^{-u}}{u} du. \tag{3.61}$$

This solution has the correct asymptotic behaviour of $\hat{W}_1$ increasing towards $1/\phi$ as $\hat{t} \to \infty$. For this limit to always apply, since $\phi \gg 1$, the concentration of species one is always very much less than species two, and the reaction is again pseudo first order, now limited by the (low) concentration in the incoming plume fluid.

For both of these limits, the concentrations of the reacting chemical species are predicted to approach their asymptotic values on the fluid replacement time scale t_r, at least to leading order. The reaction, because of the (assumed) wide disparity in the concentrations of the two species is a higher order effect. This is because the evolution of the chemical species is dominated by the volume flux into and out of the room (just as is the well-mixed fluid density concentration $\hat{C}_W$ defined in (3.33)) rather than by the chemical reactions, which is "slow" in some sense, because the limiting assumptions are only satisfied if the reaction rate λ is relatively small. As can be seen from (3.56), it is not immediately clear whether the replacement time scale is the natural time scale for reactions with larger λ, consistent of course with the quasi-steady assumption through satisfying (3.39). To investigate this issue and others, we wish to compare the various well-mixed models both with the predictions of the full models and with the results of laboratory experiments, where, as discussed below, for technical reasons we find it convenient to use extreme values of ϕ (both large and small).

3.4 Numerical modelling

3.4.1 Numerical method

We solved the plume evolution equations (3.42), the ambient concentration equation (3.45), the room chemical equations (3.46), and the plume chemical equations (3.51), subject to the boundary and initial conditions (3.43) and (3.53)

using the numerical integration scheme of Germeles (1975). With this method the ambient density and chemical concentrations are discretized into a finite number of layers, separated by sharp interfaces. As already noted, quasi-steady assumptions (3.11) and (3.39) allow us, at every timestep, to solve the spatial evolution equations for the plume dynamical and chemical properties using a fourth order Runge–Kutta scheme from the given source conditions $\hat{z}_e$, $\hat{M}_s$ and ϕ to the top of the room with "frozen" ambient profiles of density and chemical species concentration. Any density dependence of the reaction rate λ can be straightforwardly included as the density in the plume at each height is known. We then update the ambient profiles, installing a new layer at the top of the room consisting of the arriving plume fluid, changing the layer depths consistently with the entrainment into the plume, (or equivalently the velocity of the various interfaces given by (3.45)). We also evolve the various chemical species within each layer using (3.48), as solving for each of the species in each layer is equivalent to solving the reaction equation following fluid parcels, with the reaction rate determined if necessary by the local density of the fluid layer. We continue to evolve our calculation until the flow reaches its ultimate steady state, with the room completely filled with fluid of source density $\hat{C}_R \to 1$, and chemical species $\hat{R}_1 \to 1/\phi$. Typically this occurs over time scales of the order of a few fluid replacement times.

3.4.2 Parameter ranges

The complete system (3.42), (3.45)-(3.51), with boundary and initial conditions (3.43) and (3.53) is thus described by five parameters: $\hat{z}_e$ and $\hat{M}_s$ which essentially determine the source conditions for the plume; ϕ which determines the source conditions for the chemical species; $\lambda(\hat{C})$ which determines the reaction rate, and which may be a function of the local fluid density concentration; and θ which determines the room aspect ratio. Central to the quasi-steady assumptions necessary for this model is that θ is sufficiently large, and $\lambda\hat{z}_e^{5/3}$ is sufficiently small so that (3.11) and (3.39) are satisfied but there is clearly still a very large

parameter space that can be described by this model. We shall follow two guiding principles in our choice of parameters to discuss, without presenting an overwhelming number of studies. As our primary focus is the behaviour of the chemically reacting species, our discussion will focus on the dependence of the system on the two chemically related parameters λ and ϕ. The choices of the other parameters will be restricted to specific values characteristic of physically realistic situations, as we discuss in more detail below.

Although the condition on the aspect ratio parameter θ is implicit in previous studies of non-reacting filling box flows, it does not play an explicit role provided an appropriate nondimensional formulation is used. Here, however, due to the presence of the competing time dependent processes of the filling box process and the reaction between the two species, the particular value of θ is essential to the formulation, as it inevitably appears in the equation for the evolution of $\hat{P}_i$ in (3.51). For rooms which are roughly cubic, (and so $A_c \sim H^2$) $\theta \sim 20$–30, (which is naturally consistent with the quasi-steady approximation) since typical values of the entrainment constant are of the order of $\alpha \sim 0.1$, and so in this section we fix $\theta = 20$.

There are also sensible restrictions which can be placed on the value of the effective origin $\hat{z}_e$. For at least four reasons it is natural to consider flows where $\hat{z}_e$ is significantly less than one. Firstly, such flows, where the plume undergoes substantial entrainment before it reaches the top of the enclosed space, are commonplace in environmental and industrial applications. Secondly, such flows are more likely to enable a quasi-steady filling box process to develop. Thirdly, as is well known, such flows are more straightforward to model experimentally (as discussed in more detail below) and therefore are more likely to allow the direct experimental verification of our theoretical model. Finally, for such flows the well-mixed models are likely to be approximations of at least some utility, and so the comparison between the detailed and more reduced models are likely to be more meaningful. Therefore, in this section we consider $\hat{z}_e = 0.1$.

There are then two natural choices for the source momentum flux $\hat{M}_s$. Firstly, choosing $\hat{M}_s = 1$ implies that initially the plume is in pure plume balance, and therefore follows the similarity solution defined in (3.44). This is useful for illustrative purposes, has been commonly done previously, and is what we choose to do in this section. A particular attraction of this choice is that an analytical expression can be derived for the nondimensional arrival time $\hat{t}_a$ of the first front at the source location $\hat{z} = 0$, which, as we see below, is an important separating time in the flow evolution. Indeed, as discussed in more detail in CW02, for the similarity solution (3.44) it is clear that

$$\hat{t}_a \equiv \int_1^0 \frac{d\hat{z}}{\hat{w}_r} = \int_0^1 \frac{d\hat{z}}{\hat{Q}} = \frac{3}{2}\hat{z}_e \left(1 - \left[\frac{\hat{z}_e}{1+\hat{z}_e}\right]^{2/3}\right), \tag{3.62}$$

which can be significantly less than one (and hence dimensionally significantly less than the replacement time scale of the room) when $\hat{z}_e \ll 1$.

It is important to stress that after this time, since the source buoyancy flux drops from its initial value, the plume ceases to be in pure plume balance, and becomes forced, with the source momentum flux playing an increasingly more important role as the flow tends towards its steady state with the room completely filled by source fluid, and the source behaving like a pure momentum jet (see CW02 for a more detailed discussion). Furthermore, a possible area for lack of agreement between the various well-mixed models and the detailed plume filling box model is due to the difference of behaviour of the two systems before this time. All the well-mixed models assume from the initial instant that fluid at least slightly affected by the plume (either through having a density less than the initial room density or through having a nonzero concentration of species one) leaves through the vent. However, in reality, fluid that has been cycled through the plume only leaves once the first front reaches the floor, and hence the opening to the exterior. In circumstances where the effective origin $\hat{z}_e \ll 1$, this time is significantly shorter than the characteristic replacement time for the room to approach its final steady state, and so we expect that the influence of this initial mismatch might be small.

The other natural choice for a source condition for the momentum flux is motivated by conventional experimental techniques. For a source of a given area A_s, if it is assumed that the source velocity is constant across this area, then dimensionally $M_s = Q_s^2/A_s$, or equivalently, using the scalings of this Chapter

$$\hat{M}_s = \frac{A_c}{A_s}\frac{\hat{z}_e^2}{\pi\theta}. \tag{3.63}$$

We use this scaling in § 3.5 when we compare our model to our experiments.

For these particular choices of the parameters governing the plume dynamics, the vertically averaged fluid density concentration $\bar{\hat{C}}_R$ remains very close to the fluid density concentration $\hat{C}_W$ predicted by the well-mixed model defined in (3.33). In particular, the fluid density evolves on the time scale of the fluid replacement time scale defined in (3.32). Since we wish to focus on the evolution of the chemical species, we do not show the time evolution of the density concentrations in this Chapter. The time dependence of the vertically averaged concentration is discussed in some detail in CW02. Indeed, these fixed, and reasonable, choices of three of the parameters allow us to devote our attention to the effect of variations in the chemically related parameters.

Since it is still necessary for our quasi-steady approximation (3.39), λ is restricted such that

$$\lambda \ll \frac{\theta}{\hat{z}_e^{5/3}} \sim 1000, \tag{3.64}$$

for the chosen values of the other parameters. This is not very restrictive, and so to understand the effect of marked variations in λ, we consider the two choices $\lambda = 0.1$ and 10, both of which still satisfy (3.64). This allows us to investigate what the appropriate time scales for the chemical species are when the reaction rate λ is sufficiently large to be significant compared to the finite volume flux filling box process, which occurs on the fluid replacement time scale. Furthermore, as we discuss in § 3.5, this range is appropriate for the experimental system we considered.

On the other hand, ϕ is not constrained by an essential assumption.

However, since we derived above particular explicit reduced models for $\lambda\phi \ll 1$ and $\lambda/\phi \ll 1$, (i.e. (3.58) and (3.60)), we consider the two choices $\phi = 0.1$ and $\phi = 10$. These choices also are of the order that are feasible in the laboratory.

3.4.3 Vertically averaged results

Since we are interested in the quality of the predictions of the reduced models in comparison to the full numerical model, for each of the four possible combinations of λ and ϕ, we first consider various vertically averaged chemical quantities in the room. In Figures 3.2 and 3.3, we plot the evolution against time of $\bar{\hat{R}}_i$ for $i = 1, 2, 3$ where the overbar denotes vertical averaging in the room, for flows with $\phi = 0.1$ and $\phi = 10$ respectively. We also plot the predictions of the various well-mixed models: $\hat{W}_i$ for $i = 1, 2$ as defined by the well-mixed model (3.56); $\hat{W}_{ia}$ for $i = 1, 2$ for the analytical model when $\lambda\hat{W}_2 \ll 1$ as defined in (3.58); and $\hat{W}_{ib}$ for $i = 1, 2$ for the analytical model when $\lambda\hat{W}_1 \ll 1$ as defined in (3.60). We expect $\hat{W}_{ia}$ to be most applicable when $\lambda = 0.1$, $\phi = 0.1$, (i.e. figures 3.2a and 3.2c) and $\hat{W}_{ib}$ to be most applicable when $\lambda = 0.1$, $\phi = 10$ (i.e. figures 3.3a and 3.3c). Because of the wide disparity, for these values of ϕ, between the initial values of $\bar{\hat{R}}_2 = \phi$ and the final values of $\bar{\hat{R}}_1 = 1/\phi$, we plot $\bar{\hat{R}}_3$ (using a thick solid line) for each of the four flows on the panel with the smallest vertical extent: i.e. with $\bar{\hat{R}}_2$ when $\phi = 0.1$ in figure 3.2, and with $\bar{\hat{R}}_1$ when $\phi = 10$ in figure 3.3. This is because the magnitude of the concentration of the reaction product will naturally be determined by the lesser magnitude of the concentrations of the reactants.

In general, it is clear from the figure that the concentration of species one (initially input from the source) within the room approaches its steady state value (of $1/\phi$) on the time scale of a few fluid replacement time scales. The only exception to this observation appears to be shown in figure 3.3b. This is due to the effect of a large reaction rate (i.e. $\lambda \gg 1$) and a significantly larger initial concentration of species two in the room, thus leading to initial suppression in the

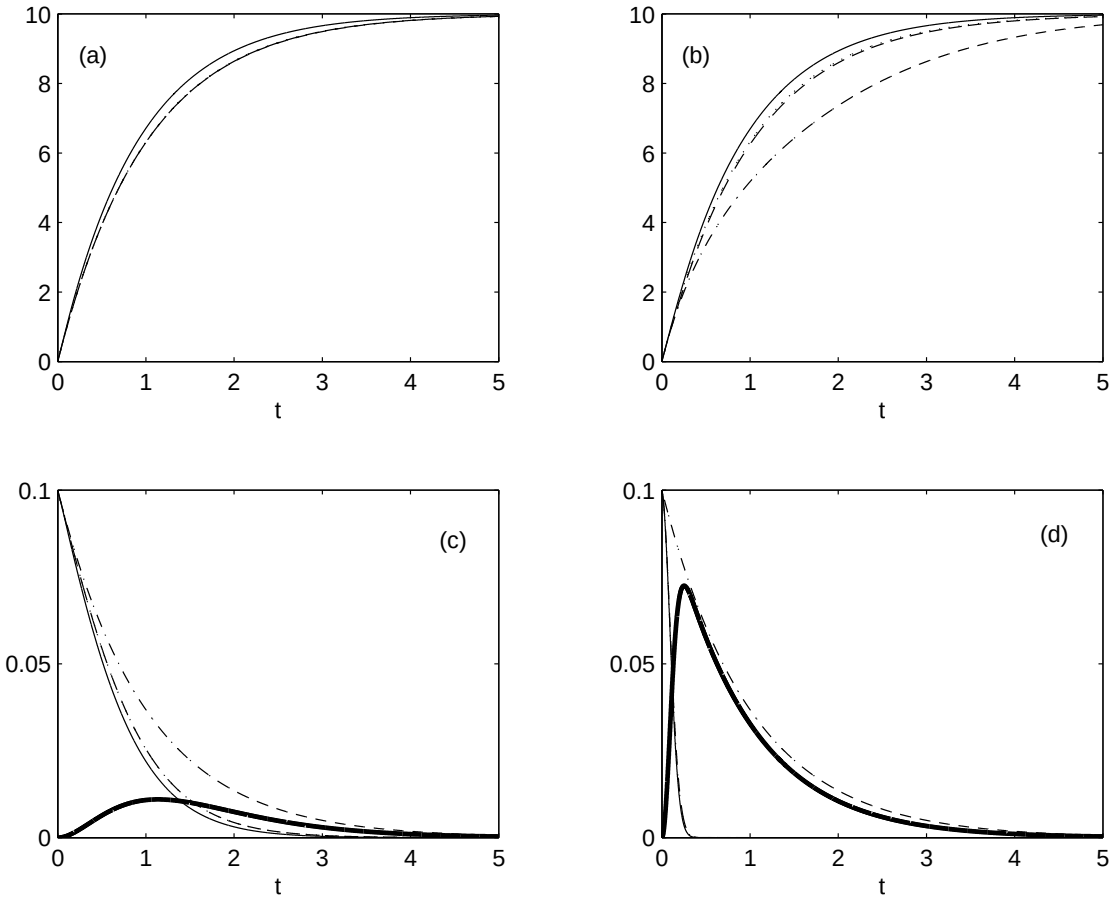

Figure 3.2: Variation with time of vertically averaged concentrations $\bar{\hat{R}}_1$ (plotted with a solid line), $\hat{W}_1$ as defined by (3.56) (dashed line), $\hat{W}_{1a}$ as defined by (3.58) (dotted line), and $\hat{W}_{1b}$ as defined by (3.60) (dot-dashed line), for flows with $\hat{M}_s = 1$, $\hat{z}_e = 0.1$, $\theta = 20$, $\phi = 0.1$ and (a) $\lambda = 0.1$; (b) $\lambda = 10$. Variation with time of vertically averaged concentrations $\bar{\hat{R}}_2$ (plotted with a solid line), $\bar{\hat{R}}_3$ (thick solid line), $\hat{W}_2$ as defined by (3.56) (dashed line), $\hat{W}_{2a}$ as defined by (3.58) (dotted line), and $\hat{W}_{2b}$ as defined by (3.60) (dot-dashed line), for flows with $\hat{M}_s = 1$, $\hat{z}_e = 0.1$, $\theta = 20$, $\phi = 0.1$ and (c) $\lambda = 0.1$; (d) $\lambda = 10$.

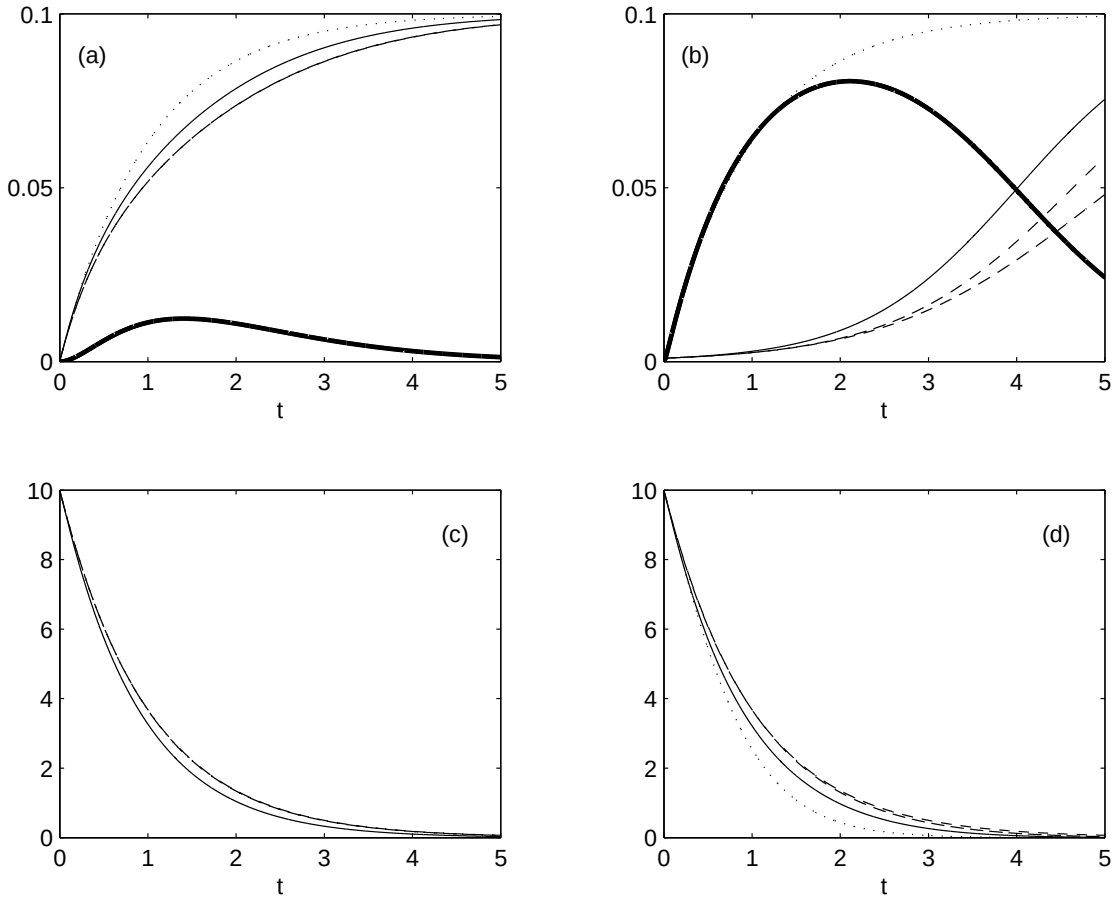

Figure 3.3: Variation with time of vertically averaged concentrations $\bar{\hat{R}}_1$ (plotted with a solid line), $\bar{\hat{R}}_3$ (thick solid line), $\hat{W}_1$ as defined by (3.56) (dashed line), $\hat{W}_{1a}$ as defined by (3.58) (dotted line), and $\hat{W}_{1b}$ as defined by (3.60) (dot-dashed line), for flows with $\hat{M}_s = 1$, $\hat{z}_e = 0.1$, $\theta = 20$, $\phi = 10$ and (a) $\lambda = 0.1$; (b) $\lambda = 10$. Variation with time of vertically averaged concentrations $\bar{\hat{R}}_2$ (plotted with a solid line), $\hat{W}_2$ as defined by (3.56) (dashed line), $\hat{W}_{2a}$ as defined by (3.58) (dotted line), and $\hat{W}_{2b}$ as defined by (3.60) (dot-dashed line), for flows with $\hat{M}_s = 1$, $\hat{z}_e = 0.1$, $\theta = 20$, $\phi = 10$ and (c) $\lambda = 0.1$; (d) $\lambda = 10$.

rate of increase of species one within the room, until all species two is lost. Since there is a large initial concentration of species two, this takes a relatively long time.

Analogously, species two appears to drop to zero on the same time scale except in the case where there is a small initial concentration (i.e. $\phi \ll 1$) and the reaction rate is high, as shown in figure 3.2d. This is unsurprising, as the large reaction rate rapidly depletes the small initial room concentration of species two in this case. The effect of high reaction rate is also apparent in the evolution of the product species three, whose peak value is substantially higher in the cases of large λ (figures 3.2d and 3.3c) than when $\lambda \ll 1$.

It is also apparent that the well-mixed models capture much of the character of the evolution of the concentrations within the room when they are expected to be relevant, (i.e. figures 3.2a and 3.3a) for the range of parameter choices presented. On the other hand, $\hat{W}_{1a}$ is a very poor approximation when $\lambda = 10$, $\phi = 10$ (i.e. the dotted line in figure 3.3b). This is unsurprising, since this choice of parameters violates strongly the assumption for this reduced well mixed model, namely that $\lambda\phi \ll 1$. However, there is a clear systematic error, with at a given time the well-mixed models over-estimating $\bar{\hat{R}}_2$ and underestimating $\bar{\hat{R}}_1$. This can be straightforwardly understood from consideration of the behaviour of the system at early times. The well-mixed models assume that some species one (input by the source in fact) is vented from the opening at the floor of the room from the very first instant. Therefore, the well-mixed models assume that the vented fluid has concentration of species two less than its original concentration. However, until the first front has reached the floor of the room, none of species one is actually vented, and all the fluid which is vented has the initial room concentration of species two. Although, for the choice of the parameters presented here the arrival time, as defined in (3.62) is $\hat{t}_a = 0.1197 \ll 1$, nevertheless the initial period leads to the well-mixed models overpredicting the amount of species one and underpredicting the amount of species two vented from the room. This leads to the observed underprediction of species one within the room, and overprediction of species two

within the room. For the particular parameter choices shown, there is typically little difference between the numerical and analytical well-mixed models defined by (3.56)-(3.60).

The evidence points to the fluid replacement time scale is also an appropriate time scale for the chemical concentrations within the room, a fact that can also be deduced from the reduced models, except when $\lambda \gg 1$. However, an important aspect of the flow, (particularly for application to hazard analysis) is the dependence of the (product) species three on the two chemical parameters: i.e. nondimensional initial room concentration ϕ and the reaction rate λ. As can be observed qualitatively in figures 3.2 and 3.3, increasing λ leads to a larger peak value of $\bar{\hat{R}}_3$, while increasing ϕ leads to the later occurrence of this peak. To understand this behaviour quantitatively, and also to identify the relevance of the well-mixed model concentration $\hat{W}_3$ defined by (3.56), in figure 3.4 we plot the peak values of $\bar{\hat{R}}_3$ and $\hat{W}_3$, and the (nondimensional) time $\hat{t}_p$ of occurrence of this peak against ϕ for the two values $\lambda = 0.1$ and $\lambda = 10$ used in figures 3.2 and 3.3.

Certain characteristics are apparent. As already noted, larger values of λ correspond to larger values of peak values of the product concentration, unsurprisingly, since larger values of λ imply more vigorous reaction before the filling box process leads to loss of the finite quantity of species two (initially in the room) through the external vent. There is also a clear non-monotonic variation of the peak value with ϕ for a given value of λ, with a maximum occurring around $\phi \sim 1$. For small values of ϕ, the concentration of the product species three is limited by the initial concentration ϕ of species two in the room. In particular if ϕ is very small, it is rapidly depleted by any reaction and the peak concentration of species three occurs at a very small value. On the other hand, for large values of ϕ, the concentration of species three is limited by the source concentration $1/\phi$ of species one entering the room through the source, and in particular when λ is large, the peak concentration of species three exhibits a $1/\phi$ dependence at large ϕ.

Turning attention to the usefulness of the well-mixed model, for both

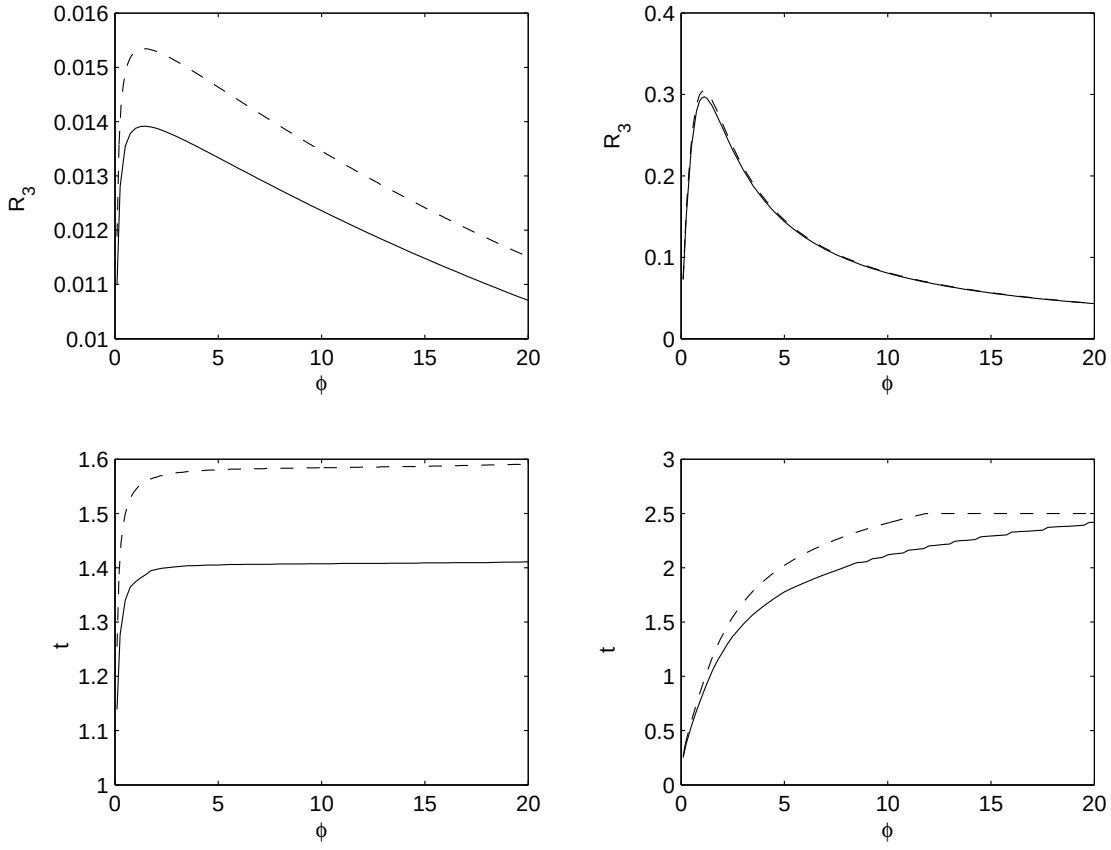

Figure 3.4: Variation with ϕ of the peak value of the vertically averaged concentration $\bar{\hat{R}}_3$ of the chemical product (plotted with a solid line), and the well-mixed concentration $\hat{W}_3$ as defined by (3.56) (dashed line), for flows with $\hat{M}_s = 1$, $\hat{z}_e = 0.1$, $\theta = 20$, and (a) $\lambda = 0.1$; (b) $\lambda = 10$. Variation with ϕ of the time $\hat{t}_p$ for the occurrence of the peak value of the vertically averaged concentration $\bar{\hat{R}}_3$ of the chemical product (plotted with a solid line), and the time for the occurrence of the peak value of the well-mixed concentration $\hat{W}_3$ as defined by (3.56) (dashed line), for flows with $\hat{M}_s = 1$, $\hat{z}_e = 0.1$, $\theta = 20$, and (c) $\lambda = 0.1$; (d) $\lambda = 10$.

shown values of λ, $\hat{W}_3$ over-estimates the actual peak value of the product chemical species concentration, although the well-mixed model does appear to be a good approximation, particularly when $\lambda = 10$ (figure 3.4). This over-estimation is principally due to the fact, as noted above, that the well-mixed model over-estimates the concentration of species two, i.e. the species initially within the room. Since more of species two is assumed to remain within the room by the well-mixed model, more reaction is assumed to take place than actually occurs within the full model. This effect is not so significant for larger values of λ, as for flows with higher reaction rates, differences in the evolution of species two between the well-mixed model and the full model are not so important, and the evolution is more strongly determined by the reaction rate.

The time t_p for the occurrence of the peak value of the product species three concentration also exhibits qualitatively different behaviour for small and large values of ϕ. For smaller values of λ (figure 3.4c), this time is essentially constant, and of the order of the fluid replacement time except when ϕ is very small. When ϕ is very small of course, species two is rapidly depleted, and so the reaction ends very early. However, for larger values of ϕ the chemical species concentrations within the flow evolve on the filling box replacement time scale, and so the time to peak concentration varies only weakly with ϕ. The well-mixed model systematically over-estimates $\hat{t}_p$, due as usual to the fact that it systematically over-estimates the amount of species two remaining in the room, and thus the potential for further reaction to take place between the incoming source fluid (containing only species one) and the finite quantity of species two.

For larger values of λ, (as shown in figure 3.4d) t_p behaves in a qualitatively different manner, both in not being so strongly determined by the fluid replacement time scale (which has been used in the nondimensional scheme, and thus corresponds to $\hat{t}_p = 1$) and also in showing a strong dependence on ϕ. For smaller values of ϕ, increasing λ actually reduces t_p. As is apparent in figure 3.2, when ϕ is small, and so the reaction is limited by the concentration of species two

initially in the room, high reaction rates rapidly deplete this species, and so the product species three reaches its maximum concentration very quickly, in a manner that does not depend strongly on the filling box process. Conversely, when ϕ is large, the reaction is limited by the low incoming source concentration $1/\phi$ of species one. For flows with higher reaction rates, peak concentrations of the product species three can occur even after significant loss of species two through the external opening, (due to the filling box process) since the cumulative input of species one associated with the large initial concentration of species two in the room can lead to more efficient reaction than in flows with smaller values of λ. Nevertheless, the peak concentration of the reaction species still occurs within a relatively small number of fluid replacement times, as inevitably species two will all be lost from the room through the external opening, as source fluid completely fills the room.

3.4.4 Vertical profile results

We are not only interested in vertically averaged outputs form our models, but also in the time-dependent behaviour of vertical profiles of the various flow quantities of interest. In figures 3.5 and 3.6, we plot vertical profiles for each of the four quantities of interest ($\hat{C}_R$ and $\hat{R}_i$ for $i = 1, 2, 3$) at evenly spaced time intervals $\hat{t}_j = j/5$; $j = 1, 2, 3 \ldots$, i.e. at intervals of 20% of the fluid replacement time t_r defined by (3.32) for the same parameter choices considered in figures 3.2 and 3.3 respectively. Similarly to the fluid density concentration profile $\hat{C}_R$ as considered previously in CW02, each of the profiles shows a clear vertical concentration gradient, strongest near the floor of the room. In each case, the gradient approaches zero over time. Unsurprisingly, it is clear that, when $\lambda = 10$ and $\phi = 0.1$, so that the reaction is both fast, and the initial concentration of $\hat{R}_2$ is small, the room is rapidly depleted of species two, as shown in figure 3.5g. Also, it is clear in the last column (figures 3.5d, 3.5h, 3.6d and 3.6h) that $\hat{R}_3$ increases from zero in the room as reactions take place, and then drops towards zero as species two is completely

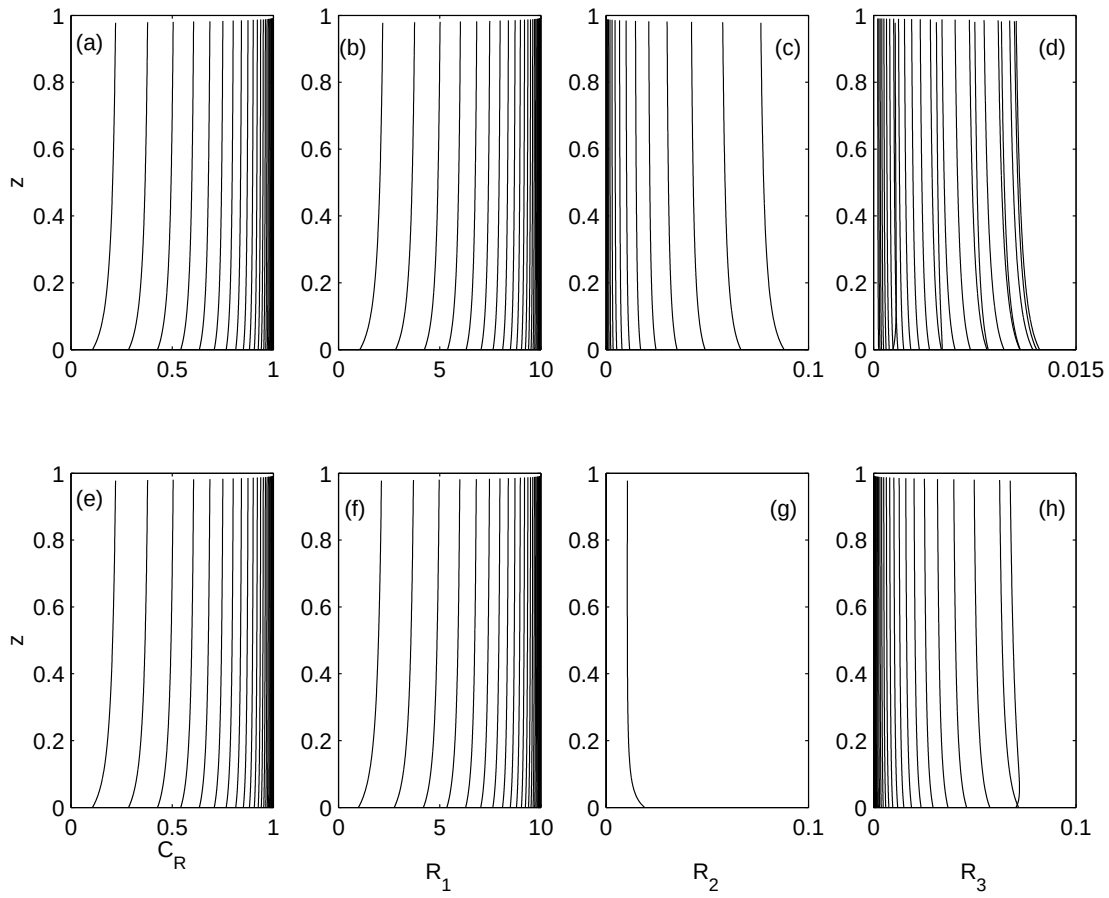

Figure 3.5: Concentration profiles as a function of height at times $\hat{t}_j = j/5$; $j = 1, 2, 3 \ldots$ for: $\hat{C}_R$, (panels a, e); $\hat{R}_1$, (panels b, f); $\hat{R}_2$, (panels c, g); $\hat{R}_3$, (panels d, h). In all cases $\hat{M}_s = 1$, $\hat{z}_e = 0.1$, $\theta = 20$, and $\phi = 0.1$ while: $\lambda = 0.1$ in panels a-d; $\lambda = 10$ in panels e-h.

depleted.

Interestingly, species one (the species input from the source) and species two (the species initially in the room) are qualitatively different in their vertical structure. Species one is similar to the density concentration, in that it has smallest value near the floor of the room, increasing towards the ceiling. This is unsurprising, as both enter the room through the plume. As the flow evolves, and the plume rises through and re-entrains fluid that has already been cycled through the plume, the concentration of both fluid density and species one in the plume

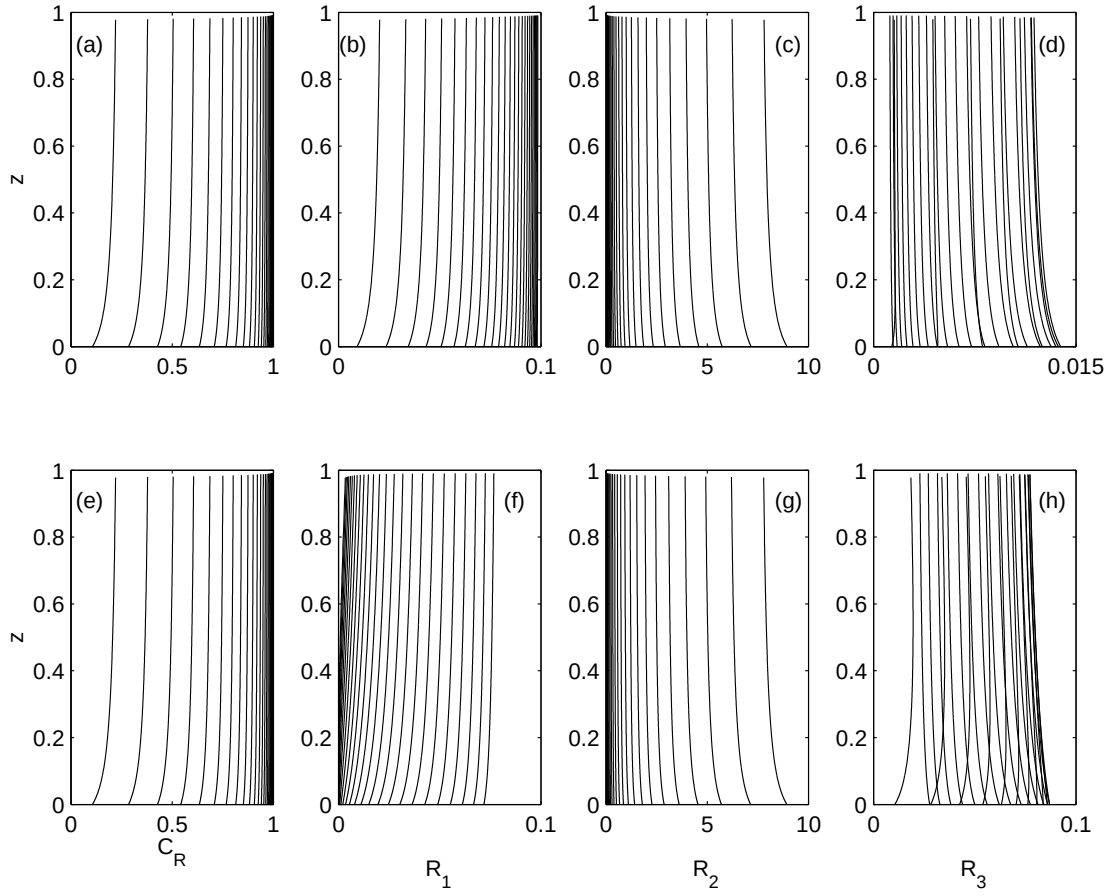

Figure 3.6: Concentration profiles as a function of height at times $\hat{t}_j = j/5$; $j = 1, 2, 3 \ldots$ for: $\hat{C}_R$, (panels a, e); $\hat{R}_1$, (panels b, f); $\hat{R}_2$, (panels c, g); $\hat{R}_3$, (panels d, h). In all cases $\hat{M}_s = 1$, $\hat{z}_e = 0.1$, $\theta = 20$, and $\phi = 10$ while: $\lambda = 0.1$ in panels a-d; $\lambda = 10$ in panels e-h.

as it reaches the ceiling (and spreads out as a new layer) must increase, thus leading to a positive vertical gradient. Conversely, the concentration of species two is greater near the floor of the room, since species two is originally in the room alone. Therefore, the layers within the room which have had a longer residence time, and have been less affected by the plume, will tend to have higher concentrations of species two. These layers naturally are closer to the floor.

Finally, the product species three exhibits aspects of both of these behaviours. At early times, when both species one and species two are present in nontrivial quantities, vertical profiles of species three behave like those of species one, with higher concentrations at higher points in the room. This is due to the fact that fluid cycled through the plume is accessing sufficient quantities of species two to lead, through reaction, to creation of the product species three. Therefore, more recently created layers, near the ceiling of the room, will have higher concentrations of species three. However, eventually species two becomes depleted, and so less and less creation of the product species three occurs. The older layers (which were generated when reaction was more prevalent) have higher concentrations of species three. Therefore, at later times, profiles of species three are similar to those of species two, with greater concentrations closer to the floor of the room. Having developed these models, we now investigate whether their predictions agree with the results of analogue laboratory experiments.

3.5 Experiments

3.5.1 Experimental method

We conducted the experiments in a plexiglass tank (43 cm $\times$ 28 cm $\times$ 28.8 cm) open to the exterior at the upper surface with two evenly spaced holes drilled in the tank bottom. The first hole contained a plume source, located far enough away from the walls so that $A_c \gg b^2$ at all heights within the plume. The source consisted of a small tube connected to an expansion chamber with a pin

sized hole on the upstream side, following a design originally due to Dr Paul Cooper (see Hunt & Linden (2001) for a more detailed description of the design). On the downstream side of the chamber is plastic gauze leading to a 5 mm diameter orifice, through which the final discharge occurs. The flow is essentially turbulent on exit. A tank mounted at the ceiling of the laboratory supplied the source. The level of the supply tank was maintained by a pump and overflow system connected to a larger tank located on the floor, and hence the hydrostatic pressure head between the supply tank and experimental tank was constant. During the experiment the pump was only turned on intermittently so as to not increase the fluid temperature, as the reaction rate of the chemical species which we used is strongly sensitive to temperature. The second hole in the experimental tank was connected to a vertical tube opening to the exterior air. The level of the top of this tube was modified until a hydrostatic balance was reached with the fluid inside the experimental tank, such that throughout the entire course of the experiment, the depth of fluid in the experimental tank remained constant, with extremely small fluctuations. Therefore, we were confident that the flows into and out of the experimental tank were constant and equal to Q_s (which we were able to modify).

Density variations between the plume fluid and the room were caused in the conventional way by varying the concentration of sodium chloride in the room fluid initially. In all cases, the source fluid had no salt content, and so was buoyant relative to the initial room fluid, whose density could be varied experimentally. The two chemical species used in the experiments were malachite green, a triphenylmethane dye, and sodium hydroxide, a strong base. In the presence of a strong base the malachite green, which is green in solution, bonds with the hydroxide anion to form a colorless molecule. There are three reasons why these two species are appropriate for an experimental verification of our model. Firstly, the reaction rate is sufficiently slow for the quasi-steady assumption to be valid for the range of concentrations that we consider. Secondly, although there is some energy release during the reaction, it can be shown to be sufficiently small to have a

negligible effect on the fluid density and reaction rate. Finally, it is straightforward to measure quantitatively changes in color of the solution experimentally, and thus to measure the changing concentration of one of the chemical species with time.

We lit the experimental apparatus uniformly from one side, and videoed the experimental tank through the other side using a digital monochrome ccd camera. The light intensity of this image then acts as a proxy for the colored dye still remaining in the tank, and hence the concentration of one of the chemically reacting species, when the time sequence of images are analyzed with appropriate image analysis software. We used the package DigImage, (see for example Dalziel 1993) and so we were able to measure how both vertical profiles and the mean concentration of one of the species varied with time. In most experiments, we used malachite green as species one, and so the source contained only malachite green, while the room initially had a nonzero concentration of sodium hydroxide (as species two). In this case, we tracked how the light intensity changed as the room approached being filled with green fluid alone. However, we also considered the reversed situation, where the source had a nontrivial concentration of sodium hydroxide, and the room was initially filled with some concentration of malachite green. In this case we were able to track how the color decreased in the room as both reaction and outflow through the opening led to the loss of malachite green.

Essential to this experimental technique is of course the calibration of light intensity with concentration of the malachite green chemical species. We determined this by placing a known concentration, determined on a mass basis, in the tank, and then recording the measured light intensity. This process was repeated about 20 different times between the maximum concentration used in the experiment and the smallest concentration distinguishable by the camera.

For the comparison of our experimental results with our theoretical models, it was also necessary to determine the (dimensional) rate constant K, which needs to be considered carefully. Although sodium chloride, which as noted above was used to increase the density of the ambient fluid, does not have a significant

side reaction with the reacting chemical species, its presence does increase the ionic strength of the solution, and thus decreases the rate constant of the reaction. Since the concentration of salt in the tank changes with time we needed to determine experimentally how the rate constant varied with salt concentration. Also, K is unsurprisingly a strong function of temperature. Therefore, through each experiment we carefully monitored the fluid temperature, and minimized temperature fluctuations. The peak variation in temperature was always less than 0.5°C.

To determine the functional form of K, we placed a known concentration of malachite green G_0 and sodium hydroxide H_0 in the tank with a known quantity of salt and digitally analyzed the change in the light intensity with time associated with the color change of the fluid from green to clear. To simplify our analysis, the concentration of sodium hydroxide was two to three orders of magnitude larger than the concentration of malachite green in these calibration experiments, and so the reaction was pseudo first order. Therefore, the time dependent concentration $G(t)$ of malachite green is given by the expression

$$\log\left(\frac{G(t)}{G_0}\right) \simeq -KH_0t. \tag{3.65}$$

For a range of saline solutions between zero and seven per cent, by plotting $\log(G/G_0)$ against time, and determining the best fit to the slope of the resulting line, we calculated the dependence of the rate constant on salinity. This salinity, and hence density dependent, rate constant could then be straightforwardly included within our code, to generate model predictions as discussed above.

We conducted seven experiments, with a range of parameters. We present the results of three characteristic experiments in this Chapter, with parameters given in table 1. For agreement with our calibration curves for the rate constant, the initial concentration of malachite green was always substantially less than the concentration for sodium hydroxide, and so it is at least plausible that one or other of the limiting well-mixed models (defined in (3.58) and (3.60)) will describe the experimental data well. As already noted, in all but one experiment, malachite green corresponded to species one, input by the source, and so we are able to

Table 3.1: Nondimensional constants and initial fluid density in the tank for each experiment performed. The values for λ are multiplied by the rate constant K, which varies between 0.3 and 1.2 depending on the salinity.

Experiment	$\hat{z}$	$\hat{M}_s$	ϕ	θ	λ	$\rho_R(\mathrm{kg/m^3})$
A	0.054	0.176	10	32.1	$1.05K$	1.001
B	0.054	0.176	15.1	32.1	$1.38K$	1.05
C	0.054	0.176	.0644	32.1	$1.42K$	1.02

monitor the concentration of the dye that comes into and eventually thoroughly contaminates the tank. In the other experiment, (experiment C) we initially placed the dye in the tank (i.e. as species two) and we monitored its concentration until it eventually got completely vented out and consumed by the reaction.

3.5.2 Experimental results and discussion

We have plotted the results from both the experiment and numerical method in figures 3.7–3.9. We have used $\alpha = 0.1$, a common value used in experiments. Small variations of this parameter have a negligible effect on our results. We have also assumed that the velocity was constant at the source so that given some source flow rate the source momentum flux could be determined by $M_s = Q_s^2/A_s$. In figures 3.7 and 3.8 we first plot the vertically averaged concentration of species one in the room, i.e. $\bar{\hat{R}}_1$, as a function of time, and then two height-dependent concentration profiles at different times. In figure 3.9, we plot the same quantities for species two. In all cases, we compare the experimental measurements with numerical solutions using the full model discussed in Section 3.4.

In all cases $\hat{z}_e \ll 1$, giving us a large fluid entrainment and a subsequent fast downward ambient layer velocity. Because of this, the time it takes for the first front to reach the vent in the figures shown is $\hat{t}_a = 0.075 \ll 1$. It should be noted that in all cases the initial concentration of sodium hydroxide is about two hundred times larger than that of the dye, leading to extreme values for ϕ,

for consistency with our calibration. Therefore in a region of fluid containing this large imbalance in chemical concentration, the rate of change of the base will be much slower than dye, and the reaction is pseudo first order. Indeed, since it can be established for the experiments shown in figures 3.7 and 3.8 that $\lambda/\phi \ll 1$, we also compare the average room concentration of species one with $\hat{W}_{1b}$ from the well-mixed solution (3.60), while for the experiment shown in figure 3.9, $\lambda\phi \ll 1$, and so we compare with $\hat{W}_{2a}$ as defined in (3.58). In addition we have plotted the numerical solution to the well-mixed models from equations (3.54-3.55). In all cases the rate constant in the well-mixed models is a function for fluid density for consistency with the experimental results.

The error bars shown in the averaged concentration profiles are due to the uncertainty in the laboratory equipment used, such as the scale, beakers and flow meter, all of which were taken from the manufacturer's listed data. The error comes into effect in the experimental results mainly through the color intensity-concentration calibration data and in the numerical method via the nondimensional constants and the correction to the rate constant for density variations. It should be noted that the error bars shown in the average concentration profiles also apply to the height dependent profiles even though they are not indicated in those figures. In all of the figures shown there is good agreement between the numerical and experimental data; the curves lie within the range of experimental uncertainty. The fluctuation in the concentration for the experiment, seen by the jagged appearance, is a consequence of the optical method used and the mean profile contains all the important physical information.

As noted above, the most obvious point of difference between the well-mixed models and both the experimental and full numerical data is during the initial stage of flow evolution, before the time $\hat{t}_a$ when the first front arrives at the opening and contaminated fluid starts to be vented through the opening. Although this time is early in the overall flow evolution, the early behaviour has a lasting effect, and so it is clearly necessary to model the plume dynamics. The plume

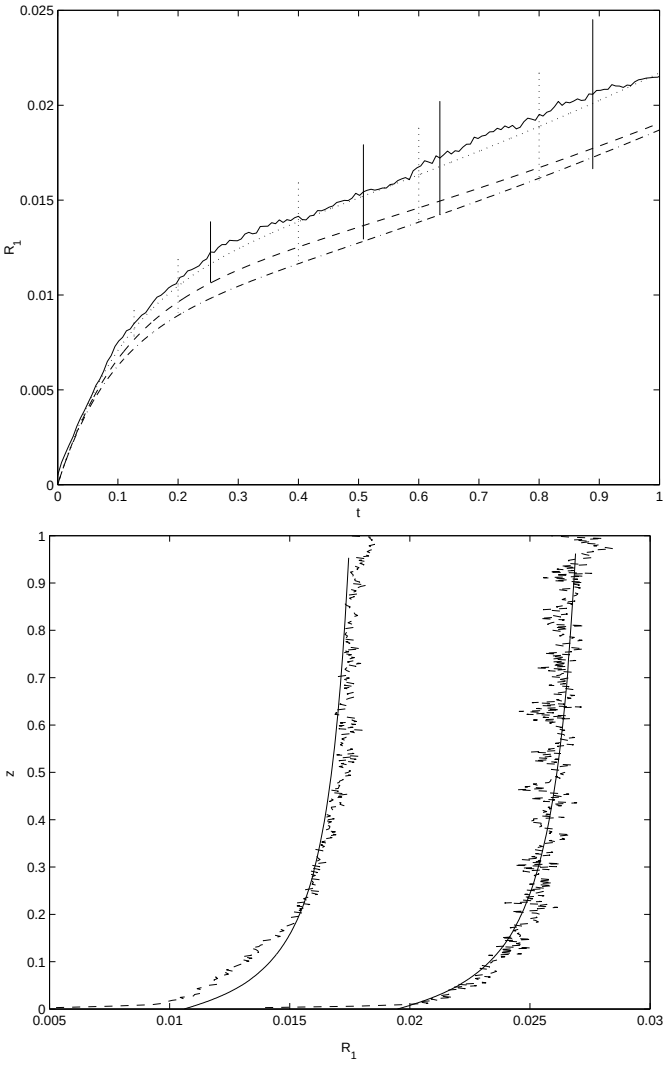

Figure 3.7: Vertically averaged (top) and height dependent (bottom) plots of species one for experiment A (solid jagged line) and the plume model (dotted line on upper plot and solid line on bottom plot), as defined in § 3.4. The two profiles on the bottom plot represent $\hat{t} = 0.59$ and $\hat{t} = 1.24$. The vertical lines on the upper plot are error bars for the numerical solution (dotted line) and experiment (solid line). We also plot the predicted concentration for species one from the well-mixed model (3.54)–(3.55) (dashed line) and the reduced model (3.60) (dot-dashed line) in the upper panel. The parameters are given in table 1.

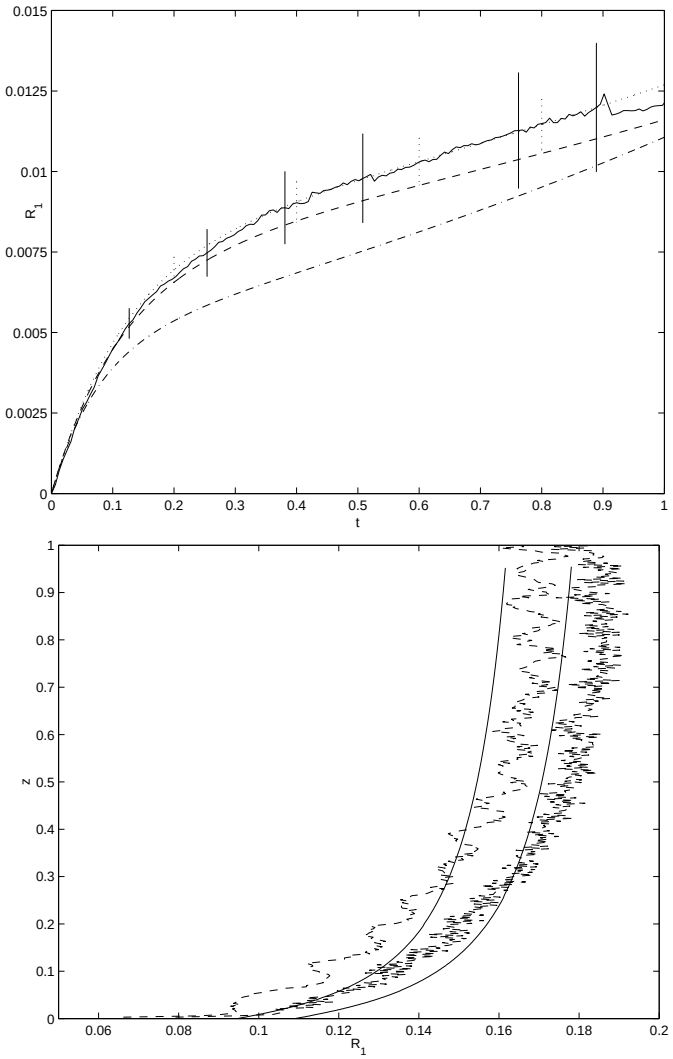

Figure 3.8: Vertically averaged (top) and height dependent (bottom) plots of species one for experiment B (solid jagged line) and the plume model (dotted line on upper plot and solid line on bottom plot), as defined in § 3.4. The two profiles on the bottom plot represent $\hat{t} = 0.50$ and $\hat{t} = 0.68$. The vertical lines on the upper plot are error bars for the numerical solution (dotted line) and experiment (solid line). We also plot the predicted concentration for species one from the well-mixed model (3.54)–(3.55) (dashed line) and the reduced model (3.60) (dot-dashed line) in the upper panel. The parameters are given in table 1.

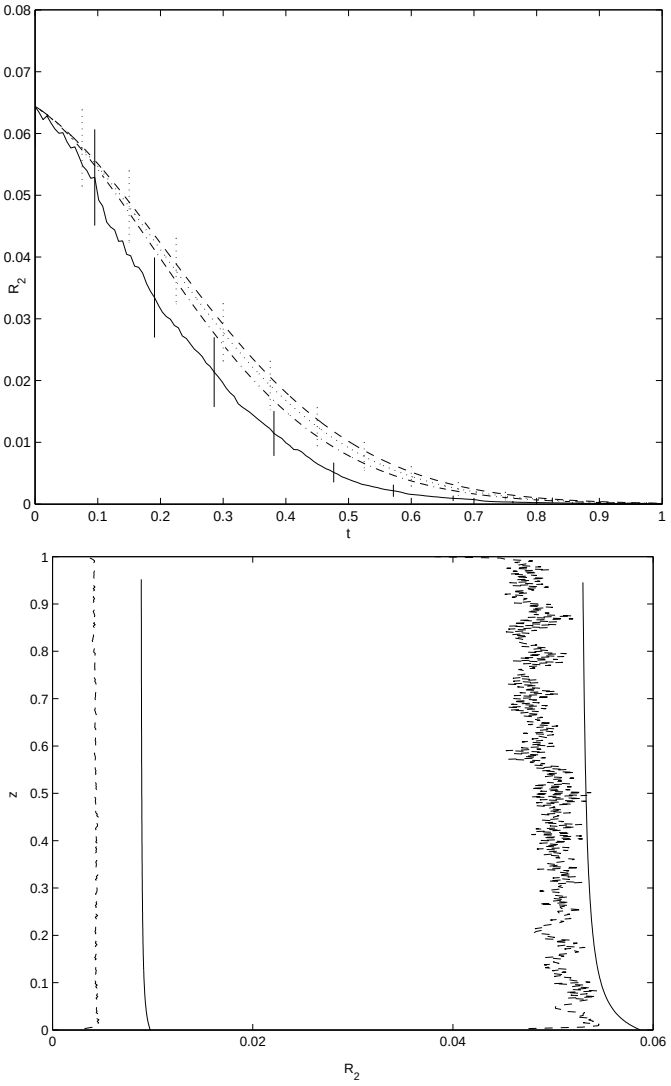

Figure 3.9: Vertically averaged (top) and height dependent (bottom) plots of species two for experiment C (solid jagged line) and the plume model (dotted line on upper plot and solid line on bottom plot) as defined in § 3.4. The two profiles on the bottom plot represent $\hat{t} = 0.50$ and $\hat{t} = 0.11$. The vertical lines on the upper plot are error bars for the numerical solution (dotted line) and experiment (solid line). We also plot the predicted concentration for species two from the well-mixed model (3.54)–(3.55) (dashed line) and the reduced model (3.58) (dot-dashed line) in the upper panel. The parameters are given in table 1.

model sets up a concentration gradient of $\hat{R}_2$, (the concentration of the chemical species initially in the room) which decreases with height, where the oldest and most concentrated layer is at the bottom $\hat{z} = 0$. As a result a larger quantity of species two leaves the room sooner than if the space were well mixed, while conversely a smaller quantity of species one leaves the room, thus leading to a higher concentration of $\bar{\hat{R}}_1$ at any particular instant compared to the well-mixed model. This result can be seen clearly in figures 3.7-3.9. (As an aside, it is necessary to allow the rate constant to increase as the density, and hence the concentration of salt, within the room decreases. This of course can be embedded straightforwardly in the numerical model, as noted above.) Overall there is good agreement between the numerical and experimental results for the plume, and in particular, it is important to stress that, particularly for species one, the full plume model predicts the experimental results more accurately than the well-mixed models in a quantifiable way. In all cases, there is also a measurable vertical profile in concentration, whose amplitude decreases with time (consistently with the results of CW02 for density).

There are three distinct regions in figures 3.7 and 3.8 with different slopes that need further discussion. Before the arrival of the first front, (at $\hat{t}_a = 0.075$) the concentration in the room of species one (i.e. the species entering through the plume) increases rapidly, as the only sink of this species is due to reaction with species two initially within the room. However, subsequently to the arrival of the first front at $z = 0$, fluid containing species one starts to be vented from the opening. Therefore there is another sink of species one, and so the rate of increase of $\hat{R}_1$ drops somewhat. This drop in the rate of increase is also related to the fact that the reaction rate increases due to a drop in the ionic strength of the fluid within the room, as salty water is replaced by the fresh water from the source. Eventually however, all the (finite quantity of) species two fluid initially in the room must be lost, due to both reaction and outflow through the vent. Therefore, the fluid within the room will approach the composition of the source fluid.

The situation is different for the evolution of species two however, as shown in figure 3.9. From the first instant of the experiment, since species two is initially present at all heights in the room, species two fluid is both vented from the room, and lost through reaction. Therefore, there is no markedly different behaviour for species two before the arrival of the first front. At later times, as all of species two is lost to reaction and venting, the rate of decrease drops, in a largely exponential fashion. This clearly demonstrates the approach of the system to its final steady state, with the room being completely filled with source fluid.

3.6 Conclusions

In this Chapter we have considered the theoretical, numerical and experimental aspects of a chemical reaction in an enclosed ventilated space where the flow is driven by a turbulent buoyant plume. We restricted our study to flows in which there is no diffusion between adjacent ambient layers and negligible density change from reaction. We have determined that the dynamics of this model flow can be described by five nondimensional parameters: θ; $\hat{z}_e$; $\hat{M}_s$; λ; and ϕ (as defined in (3.11), (3.29), (3.31), (3.36), and (3.38) respectively). These parameters describe the room aspect ratio, the source volume flux, the source (specific) momentum flux, the chemical reaction rate, and the relative concentrations of the species initially in the source fluid and the room fluid. As a result of a quasi-steady state approximation essential to the model, we are restricted to a class of problems such that $\lambda \ll \theta/\hat{z}_e^{5/3}$. To generalize the previous work of CW02, we restricted ourselves to consideration of flows where the plume entrained significant amounts of fluid as it rose from the floor to the ceiling, and so we required $\hat{z}_e \ll 1$. Unsurprisingly, as observed by CW02, well-mixed models described the evolution of the vertically averaged concentration in the room well. Nevertheless, there were measurable and observable discrepancies, principally associated with the behaviour of the system before the arrival of the first front of fluid which has been cycled through the

plume.

As is apparent from the well-mixed models, the natural time scale for the fluid flow to approach its final steady state is the fluid replacement time scale t_r defined by (3.32). This illustrates the critical importance in general of the source volume flux Q_s in determining the transient behaviour of the chemical species. Typically, on this time scale, species two (the species initially in the room) is depleted through both reaction and outflow through the vent, while species one (input through the source) completely fills the room.

However, it is important to stress that this generic picture does not apply when the reaction rate is relatively large, i.e. $\lambda \gg 1$. In this case, if ϕ (as defined in (3.36)) is small, and hence the initial concentration of species two is relatively low in the room compared to the input concentration $1/\phi$ of species one in the source, species two is rapidly depleted if λ is large, on a time scale short in comparison to the fluid replacement time. Conversely, if ϕ is very large, and so the initial concentration of species two within the room is significantly larger than the source concentration of species one, the rate of increase of species one in the room is relatively slow. This is because what little species one is entering the room is being significantly depleted by rapid reaction. This leads to high transient concentrations of the product species three, and a delayed approach to the final steady state, showing that rapid reactions can dominate the fluid-dynamical filling box process for either the species entering through the source, or the species initially in the room.

Within the room, we found that the largest concentrations of the reaction product were associated with larger values of the nondimensional reaction rate λ. This occurs because more reaction is able to occur before species two is depleted too much due to the inevitable outflow through the vent due to the input of fluid at the source. Naturally, the maximum concentration of the product species is limited by the smaller of the peak concentrations of the reacting species, as the creation of product relies inherently on the presence of both reacting species.

All chemical species were observed to exhibit non-trivial vertical profiles at finite times. Species one had a vertical structure similar to the density distribution, with higher concentrations near the ceiling of the room, associated with newer fluid layers which have been more recently cycled through the plume. On the other hand, the concentration of species two decreased with height within the room, as newer fluid layers higher in the room contained more and more fluid from the source, and less and less of the species two-rich fluid initially in the room. Both types of profile are observed for the product species three, which at early times has profiles similar in character to species one, (the species initially in the plume) while at later times, as its concentration drops towards zero, it exhibits vertical profiles reminiscent of those of species two (the species initially in the room). In all cases, the magnitude of the gradient was largest in the vicinity of the source, and decreased towards zero with time as the flow approached its steady state.

These observations have significant implications for assessment of the time-dependent behaviour of chemically reacting species within an enclosed, ventilated space. It is clear that modelling the plume dynamics using the MTT56 model improves the quality of the prediction of the evolution of the various chemical species. In particular, the early time dynamics are critical for understanding the evolution of the various species. The filling box process both leads to the development of vertical variation in concentration, but also, perhaps more importantly, a time-lag before the input species is vented from the opening which inevitably leads to a mismatch between the actual flow dynamics and the behaviour predicted by well-mixed models. Even when this time-lag is relatively short in terms of the time scale of the overall flow evolution towards steady state, it still leads to an observable effect on the concentration distribution within the room of the various chemical species for a significant period of time.

Now that the importance of the filling box process has been demonstrated for the evolution of chemically reacting species in an enclosed ventilated space, there are at least three straightforward, yet relevant generalizations which should

be considered. Firstly, the particular location of the vent to the exterior considered in this Chapter is very specific. It is of undoubted interest to generalize both the location and number of the vents considered. In particular, if there are two vents at different heights within the room, there is the possibility of both "blocked" ventilation, where the room ultimately fills with source fluid analogously to the situation described here, and also "natural" ventilation where a two-layer density distribution develops (see Woods et al. 2003 for a detailed discussion, generalizing to nonzero source volume fluxes the seminal study of Linden, Lane-Serff & Smeed 1990). The evolution of the chemical species in such a layered flow would obviously be of interest.

Secondly, the particular distribution of the chemically reacting species considered in this Chapter, though plausible, is clearly quite special. Another highly relevant situation would be where two plumes, each of which contain a different chemical species, issue into an enclosed ventilated space. Reaction would then ensue through the mutual entrainment of fluid which has been cycled through each plume, leading to a reactive mixture of the two different species. In the absence of chemical reaction, Cooper & Linden (1996) demonstrated that such flows lead to a complex, layered final steady state, yet the transient dynamics associated with finite source volume fluxes is an open, important question.

Finally, and perhaps most significantly, the initial simplifying assumption that the chemical reaction has no dynamic role is certainly not valid in many circumstances. If the reaction is exothermic, and hence a significant amount of heat is released, the plume buoyancy flux will be increased, while conversely if the reaction is non-trivially endothermic, the plume buoyancy flux will be decreased. Such dynamic effects will modify the filling box process in a complex manner, which is undoubtedly worthy of study. For example, an endothermic reaction may actually lead to the plume fluid being dense compared to its surroundings, thus leading to deceleration of the plume fluid, and potentially collapse back towards the neutral buoyancy height for the plume fluid (see Woods & Caulfield 1992 and Caulfield &

Woods 1995 for discussion of the behaviour of such reversing buoyancy plumes). Such collapse modifies qualitatively the evolution of the ambient fluid distribution, as it is necessary to model another entrainment process associated with this fluid collapse (see, for example Cardoso & Woods 1993). Furthermore, exothermic or endothermic reactions within the room fluid itself may lead to convective overturnings in the room, hence driving mixing in another non-trivial and different manner. To gain a full understanding of the evolution of chemically reacting plumes in an enclosed environment it is necessary to consider such issues, and we will report the results of our investigations in the next chapter.

This Chapter has been published in *Journal of Fluid Mechanics*, 2005, Conroy, D. T., S. G. Llewellyn Smith and C. P. Caulfield (Cambridge University Press).

4

Chemically reacting plumes with an exothermic and endothermic reaction

4.1 Abstract

We develop a model for a turbulent plume in an unbounded ambient that takes into account a general exothermic or endothermic chemical reaction. These reactions have important effects on the plume dynamics since the entrainment rate, which scales with the vertical velocity, will be a function of the heat release or absorption. Specifically, we examine a second order non-reversible reaction, where one species is present in the plume from a pure source and the other is in the environment. For uniform ambient density and species fields the reaction has an important effect on the deviation from pure plume behaviour as defined by the source parameter Γ. In the case of an exothermic reaction the density difference between the plume and the reference density increases and the plume is 'lazy', whereas for an endothermic reaction this difference decreases and the plume is more jet-like. Furthermore, for chemical and density stratified environments, the reaction will have an important effect on the buoyancy flux because the entrainment

rate will not necessarily decrease with distance from the source, as in traditional models, since the reaction will contribute to the velocity of the plume. As a result, the maximum rise height of the plume for exothermic reactions, may actually decrease with reaction rate if this occurs in a region of high ambient density. In addition, we investigate the Boussinesq assumption, which is valid for relatively small heats of reaction and compare it with the non-Boussinesq model.

4.2 Introduction

Convection induced by chemical reactions is an important process in many industrial and environmental settings. For example, a plume will develop above a pool fire if the vaporization rate is large enough (Tieszen, 2001). A plume forms with two distinct stages. In the first stage a reacting plume rises above the fuel source in which hot buoyant fuel mixes with entrained ambient air. The highly exothermic reaction increases the buoyancy of the plume until the initial plume species is completely consumed. In the second stage, from this height up, the plume behaves as a non-Boussinesq plume without reaction and with a virtual origin correction. Furthermore, many industrial chemicals such as pyrophoric materials undergo a reaction with air or water vapour at normal ambient condition. An accidental release of such a buoyant chemical in a an occupied space is potentially very hazardous. In the aqueous phase, there are many acid-base reactions such as the neutralization reaction between sodium hydroxide and hydrochloric acid which can be exothermic (Patnaik, 1999).

A similar process occurs in relation to evaporative cooling which has been used for years in cooling towers to cool circulated water (Fisenko et al., 2004) and in air conditioning systems in hot dry climates. The fundamental fluid-dynamical aspect of this problem is the presence of a distribution of water droplets with variable size and concentration within a turbulent plume. As the plume entrains ambient fluid, the water droplets will evaporate (provided the air is sufficiently

dry) in order to maintain the equilibrium vapour concentration. Latent heat will be absorbed, thus increasing the density of the gaseous phase. This will couple to the plume dynamics through the buoyancy force.

The plume theory developed by Morton et al. (1956, henceforth MTT56) relies on an entrainment assumption that scales the rate at which turbulent eddies are engulfed into the plume with the center line velocity. This assumption leads to a simple set of equations describing the flux of volume, momentum and buoyancy. The Boussinesq approximation is often used, but is not always appropriate. A rational derivation of the non-Boussinesq plume equations was given by Rooney & Linden (1996). In all plume models the buoyancy flux is a function of ambient stratification and the plume will keep rising in an unstratified or weakly-stratified ambient, although in a stratified ambient the plume will reach a maximum height (Caulfield & Woods, 1998).

Chemistry was added to the original plume model of MTT56 by Conroy et al. (2005, henceforth CLSC) for a passive chemical reaction that decouples from the plume dynamics. The species concentrations in the plume are treated in the same fashion as the dynamic fluxes, starting from the conservation of species. CLSC considered the ventilated filling box problem and compared experiment to theory, finding good agreement. However, in cases where the reaction is strongly exothermic or endothermic, this model is inadequate since the buoyancy flux must be modified to account for the heat absorption or release due to reaction.

Plumes with volumetric heating supplied by a line source of heat were investigated experimentally and theoretically by Bhat & Narashima (1996). This model was extended by Hunt & Kaye (2005) to analyze the plume-like or jet-like nature of plumes with an internal buoyancy flux gain represented as a constant source of heat. However, these studies were not concerned with exothermic or endothermic reactions between the source fluid and the ambient.

In this Chapter we generalize previous work on turbulent plumes to include a general reaction mechanism with a non-negligible heat of reaction. The

buoyancy flux is a function of the addition or removal of heat by the chemical reaction. Hence it can be a non-uniform function of height and is coupled to the entrainment rate. Since many reactions have a large chemical heat release we consider both non-Boussinesq plumes and Boussinesq plumes. We limit ourselves to pure plume source conditions, following MTT56, Rooney & Linden (1996), Caulfield & Woods (1998) and others, although a forced plume can be investigated in a similar fashion.

The Chapter is organized as follows. In § 4.3, we formulate the energy equation in terms of density, taking into account the heat of reaction. The reaction mechanism is expressed in general terms but we limit ourselves subsequently to a second order non-reversible reaction for comparison with CLSC and also to perfect gases. In § 4.4 we develop the plume model following MTT56 for a Boussinesq plume, which is valid for sufficiently small heats of reaction. We examine the deviation from pure plume behaviour with uniform ambient density and species stratification and investigate the maximum rise height in ambient chemical stratifications with power law behaviour. In § 4.5 we extend the analysis to non-Boussinesq plumes. Finally we conclude in § 4.6.

4.3 Model description

4.3.1 Governing equations

We consider a body of fluid rising in an infinite medium due to the action of buoyancy forces with a sufficiently large velocity so that diffusion of momentum, energy and species is negligible. An exothermic and/or endothermic chemical reaction is allowed to occur within the body thus increasing or decreasing the relative buoyancy force of the fluid. In general an unsteady, reacting high-Reynolds number three-dimensional flow with negligible diffusion is governed by the equations

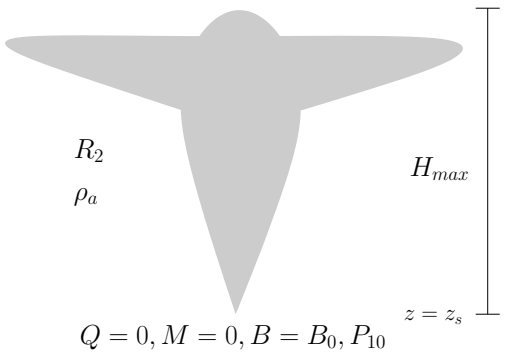

Figure 4.1: Pure plume entering an infinite ambient with concentration R_2 of species 2 from a source with concentration P_{10} of species 1.

(Williams, 1985)

$$\frac{\mathrm{D}\rho}{\mathrm{D}t} + \rho\boldsymbol{\nabla}\cdot\mathbf{v} = 0, \tag{4.1a}$$

$$\rho\frac{\mathrm{D}\mathbf{v}}{\mathrm{D}t} = \boldsymbol{\nabla}p - \rho g, \tag{4.1b}$$

$$\rho\frac{\mathrm{D}e}{\mathrm{D}t} = -p\boldsymbol{\nabla}\cdot\mathbf{v}, \tag{4.1c}$$

$$\rho\frac{\mathrm{D}Y_i}{\mathrm{D}t} = \omega_i. \tag{4.1d}$$

Here ρ is the density, $\mathbf{v}$ is the bulk fluid velocity, p is the pressure, g is the acceleration of gravity downwards, e is the internal energy, $Y_i = \rho_i/\rho$ is the mass fraction of species i and ω_i is the reaction rate which will be specified in section (4.3.2). We define the enthalpy $h = e + p/\rho$ to be an average enthalpy of the mixture with $h = \sum_{i=1}^{N} h_i Y_i$ and $h_i = h_i^o + \int_{T_0}^{T} C_{p,i}\, dT$, where h_i^o is the standard enthalpy at the standard temperature, T_0, and $C_{p,i}$ is the specific heat of species i.

We seek an alternative form to equation (4.1c) that describes the change in density of a material particle due to reaction effects. In general the change in internal energy of a fluid particle is governed by the first and second laws of thermodynamics as follows:

$$\mathrm{d}e = T\,\mathrm{d}s - p\,\mathrm{d}(1/\rho) + \sum_{i=1}^{N}(\mu_i/W_i)\,\mathrm{d}Y_i, \tag{4.2}$$

where s is the entropy, μ_i is the chemical potential and W_i is the molecular weight of species i. Substituting this relationship and (4.1a) into (4.1c) yields

$$\frac{\mathrm{D}s}{\mathrm{D}t} = -\frac{1}{T}\sum_{i=1}^{N}\frac{\mu_i}{W_i}\frac{\mathrm{D}Y_i}{\mathrm{D}t}, \tag{4.3}$$

which expresses the rate of production of entropy by the irreversible chemical reaction.

On substituting this equation into the mathematical identity

$$\frac{\mathrm{D}\rho}{\mathrm{D}t} = \left(\frac{\partial\rho}{\partial p}\right)_{s,Y_i}\frac{\mathrm{D}p}{\mathrm{D}t} + \left(\frac{\partial\rho}{\partial s}\right)_{p,Y_i}\frac{\mathrm{D}s}{\mathrm{D}t} + \sum_{i=1}^{N}\left(\frac{\partial\rho}{\partial Y_i}\right)_{s,p,Y_j(i\neq j)}\frac{\mathrm{D}Y_i}{\mathrm{D}t}, \tag{4.4}$$

one can show by thermodynamic arguments (cf. e.g. Clarke and McChesney 1964)

$$\frac{\mathrm{D}\rho}{\mathrm{D}t} = \frac{1}{a_f^2}\frac{\mathrm{D}p}{\mathrm{D}t} + \rho\sum_{i=1}^{N}\left[\frac{\beta}{C_p}\left(\frac{\partial h}{\partial Y_i}\right)_{p,T,Y_{j(i\neq j)}} - \rho\left(\frac{\partial\rho^{-1}}{\partial Y_i}\right)_{p,T,Y_{j(i\neq j)}}\right]\frac{\mathrm{D}Y_i}{\mathrm{D}t} \tag{4.5}$$

where a_f is the frozen speed of sound defined by $a_f^2 = (\partial p/\partial\rho)_{s,Y_i}$, $\beta = \rho(\partial\rho^{-1}/\partial T)_{p,Y_i}$ is the frozen volumetric thermal expansion coefficient and $C_p = (\partial h/\partial T)_{p,Y_i}$ is the frozen specific heat at constant pressure.

For a perfect gas with equation of state $p = \rho RT\sum_{i=1}^{N} Y_i/W_i = \rho RT\bar{Y}$, evaluating the derivatives gives

$$\frac{\mathrm{D}\rho}{\mathrm{D}t} = \frac{1}{a_f^2}\frac{\mathrm{D}p}{\mathrm{D}t} + \frac{\beta}{C_p}\sum_{i=1}^{N}h_i\omega_i - \frac{1}{\bar{Y}}\sum_{i=1}^{N}\frac{\omega_i}{W_i} = \frac{1}{a_f^2}\frac{\mathrm{D}p}{\mathrm{D}t} + \rho\sigma. \tag{4.6}$$

This equation represents the change in density due to pressure, chemical energy released or absorbed by reactions and changes in mixture concentrations. The latter two changes are regrouped into σ. In general the first term can be neglected for fluid velocities that are small compared to the speed of sound, and we do so here, since we will not be dealing with extremely large values of σ.

For steady flow with no swirl, i.e. $\mathbf{v} = (u, 0, w)$ in cylindrical coordinates (r, θ, z), the equations underlying plume dynamics can be written in almost-

conservative form as

$$\begin{aligned}
\frac{1}{r}\frac{\partial}{\partial r}(ru\rho) + \frac{\partial}{\partial z}(w\rho) &= 0, && (4.7a)\\
\frac{1}{r}\frac{\partial}{\partial r}(ruw\rho) + \frac{\partial}{\partial z}(w^2\rho) &= g(\rho_a - \rho), && (4.7b)\\
u\frac{\partial \rho}{\partial r} + w\frac{\partial \rho}{\partial z} &= \rho\sigma, && (4.7c)\\
\frac{1}{r}\frac{\partial}{\partial r}(ru\rho Y_i) + \frac{\partial}{\partial z}(w\rho Y_i) &= \omega_i && (4.7d)
\end{aligned}$$

for mass, vertical momentum, energy and species respectively, using (4.6). We have assumed the plume to be thin so that $\partial_r p \ll \partial_z p$ in which case the pressure may be shown to be hydrostatic: $\mathrm{d}p/\mathrm{d}z = -\rho_a g$, where $\rho_a(z)$ is the ambient fluid density (Rooney & Linden, 1996). The additional term in (4.7c) is due to fluid expansion or compression via reaction, while the additional term in (4.7d) is due to reaction.

For Boussinesq plumes, the equations simplify to

$$\begin{aligned}
\frac{1}{r}\frac{\partial}{\partial r}(ru) + \frac{\partial w}{\partial z} &= 0, && (4.8a)\\
\frac{1}{r}\frac{\partial}{\partial r}(ruw) + \frac{\partial w^2}{\partial z} &= \frac{g}{\rho_0}(\rho_a - \rho), && (4.8b)\\
u\frac{\partial \rho}{\partial r} + w\frac{\partial \rho}{\partial z} &= \rho_0\sigma, && (4.8c)\\
\frac{1}{r}\frac{\partial}{\partial r}(ruY_i) + \frac{\partial}{\partial z}(wY_i) &= \frac{\omega_i}{\rho_0}, && (4.8d)
\end{aligned}$$

where ρ_0 is a reference density. Here the mass fractions are given by $Y_i = \rho_i/\rho_0$. The flow is incompressible, but density can change due to the reactions. If $\sigma \ll 1$, the right-hand side of (4.8c) vanishes and we recover the equations of CLSC.

4.3.2 Chemical reaction mechanism

A general chemical reaction mechanism can be represented as (Williams, 1985)

$$\omega_i = W_i \sum_{k=1}^{n} (\nu''_{i,k} - \nu'_{i,k}) K_k \prod_{j=1}^{N} c_j^{\nu'_{j,k}}, \qquad (4.9)$$

where $c_j = Y_j\rho/W_j$ is the molar concentration of species j, K_k is the rate constant (in general a function of temperature) of the k^{th} reaction, $\nu'_{i,k}$ is the stoichiometric coefficient of reactants and $\nu''_{i,k}$ is the stoichiometric coefficient of products. Conservation of mass at the molecular level implies that $\sum_i \omega_i = 0$, which can also be written as a constraint on the W_i, $\nu''_{i,k}$ and $\nu'_{i,k}$.

In this Chapter we will only consider second-order reactions of the form $c_1 + c_2 \rightarrow c_3$, although other forms are possible. Therefore

$$\omega_i = \pm W_i K c_1 c_2 = \pm \frac{K W_i \rho^2}{W_1 W_2} Y_1 Y_2, \tag{4.10}$$

where the sign is negative for ω_1 and ω_2, and positive for ω_3. Note that $W_1 + W_2 = W_3$.

In the case of the perfect gas we have the following expression

$$\sigma = \left[\frac{\beta}{C_p}(-h_1 W_1 - h_2 W_2 + h_3 W_3) + \frac{1}{\bar{Y}} \right] \frac{K\rho^2}{W_1 W_2} Y_1 Y_2 = \Omega \rho^2 Y_1 Y_2, \tag{4.11}$$

which defines Ω. The term in brackets is just the heat of reaction ΔH_r which is positive for an endothermic reaction. The $\bar{Y}$ term is present for the second-order reaction considered here, but in general is multiplied by a numerical factor which can be zero.

In the Boussinesq case, ρ in (4.10) is to be replaced by ρ_0, and all quantities in (4.11) are to be evaluated using the reference value ρ_0 for ρ. While Ω is in general a function of temperature (through K and h_i) and of pressure (since by the perfect gas law T is a function of ρ, p and Y_j), we ignore these considerations here and take Ω and K to be constant. The pressure dependence, which enters via the hydrostatic relation, is very weak unless the plume extends a scale height. The temperature dependence is negligible unless the reaction is very exothermic or endothermic.

4.4 Boussinesq plume

4.4.1 Plume equations

We consider an isolated source of buoyancy released into an infinite environment. Following MTT56 we define the plume volume flux πQ, momentum flux πM, buoyancy flux πB and species flux πP_i as follows:

$$\pi Q(z) = 2\pi \int_0^\infty rw \, \mathrm{d}r = \pi \bar{w} b^2, \tag{4.12a}$$

$$\pi M(z) = 2\pi \int_0^\infty rw^2 \, \mathrm{d}r = \pi \bar{w}^2 b^2, \tag{4.12b}$$

$$\pi B(z) = 2\pi \int_0^\infty rwg \frac{\rho_a - \rho}{\rho_0} \, \mathrm{d}r = \pi g \frac{\rho_a - \bar{\rho}}{\rho_0} \bar{w} b^2 = \pi g' \bar{w} b^2, \tag{4.12c}$$

$$\pi P_i(z) = 2\pi \int_0^\infty Y_i rw \, \mathrm{d}r = \pi \bar{Y}_i \bar{w} b^2. \tag{4.12d}$$

We take top hat profiles for quantities in the plume so that the integrals extend to b, the plume width, and quantities with over bars are functions of z only. Also g' is the reduced gravity of the plume relative to the local ambient fluid.

The plume equations for volume and momentum flux are as in MTT56:

$$\frac{\mathrm{d}Q}{\mathrm{d}z} = 2\alpha M^{1/2}, \qquad \frac{\mathrm{d}M}{\mathrm{d}z} = \frac{BQ}{M}. \tag{4.13}$$

Note that $b^2 = Q^2/M$ and $\bar{w} = M/Q$. The buoyancy flux is found by differentiating (4.12c) with respect to height and using (4.8a) and (4.8c), yielding

$$\frac{\rho_0}{2g}\frac{\mathrm{d}B}{\mathrm{d}z} = \int_0^\infty rw \frac{\mathrm{d}\rho_a}{\mathrm{d}z} \, \mathrm{d}r - \int_0^\infty \rho_0 \sigma r \, \mathrm{d}r + \int_0^\infty ru(\rho - \rho_a)_r \, \mathrm{d}r - \int_0^\infty (\rho_a - \rho)(ru)_r \, \mathrm{d}r. \tag{4.14}$$

The last two terms integrate to zero and we find

$$\frac{\mathrm{d}B}{\mathrm{d}z} = -N^2 Q - g\sigma \frac{Q^2}{M}, \tag{4.15}$$

where $N^2 = -(g/\rho_0)\mathrm{d}\rho_a/\mathrm{d}z$. This buoyancy flux changes because of the exothermic or endothermic reaction and changes in average molecular weights. Integrating (4.8d) across the plume gives

$$\frac{\mathrm{d}P_i}{\mathrm{d}z} = 2\alpha R_i M^{1/2} + \frac{\omega_i}{\rho_0}\frac{Q^2}{M}, \tag{4.16}$$

where R_i is the mass fraction of species i in the ambient.

To compute the right-hand sides of these equations for our case, we express concentrations in terms of fluxes through the plumes using $P_i = Q\bar{Y}_i$. Then, replacing Y_i by $\bar{Y}_i$ so as to work with plume variables as in the derivation of the equation for $\mathrm{d}M/\mathrm{d}z$ above

$$\frac{\omega_i}{\rho_0}\frac{Q^2}{M} = \pm\frac{KW_i\rho_0}{W_1W_2}\frac{P_1P_2}{M} = \psi_i\frac{P_1P_2}{M} \tag{4.17}$$

and similarly

$$g\sigma\frac{Q^2}{M} = g\Omega\rho_0^2Y_1Y_2\frac{Q^2}{M} = g\rho_0^2\Omega\frac{P_1P_2}{M} = \kappa\frac{P_1P_2}{M}, \tag{4.18}$$

where

$$\kappa = g\rho_0\psi_3\left[\frac{\beta\Delta H_r}{W_3C_p} + \frac{Q}{\bar{P}}\right] = \hat{\psi}_3(\hat{H}_r + Q/\bar{P}), \tag{4.19}$$

and $\bar{P} = \sum_{i=1}^{3} W_3P_i/W_i$. Now the terms within the brackets are non-dimensional.

At the plume source we will only consider a pure plume as in Morton et al. (1956) and Caulfield & Woods (1998) so that $Q(z_s) = M(z_s) = 0$ and $B(z_s) = B_0$. In addition we will only consider a single species at the source so that $P_1(z_s) = P_{10}$, $P_2(z_s) = 0$ and $P_3(z_s) = 0$.

4.4.2 No ambient stratification

For weakly stratified environments with $N^2 \approx 0$ the buoyancy flux is controlled by the chemistry, while the species concentrations when the ambient concentrations are uniform are governed by the entrainment and reaction rates. The governing equations are

$$\frac{\mathrm{d}Q}{\mathrm{d}z} = 2\alpha M^{1/2}, \qquad \frac{\mathrm{d}M}{\mathrm{d}z} = \frac{BQ}{M}, \tag{4.20a}$$

$$\frac{\mathrm{d}B}{\mathrm{d}z} = -\kappa\frac{P_1P_2}{M}, \qquad \frac{\mathrm{d}P_i}{\mathrm{d}z} = 2\alpha R_iM^{1/2} + \psi_i\frac{P_1P_2}{M}, \tag{4.20b}$$

When the reaction rate is small, i.e. $\kappa \approx 0$, and $B = B_0$, we recover the well-known similarity solution of MTT56

$$Q = \frac{6\alpha}{5}\left(\frac{9\alpha B_0}{10}\right)^{1/3} z^{5/3}, \quad M = \left(\frac{9\alpha B_0}{10}\right)^{2/3} z^{4/3}, \tag{4.21}$$

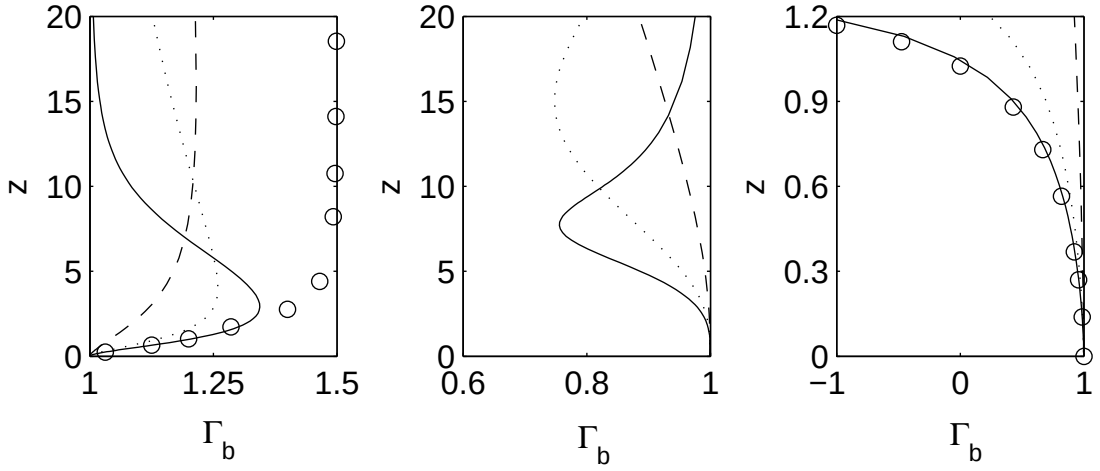

Figure 4.2: Numerical solutions to equations (4.20a)–(4.20b), showing Γ_b profiles for $\hat{H}_r = -10$ (left), 0 (center), 10 (right) and $\psi_3 = .1$ (dashed line), 1 (dotted line), 10 (solid line). The circles represent the profiles of Γ_b corresponding to the exact solution (4.27) in the large reaction rate limit with $\psi_3 = 10$. Here $\nu = 100$, $P_{10} = 1$, $R_c = 1$, $W_1 = W_2 = 1$, and $\hat{\psi}_3 = \psi_3$.

for which the volume flux increases monotonically and the velocity decreases monotonically due to entrainment.

For forced plumes one may define the nondimensional parameter (see Hunt & Kaye, 2005)

$$\Gamma_b = \frac{5Q^2B}{8\alpha M^{5/2}} \tag{4.22}$$

which is a function of height. This parameter has been used to indicate whether the plume is forced ($\Gamma_b < 1$) and is hence jet-like, pure ($\Gamma_b = 1$) or lazy ($\Gamma_b > 1$). For our model, where the plume is pure at the source, we can use this parameter to determine quantitatively the deviation from pure plume behaviour with chemical reactions.

In Figure 4.2 we plot profiles of Γ_b for different values of $\hat{H}_r$ and ψ_1 in order to discuss three distinct behaviours of the plume. In the first case the

reaction is exothermic ($\hat{H}_r < 0$) so the plume density decreases in opposition to the increase in density by entrainment. As fluid is entrained, the reaction plays a more important role and the plume becomes lazy with a deficit of momentum, but if κ or P_1 is too small the effects of reaction never dominate and the solution continues to behave as a pure plume described by equations (4.21). In any case, at large distances from the source species P_1 will be completely consumed and we can use the similarity solutions with a virtual origin correction (Caulfield & Woods, 1995).

In the second case there is no heat generated or absorbed ($\hat{H}_r = 0$) but for this reaction the production of species 3 acts to increase the average density of the plume. Since the chemical components have different densities, the buoyancy flux will be a function of the average mixture concentration ($\bar{Y}$), which is coupled to the entrainment and reaction rates. Therefore, the plume will be dominated by momentum with jet-like characteristics ($\Gamma_b < 1$), while there is sufficient quantities of species 1 but will behave as a pure plume at larger distances from the source, where the reaction is weak. Finally, in the endothermic case we expect similar characteristics, although with an approximately constant κ. Since the heat of reaction is relatively large, the density difference, $\rho_0 - \rho > 0$, will decrease and the plume will have jet like characteristics. Ultimately the reaction will absorb a sufficient amount of thermal energy and the density deference $\rho_0 - \rho < 0$ will led to a negatively buoyant plume that will behave as a fountain (Bloomfield & Kerr, 2000).

We can quantify the critical conditions for the plume to be bounded or unbounded as a function of the chemically related parameters $P_{10}, \hat{H}_r$ and ψ_3. This is shown in Figure 4.3. For relatively small source concentrations and heats of reaction the chemistry will be unable to decrease the density below the ambient and the plume will be unbounded. For a large source concentration and heat of reaction, the plume will eventually become neutrally buoyant and spread out horizontally. We have quantified the transition zone between lazy and forced plumes in Figure

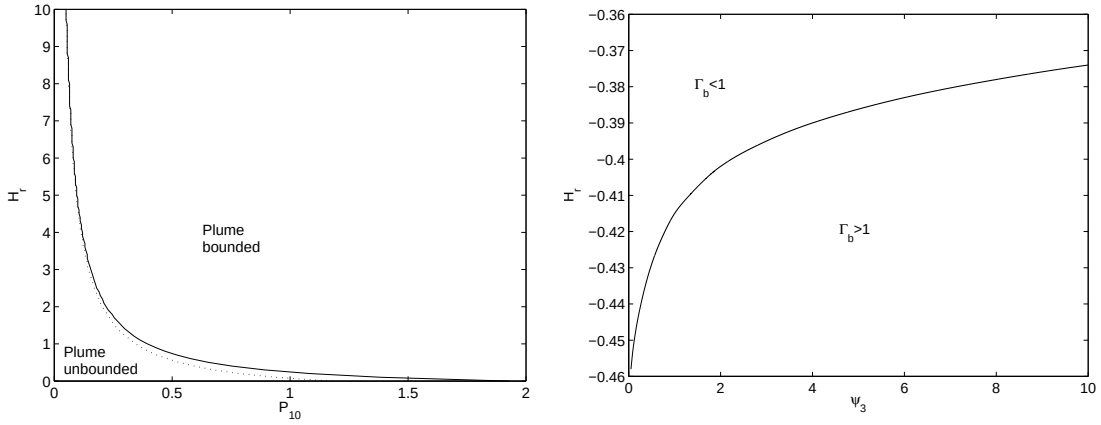

Figure 4.3: (Left) Variation in the heat of reaction separating bounded and unbounded solutions as a function of the source concentration P_{10} for $\psi_3 = .1$ (dotted line) and 10 (solid line). (Right) Boundary separating a lazy and forced plume as a function of H_r and ψ_3 for $P_{10} = 1$. Here $\nu = 100$, $R_c = 1$, $W_1 = W_2 = 1$ and $\hat{\psi}_3 = \psi_3$.

4.3. Because of the term $Q/\bar{P}$ in 4.19, the heat of reaction and reaction rate must be sufficiently large for an effectively exothermic reaction to exist.

4.4.3 Large reaction rate and large heat of reaction

When the reaction is very fast, i.e. $K \gg 1$, the ambient chemical species in the plume (2) is consumed on a time scale much shorter than the residence time in the plume. As a result the concentration of species 2 in the plume is very small and the vertical gradient in the flux P_2 is approximately zero ($\mathrm{d}P_2/\mathrm{d}z \approx 0$). Then the constancy of P_2 shows that $\psi_2 P_1 P_2 M^{-1} \approx -2\alpha R_2 M^{1/2}$ and this may be substituted into the equations for B and P_1 to give

$$\frac{\mathrm{d}Q}{\mathrm{d}z} = 2\alpha M^{1/2}, \qquad \frac{\mathrm{d}M}{\mathrm{d}z} = \frac{BQ}{M}, \tag{4.23}$$

$$\frac{\mathrm{d}B}{\mathrm{d}z} = -2\alpha M^{1/2}\chi, \qquad \frac{\mathrm{d}P_1}{\mathrm{d}z} = -2\alpha R_c \frac{\psi_1}{\psi_2} M^{1/2}, \tag{4.24}$$

where $\chi = -R_c\psi_2^{-1}\kappa = gR_c\rho_0\beta\Delta H_r/C_pW_2$ and we have assumed that $\bar{Y} \ll \beta\Delta H_r/C_p$ for convenience. The quantity χ is positive for endothermic reactions

and negative for exothermic reactions. Once the source chemical is completely consumed so that $P_1 = 0$, the reaction stops and we have the usual plume equations of MTT56 from that height up. There is a boundary layer in which the buoyancy flux tends to a constant, that we ignore.

The buoyancy and volume flux equations can be combined and integrated to obtain

$$B = B_0 - \chi Q. \tag{4.25}$$

The three equations (4.23) and (4.25) can be combined to form a single equation in terms of volume and momentum fluxes and integrated to obtain

$$\frac{\mathrm{d}Q}{\mathrm{d}z} = 2\alpha \left(\frac{5\chi}{12\alpha}\right)^{1/5} Q^{2/5} \left(\epsilon - Q\right)^{1/5}, \tag{4.26}$$

where $\epsilon = 3B_0/2\chi$.

Now (4.26) can be integrated to give

$$2\alpha \left(\frac{5|\chi|}{12\alpha}\right)^{1/5} (z - z_s) = \int_0^Q \frac{q^{-2/5}}{(|\epsilon| \mp q)^{1/5}} \mathrm{d}q = \frac{5}{3} |\epsilon|^{-1/5} Q^{3/5} \; {}_2F_1(1/5, 3/5; 8/5; Q/\epsilon), \tag{4.27}$$

in terms of hypergeometric functions and where the choice of signs is $-$ for $\chi > 0$ and $+$ for $\chi < 0$. In both cases, we find for small $z - z_s$

$$Q = \left(\frac{6\alpha}{5}\right)^{5/3} \left(\frac{5\epsilon\chi}{12\alpha}\right)^{1/3} (z - z_s)^{5/3}. \tag{4.28}$$

In the endothermic case with $\chi > 0$, the plume becomes a fountain, provided P_{10} is not too small, and terminates at $Q = \epsilon$ with

$$2\alpha \left(\frac{5\chi}{12\alpha}\right)^{1/5} (z_{max} - z_s) = \frac{5}{3} \epsilon^{2/5} \frac{\Gamma(8/5)\Gamma(4/5)}{\Gamma(7/5)}. \tag{4.29}$$

In the exothermic case, the plume continues to rise and behaves for large z as

$$2\alpha \left(\frac{5|\chi|}{12\alpha}\right)^{1/5} (z - z_s) = \frac{5}{3} Q^{2/5} \frac{\Gamma(8/5)\Gamma(2/5)}{\Gamma(3/5)\Gamma(7/5)}. \tag{4.30}$$

The mass flux has a $(z - z_s)^{5/2}$ dependence. Of course this is a transitory phase until $P_1 = 0$ at which the usual MTT56 solution applies again. This scenario is

similar to plumes with decreasing source strengths (Scase *et al.*, 2006), in which there is a narrowing of the plume at some height.

The parameter Γ starts at 1 and tends to $-\infty$ as $z \to z_{max}$ in the endothermic case. It starts at 1 and grows slowly in the exothermic case, before ultimately returning to 1 when the reaction ends. We have plotted the Γ_b profiles against the numerical solution in Figure 4.2 for $\psi_3 = 10$. The reduced model yields a good approximation until species 1 has reduced to a sufficiently small value, so that $\mathrm{d}P_2/\mathrm{d}z \approx 0$ is no longer valid. At this point the reaction no longer dominates the buoyancy flux and the plume transitions to the usual plume model of MTT56 with similarity solutions (4.21).

4.4.4 Stratified ambient

In order to examine the importance of non-uniform stratification and how the properties of the plume depend on the coupling between species and density entrainment, we extend the results of Caulfield & Woods (1998) to the case with reaction. We define static ambient profiles of power-law form ($\beta \geq 0$)

$$\rho_a = \rho_0 \, (z/z_s)^{\beta}, \qquad N^2 = N_s^2 \, (z/z_s)^{\beta-1}, \qquad R_2 = R_c (z/z_s)^{\gamma}, \tag{4.31}$$

where z_s is the height of the source, N_s^2 is the stratification of the ambient and R_c is the concentration of species 2 at the source. In order to focus on the effects of chemistry in a simple yet informative way we will not examine the effects of others species in the ambient, so we take $R_1 = 0$.

For a plume in a constant-stratification ambient, MTT56 found that the maximum rise height of the plume is determined from

$$H = (2\alpha)^{-1/2} B_0^{1/4} N_s^{-3/4}, \tag{4.32}$$

as a function of initial buoyancy flux and buoyancy frequency. We use this to scale vertical height and the other quantities of interest.

$$z = \hat{z} H, \qquad B = \hat{B} B_0, \qquad Q = \hat{Q} (2\alpha)^{4/3} B_0^{1/3} H^{5/3}, \tag{4.33}$$

$$M = \hat{M} (2\alpha)^{2/3} B_0^{2/3} H^{4/3}, \quad P_i = R_c \hat{P}_i (2\alpha)^{4/3} B_0^{1/3} H^{5/3}. \tag{4.34}$$

With this same scaling in mind we scale the reaction rate and enthalpy of reaction as follows

$$\lambda_i = \psi_i \frac{R_c(2\alpha)^{2/3}H^{7/3}}{B_0^{1/3}}, \quad \varpi = \kappa B_0^{-1} R_c^2 (2\alpha)^2 H^{7/3} = \hat{\lambda}_3(\hat{H}_r + Q/\bar{F}). \tag{4.35}$$

In addition we scale the density, ambient species concentration and buoyancy frequency with ρ_0, R_c and N_s^2 respectively and the ambient stratification becomes

$$\rho_a = (\nu z)^\beta, \quad N^2 = (\nu z)^{\beta-1}, \quad R_2 = (\nu z)^\gamma. \tag{4.36}$$

In non-dimensional form the plume equations with hats dropped are

$$\frac{\mathrm{d}Q}{\mathrm{d}z} = M^{1/2}, \tag{4.37a}$$

$$\frac{\mathrm{d}M}{\mathrm{d}z} = \frac{BQ}{M}, \tag{4.37b}$$

$$\frac{\mathrm{d}B}{\mathrm{d}z} = -N^2 Q - \varpi \frac{P_1 P_2}{M}, \tag{4.37c}$$

$$\frac{\mathrm{d}P_i}{\mathrm{d}z} = R_i M^{1/2} + \lambda_i \frac{P_1 P_2}{M}, \tag{4.37d}$$

and the boundary conditions are

$$Q = M = P_2 = 0, \quad B = 1, \quad P_1 = \frac{P_{10}}{R_c(2\alpha)^{4/3}B_0^{1/3}H^{5/3}} = \phi \qquad \text{at} \quad z = \frac{1}{\nu} \tag{4.38}$$

We have solved the governing equations (4.37a–4.37d) numerically and plotted our results in Figure 4.4 and 4.5. Since we are mainly interested in the effect of chemistry on the maximum rise height, we only vary the chemically related parameters and set the ambient density stratification to be linear, i.e. $\beta = 1$. In addition we fix the chemical concentration ratio $\phi = 1$ in order to reduce our parameter space and concentrate on the effect of λ, ϖ and γ.

In Figure 4.4 we have plotted the profiles for a positive, zero and negative heat of reaction ϖ to be consistent with the rest of the Chapter. We have chosen to display a large rate constant, $\lambda_3 = 10$ to elucidate the effects of reaction and a power coefficient $\gamma = -.1$, which one would likely encounter in industrial settings. The species fluxes in the plume are a function of entrainment and reaction rate,

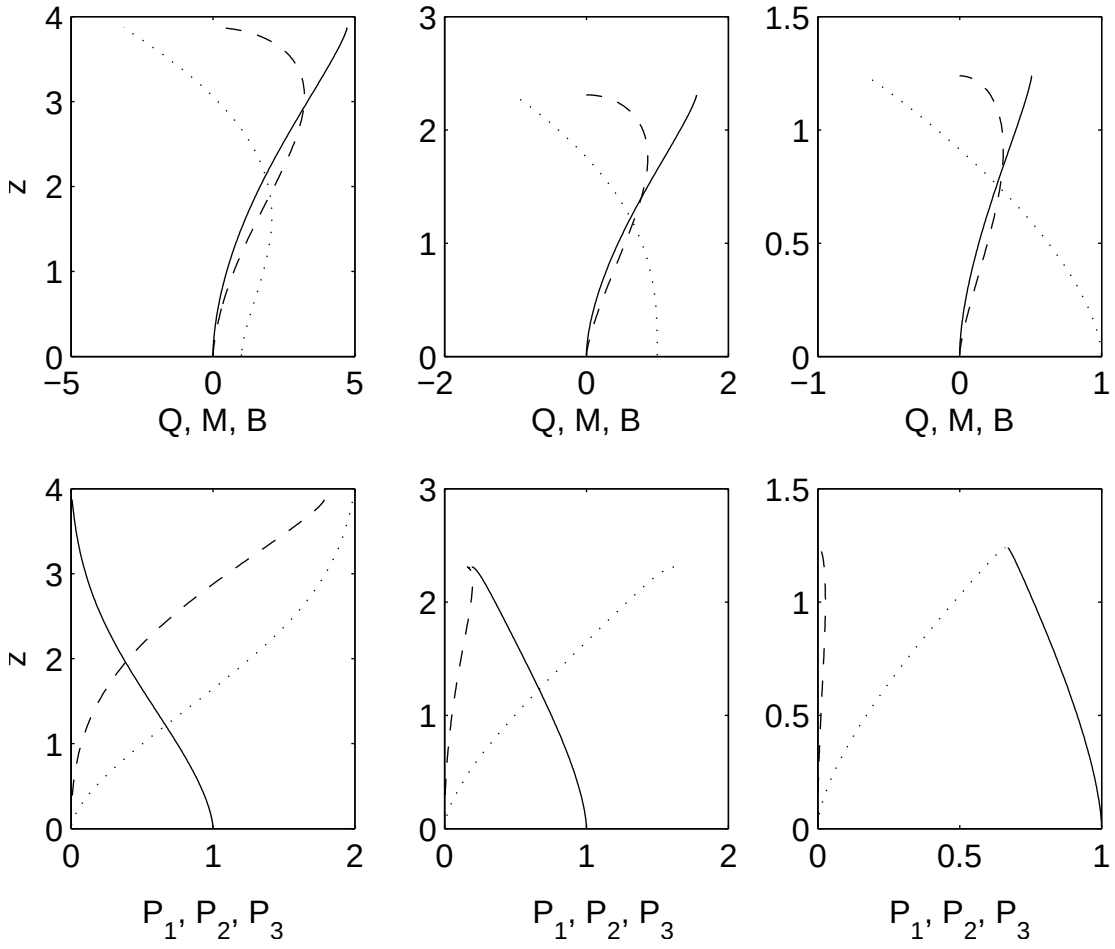

Figure 4.4: Numerical solution to (4.37a)–(4.37d) showing Q, P_1 (solid); M, P_2 (dashed); B, P_3 (dotted) for $\hat{H}_r = -2$ (left), 0 (center) and 2 (right). Here $\nu = 100$, $\phi = 1$, $W_1 = W_2 = 1$, $\lambda_3 = 10$, $\hat{\lambda}_3 = \lambda_3$, $\gamma = -.1$ and $\beta = 1$.

which of course is dependent on the heat of reaction and average mixture density. Nonetheless P_1 has a maximum value at the source which decreases with height by reaction and P_2 has a minimum value at the source that increases by entrainment and decreases by reaction. Similarly P_3 increases with reaction from an initially zero boundary condition and has the same characteristics as species one since $\mathrm{d}P_1/\mathrm{d}z \propto \mathrm{d}P_3/\mathrm{d}z$. Naturally, the reaction will have the largest contribution to the plume dynamics near the source but far above this point the source species will be sufficiently small and the plume will be governed by the model of MTT56.

The buoyancy flux is controlled by two processes: entrainment of dense ambient fluid and exothermic or endothermic chemical reactions. In the case of a constant ambient density gradient the former always acts to decrease the buoyancy flux and ultimately force the plume to become neutrally buoyant and spread out horizontally. For environments with a decreasing stratification in height the plume will be unbounded but we will not discuss this case further (Caulfield & Woods, 1998). The latter will cause B to increase near the source for exothermic reactions but decrease faster for endothermic reactions. The momentum flux, generally grows with distance from the source but ultimately becomes zero, which corresponds to the maximum rise height when the plume density is larger than the ambient. For an exothermic or endothermic reaction this point will occur at a larger or smaller value respectively, compared to a plume with no reaction. Finally, the volume flux will always increase with distance from the source although it will be coupled to the reaction dynamics through the entrainment rate. Since we have made the Boussinesq assumption, the plume radius cannot expand or contract with an exothermic or endothermic reaction respectively, which is appropriate for relatively weak heats of reaction.

We have plotted the maximum rise height $H_{max} = z_{max}/2.57$ scaled with the exact solution (see MTT56) when no reaction is present in Figure 4.5. In this case the density field is linear ($N^2 = 1$) and the species concentration R_2 is allowed to vary as a power law with exponent γ. Therefore for $\gamma < 0$ the concentration

decreases with height and for $\gamma > 0$ the concentration increases with height. In general, when $\gamma \ll 1$ the ambient species will only exist at levels very close to the source and as a result the plume can only entrain a very small amount of this chemical which leads to small amount of reaction and the maximum rise height will be approximately the same at MTT56. When $\gamma \gg 1$ the ambient species concentrations is very large above $z = 1$. Since this chemical concentration is very large here, species 1 gets consumed rapidly in this region regardless of reaction rate and the solutions converge onto a single value. In addition the maximum rise height increases with an exothermic reaction and decreases with an endothermic reaction as we expect.

There is an interesting behaviour near $\gamma = 1$ for the exothermic case since H_{max} is larger for smaller reaction rate constants. This occurs because the entrainment rate is larger in a region of denser ambient fluid when the reaction is fast due to the reaction induced fluid acceleration in this region. In addition, there is an interesting result for $\gamma \gg 1$ and $\hat{H}_r = 0$ since $H_{max} \approx 1$ and therefore independent of the chemical reaction. In this case $\varpi \propto Q/\bar{F}$, a function of height and $\bar{F} \propto Q(\nu z)^{\gamma}$, which increases non-linearly with γ. Therefore $\varpi \approx 0$ for $\gamma \gg 1$ and the reaction has a negligible effect on the plume dynamics.

4.5 Non-Boussinesq plume

4.5.1 Plume equations

When the plume density is much larger than a reference density, corresponding to the ambient, the Boussinesq assumption breaks down. In this case we need to reformulate the problem without this assumption. We follow Rooney &

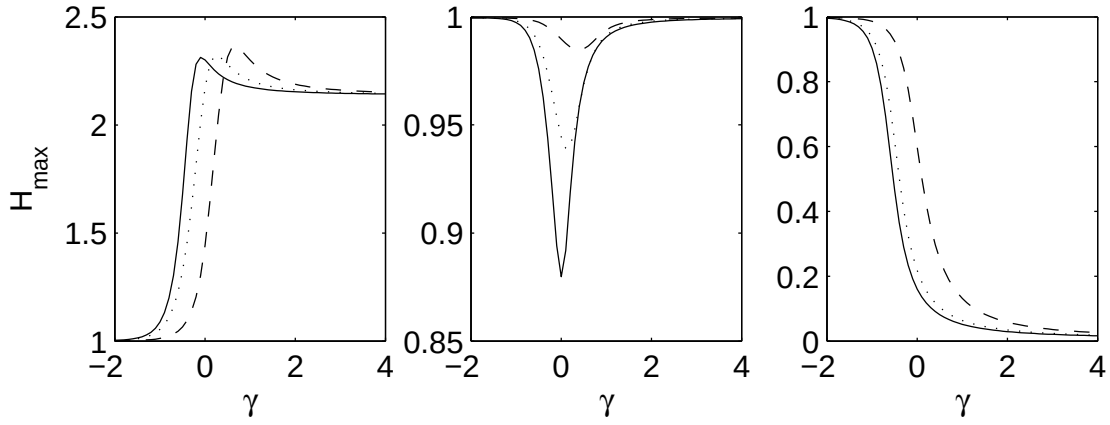

Figure 4.5: Numerical solutions showing the maximum rise height of the plume (H_{max}) for $\hat{H}_r = -10$ (left), 0 (center), 10 (right) and $\lambda_3 = .1$ (dashed line), 1 (dotted line), 10 (solid line). Here $\nu = 100$, $\phi = 1$, $W_1 = W_2 = 1$, $\hat{\lambda}_3 = \lambda_3$ and $\beta = 1$.

Linden (1996) and define fluxes with top hat profiles as

$$\pi\rho_0 Q'(z) = 2\pi\int_0^\infty rw\rho \, \mathrm{d}r = \pi\bar{\rho}\bar{w}b^2, \tag{4.39a}$$

$$\pi\rho_0 M'(z) = 2\pi\int_0^\infty \rho r w^2 \, \mathrm{d}r = \pi\bar{\rho}\bar{w}^2 b^2, \tag{4.39b}$$

$$\pi V'(z) = 2\pi\int_0^\infty rw \, \mathrm{d}r = \pi\bar{w}b^2, \tag{4.39c}$$

$$\pi\rho_0 P_i'(z) = 2\pi\int_0^\infty \rho Y_i rw \, \mathrm{d}r = \pi\bar{\rho}\bar{Y}_i\bar{w}b^2 \tag{4.39d}$$

for mass, momentum, volume and species respectively. Following the procedure for a Boussinesq plume the appropriate equations can be derived by integrating

equations (4.7a–4.7d) across the plume, yielding

$$\frac{\mathrm{d}Q'}{\mathrm{d}z} = 2\alpha\left(\frac{\rho_a}{\rho_0}\right)^{1/2} M'^{1/2}, \tag{4.40a}$$

$$\frac{\mathrm{d}M'}{\mathrm{d}z} = g\left(\frac{\rho_a}{\rho_0} - \frac{Q'}{V'}\right)\frac{Q'V'}{M'}, \tag{4.40b}$$

$$\frac{\mathrm{d}V'}{\mathrm{d}z} = 2\alpha\frac{M'^{1/2}}{(\rho_a/\rho_0)^{1/2}} - \sigma\frac{Q'V'}{M'}, \tag{4.40c}$$

$$\frac{\mathrm{d}P_i'}{\mathrm{d}z} = 2\alpha R_i\left(\frac{\rho_a}{\rho_0}\right)^{1/2} M'^{1/2} + \frac{\omega_i}{\rho_0}\frac{Q'V'}{M'}. \tag{4.40d}$$

With these definitions the density is $\bar{\rho} = \rho_0 Q'/V'$, the velocity is $\bar{w} = M'/Q'$ and the plume radius is $b^2 = Q'V'/M'$. In this analysis we have used the entrainment assumption $u_e = \alpha w(\rho/\rho_a)^{1/2}$, which is consistent with the experimental results of Ricou & Spalding (1961) and has been used by Rooney & Linden (1996) and Woods (1997). To compute the right hand sides of equations (4.40c) and (4.40d) we express the concentrations in terms of fluxes using $P_i' = \rho\bar{Y}_i V'/\rho_0$. Then

$$\sigma\frac{Q'V'}{M'} = \Omega\rho^2 Y_1 Y_2\frac{Q'V'}{M'} = \rho_0^2\Omega\frac{P_1'P_2'}{M'}\frac{Q'}{V'}, \tag{4.41}$$

$$\frac{\omega_i}{\rho_0}\frac{Q'V'}{M'} = \pm\frac{\rho_0 K W_i}{W_1 W_2}\frac{P_1'P_2'}{M'}\frac{Q'}{V'} = \psi_i\frac{P_1'P_2'}{M'}\frac{Q'}{V'}. \tag{4.42}$$

In addition we can define a buoyancy flux as in equation (4.12c); this gives

$$B = gV'\left(\frac{\rho_a}{\rho_0} - \frac{Q'}{V'}\right), \tag{4.43}$$

and the momentum flux equation becomes

$$\frac{\mathrm{d}M'}{\mathrm{d}z} = \frac{BQ'}{M'}. \tag{4.44}$$

The governing equation for B is then

$$\frac{\mathrm{d}B}{\mathrm{d}z} = -N^2V' - \kappa\frac{\rho_a}{\rho_0}\frac{P_1'P_2'}{M'}\frac{Q'}{V'}, \tag{4.45}$$

where

$$\kappa = g\rho_0\psi_3\left[\frac{\beta\Delta H_r}{W_3 C_p} + \frac{Q'}{\bar{P}'}\right] = \hat{\psi}_3(\hat{H}_r + Q/\bar{P}'), \tag{4.46}$$

and $\bar{P}' = \sum_{i=1}^{3} W_3 P_i'/W_i$. Finally, the boundary conditions at the source are

$$Q' = M' = 0, \quad B = B_0, \quad V' = B_0\rho_0/g\rho_a, \quad P_2' = P_3' = 0, \quad P_1' = P_{10}' \quad \text{at} \quad z = z_s. \tag{4.47}$$

Note that these equations are formally identical to the Boussinesq equations for a uniform ambient density and negligible reaction rate but generally differ, owing to the factor $(\rho_a/\rho_0)^{1/2}$ and Q'/V' appearing in the equations. One important difference is the extra term in the volume flux equation (4.40c) that allows the plume to expand or contract with an exothermic or endothermic reaction respectively.

We do not pursue the stratified non-Boussinesq case: it is relevant only to situations like volcanic plumes with very hot gases rising high into the stratified atmosphere. In engineering applications with non-Boussinesq plumes, stratification does not play an important role. Of course this case can be investigated as a straightforward combination of § 4.4.4 and of § 4.5.1.

4.5.2 No ambient stratification

Following § 4.4.2, the equations take on a simpler form when the vertical density and species gradients go to zero. When $\kappa' \approx 0$ the reaction has a negligible effect on the plume dynamics and we may combine the above equations with $B = B_o$ to obtain

$$Q' = \frac{6\alpha}{5}\left(\frac{9\alpha B_o}{10}\right)^{1/3} z^{5/3}, \quad M' = \left(\frac{9\alpha B_o}{10}\right)^{2/3} z^{4/3}. \tag{4.48}$$

These solutions are the analog of the Boussinesq similarity solutions and may be shown to be equivalent equivalent when $\rho = \rho_0$. We should note that $\rho_a = \rho_0$ when the ambient density is uniform. From these solutions we can define a non-dimensional source parameter as (Carlotti & Hunt, 2005)

$$\Gamma_{nb} = \frac{5BQ'^2}{8\alpha M'^{5/2}} \tag{4.49}$$

which may be defined at any height to indicate whether the plume is dominated by buoyancy or momentum.

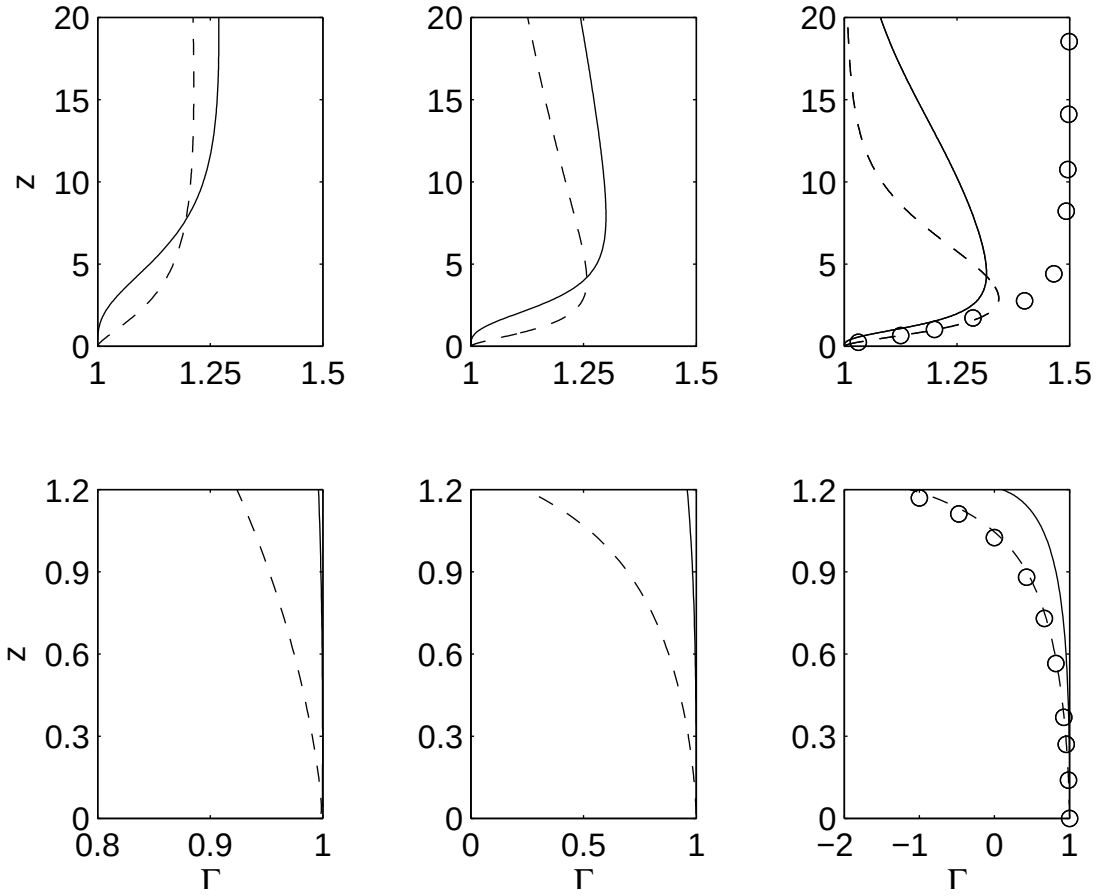

Figure 4.6: Numerical solution to the Boussinesq and non-Boussinesq equations for no ambient stratification showing Γ_b (dashed line) and Γ_{nb} (solid line) corresponding to $\psi_3 = .1$ (left), 1 (center) and 10 (right) and $\hat{H}_r = 10$ (upper) and 10 (lower). The circles represent the infinite reaction model. Here $\nu = 100$, $P_{10} = 1$, $R_2 = 1$, $W_1 = W_2 = 1$, and $\hat{\psi}_3 = \psi_3$

In Figure 4.6 we plot profiles of Γ and Γ_{nb} as a function of the reaction rate for a strongly exothermic and endothermic reaction. The two models are identical in form except for the factor Q'/V', multiplying the reaction rate in equations (4.41, 4.42, 4.45). This term is always less than one (otherwise we have a fountain) and $\mathrm{d}P_1'/\mathrm{d}z$ effectively reduced in comparison to the Boussinesq model. Therefore, for regions close to the source (where species 1 is relatively large) the Boussinesq model releases more thermal energy for an exothermic reaction ($\Gamma_b > \Gamma_{nb}$) and absorbs more thermal energy for an endothermic reaction ($\Gamma_b < \Gamma_{nb}$). For large z there is a higher concentration of species 1 in the plume for the non-Boussinesq model, which allows the density to sustain a smaller value ($\Gamma_b < \Gamma_{nb}$).

We have plotted the plume radius as a function of height in Figure 4.7 for the Boussinesq and non-Boussinesq formulations. Near the source, the density of the plume is small relative to the ambient and since the mass flux of both formulations are the same, the volume flux for the non-Boussinesq plume is larger (Woods, 1997). The effect of an exothermic reaction is then to make the expansion larger, since the density difference will have a greater sustained value above the source. At sufficiently large distance above the source, such that species 1 is sufficiently consumed, the plume density will approach the ambient density and the volume flux will behave as a Boussinesq plume. In the case of an endothermic reaction the absorption of thermal energy will cause the density of the plume to decrease relative to the ambient. For sufficiently large heats of reaction the plume density will be larger than the ambient density and since the mass flux for both formulations is the same, the volume flux will be smaller for the non-Boussinesq formulation. Since the volume flux for the non-Boussinesq formulation experiences a change in volume with reaction, the plume radius will narrow for large endothermic reactions as opposed to the Boussinesq model.

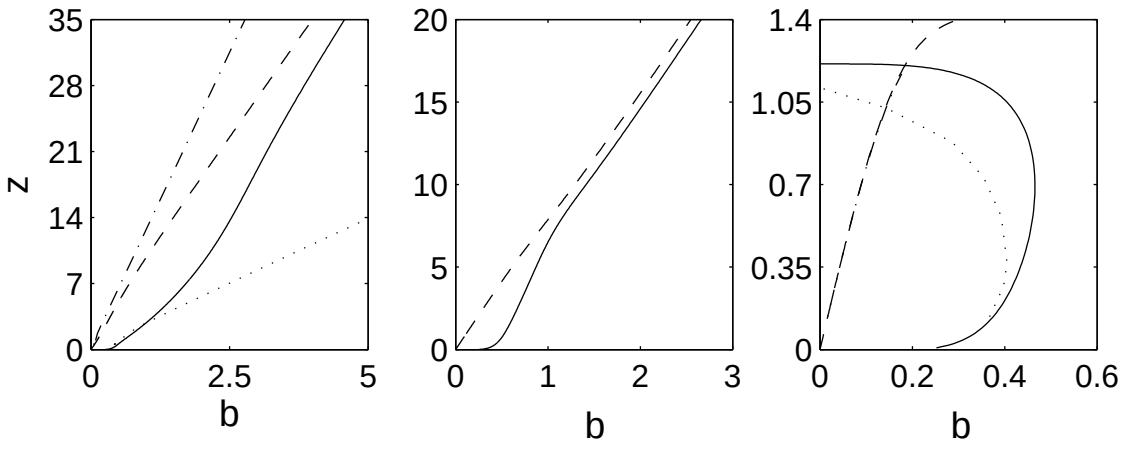

Figure 4.7: Numerical solution to the Boussinesq (dashed line) and non-Boussinesq (solid line) equations for no ambient stratification, showing the plume radius b corresponding to $H_r = -10$ (left), 0 (center) and 10 (right). Here $\psi_3 = 10$, $\nu = 100$, $P_{10} = 1$, $R_2 = 1$, $W_1 = W_2 = 1$, and $\hat{\psi}_3 = \psi_3$. The dashed and dot-dashed lines are the non-Boussinesq and Boussinesq infinite reaction rate solutions respectively.

4.5.3 Large reaction rate and no ambient stratification

As for the Boussinesq plume, we can determine an asymptotic solution for a non-Boussinesq plume rising in an ambient with zero stratification and a large reaction rate K. In this case the rapid consumption of of species 2 leads to $\psi_2 P_1' P_2' Q'/M'V' \approx -2\alpha R_c \rho_a^{1/2} M'^{1/2}/\rho_0^{1/2}$ and the volume and buoyancy flux integrate to

$$B = B_0 - \chi Q'. \tag{4.50}$$

Since the equations are the same as for the Boussinesq case, we recover the same results as (4.26)–(4.30) with Q replaced with Q'; thus

$$2\alpha \left(\frac{5|\chi|}{12\alpha}\right)^{1/5} (z - z_s) = \frac{5}{3}|\epsilon|^{-1/5} Q'^{3/5}\ {}_2F_1(1/5, 3/5; 8/5; Q'/\epsilon). \tag{4.51}$$

4.6 Conclusion

We have developed a model for a plume rising into an unbounded ambient with a reaction between the source plume chemical species and the ambient with a non-negligible heat of reaction, in the case of a second-order non-reversible chemical reaction. This model extends the work of CLSC to account for a source term on the buoyancy flux, which is a function of the heat released or absorbed. We first investigate the limiting case of a Boussinesq plume, where density effects are only important on the buoyancy terms. The difference with respect to the original plume equations of MTT56 is an extra term in the buoyancy flux equation which depends strongly on the species flux equations. In the case of an unstratified ambient and with certain approximations, we can obtain an exact solution for an infinite reaction rate, which indicates that the volume ($Q \propto z^{5/2}$) and momentum flux equations have different power laws than the similarity solution of MTT56 ($Q \propto z^{5/3}$). Furthermore, we showed that the reaction will cause the plume to behave 'lazy' for an exothermic reaction and 'forced' for an endothermic reaction. In the former case the plume ultimately asymptotes to a pure plume when the sources species is consumed but in the later case a fountain may form provided the reaction rate and heat of absorption is sufficiently large.

For a density and chemically stratified ambient we examined the effects of reaction rate and heat of reaction on the maximum rise height of the plume in comparison to the linear density model of MTT56. Interestingly, the maximum rise height may decrease for large reaction rates and an exothermic reaction since the reaction will be strongest near the source, where the source species and density are the largest. Moreover, for strongly decreasing ambient chemical stratifications the maximum rise height will be the same as for a non-reacting plume, since only a small amount of species 2 can be entrained.

Finally we have extended our model to a non-Boussinesq plume using an entrainment rate that depends on the ratio of plume to reference density. In this

case the two formulations are comparable only when the plume density is similar to the ambient density, which is always true at large heights above the source. Either way an exothermic reaction will cause the reaction rate to decrease, since it depends on the density and an endothermic reaction will cause the reaction rate to increase. This will have an important effect of the source parameter Γ and plume property profiles since the reaction rate in non-uniformly modified. Furthermore, the plume radius can have very different profiles, owing to the effects of compressibility on the non-Boussinesq formulation. In the case of an exothermic or endothermic reaction the plume will expand or contract respectively, more than the Boussinesq model.

This Chapter, in part, has been submitted to *Journal of Fluid Mechanics*, 2008, Conroy, D. T. and S. G. Llewellyn Smith (Cambridge University Press).

II

Gas hydrates

5

Introduction to gas hydrates

5.1 Background

Below the sea floor methane gas is known to exist in extremely large quantities, accumulating in the sediment of the deep and cold oceanic and permafrost regions. Due to the large pressure and cool temperatures the gas reacts with the surrounding water to form a crystalline substance known as a clathrate. The fate of these reserves is very important to climate on earth because methane is a much more efficient greenhouse gas then carbon dioxide (Kvenvolden 1993).

Gas hydrates are crystalline compounds made up of water molecule cages held together by hydrogen bonding. A guest gas contained within the center cavity stabilizes the structure under low temperatures and high pressures. A picture illustrating this molecular structure is shown in figure 5.1 with about 21 water molecules forming the cage and one methane molecule in the center. Depending on the size of the guest gas, hydrates are known to form type 1, 2 or H. For example methane and hydrogen form type 1 and isobutane and propane (these are larger molecules) form type 2 (Sloan 1990, Sloan 2003). In addition the bulk gas concentration is related to the hydrate number, $n_h = N_w/N_g$, which is the molar ratio of water to gas. For methane and isobutane $n_h \approx 5.75$ and 17 respectively.

Naturally formed gas hydrates contain mostly methane and a few hy-

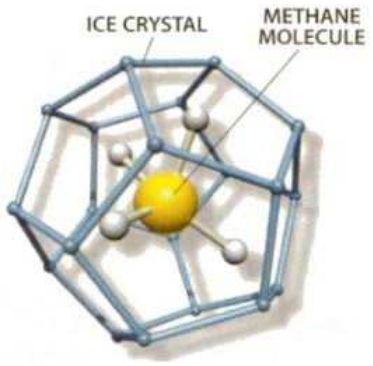

Figure 5.1: Clathrate hydrate structure for methane. There are approximately 21 molecules of water to every molecule of methane. For a large number of molecules bound together there are about 5.75 molecules of water to gas since a water molecule is associated with multiple cages (Kenneth D. Jordan personal communication).

drocarbons such as ethane, propane and iso-butane. These crystals are generally found in the ocean attached to the sediment that makes up the sea floor, where the temperatures are cold and pressures high. Their location is additionally constrained to regions of sufficiently high gas concentration such as the mid ocean ridges, where there is a large source of organic matter. The current research and interest in this substance generally falls within the following seven categories:

1. **Energy source**

   Conservative estimates of methane gas supplies in oceanic sediments are placed at around 10^{16} kg of carbon, making this the largest supply of hydrocarbons on earth (Kvenvolden 1993, Buffett 2000). Because of this large potential supply of energy many countries have shown interest in mining these reserves as a supplement or alternative to petroleum based fuels. One strategy for recovery is to convert a hydrate-bearing region into a well, where gas is removed from its crystal structure by depressurization or thermal stimulation (Holder 1984). Other techniques are possible, such as inhibitor or steam injection and research on this topic is still in the beginning stages.

2. **Chemosynthetic colonies**

   Ice worms have been found on exposed mounds using the methane rich deposits as food and shelter in the deep unlit places of the ocean (Sassen 1999). These organisms are non-photosynthetic life forms that use a process known as chemosynthesis to convert methane into energy. Due to their relatively new discovery and unique life history, an active area of research centers around them.

3. **Gas storage**

   Because of the high concentration of gas stored in hydrates, about 170 m^3 of gas per 1 m^3 of methane hydrate at STP conditions, the hydrate form has become a recent topic of interest for the transport of gases such as methane and hydrogen. A project is currently being undertaken by the Department of Energy on the storage of natural gas (http://www.doe.gov) The hope is that the clathrate structure can hold large concentration of gas at much lower pressures than their liquid counterpart.

4. **Carbon sequestration**

   The potential onset of global warming due to industrial carbon dioxide emissions, has resulted in an interest in carbon dioxide sequestration in the form of hydrates at the bottom of the ocean. This idea is being actively pursued by many agencies such as the Department of Energy. The idea is to pump the gas into the sediment, where it forms a hydrate that binds to the porous skeleton (Brewer 2000). Indeed this process will be necessary to replace mined methane hydrates in order to prevent sediment weakening that could lead to slope instability.

5. **Inhibition in gas pipelines**

   Hydrate inhibition in pipelines historically was the first major research endeavor on this substance. Essentially, if any moisture is present in the system and the proper conditions are met (i.e. cool temperatures and high

pressure), hydrates will grow on the walls and ultimately block the pipeline (Sloane 1990). This problem inspired the establishment of the hydrate phase diagram, figure 5.2, and the pursuit of chemicals, such as salt and methanol, that depress the melting point and inhibit formation.

6. **Desalination**

   Due to the fact that gas hydrates reject salt as they grow and can form at high pressures and relatively moderate temperature, there has been some interest in using them to desalinate sea water. This idea is actively being pursued by many commercial and government agencies such as Oak Ridge National Laboratories (http://sps.esd.ornl.gov/desalinationpage.html). The objective here is similar to the effect of freezing sea water by bringing the temperature below its freezing point, but using pressure which may be more efficient. One possible technique is to utilize the ocean water column to achieve the high pressure needed to increase the three-phase temperature above the local water temperature and bubble carbon dioxide gas through a long tube that spans the whole depth. The hydrate will form a rind around the bubbles and subsequently rise to the surface, where it melts to form freshwater. Over time the rejected salt will occupy the lower section of the pipe and expelled fresher water at the top, similar to a natural convection regime.

7. **Global warming**

   Since there are large quantities of methane contained at the bottom of the ocean world wide and the fact that CH_4 is 23 times more effective as a greenhouse gas than CO_2 on a per mole basis, it would be catastrophic if even a small fraction of this gas were to reach the atmosphere (Kvenvolden 1993, Buffett 2000). In fact one proposed end to the last ice age has been attributed to a large sudden release of these stored methane deposits. A positive feedback loop occurs when an increase in sea floor water temperature destabilizes the hydrate, releasing gas into the atmosphere (Dickens

1999). As a result the atmospheric temperature rises, melting the polar ice caps and increasing the ocean water level. Eventually the large hydrostatic pressure could re-stabilize the remaining hydrate reserves, thus reaching an equilibrium.

5.2 In-situ setting

Most of the world's supplies of methane hydrates are located on the continental margins, where they are attached to the sea floor sediment. These areas are rich with thermogenic based methane deposits and organic matter, which partially turns into methane gas after bacterial methanogenesis. In addition the sea bed is sufficiently deep ($\approx O(1\text{km})$ below the ocean surface), where gas hydrates are in equilibrium with the surrounding sea water, as a result of the large hydrostatic pressure and relatively cool temperatures.

A representative stability diagram is shown in figure 5.3 for the deep ocean regions. The bold curve represents the three-phase boundary (water, hydrate, gas) which increases with the hydrostatic pressure. The dotted lines represent actual temperature profiles which are shown to increase with depth caused by the geothermal gradient and towards the ocean surface due to solar radiation. Because of the equilibrium constraint the hydrate can only exist if the temperature is less than its equilibrium value or to the left of the bold curve in the diagram. In addition, the equilibrium curve will depend on the dissolved methane and salt concentration and therefore the true profile will be site-dependent.

The hydrate-bearing region may be determined by core sample or bottom simulating reflector (a method for determining the base of the hydrate stability zone through an anomalous seismic reflection) and is generally found to be a band of some thickness and depth below the seafloor (Kvenvolden et al., 1993). The top of this layer cannot exist above the seafloor since the sediment acts as a barrier to keep the hydrate in place. The bottom of the hydrate layer is bound by the

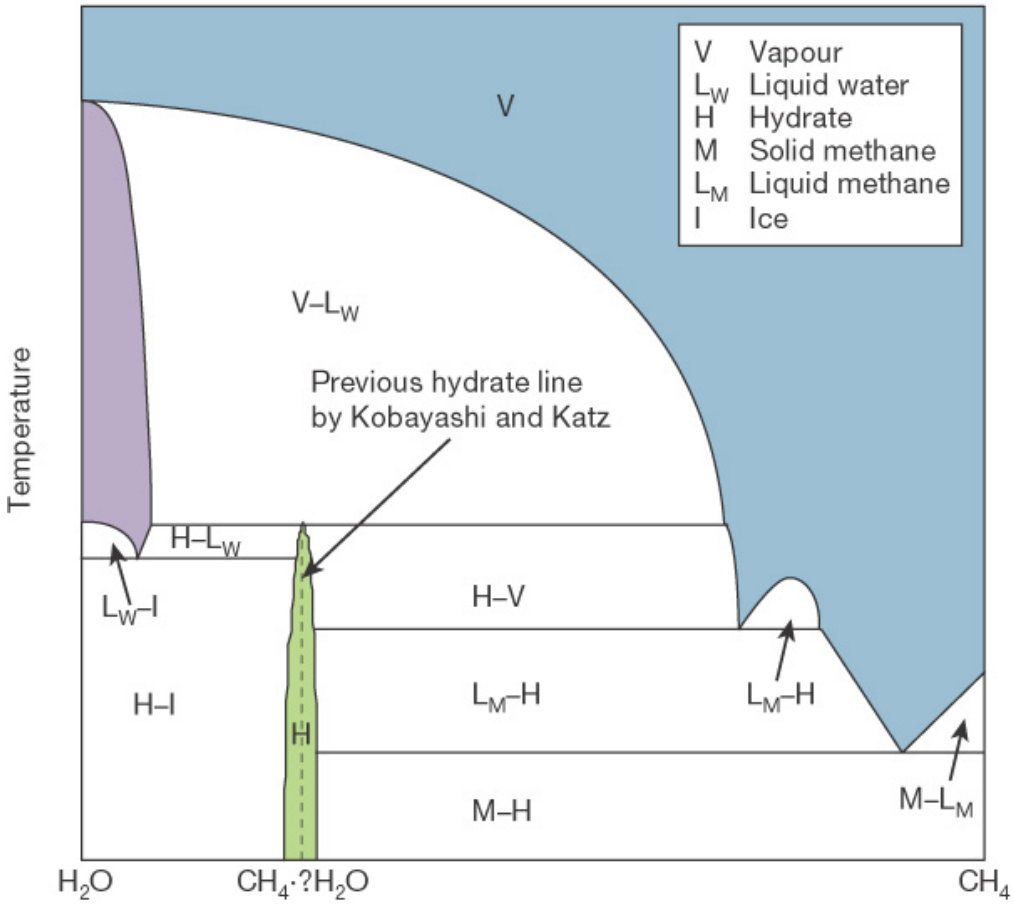

Figure 5.2: Gas hydrate equilibrium phase diagram for methane and water. The different labeled regions show the phases that exist for a given sample with temperature and bulk composition. The diagonal line separating the mixed hydrate-water region (H-L_w) and the liquid region is called the liquidus curve. Here, it is approximately linear and governs the interface temperature for dissolution or melting models. The line separating the mixed hydrate-water region (H-L_w) and the vapor-liquid water region (V-L_w) is the three phase-curve and governs the maximum temperature the hydrate can reach in dissociation models. From Sloane (2003).

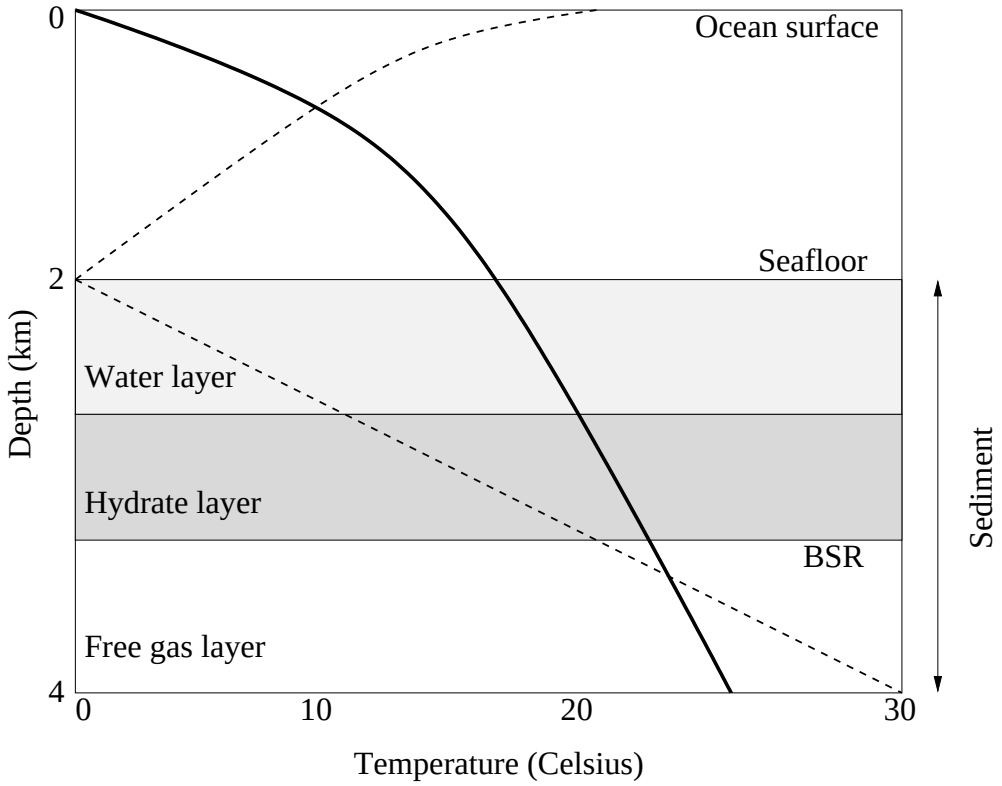

Figure 5.3: Diagram for *in situ* hydrate deposits. The bold curve represents the three-phase line as a function of pressure and the dotted line represents the temperature as a function of depth in the ocean. The seafloor is idealized as the coldest point in the system, with the temperature increasing towards the ocean surface due to solar radiation and increasing towards the Earths center because of the geothermal gradient.

three-phase curve and exists as a result of a flux of heat from the Earth's core.

The distribution of gas hydrates within the oceanic sediments varies by location, although in general there will always be a mixture of sediment, seawater and hydrate. The sediment varies from course grains to silt, corresponding to a hydrate distribution of disseminated grains and pore fillings to nodules and veins respectively (Dillon 2003). The bottom of the BSR (bottom simulating reflector) varies by location. For example, at Blake Ridge in the Gulf of Mexico, the location of the BSR varies from around 0.2-0.8 km corresponding to a water column depth

Table 5.1: Properties of the fluid hydrate and sediment used in the plots. Taken from Rempel (1997).

Constant	Value	Constant	Value
ρ_l	1000 kg/m^3	K_H	.49 $W/(m \cdot K)$
ρ_H	930 kg/m^3	K_l	.569 $W/(m \cdot K)$
ρ_s	2240 kg/m^3	K_s	1.9 $W/(m \cdot K)$
$C_{P\ell}$	4200 $J/(kg \cdot K)$	D_g	10^-9 m^2/s
C_{PH}	2080 $J/(kg \cdot K)$	D_s	10^-9 m^2/s
C_{Pp}	900 $J/(kg \cdot K)$	L	430×10^3 J/kg
n	0.5		

of approximately 1-4 km (Dillon 2003).

5.2.1 Cold vents

There are offshore regions such as Vancouver island where cold vents seep high concentrations of methane through the sediment. As a result large concentrations of methane hydrate are found near the seafloor and may span horizontal distances reaching in the range of kilometers. At the Vancouver island site, sediment core samples taken by Lu et al.(2005) and Riedel et al.(2006) were between 2-8 meters below the seafloor. This sediment consisted of finely laminated glaciomarine clays and silts with massive hydrates containing saturations up to $S_h = .78$. In some cases this level of saturation spanned several meters but ultimately decreased rapidly with depth.

5.2.2 Gas hydrate physical properties

Physical properties associated with methane gas hydrates such as thermal, chemical and phase equilibrium have been investigated by many authors (see Rempel 1997, Sloane 1990, Handa 1990, etc.). We have included only a small fraction of that data in tables (5.1) and (5.2).

Table 5.2: Solubility of methane in water as a function of temperature. Taken from Rempel (1997) and Handa (1990).

Pressure	65 bar
salinity	0
Γ	$1.05 \times 10^4 K$
T_{eq}	$282.05K$
$C_\ell(T_{eq})$	1.85×10^{-3}
T_o	$275.25K$
$C_\ell(T_o)$	1.201×10^{-3}
C_h	.13

5.3 Previous work

Gas hydrate dissociation essentially relies on deviations in system properties from equilibrium, which may arise through temperature, pressure and concentration. In response, the hydrate changes phase, since it is now theoretically unstable, in order to bring system back into equilibrium. These types of processes are known as moving boundary problems and have been widely studied with reference to ice formation, the casting of alloys, liquid spray combustion and many more. A good introduction to these topic can be found in the classic texts of Crank (1984) and Carslaw and Jaeger (1946) in which the process can be described by heat conduction with an appropriate condition for the moving interface that depends on the latent heat of formation. More complicated models arise for binary or supercooled systems due to interfacial instability, where the phase boundary becomes unstable, forming an array of dendritic structures. These are most commonly seen naturally in snow flakes and sea ice and an excellent introduction can be found in Davis (2001) and Worster (2000). A similar process occurs in connection with gas hydrate formation and dissociation, which are described further below.

5.3.1 Dissolution and Formation

When in-situ conditions are within the hydrate stability zone, hydrate will decompose if the dissolved methane concentration in the water is less than the equilibrium concentration at the water temperature. This condition is usually constrained by the liquidus relationship which expresses the melting temperature as a function of species concentration and pressure. Alternatively if the gas concentration is larger than its equilibrium value the hydrate will grow either internally by increasing the hydrate saturation and/or externally by thickening the hydrate zone.

In the literature most studies have concentrated on the latter, with the purpose of predicting the methane hydrate distribution in the sediment. Rempel and Buffett (1997) considered a two-phase (hydrate and water) system in a porous medium of constant porosity, with a cooled lower boundary and a constant dissolved methane concentration upper boundary. The location of the hydrate-water interface was determined as a function of time by solving the conservation equations for thermal energy, mass, and gas concentration. Xu and Ruppel (1999) considered a similar problem, but solved the system of equations with a steady-state assumption and flux of energy, mass and methane at the lower boundary and constant temperature, pressure and methane concentration on the upper boundary. The important results obtained from this analysis were an estimate for the upper and lower bound of the hydrate and methane hydrate stability zones. Liu and Flemings (2007) extended these models to include the multiphase flow of gas through the sediment that is generated from below the hydrate stability zone. They assumed that a mixed phase of hydrate, gas and water was always in equilibrium and solved the multiphase flow equations with the assumption of negligible latent heat release. They found that for large gas fluxes the hydrate concentration is larger near the surface, which is what is observed in regions with cold seeps.

5.3.2 Dissociation

When the temperature of the water increases so that the concentration of the liquid is now less than the equilibrium value at that temperature, the hydrate will dissolve in a way that can be modeled by the approaches used above. However, if the temperature of the water rises above the three-phase region, the hydrate will dissociate into a gas and a liquid rather than dissolved gas and liquid as in the dissolution case. Past studies of hydrate dissociation have primarily looked at one-dimensional Stefan problems in a porous domain with a similar formulation to the melting of ice. The complication then is to model accurately the motion of the gas and its effect on the heat and mass transfer. Kamath and Holder (1987) performed experiments for the dissociation of propane and methane hydrates by circulating relatively warm water above the upper surface. They assumed a nucleate boiling phenomenon (sometimes used in conjunction with boiling heat transfer) for the heat transfer and used Rohsenhow's correlation to obtain estimates for the rate of gas release that showed relatively good accuracy with experimental data. Selim and Sloan (1989) considered a simple analytic model for the rate of dissociation in a semi-infinite plane in response to an increase in upper boundary temperature. They ignored the motion of the water and the effect of fluid saturation on the relative permeability and determined gas release rates as a function of boundary temperature.

Tsypkin (2001) considered a multiphase flow and looked at the stratum and interface temperature as a function of permeability in response to different upper boundary pressures in a depressurizing well. He linearized the governing porous medium equations and solved for the temperature, pressure and water saturation by a similarity solution. The main results showed that under certain conditions, mainly a large drop in stratum pressure or increase in permeability, the dissociation can lead to the formation of ice, creating a boundary for gas extraction. Most recently Ahmadi et al.(2004) obtained a numerical solution for the rate of gas production from dissociating hydrate in a depressurized well. They solved the

thermal energy and pressure equation coupled to the Clausius-Clapeyron equation and Stefan condition at the moving interface. These equations were solved on both sides of the interface without consideration of a water phase, using an explicit finite difference method. The position of the moving interface was obtained from the Stefan condition and numerically was fixed until the position moved the equivalent of one grid space.

5.4 Modeling the decomposition of gas hydrates in porous media

We know from the previous section that gas hydrates are naturally found in the sediment beneath the sea-floor and in permafrost regions. A simple diagram of this situation is shown in Figure 5.4, where the region $z \leq s$ is filled with a gas hydrate with some spatially dependent hydrate saturation and water fills the pore space in the region $z \geq s$. There is an interface, labeled $z = s(t)$, separating these two regions that moves in time due to deviations in phase equilibrium. With reference to the phase diagram shown in Figure 5.2 the hydrate bearing region corresponds to the region labeled H-L_w, where hydrate is in equilibrium with the dissolved gas in the water. From the lever rule we can determine the hydrate saturation as a function of the temperature and total concentration provided we know the liquidus relationship. The liquidus is the curve separating H-L_w from the water region and is analogous to the solubility curve. In the liquid region ($z > s(t)$) the temperature may lie above the three-phase point in which case dissociation occurs when the concentration is below the liquidus value at the given temperature. Furthermore this region may lie above (as far as temperature) the three-phase point, shown as the V-L_w region of the phase diagram, in which case the hydrate will decompose into water and gas.

In the porous medium we have in general a mixed phase of hydrate, gas, water and solid matrix of some time and spatially dependent fraction. Provided

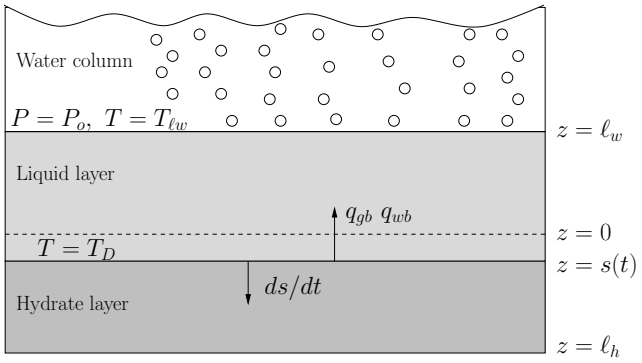

Figure 5.4: Setup for the hydrate dissolving case with hydrate in the lower half plane and water in the upper. $s(t)$ is the position of the moving interface with velocity ds/dt in the downward direction and has an initial position of $s = 0$.

the length scales at the size of the interstices are small in comparison to the size of the domain, we can treat the system in an average sense. Since gas hydrates generally occur in clays, silts and fine sands this restriction is not a problem. In this case we seek a volume averaging approach, which is taken over some representative volume R that is sufficiently large to contain many pore spaces (Bear 1991).

5.4.1 Mass conservation

We consider mass conservation within a volume V in the following form

$$\frac{\partial}{\partial t}\int_R \rho \mathrm{d}V = -\int_S (\rho_w q_w + \rho_g q_g)\cdot \mathbf{n}\,\mathrm{d}S \tag{5.1}$$

with ρ the average density defined as

$$\rho = nS_w\rho_w + nS_g\rho_g + nS_h\rho_h + (1-n)\rho_s, \tag{5.2}$$

n is the porosity, S_w is the water saturation and the subscripts w, g, h and s represent water, gas, hydrate and solid respectively. Here we take the solid matrix and hydrate to be rigid and stationary although the hydrate can grow, resulting in an increase in S_h. Applying the divergence theorem we may express the above equation as

$$\int_R \left(\frac{\partial \rho}{\partial t} + \nabla\cdot(\rho_w q_w + \rho_g q_g)\right)\mathrm{d}\,V = 0. \tag{5.3}$$

Since this equation is true for an arbitrary control volume R, this integrand must be zero everywhere,

$$\frac{\partial \rho}{\partial t} + \nabla \cdot (\rho_w q_w + \rho_g q_g) = 0. \tag{5.4}$$

Assuming that the densities of the hydrate, solid and water are constant as well as the porosity (n) we can express this as

$$\nabla \cdot (\rho_w q_w + \rho_g q_g) = n\rho_h \frac{\partial S_h}{\partial t}\left(\frac{\rho_w}{\rho_h} - 1\right) + n\rho_w \frac{\partial S_g}{\partial t}\left(1 - \frac{\rho_g}{\rho_w}\right) - nS_g \frac{\partial \rho_g}{\partial t} \tag{5.5}$$

where we have used the fact that $S_w + S_g + S_h = 1$. Therefore if the hydrate fraction or the gas fraction increase, the fluids will be squeezed out due to volume expansion associated with a change in phase.

In the porous media literature it is common to define a component mass conservation equation as follows (Bear 1991):

$$\frac{\partial}{\partial t}(nS_w\rho_w + n\rho_{w0}S_h) + \nabla \cdot (q_w\rho_w) = -r_{gw}, \tag{5.6}$$

$$\frac{\partial}{\partial t}(nS_g\rho_g + n\rho_{g0}S_h) + \nabla \cdot (q_g\rho_g) = r_{gw}, \tag{5.7}$$

which when summed is equal to the total mass conservation equation (5.4). The second term on the left hand of this equation accounts for the water or gas trapped within the solid with fraction $\rho_{w0} = n_h\rho_h M_w/(M_g + n_h M_w)$ and $\rho_{g0} = \rho_h M_g/(M_g + n_h M_w)$, were n_h is the hydrate number (≈ 5.7 for methane), M_w is the molecular weight of water and M_g is the molecular weight of gas. The term on the right hand side accounts for gas dissolution and may be defined as (see Esposito (1999))

$$r_{gw} = k_g A_g (C_{eq} - C_w), \tag{5.8}$$

which expresses the rate of dissolution or formation of gas as a function of the surface area A_g, kinetic coefficient k_g and deviation in dissolved species concentration, C_w from the equilibrium value C_{eq}. In this equation we have used a kinetic relationship where the coefficient k_g must be determined experimentally.

5.4.2 Temperature equation

For the conservation of heat in the system we assume that the temperature of each component (i.e. hydrate, water, etc.) is at the same temperature. Using similar arguments as for the mass conservation we can write the energy equation as

$$\frac{\partial \rho H}{\partial t} + \nabla \cdot (\rho_w H_w q_w + \rho_g H_g q_g) = \nabla \cdot (K \nabla T), \tag{5.9}$$

where H is the total enthalpy and K is the average conductivity

$$\rho H = nS_w \rho_w H_w + nS_g \rho_g H_g + nS_h \rho_h H_h + (1-n)\rho_s H_s, \tag{5.10}$$

$$K = nS_w K_w + nS_g K_g + nS_h K_h + (1-n)K_s. \tag{5.11}$$

In the above definition of conductivity we assumed that the direction of conductivity is parallel to the laminar layers. This assumption is appropriate because the hydrate most likely formed initially in order to align itself with the prevailing temperature gradient. Since $\mathrm{d}H/\mathrm{d}T = C_P$ by definition of specific heat, we can expand the derivatives with constant specific heats (a good approximation for small changes in temperature and pressure) as

$$\overline{\rho C_P}\frac{\partial T}{\partial t} + (\rho_w C_P^w q_w + \rho_g C_P^g q_g) \cdot \nabla T = \tag{5.12}$$

$$\nabla \cdot (K \nabla T) + n\rho_h L \frac{\partial S_h}{\partial t} + (H_w - H_g)\left(\frac{\mathrm{d}n\rho_g S_g}{\mathrm{d}t} + \nabla \cdot (q_g \rho_g)\right) \tag{5.13}$$

where $L = H_h - H_\ell$ is the latent heat of dissociation and we have assumed the densities of the water, hydrate and solid to be constant. Therefore if the hydrate dissociates, latent heat will be absorbed, and if the gas dissolves the heat of dissolution will be absorbed as well. Generally the amount of gas dissolution will be small in comparison to advection or conduction and we can ignore this term. The average specific heat is defined as

$$\overline{\rho C_p} = nS_w \rho_w C_p^w + nS_g \rho_g C_p^g + nS_h \rho_h C_p^h + (1-n)\rho_s C_p^s \tag{5.14}$$

Similarly to dissolution we can close the above equation by specifying the solidification or melting term as (see Worster 2000)

$$\frac{\partial S_h}{\partial t} = k_h A_h (T_{eq} - T) \tag{5.15}$$

which expresses the rate of decomposition or formation of gas as a function of the surface area A_h, kinetic coefficient k_h and deviation in temperature from the equilibrium value T_{eq} from the phase diagram. The common assumption with reference to mushy layers is to assume that $k_h A_h$ is large so that the phase change occurs over a smaller time scale than other processes in the system. This result implies that the hydrate is always in equilibrium with the water, $T = T_{eq}$ and we will make this assumption.

5.4.3 Species equation

In a similar way we can express the total gas concentration for an averaged region as

$$\frac{\partial C\rho}{\partial t} + \nabla \cdot (\rho_w C_w q_w + \rho_g C_g q_g) = \rho_w \nabla \cdot (D \nabla C_w) \tag{5.16}$$

where C is the total concentration which is composed of the gas concentration C_g (generally equal to unity), the dissolved gas concentration C_w. In addition, D is the mass diffusivity of dissolved gas in water and we have assumed that species can only diffuse in the water. Here we have

$$\rho C = n S_w \rho_w C_w + n S_g \rho_g C_g + n S_h \rho_h C_h, \tag{5.17}$$

$$D = n S_w D_w. \tag{5.18}$$

In this expression we have assumed that the hydrate concentration is constant (i.e. $C_h \approx .13$ for methane) and the gas concentration is constant ($C_g = 1$). Expanding this equation and rearranging we obtain

$$n S_w \frac{\partial C_w}{\partial t} + q_w \cdot \nabla C_w = \nabla \cdot (D \nabla C_w) + r_{gw}(C_w - C_g) + \tag{5.19}$$

$$n \frac{\partial S_h}{\partial t} \left(\frac{\rho_h}{\rho_w} (C_w - C_h) + \frac{\rho_g}{\rho_w} (C_g - C_w) \right), \tag{5.20}$$

an expression for the change in dissolved gas concentration in the water. The second expression on the right hand side represents the increase in concentration due to dissolution and the last term represents the change in concentration due to hydrate dissociation or formation.

We can use a similar equation for the salt concentration expressed as

$$nS_w\frac{\partial C_w^s}{\partial t} + q_w \cdot \nabla C_w^s = \nabla \cdot (D^s \nabla C_w^s) + n\frac{\partial S_h}{\partial t}\frac{\rho_h}{\rho_w}C_w. \tag{5.21}$$

Here the only production term comes from the change in hydrate saturation, which acts to increase the salt concentration when this term is positive. In general this equation can be neglected when hydrate formation or decomposition is slow.

5.4.4 Interface conditions

At the interface one can use 'pill box' arguments to obtain jump conditions across the liquid/liquid-hydrate interface. Applying Leibniz's rule to the equations in conservation form, we obtain in the limit as the control volume goes to zero

$$[q_w] = nV_n[S_w] + nV_n\frac{\rho_{w0}}{\rho_w}[S_h] \tag{5.22}$$

$$[\rho_g q_g] = nV_n[\rho_g S_g] + n\rho_{g0}V_n[S_h] \tag{5.23}$$

$$(n\rho_h L + n\rho_{g0}(H_g - H_w))V_n[S_h] = [K\nabla T \cdot \mathbf{n}] \tag{5.24}$$

$$\left(n(C_w - C_h) + n\frac{\rho_{g0}}{\rho_w}(C_g - C_w)\right)V_n[S_h] = [D\nabla C \cdot \mathbf{n}] \tag{5.25}$$

$$T = T_{eq} = T_m + \Gamma(C - C_m) \tag{5.26}$$

where [] denote jumps in the bracketed quantity, V_n is the interfacial velocity and Γ is the slope of the liquidus curve in Figure 5.2. The first two equations describe the velocity of the gas and water at the interface due to hydrate decomposition or formation. Equation (5.24) is known as the Stefan condition and expresses the velocity of the moving boundary as a function of the thermal diffusion and latent heat. In (5.25) we have assumed that the dissolution term drops out, which is consistent for an equilibrium constraint. The last equation is the equilibrium

condition and it expresses the interfacial temperature in terms of concentration (i.e. liquidus curve on the phase diagram).

5.4.5 Multiphase flow equations

The above equations are closed with an appropriate expression for the velocity, which is commonly assumed to follow Darcy's law:

$$q_w = -\frac{\Pi_w}{\mu_w}\left(\nabla P_w + \rho_w g\right), \quad q_g = -\frac{\Pi_g}{\mu_g}\left(\nabla P_g + \rho_g g\right) \tag{5.27}$$

where μ is the viscosity and $\Pi_w(S_w)$ is the saturation dependent water permeability. The permeability and capillary pressure ($P_c = P_g - P_w$) relationships are in general non-linear functions of water saturation that are determined experimentally. Here we use the model of Genuchten (1996) expressed as

$$\Pi_w = \Pi\,\Pi_{rw}, \quad \Pi_{rw} = S_e^{1/2}\left(1 - \left(1 - S_e^{1/m}\right)^m\right)^2, \tag{5.28}$$

$$\Pi_g = \Pi\Pi_{rg}, \quad \Pi_{rg} = \left(1 - S_e\right)^{1/2}\left(1 - S_e^{1/m}\right)^{2m}, \tag{5.29}$$

$$P_c = \frac{\rho_w g}{\alpha} f_c, \quad f_c = \left(S_e^{-1/m} - 1\right)^{1-m}, \tag{5.30}$$

where Π is the absolute permeability used for a single phase flow, $S_e = (S_w - S_{wo})/(1 - S_{wo})$ is the equivalent saturation, scaled by the zero water phase flow saturation S_{wo}, and the coefficients m and α are determined experimentally for the different combinations of the two fluids and sediment properties.

We can combine (5.6), (5.7) and (5.27) to obtain the saturation equation

$$n\frac{\mathrm{d}S_w}{\mathrm{d}t} + \nabla \cdot q_w = -\frac{r_{gw}}{\rho_w} - \frac{n\rho_{w0}}{\rho_w}\frac{\mathrm{d}S_h}{\mathrm{d}t}, \tag{5.31}$$

$$q_w = \frac{M_w}{M_w + M_g}\left(q_t - M_g \nabla \cdot P_c + M_g \rho_w g\left(\frac{\rho_g}{\rho_w} - 1\right)\right), \tag{5.32}$$

where $q_t = q_g + q_w$ is the total flow rate and the mobility functions are $M_w = \Pi_w/\mu_w$ and $M_g = \Pi_g/\mu_g$. In the special case of constant densities we can combine the conservation of water and gas equations to obtain

$$\nabla \cdot q_t = r_{gw}\left(\frac{1}{\rho_g} - \frac{1}{\rho_w}\right) + n\frac{\mathrm{d}S_h}{\mathrm{d}t}\left(1 - \frac{\rho_{w0}}{\rho_w} - \frac{\rho_{g0}}{\rho_g}\right), \tag{5.33}$$

which expresses the divergence in q_t in terms of gas dissolution and hydrate dissociation.

5.4.6 Discussion of boundary conditions

In general there are many ways in which a boundary condition could be applied in order to cause the hydrate to dissociate but we will only concentrate on a few that are applicable to natural settings.

Temperature increase

If the overlying water column were to increase in temperature for some reason such as a response to global warming or an anomalous pulse in temperature the hydrate would dissolve, melt or dissociate in order to maintain equilibrium with the methane and salt concentration fields. In addition, it is possible for there to be sea floor lifting that will displace the hydrate region into a level of warmer ocean water. In either case the dissociation will occur provided the temperature of the water is larger than the equilibrium value for the concentration and will be rate-limited by thermal (in the case of melting or dissociation) or mass diffusion (in the case of dissolving).

Pressure decrease

Gas hydrates are unstable to decreases in pressure, which are possible if the sea level decreases or if there is sea bed lifting. In response the equilibrium temperature of the hydrate will decrease, causing the hydrate fraction to dissociate, therefore absorbing latent heat, and decreasing the dissolved methane concentration until a new balance is reached. At the same time there will be a flux of heat from the upper fluid that will act to dissociate the hydrate from the outside.

Concentration decrease

In the case where the dissolved methane concentration in the water decreases below its equilibrium value, possibly due to the methane source turning off, the hydrate will melt or dissolve. In most cases dissolution will occur at a rate that is dependent on mass diffusion but for very large concentration differences the rate of phase change will be dependent on the rate of heat transfer and the hydrate will essentially melt.

6

Gas hydrate dissolution and melting in porous media

6.1 Abstract

In this chapter we formulate a model that is appropriate for hydrate dissociation in a porous media without an applied fluid flow. Two simplified models were developed and solved analytically in an unbounded domain, using a similarity solution in order to determine the appropriate melting or dissolution rates in natural settings. The first model uses a pure hydrate saturation, which is an idealized setting with reference to sediments containing cold seeps. The second model relaxes this assumption and allows for arbitrary hydrate saturation and a mixed medium with constant thermal properties.

6.2 Introduction

As discussed in the previous Chapter 5, gas hydrates are contained within the ocean sediment in extremely large quantities, worldwide. Since these deposits are sensitive to thermal as well as pressure fluctuations created by global warming or some other mechanism, it is important to understand the stability of the hydrates within the sedimentary layers. In this chapter we explore a model appro-

priate for temperatures below the three-phase point, such that a gas phase cannot exist. This region of the phase diagram is known as the hydrate stability zone in which conditions are similar to the melting of a solid in contact with a binary fluid. These types of problems have been studied extensively by a number of investigators using the Stefan condition, which is essentially an interfacial jump condition for the enthalpy transport. A excellent review of these methods can be found in Davis (2001), Worster (2000) and Crank (1984). Generally in multi-component models the decomposition of the solid occurs in response to deviations in phase equilibrium, which manifests itself from changes in temperature, pressure and concentration. A familiar example is the dissolution of ice cubes in saltwater, where the temperature of the solution is allowed to drop below $0°C$. Since the salt causes the melting point to be depressed, the ice dissolves and absorbs latent heat, thus dropping the temperature. Indeed this fact is the reasoning for pouring salt onto icy roads in the winter.

With reference to gas hydrates, similar processes have been examined in regards to solidification in the sediment. Rempel & Buffett (1997) considered a two-phase (hydrate and water) system in a porous medium of constant porosity, with a cooled lower boundary and an an upper boundary with a constant dissolved methane concentration. The location of the hydrate-water interface was determined as a function of time by solving the conservation equations for thermal energy, mass, and gas concentration. Xu & Ruppel (1999) considered a similar problem, but solved the system of equations with a steady-state assumption and flux of energy, mass, and methane at the lower boundary and constant temperature, pressure, and methane concentration on the upper boundary. The important results obtained from this analysis were an estimate for the height of the hydrate stability zone and methane hydrate stability zone upper and lower boundaries.

In this Chapter we examine the melting and dissolution process of gas hydrates in homogeneous porous media, in a similar fashion to the classical methods discussed in the preceding paragraphs. The sections are broken up as follows: In

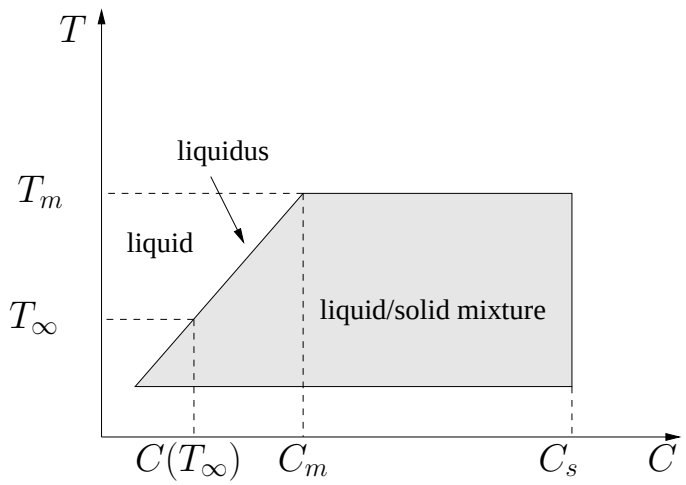

Figure 6.1: Phase diagram for a binary mixture of methane and water. The shaded area indicates a region of mixed hydrate and water and the diagonal line is the liquidus curve.

Section 3 we present the general model, in Section 4 we simplify these equations for pure hydrate saturation in one-dimension, then we relax the saturation to values less than unity in Section 5 and finally in Section 6 we conclude.

6.3 Model description

In this chapter we restrict ourselves to temperatures and concentrations that lie below the 3-phase point so that there is no gas phase. Therefore the temperature and liquid concentration in the system must be less than T_m and C_m respectively as shown in Figure 6.1. We will apply a constant temperature and concentration in the far field, which acts to destabilize the hydrate and dissolve it. This boundary condition can be imagined to be equivalent to a decrease in pressure, since the equilibrium temperature will decrease, thus setting up a similar temperature and concentration scale. One can argue that the hydrate will dissolve internally but this will act on a much faster time scale and we can just take this region at the new equilibrium state.

Here we are interested in the configuration illustrated in Figure 6.2, in

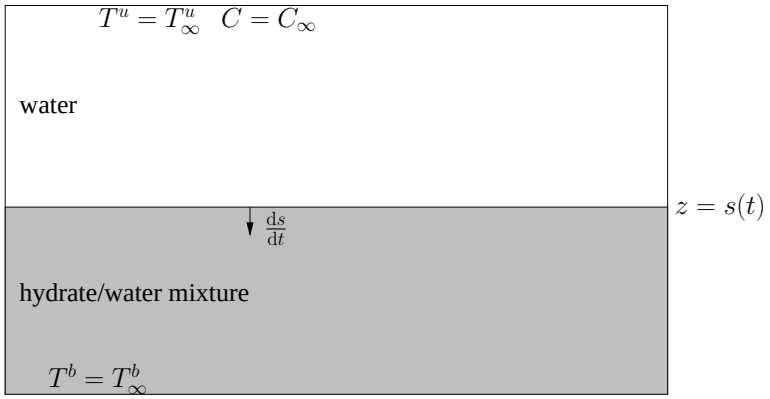

Figure 6.2: Setup for the hydrate dissolving or melting case with hydrate in the lower half plane and water in the upper. $s(t)$ is the position of the moving interface with velocity ds/dt and has an initial position of $s = 0$.

which a rigid homogeneous matrix exists in an unbounded domain. Initially the region $z \leq 0$ is filled with a gas hydrate of some spatially dependent hydrate saturation and water fills the pore space in the region $z \geq 0$. This interface, labeled $z = s(t)$, moves with time, due to deviations in phase equilibrium and therefore the velocity must scale with the magnitude of this difference (i.e. temperature and concentration).

Without the gas phase we can simplify the equations presented in Chapter 5 and we present them here for convenience.

Upper layer

Without gas or hydrate, there is no possibility of a phase change and we have the following equations in the upper layer

$$\frac{\partial q_w}{\partial z} = 0 \rightarrow q_w = q_w^s, \tag{6.1}$$

$$\frac{\partial T}{\partial t} + \xi q_w^s \frac{\partial T}{\partial z} = \alpha_u \frac{\partial^2 T}{\partial z^2}, \tag{6.2}$$

$$n\frac{\partial C_w}{\partial t} + q_w^s \frac{\partial C_w}{\partial z} = D_w \frac{\partial^2 C_w}{\partial z^2}, \tag{6.3}$$

where q_w^s is the water velocity at the interface, $z = s(t)$, and we have taken the properties to be constant,

$$\alpha_u = \frac{nK_w + (1-n)K_p}{(1-n)\rho_p C_P^s + n\rho_w C_P^w}, \qquad \xi = \frac{n\rho_w C_s^w}{(1-n)\rho_s C_P^s + n\rho_w C_P^w}, \tag{6.4}$$

where the notation has been defined in Chapter 5. We should note that a consequence of one-dimensional flow is that the temperature within the porous media is constant in space, although a function of time by mass conservation.

Lower layer

In the lower layer there is only one mobile component (i.e. water) but the hydrate, which shows up as an effective porous media, is allowed to dissolve or melt into the water. The proper equations in the case are

$$\frac{\partial q_w}{\partial z} = n\rho_h \left(1 - r\right) \frac{\partial S_h}{\partial t}, \tag{6.5}$$

$$\overline{\rho C_P}\frac{\partial T}{\partial t} + \rho_w C_P^w q_w \frac{\partial T}{\partial z} = \frac{\partial}{\partial z}\left(K\frac{\partial T}{\partial z}\right) + n\rho_h L\frac{\partial S_h}{\partial t}, \tag{6.6}$$

$$nS_w\frac{\partial C_w}{\partial t} + q_w\frac{\partial C_w}{\partial z} = \frac{\partial}{\partial z}\left(D\frac{\partial C_w}{\partial z}\right) + n(C_w - C_h)r\frac{\partial S_h}{\partial t}, \tag{6.7}$$

$$q_w = -\frac{\Pi}{\mu_w}\left(\frac{\partial P_w}{\partial z} + \rho_w g\right), \tag{6.8}$$

where $r = \rho_h/\rho_w$, and we have used the single phase flow version of Darc'y Law. These equations are much more complicated than for the upper layer, owing to the change in mixture fraction. The dissolving or melting of the hydrate acts as a heat sink and a source of dissolved methane gas. In addition we will force the reactive porous media to be in equilibrium such that the temperature and concentration are tied to the equilibrium condition,

$$T = T_m + \Gamma(C_w - C_m), \tag{6.9}$$

where Γ is the slope of the ideal liquidus line.

Interface conditions

At the interface between the two regions we have the jump conditions

$$q_w^+ = q_w^- + nS_h^- \frac{\mathrm{d}s}{\mathrm{d}t}(1-r), \tag{6.10}$$

$$n\rho_h L S_h^- \frac{\mathrm{d}s}{\mathrm{d}t} = K\frac{\partial T}{\partial z}\bigg|_- - K\frac{\partial T}{\partial z}\bigg|_+, \tag{6.11}$$

$$r\frac{\mathrm{d}s}{\mathrm{d}t}(C_w - C_h) = D_w(1-S_h^-)\frac{\partial C}{\partial z}\bigg|_- - D_w\frac{\partial C}{\partial z}\bigg|_+, \tag{6.12}$$

where the $(+)$ and $(-)$ symbols denote the upper and lower layers respectively and the interface velocity is $V_n = \mathrm{d}s/\mathrm{d}t$.

In this chapter we will consider two situations; one in which the bottom layer is completely filed with hydrate ($S_h = 1$) and the other in which we will relax this assumption.

6.4 Simple dissolution model

As noted in the introductory chapter, cold vents off Vancouver island proved to contain large concentrations of methane hydrate ($S_h \approx .79$), due to a flux of highly concentrated dissolved methane gas from below the hydrate stability zone. If the flow at this location were to suddenly turn off for whatever reason the hydrate layer may dissolve if the methane concentration of the overlying layer is less than the equilibrium value at the local ocean temperature.

In this section we will look at an idealized scenario, in which the upper and lower layers are infinitely long and the hydrate saturation is pure ($S_h = 1$) below $z < s(t)$. From the interfacial mass condition the velocity of the liquid at the interface is given as

$$q_w^s = n(1-r)\frac{\mathrm{d}s}{\mathrm{d}t}, \tag{6.13}$$

since there is no flow through the solid lower layer. From mass conservation this must also be the velocity throughout the vertical extent. Then from Darcy's equa-

tion the pressure gradient is determined from

$$\frac{\mathrm{d}P}{\mathrm{d}z} = \rho_w g - q_w^s \frac{\mu_w}{\Pi} = \rho_w g - n(1-r)\frac{\mu_w}{\Pi}\frac{\mathrm{d}s}{\mathrm{d}t}. \tag{6.14}$$

Finally we have the following governing equations

$$\frac{\partial T}{\partial t} = \alpha_b \frac{\partial^2 T}{\partial z^2}, \qquad z < s(t), \tag{6.15}$$

$$\frac{\partial T}{\partial t} + \xi q_w^s \frac{\partial T}{\partial z} = \alpha_u \frac{\partial^2 T}{\partial z^2}, \qquad z > s(t), \tag{6.16}$$

$$\frac{\partial C_w}{\partial t} + q_w^s \frac{\partial C_w}{\partial z} = D \frac{\partial^2 C_w}{\partial z^2}, \qquad z > s(t), \tag{6.17}$$

$$\frac{\partial C^s}{\partial t} + q_w^s \frac{\partial C^s}{\partial z} = D^s \frac{\partial^2 C^s}{\partial z^2}, \qquad z > s(t), \tag{6.18}$$

where we have included the salt concentration equation to be explored later the averaged thermal diffusivity ia a constant expressed as

$$\alpha_b = \frac{nK_h + (1-n)K_s}{(1-n)\rho_s C_P^s + n\rho_h C_P^h}. \tag{6.19}$$

These equations are closed provided we know the interface temperature, concentration and position. In general this requires three equations, which are satisfied by the following jump conditions

$$K\frac{\partial T}{\partial z}\bigg|_b - K\frac{\partial T}{\partial z}\bigg|_u = n\rho_h L\frac{\mathrm{d}s}{\mathrm{d}t}, \tag{6.20}$$

$$D_w\frac{\partial C}{\partial z}\bigg|_u = r\frac{\mathrm{d}s}{\mathrm{d}t}(C_H - C_I), \tag{6.21}$$

$$D^s\frac{\partial C^s}{\partial z}\bigg|_u = -r\frac{\mathrm{d}s}{\mathrm{d}t}C_I^s, \tag{6.22}$$

$$T_I = T_m + \Gamma(C_I - C_m), \quad \Gamma = \frac{\Delta T}{\Delta C} = \frac{T_\infty^u - T_\infty^b}{C(T_\infty^u) - C(T_\infty^b)}, \tag{6.23}$$

where u and b denote the upper and lower layer respectively, $T_I = T(s,t)$ the interface temperature and $C_I = C_w(s,t)$ the interface methane concentration and $C_I^s = C^s(s,t)$ is the interface salt concentration.

6.4.1 Solution

We seek a similarity solution to the governing equations with variable $\eta = z/2\sqrt{Dt}$ and interface position $s = 2\lambda\sqrt{Dt}$. Here λ is an eigenvalue to be determined as part of the solution and we have taken the interface position to scales with the rate of methane diffusion. For this solution to exist we consider the boundary and initial conditions:

$$T^b(-\infty, t) = T^b(z, 0) = T^b_\infty, \quad T^u(\infty, t) = T^u(z, 0) = T^u_\infty, \tag{6.24}$$

$$C_w(\infty, t) = C_w(z, 0) = C_\infty, \quad C^s(\infty, t) = C^s(z, 0) = C^s_\infty. \tag{6.25}$$

Using the non-dimensional scales $C_w = \mathscr{C}\Delta C + C_\infty$ and $T = \theta\Delta T + T^u_\infty$ we have the following set of ODE's

$$\theta^b_{\eta\eta} + 2\eta\theta^b_\eta L^b_e = 0 \quad \eta < \lambda, \tag{6.26}$$

$$\theta^u_{\eta\eta} + 2\theta^u_\eta L^u_e(\eta - \xi\gamma\lambda) = 0 \quad \eta > \lambda, \tag{6.27}$$

$$\mathscr{C}_{\eta\eta} + 2\mathscr{C}_\eta(\eta - \gamma\lambda) = 0 \quad \eta > \lambda, \tag{6.28}$$

$$\mathscr{C}^s_{\eta\eta} + 2\mathscr{C}^s_\eta(\eta - \gamma\lambda) = 0 \quad \eta > \lambda, \tag{6.29}$$

where $\gamma = n(1 - r)$, $L^b_e = D/\alpha_b$ ($L^u_e = D/\alpha_u$) is the Lewis number and we have assumed that the diffusivity of methane gas and salt are equal. The interface conditions are

$$\theta^b_\eta - \sigma\theta^u_\eta = 2StLe^b\lambda, \quad \eta = \lambda, \tag{6.30}$$

$$\mathscr{C}_\eta = 2r(\mathscr{C}_h - \mathscr{C}_I)\lambda, \quad \eta = \lambda, \tag{6.31}$$

$$\mathscr{C}^s_\eta = -2r\left(\mathscr{C}^s_I + \frac{C_\infty}{\Delta C}\right)\lambda, \quad \eta = \lambda, \tag{6.32}$$

$$\theta_I = \mathscr{C}_I - 1 + \mathscr{C}_\infty, \quad \eta = \lambda, \tag{6.33}$$

where $\sigma = K^u/K^b$, $St = nL\rho_h/\Delta T(\rho C_P)^b$, is the Stefan number, $\mathscr{C}_\infty = (C_\infty - C(T^b_\infty))/\Delta C$ and $\mathscr{C}_h = (C_H - C_\infty)/\Delta C$. We have the following boundary conditions:

$$\theta^b(-\infty) = -1, \quad \theta^b(\lambda) = \theta^u(\lambda) = \theta_I, \quad \theta^u(\infty) = 0, \tag{6.34}$$

$$\mathscr{C}(\infty) = 0, \quad \mathscr{C}(\lambda) = \mathscr{C}_I, \quad \mathscr{C}^s(\infty) = \mathscr{C}^s_\infty, \quad \mathscr{C}^s(\lambda) = \mathscr{C}^s_I. \tag{6.35}$$

Integrating equations (6.26)–(6.28), applying the boundary conditions and the definition of the error function (erf) we have

$$\frac{\theta^b + 1}{\theta_I + 1} = \frac{\operatorname{erfc}(-\eta\sqrt{Le^h})}{\operatorname{erfc}(-\lambda\sqrt{Le^h})}, \quad \eta < \lambda, \tag{6.36}$$

$$\frac{\theta^u}{\theta_I} = \frac{\operatorname{erfc}\left(\sqrt{Le^\ell}(\eta - \xi\gamma\lambda)\right)}{\operatorname{erfc}\left(\sqrt{Le^\ell}(\lambda - \xi\gamma\lambda)\right)}, \quad \eta > \lambda, \tag{6.37}$$

$$\frac{\mathscr{C}}{\mathscr{C}_I} = \frac{\operatorname{erfc}(\eta - \gamma\lambda)}{\operatorname{erfc}(\lambda - \gamma\lambda)} \quad \eta > \lambda, \tag{6.38}$$

$$\frac{\mathscr{C}^s - \mathscr{C}^s_\infty}{\mathscr{C}^s_I - \mathscr{C}^s_\infty} = \frac{\operatorname{erfc}(\eta - \gamma\lambda)}{\operatorname{erfc}(\lambda - \gamma\lambda)}, \quad \eta > \lambda. \tag{6.39}$$

Then from the interface flux conditions we can express the interface temperatures and concentration as

$$\theta_I = \frac{F(-\lambda\sqrt{Le^h})St\sqrt{Le^h} - 1}{1 + \sigma\frac{\sqrt{Le^\ell}}{\sqrt{Le^h}}\frac{F(-\lambda\sqrt{Le^h})}{F\left(\sqrt{Le^\ell}(\lambda - \xi\gamma\lambda)\right)}}, \tag{6.40}$$

$$\mathscr{C}_I = \frac{2r\mathscr{C}_h F(\lambda - \gamma\lambda)}{2rF(\lambda - \gamma\lambda) - 1}, \tag{6.41}$$

$$\frac{\mathscr{C}^s_I}{\mathscr{C}^s_\infty} = \frac{1 + 2rF(\lambda - \gamma\lambda)\mathscr{B}}{1 - 2rF(\lambda - \gamma\lambda)}, \tag{6.42}$$

where $F(\nu) = \sqrt{\pi}\,\lambda\operatorname{erfc}(\nu)\exp(\nu^2)/2$ and $\mathscr{B} = C_\infty/(C^s_\infty - C_\infty)$. The eigenvalue λ may be determined by combining the above expressions with the equilibrium condition

$$\frac{F(-\lambda\sqrt{Le^h})St\sqrt{Le^h}\lambda - 1}{1 + \sigma\frac{\sqrt{Le^\ell}}{\sqrt{Le^h}}\frac{F(-\lambda\sqrt{Le^h})}{F\left(\sqrt{Le^\ell}(\lambda - \xi\gamma\lambda)\right)}} = \frac{2nr\lambda\mathscr{C}_h F(\lambda - \gamma\lambda)}{-1 + 2nr\lambda F(\lambda - \gamma\lambda)} - 1 + \mathscr{C}_\infty. \tag{6.43}$$

We can further simplify this expression, since the hydrate and water densities are approximately equal (i.e. $\gamma \gg 1$). Furthermore the diffusivity of heat is

approximately 2 orders of magnitude larger than that of mass and we can make a small Lewis number limit ($Le^u, Le^b \ll 1$).

$$\frac{\frac{\sqrt{\pi}}{2} St\sqrt{Le^h}\lambda - 1}{1 + \sigma\frac{\sqrt{Le^\ell}}{\sqrt{Le^h}}} = \frac{2n\lambda\mathscr{C}_h F(\lambda)}{-1 + 2n\lambda F(\lambda)} - 1 + \mathscr{C}_\infty. \tag{6.44}$$

This is an eigenvalue equation for the eigenvalue λ and is represented as a function of S_t, $\mathscr{C}_h$ and $\mathscr{C}_\infty$.

We solved equation (6.44) numerically and plotted the solution as a function of the three parameters $\mathscr{C}_\infty, \mathscr{C}_h$ and St in Figure 6.3. $\mathscr{C}_h$ is the ratio of the typical difference in gas concentration between the hydrate and liquid to the scale of concentration variations in the liquid. Since mass diffusion is our slowest scale, this is the governing parameter in the system rather than the Stefan number, St, as seen in Figure 6.3. In our case $C_h \gg C_\infty$, so this parameter is controlled by ΔC, which by equilibrium is equivalent to the temperature difference ΔT. Thus as the far field temperature is increased, $\mathscr{C}_h$ is decreased and the melting rate is subsequently increased as we expect. In addition the parameter $\mathscr{C}_\infty$ has an important effect on the dissolution rate because it controls the far field gas concentration. As C_∞ is decreased, mass diffuses away from the boundary, causing the liquidus temperature to decrease. This has the effect of dissolving the hydrate and therefore as $\mathscr{C}_\infty$ is decreased further the dissolving rate of hydrate increases in tandem.

In the previous analysis we have ignored the effect of salinity on the system, which will alter the equilibrium condition at the boundary. This assumption is valid provided the salt concentration is approximately uniform. We expect this to occur if the dissolution process is slow, since the salinity field will be able to diffuse at a faster rate than the moving boundary. Therefore, in the limit $\lambda \sim 0$ equation (6.42) is approximately

$$\frac{\mathscr{C}_I^s}{\mathscr{C}_\infty^s} = 1 + \frac{2F(\lambda)}{1 - 2F(\lambda}(1 - \mathscr{B}) \approx 1 + \sqrt{\pi}\lambda(1 - \mathscr{B}) \approx 1, \tag{6.45}$$

and the interfacial salt concentration is approximately equal to the far field condition.

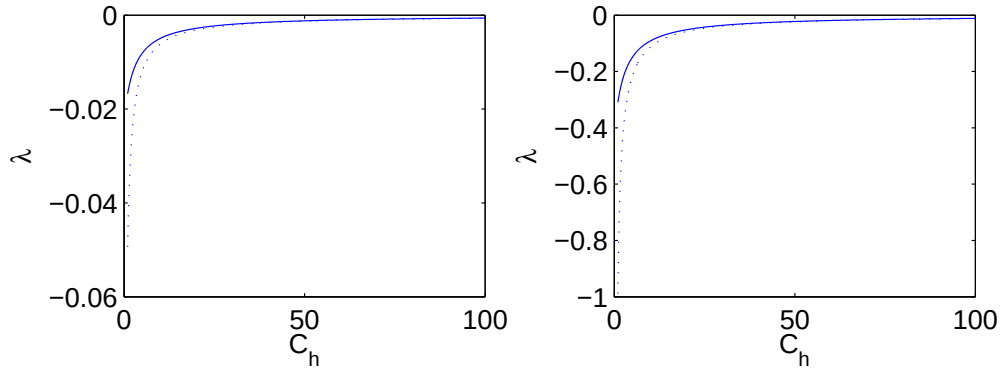

Figure 6.3: Eigenvalue λ as a function of $\mathscr{C}_h$ from the solution to equation (6.44) for $St = 10$ (dotted line) and 100 (solid line) and $\mathscr{C}_\infty = .5$ (left) and $-.5$ (right). Here $Le^h = .004$, $Le^\ell = .0063$ and $n = .5$.

6.5 Simple mushy layer model

As we can see from Table 5.1 in Chapter 5 the thermal conductivities of the hydrate and liquid are very similar as well as their densities therefore we will take $K_h = K_\ell$ and $\rho_h = \rho_\ell$ (thus $r = 1$). In this case there is no fluid velocity and the governing equations become

$$\frac{\partial T}{\partial t} = \frac{K}{(\rho C_P)^b}\frac{\partial^2 T}{\partial z^2} + \frac{n\rho_h L}{(\rho C_P)^b}\frac{\partial \phi}{\partial t}, \quad z < s(t), \tag{6.46}$$

$$\frac{\partial C}{\partial t} = \frac{\partial}{\partial z}\left(D\frac{\partial C}{\partial z}\right), \quad z < s(t), \tag{6.47}$$

$$\frac{\partial T}{\partial t} = \alpha_w \frac{\partial^2 T}{\partial z^2}, \quad z > s(t), \tag{6.48}$$

$$\frac{\partial C_\ell}{\partial t} = D_w \frac{\partial^2 C_\ell}{\partial z^2}, \quad z > s(t), \tag{6.49}$$

$$T = T_m + \Gamma(C_w - C_m), \tag{6.50}$$

with the following interfacial conditions

$$q_w^+ = q_w^-, \tag{6.51}$$

$$n\rho_h L S_h^- \frac{\mathrm{d}s}{\mathrm{d}t} = K\frac{\partial T}{\partial z}\bigg|_- - K\frac{\partial T}{\partial z}\bigg|_+, \tag{6.52}$$

$$\frac{\mathrm{d}s}{\mathrm{d}t}(C_w - C_h) = D_w(1 - S_h^-)\frac{\partial C}{\partial z}\bigg|_- - D_w\frac{\partial C}{\partial z}\bigg|_+. \tag{6.53}$$

Since the Lewis number is small for this system, as discussed previously, we will examine the solutions for a small Lewis number $L_e \ll 1$. This implies that we can ignore mass diffusion in comparison to thermal diffusion to leading order, which is commonly done in connection to solidification (Rempel & Buffett 1997 and Worster 2000). As a consequence of this assumption we have $S_h = 0$ at the interface and the conditions here reduce to

$$S_h = 0, \quad [T_z] = 0. \tag{6.54}$$

Furthermore, equation (6.47) requires the total concentration $C = \bar{C}(z)$ to be constant in time with some initial hydrate distribution. Solving this equation for S_h, differentiating with respect to time and combining with internal equilibrium we obtain the following expression

$$S_h = \frac{\bar{C}(x)/n - C_w}{C_h - C_w}, \tag{6.55}$$

$$\frac{\partial S_h}{\partial t} = \frac{\partial T}{\partial t}\frac{\Gamma^{-1}}{(C_h - C_w)^2}\left(\frac{\bar{C}}{n} - C_h\right), \tag{6.56}$$

which expresses the change in hydrate saturation in terms of temperature. Therefore if the temperature of the bottom layer increases the hydrate will dissolve in order to increase the methane concentration in the water to its new equilibrium value.

We can combine equations (6.46) and (6.56) to obtain a modified version of the heat equations as

$$\frac{\partial T}{\partial t}\left[1 - \frac{n\rho_h L}{(\rho C_P)^b \Gamma C_h n}\frac{\bar{C}/C_h - n}{(1 - C_w(T)/C_h)^2}\right] = \frac{K}{(\rho C_P)^b}\frac{\partial^2 T}{\partial z^2} = \Omega\frac{\partial T}{\partial t}, \tag{6.57}$$

which is nonlinear due to the hydrate fraction dependence of the specific heat, ρC_P, and the temperature dependence of the internal dissolved hydrate concentration, C_w.

6.5.1 Solution

The modified form of the temperature equation (6.57) for the reactive porous media is difficult to solve in closed form but we can make some appropriate simplifications for our system. For methane hydrate there is a relatively high gas concentration so $C_h \gg C_w$ and we can neglect the term C_w/C_h in this equation. In addition we will assume that the total concentration of gas is constant in space ($\bar{C} = C_0$) and that the average specific heat is constant. Therefore,

$$\Omega = 1 + \frac{St}{\mathscr{C}_h}\left(1 - \frac{\beta}{\mathscr{C}_h}\right), \tag{6.58}$$

where $\beta = C_0/2n\Delta C$ and we note the fact that $C_0 = S_h n C_h + n(1 - S_h)C_w$. Now we have the simplified set of equations

$$\frac{\partial T}{\partial t} = \hat{\alpha}\frac{\partial^2 T}{\partial z^2}, \quad z < s(t), \tag{6.59}$$

$$\frac{\partial T}{\partial t} = \alpha_u \frac{\partial^2 T}{\partial z^2}, \quad z > s(t), \tag{6.60}$$

$$C_\ell = C_\infty, \quad z > s(t), \tag{6.61}$$

$$T_I = T_m + \Gamma(C_\infty - C_m), \quad z = s(t), \tag{6.62}$$

$$\left.\frac{\partial T}{\partial z}\right|_u = \left.\frac{\partial T}{\partial z}\right|_b, \quad z = s(t), \tag{6.63}$$

where the concentration in the upper layer is equal to its initial condition and the equation in the bottom layer has a modified term for the thermal diffusivity $\hat{\alpha} = \alpha_b/\Omega$. We solve the above equation, using a similarity variable defined as $\eta = z/2\sqrt{\alpha_u t}$ and interface speed $s = 2\lambda^m\sqrt{\alpha_u t}$ with the same non-dimensionalization of the temperature and concentration of the previous section.

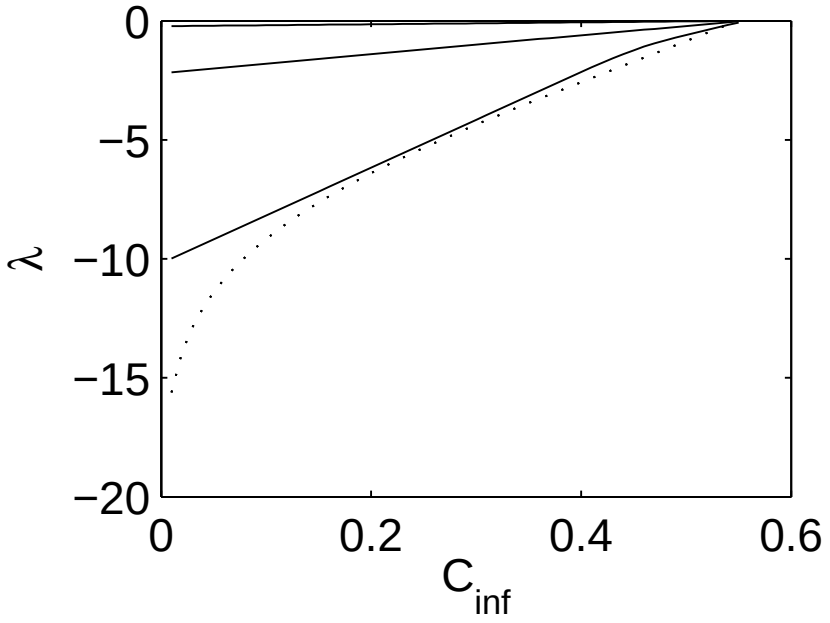

Figure 6.4: Eigenvalue λ (solid line) and $\lambda^m\sqrt{\alpha_u/D}$ (dotted line) as a function of $\mathscr{C}_\infty$ from the solution to equation (6.67) and (6.44) for $St = 2, 10, 100$. Here $\alpha_u/\alpha_b = .62$, $\mathscr{C}_H = 100$ and $n = .5$.

$$\frac{\theta^b + 1}{\theta_I + 1} = \frac{\operatorname{erfc}(-\eta\sqrt{\omega})}{\operatorname{erfc}(-\lambda^m\sqrt{\omega})} \quad \eta < \lambda^m, \tag{6.64}$$

$$\frac{\theta^u}{\theta_I} = \frac{\operatorname{erfc}(\eta)}{\operatorname{erfc}(\lambda^m)} \quad \eta > \lambda^m. \tag{6.65}$$

$$\tag{6.66}$$

Here $\omega = \alpha_\ell/\hat{\alpha} = \alpha_\ell\Omega/\alpha_H$ and $\theta_I = \mathscr{C}_\infty - 1$. From the continuity of heat flux condition at the interface, the eigenvalue equation is

$$\frac{1 - \mathscr{C}_\infty}{F(\lambda^m)} = \frac{\sqrt{\omega}\,\mathscr{C}_\infty}{F(-\lambda^m\sqrt{\omega})}, \quad \eta = \lambda^m. \tag{6.67}$$

The formulations for the two methods presented in this chapter are inherently different because we have relaxed the pure hydrate saturation assumption

in the last case. The assumptions however, going into these two methods are essentially the same (i.e. $Le \ll 1$ and $\gamma \ll 1$) and it is interesting to compare the two methods. We have plotted the solutions to the two methods in Figure 6.4, corresponding to equations (6.44) and (6.67) as a function of the parameter $\mathscr{C}_\infty$. As we expect the two solutions show that the decomposition rate is larger when the concentration at infinity is less than the equilibrium value and as the temperature difference in the system increases. Clearly the mushy layer model yields larger eigenvalues λ, since the hydrate saturation is less than unity and the decomposition rate scales with the thermal diffusion rather than mass diffusion.

It is interesting to note from this figure that for large values of $\mathscr{C}_\infty$ the hydrate is dissolving because the eigenvalue scales with mass diffusion (indicated by a $\lambda = O(1)$). On the other hand when the temperature or concentration scale is relatively large λ increases and the appropriate scale for the advancing front is with thermal diffusion (i.e. the hydrate is melting).

Relationship to *in situ* deposits

Gas hydrates initially form in the ocean because there is a source of methane and the temperature, pressure and concentration conditions are optimal for growth. If the source is ever turned off or the surrounding water temperature increases the hydrate will dissolve or melt until the appropriate equilibrium conditions are met. This result may not be all that important with respect to global warming because the methane is in aqueous form and the time scale for the ocean to turn over is very large. This model gives us a physical understanding of the dissolution mechanism and an idea of the dissolution rates. For example, with a value of λ in the range .01-10 the interface may have displaced a distance of a few meters, depending on the temperature and concentration conditions.

6.6 Conclusion

In this chapter we investigated the dissolution and melting of gas hydrates in response to deviations in phase equilibrium in the case that temperature is below the three phase point. Two simplified models were developed and solved analytically to determine the velocity of the interface as a function of the temperature and concentration difference in the system. In the first model, we assumed a pure hydrate lower layer, which is a simplified analogue to sedimentary regions with cold vents. In this case we found that the hydrate dissolves if the temperature is increased above its equilibrium value at the local methane concentration and if the far field concentration is dropped below the equilibrium value at the far field temperature. In the second model we relaxed the pure hydrate assumption and formulated the problem with an arbitrary hydrate saturation in the lower layer. Since the Lewis numbers are small for natural systems we neglected mass diffusion and obtained a modified heat equation with an effective diffusivity that decrease with phase change via latent heat release. The interface velocity in this case was shown to depend on the same environmental conditions such as temperature and concentration but were faster, owing to the internal dissolution.

7

Gas hydrate dissociation in porous media

7.1 Abstract

The dissociation of gas hydrates in the ocean sediment by warming ocean water temperatures may contribute to global warming by the release of stored methane into the atmosphere. Gas hydrates are a solid compound composed of water and gas that will decompose by the transfer of thermal energy supplied by the environment. Since naturally occurring deposits exist in conjunction with the sedimentary layer that make up the sea-floor, the dissociation process will generate a two-phase flow that will be transported through the sediment and into the ocean water column. We develop a mathematical model based on a set of conservation laws for temperature, mass and momentum that are then solved numerically and also analytically for some reduced cases. We compare solutions for gas flow rate, gas saturation profiles as well as the evolution of the upper and lower gas flow rates and moving boundary velocity as a function of the degree of thermal forcing and sediment properties. Finally we discuss possible gas fluxes into the ocean, which may have practical applications to *in situ* deposits.

7.2 Introduction

Gas hydrates are crystalline ice-like compounds made up of water molecule cages held together by hydrogen bonding. A guest gas contained within the center cavity stabilizes the structure under low temperatures and high pressures. They can be found below the seafloor attached to the sediment that makes up the continental margins or bound to the subsurface of the permafrost regions. Generally the geographical locations of *in situ* deposits are constrained by the source of methane, which may form by bacterial methanogenesis of buried organic matter. The formation mechanism can be described by Rempel & Buffett (1997) by the extraction of dissolved gas at a hydrate boundary in order to maintain thermodynamic and compositional equilibrium. There are offshore regions such as Vancouver island, where cold vents seep high concentrations of methane through the sediment. As a result large concentrations of methane hydrate are found near the seafloor and may span horizontal distances reaching in the range of kilometers. At the Vancouver island site, sediment core samples taken by Lu *et al.* (2005) and Riedel *et al.* (2006) were between 2-8 meters below the seafloor. This sediment consisted of finely laminated glaciomarine clays and silts with massive hydrates containing saturations up to $S_h = .78$. In some cases this level of saturation spanned several meters but ultimately decreased rapidly with depth.

It is widely believed that large quantities of methane gas are trapped within oceanic sediments and could potentially surpass known fossil fuel reserves to make them the largest hydrocarbon sources on earth (Buffett, 2000). Since hydrates will decompose in response to an increase in water temperature above the three-phase point, there is concern over the fate of these methane deposits, since methane is a strong greenhouse gas, as a result of continued global warming (Kvenvolden, 1993; MacDonald, 1990). In addition there has been global interest in the recovery of these hydrocarbons as a potentially new energy source using various extraction schemes such as depressurization or hot water injection. It is

for these reasons that we are interested in the dissociation rates and gas fluxes through the sediment in response to an increase in boundary temperatures.

Previous mathematical models have centered around one-dimensional Stefan type melting problems attributed to Stefan (1891) and discussed extensively in Crank (1984). In these types of models the transport of thermal energy to the solid-liquid phase boundary causes decomposition and subsequent movement of this interface at a non-linear rate. Naturally the change in density between the two phases induces fluid motion by mass conservation, which in the case of a porous medium can be described by Darcy's law. Using this basic mechanism Selim & Sloan (1989) considered a simple analytic model for the rate of dissociation in a semi-infinite plane in response to an increase in upper boundary temperature. They ignored the motion of the water and the effect of fluid saturation on the relative permeability and determined gas release rates as a function of boundary temperature. Tsypkin (2001) considered a multiphase flow and looked at the stratum and interface temperatures as a function of permeability in response to different upper boundary pressures in a depressurizing well. He linearized the governing porous medium equations and solved for the temperature, pressure and water saturation by a similarity solution. The main results were that under certain conditions, mainly a large drop in stratum pressure or increase in permeability, the dissociation can lead to the formation of ice, creating a boundary for gas extraction. Most recently Ahmadi et al. (2004) obtained a numerical solution for the rate of gas production from dissociating hydrates in a depressurized well. They solved the thermal energy and pressure equation coupled to the Clausius–Clapeyron equation and Stefan condition at the moving interface. These equations were solved on both sides of the interface without consideration of a water phase, using an explicit finite difference method. The position of the moving interface was obtained from the Stefan condition, using a low-order numerical scheme.

Experimentally, gas hydrate dissociation schemes have been performed in the laboratory under high pressures in which the hydrates were formed from

dissolved methane gas rather than from fine snow (Stern et al., 2003). Kamath & Holder (1987) performed experiments with a mixture of propane and methane hydrates by circulating relatively warm water above the upper surface. They assumed a nucleate boiling phenomenon for the heat transfer using Rohsenhow's correlation to obtain estimates for the rate of gas release that they attempted to fit with experimental data. Yousif et al. (1990) used a depressurization scheme at isothermal conditions and tracked the position of the moving boundary and gas volume exiting the porous medium. They compared there results with an analytical solution based on Darcy's law with a formulation in terms of pressure with a negligible change in gas saturation.

All of these studies have ignored the inherent non-linearity in a multiphase porous media flow as a result of the coupling between the two immiscible fluids. As a result the models developed in these studies will have significant inaccuracies unless the properties of the system fall within a narrow parameter space. In this Chapter we model the problem by employing a set of one-dimensional conservation laws that describe the transport of thermal energy, mass and momentum through a homogeneous porous media, including the effect of strong non-linearities due to the saturation-dependent capillary pressure and permeability functions. The non-linear coupled partial differential equations are solved numerically and also exactly for some reduced cases to determine the gas flux out of the sediment as a function of thermal forcing and sediment properties. In order to understand the most basic mechanism in hydrate dissociation we will take the hydrate saturation to be very large, such that there cannot be any internal phase changes often encountered with mushy layers (Worster, 2000). This idealized model is appropriate in sediments with cold seeps, where the hydrate concentration are extremely high.

In section 7.3 we develop the appropriate model for the dissociation problem and in section 7.4 we non-dimensionalize these equations and describe the appropriate scaling. In section 7.5 we present solutions to some reduced models. In section 7.6 we show some result from the numerical solution and compare them

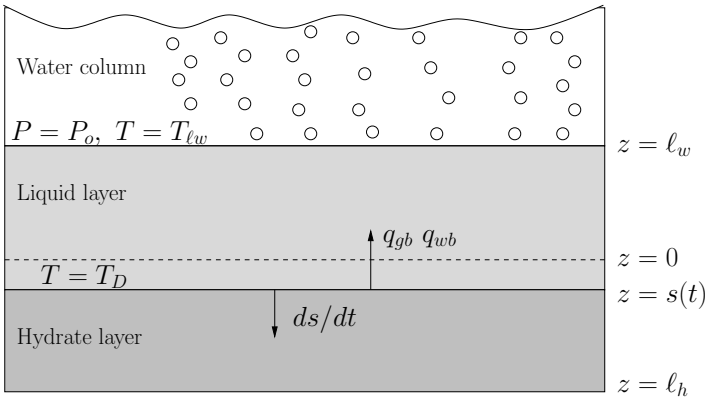

Figure 7.1: Diagram showing a porous medium of finite size, containing a hydrate layer (initial thickness ℓ_h) below $z = s(t)$ and a liquid layer (initial thickness ℓ_w) above $z = s(t)$. The dissociation front moves downwards with velocity $V = \mathrm{d}s/\mathrm{d}t$ and the hydrate is replaced with water and gas with boundary velocities q_{wb} and q_{gb} for the water and gas respectively. The gas is transported through the sediment and finally enters the water column, where the gas rises as bubbles.

against the reduced models. Finally in section 7.7 we conclude.

7.3 Model Formulation

In this analysis we focus only on the sediment, which we consider to be a homogeneous, rigid matrix as shown in Figure 8.1. The sediment is separated into two regions: a hydrate layer below the solid-fluid phase boundary $z = s(t)$ and a liquid layer above $z = s(t)$. We are interested in modeling the dissociation and flux rate of gas through the sediment in response to a sudden application of a constant temperature boundary condition at $z = \ell_w$. The application of this thermal field will destabilize the crystalline solid, which will release water and gas that will be transported as a two-phase flow. Since hydrate dissociation requires the fluid adjacent to the three-phase boundary (hydrate-water-gas) to be warmer than the dissociation temperature and the rate will depend on the degree of this difference, the flow field is intimately coupled to the rate of thermal energy transport.

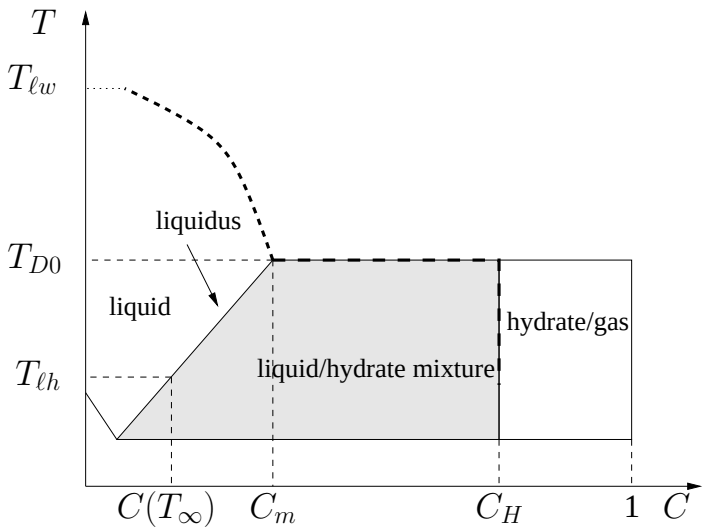

Figure 7.2: Typical phase diagram for a binary mixture of methane gas and water in which gas hydrates (solid ice-like structure) form. The thick dashed line represents the path for the problem presented in this Chapter.

Since we are dealing with a binary system, we are naturally concerned with the phase diagram. Our path corresponds to the thick dashed line in Figure 7.2, where the conditions in the hydrate never enter the mixed phase region because we assume pure hydrate saturation. Generally, one would need to consider the transport of species such as dissolved methane and salt but we make a small Lewis number assumption. Therefore the the salt concentration is zero and dissolved methane concentration is constant ($C = C(T_{D0})$) at the interface.

In the sections that follow we will develop the model corresponding to the three parts of the problem: thermal energy transport, two-phase flow in a porous medium and moving boundary problem.

7.3.1 Thermal Energy Transport

A constant temperature is applied at the upper boundary, $z = \ell_w$, which will diffuse downwards, towards the hydrate layer. Once the temperature adjacent to the hydrate-fluid boundary is larger than the dissociation temperature there will

be a flux of gas and water through the porous media from the decomposing hydrate surface. The presence of the gas in the sediment will change the average thermal properties of the system and a positive flux of mass can transport cool fluid away from the phase boundary, thus reducing the dissociation rate. The transport of thermal energy in this way can be described by the following advection-diffusion equations

$$C_e \frac{\partial T_w}{\partial t} + V_e \frac{\partial T_w}{\partial z} = \frac{\partial}{\partial z}\left(K_e \frac{\partial T_w}{\partial z} \right), \quad s(t) < z < \ell_w, \tag{7.1}$$

$$\frac{\partial T_h}{\partial t} = \alpha_{he} \frac{\partial^2 T_h}{\partial z^2}, \quad \ell_h < z < s(t), \tag{7.2}$$

where T_w is the temperature in the upper layer, T_h is the temperature in the lower layer and we assume that there is no flow of water in the hydrate bearing region. The variables C_e, V_e, K_e and α_{he} are defined in terms of fluid and sediment properties as

$$C_e = nS_w\rho_w C_w + nS_g\rho_g C_g + (1-n)\rho_s C_s, \tag{7.3}$$

$$V_e = nS_w\rho_w C_w V_w + nS_g\rho_g C_g V_g, \tag{7.4}$$

$$K_e = nS_w K_w + nS_g K_g + (1-n)K_s, \tag{7.5}$$

$$\alpha_{he} = \frac{nS_h K_h + nS_w K_w + (1-n)K_s}{nS_h\rho_h C_h + nS_w\rho_w C_w + (1-n)\rho_s C_s} = \frac{K_h}{C_h} \tag{7.6}$$

where n is the porosity, C is the specific heat, ρ is the density, K is the thermal conductivity, V is the velocity, S is the saturation and the subscripts w, h, g and s correspond to water, hydrate, gas and solid matrix respectively. In this Chapter we will set $S_h = 1$, corresponding to a hydrate saturated pore space, which is the maximum amount of gas storage possible.

In addition we apply the following boundary and initial conditions

$$T_w(0, z_w) = T_{w0}, \qquad T_w(t, \ell_w) = T_{\ell w}, \tag{7.7}$$

$$T_h(0, z_h) = T_{D0}, \qquad T_h(t, -\ell_h) = T_{D0}, \tag{7.8}$$

where T_{D0} is the initial dissociation temperature and the initial temperature in the liquid layer has some vertical profile that will be taken in this Chapter to be either T_{D0} or $T_{\ell w}$.

7.3.2 Two–phase flow in a porous medium

Once the hydrate decomposes, there will be a flux of both water and gas out of the interface that will move up or down depending on the properties of the system. The gas will then migrate through the sediment as a multiphase flow until it reaches the upper boundary and exits the sediment. These types of flows have commonly been studied in hydrology and petroleum engineering using multiphase flow extensions to the well-known single-phase porous medium equations (Bear, 1991; Aziz & Settari, 1979; Peaceman, 1977). The equations for mass and momentum conservation are

$$\frac{\partial\, nS_w\rho_w}{\partial t} + \frac{\partial q_w\rho_w}{\partial z} = 0, \tag{7.9}$$

$$\frac{\partial\, nS_g\rho_g}{\partial t} + \frac{\partial q_q\rho_g}{\partial z} = 0, \tag{7.10}$$

$$q_w = nS_wV_w = -\frac{\kappa_w}{\mu_w}\left(\frac{\partial P_w}{\partial z} + \rho_w g\right), \tag{7.11}$$

$$q_g = nS_gV_g = -\frac{\kappa_g}{\mu_g}\left(\frac{\partial P_g}{\partial z} + \rho_g g\right), \tag{7.12}$$

where n is the porosity, $\kappa_w(S_w)$ and $\kappa_g(S_w)$ are the water and gas permeability's and μ is the viscosity. By definition the water saturation is the ratio of water volume to volume of void space so naturally the following condition holds $S_w + S_g = 1$. In addition we can relate the difference in phase pressure to the capillary pressure $P_c(S_w) = P_g - P_w$, which depends on the surface tension in the sediment.

The permeability and capillary pressure relationships are in general non-linear functions of water saturation that are determined experimentally. Here we use the model attributed to Genuchten (1996) expressed as

$$\kappa_w = K\, k_{rw}, \quad k_{rw} = S_e^{1/2}\left(1 - \left(1 - S_e^{1/m}\right)^m\right)^2, \tag{7.13}$$

$$\kappa_g = Kk_{rg}, \quad k_{rg} = (1 - S_e)^{1/2}\left(1 - S_e^{1/m}\right)^{2m}, \tag{7.14}$$

$$P_c = \frac{\rho_w g}{\alpha} f_c, \quad f_c = \left(S_e^{-1/m} - 1\right)^{1-m}, \tag{7.15}$$

where K is the absolute permeability used for a single phase flow, $S_e = (S_w -$

$S_{wo})/(1 - S_{wo})$ is the equivalent saturation, scaled by the zero water phase flow saturation S_{wo}, and the coefficients m and α are determined experimentally for the different combinations of the two fluids and sediment properties. Finally, the gas density can be determined from the ideal gas law

$$\rho_g = \frac{P_g}{RT}, \tag{7.16}$$

where R is the gas constant and we assume the water density to be constant.

Pressure and saturation equation

Combining equations (7.9)-(7.12) to eliminate the time derivative of saturation, assuming that the density of water is constant and that the density of gas is a function of pressure only, which is valid for small temperature changes, we get

$$n(1 - S_w)\frac{\partial \rho_g}{\partial P_g}\frac{\partial P_g}{\partial t} = \rho_g \frac{\partial}{\partial z}\left[\frac{K_W}{\mu_w}\left(\frac{\partial P_g}{\partial z} - \frac{\partial P_c}{\partial z} + \rho_w g\right)\right] + \frac{\partial}{\partial z}\left[\frac{\rho_g K_g}{\mu_g}\left(\frac{\partial P_g}{\partial z} + \rho_g g\right)\right], \tag{7.17}$$

which is known as the pressure equation (Bear, 1991; Aziz & Settari, 1979). Similarly equations (7.9)-(7.12) can be combined to eliminate pressure in favor of the water saturation to obtain

$$n\frac{\partial S_w}{\partial t} + \frac{\partial q_w}{\partial z} = 0, \tag{7.18}$$

$$q_w = \frac{M_w}{M_w + M_g}\left[q_t + M_g\frac{\partial P_c}{\partial z} + M_g \rho_w g\left(\frac{\rho_g}{\rho_w} - 1\right)\right]. \tag{7.19}$$

Here $M_w = K/\mu_w$ is the water mobility, $M_g = K/\mu_g$ is the mobility for the gas phase and $q_t = q_w + q_g$ is the total flow rate.

In the special case that the gas density is constant, which will only be true to leading order when ℓ_w and the fluid velocity are small, the pressure equation (7.17) takes on the much simpler form

$$\frac{\partial q_t}{\partial z_w} = 0, \tag{7.20}$$

in which case the total flow rate is constant in space.

Upper Boundary Condition

At the upper boundary, where the gas discharges into the ocean water column, the conditions on saturation, flow rate and pressure are unknown and must be determined as part of the solution. For large reservoirs the flow of fluid leaving the sediment will be quickly dissipated and we can assume that a boundary layer exists such that outside this region the velocity is zero and the pressure is equal to the hydrostatic pressure P_o. Since a multiphase flow will still exist outside the porous medium, we can assume that the form of equations (7.9)-(7.12) still applies and write the Darcy's law-assuming that the thickness of the boundary layer is very small, following Wu et al. (1996) as

$$q_w = q_{wu} = -\frac{Kk_{rw}}{\mu_w}\left(-\chi(P_w - P_o) + \rho_w g\right), \tag{7.21}$$

$$q_g = q_{gu} = -\frac{Kk_{rg}}{\mu_g}\left(-\chi(P_g - P_o) + \rho_g g\right), \tag{7.22}$$

where $\chi = 1/\Delta z$, is some arbitrarily large number and P_o is the pressure just outside the porous medium. This formulation essentially is the simplest approach without solving the outer problem.

7.3.3 Moving Boundary Problem

As the hydrate dissociates there will, in general, be a change in density that by mass conservation will induce a fluid velocity adjacent to the phase boundary $z = s(t)$. By transforming the mass conservation equations (7.9) and (7.10) into integral form and applying them across the interface we obtain the jump conditions

$$q_w = n\frac{\mathrm{d}s}{\mathrm{d}t}(S_w - \beta_w), \quad \beta_w = \frac{\rho_{wo}}{\rho_w}, \quad \rho_{wo} = \frac{n_h \rho_h M_w}{M_g + n_h M_w}, \tag{7.23}$$

$$q_g = n\frac{\mathrm{d}s}{\mathrm{d}t}(S_g - \beta_g), \quad \beta_g = \frac{\rho_{go}}{\rho_g}, \quad \rho_{go} = \frac{\rho_h M_g}{M_g + n_h M_w}, \tag{7.24}$$

for the water and gas velocities. Since the hydrate is some mixture of gas and water we define the equivalent partial densities, ρ_{wo} and ρ_{go}, as a function of hydrate

number, n_h, hydrate density, ρ_h and molecular weight, M. Adding equations (7.23) and (7.24) the total velocity for incompressible flow is

$$q_t = \sigma \frac{\mathrm{d}s}{\mathrm{d}t}, \qquad \frac{\sigma}{n} = 1 - 1\left(\frac{\rho_{wo}}{\rho_w} + \frac{\rho_{go}}{\rho_g}\right), \tag{7.25}$$

At the hydrate-liquid interface we assume that when the water temperature rises above the dissociation temperature, the solid decomposes at a rate dependent on the difference in heat flux flowing into and out of this interface. This conservation law, known as the Stefan condition, is

$$K_h \frac{\partial T_h}{\partial z} - K_e \frac{\partial T_w}{\partial z} = n\rho_h L \frac{\mathrm{d}s}{\mathrm{d}t}, \quad T_h = T_w = T_D. \tag{7.26}$$

In general the hydrate dissociation temperature is some function of pressure, which can be defined by the well known Clausius–Clapeyron equation

$$\ln P = A - \frac{B}{T_D}, \tag{7.27}$$

for hydrate-specific constants A and B (Sloan, 1990).

7.4 Non-dimensionalization

The system of equations presented so far may be non-dimensionalized in the following way

$$\hat{z}_w = \frac{z_w}{\ell_w}, \quad \hat{z}_h = \frac{z_h}{\ell_h}, \quad \hat{s} = \frac{s}{\ell_h}, \tag{7.28}$$

$$\hat{T} = \frac{T - T_{D0}}{T_{\ell w} - T_{D0}}, \quad \rho_g = \hat{\rho}\rho_{gb}, \quad P = \hat{P}\rho_w g \ell_w + P_o, \tag{7.29}$$

where ρ_{gb} is the gas density at $z = 0$, P_o is the pressure at the seafloor $z = \ell_w$ and T_{D0} is the initial dissociation temperature evaluated at the hydrostatic pressure. Naturally the velocity in the system scales with the dissociation rate, which from the Stefan condition has the form $q_{st} = \Delta T\, K_{avg}/(\rho_h L\, \ell_w)$. With this boundary speed we scale the fluid velocities as follows

$$\hat{q} = \frac{q}{n q_{st}}, \quad \hat{t} = \frac{t\, q_{st}}{\ell_w}. \tag{7.30}$$

Finally the average thermal conductivity and specific heat are scaled with there initial values as

$$\hat{C}_e = \frac{C_e}{n\rho_w C_w + (1-n)\rho_s C_s} = \frac{C_e}{C_{avg}}, \tag{7.31}$$

$$\hat{K}_e = \frac{K_e}{nK_w + (1-n)K_s} = \frac{K_e}{K_{avg}}, \tag{7.32}$$

The resultant form of the governing equations with these non-dimensional variables will be discussed in the subsequent sections. We now drop hats on all non-dimensional quantities.

7.4.1 Thermal Energy

With these new variables the governing equations for thermal energy take on the following form

$$C_e \frac{\partial T_w}{\partial t} + V_e \frac{\partial T_w}{\partial z_w} = \frac{1}{P_{ew}} \frac{\partial}{\partial z_w}\left(K_e \frac{\partial T_w}{\partial z_w} \right), \tag{7.33}$$

$$\frac{\partial T_h}{\partial t} = \frac{1}{P_{eh}} \frac{\partial^2 T_h}{\partial {z_h}^2}, \tag{7.34}$$

$$\frac{\mathrm{d}s}{\mathrm{d}t} = d_1 \frac{\partial T_h}{\partial z_h} - r_\ell K_e \frac{\partial T_w}{\partial z_w}, \tag{7.35}$$

$$V_e = q_w \left(c_w - \rho c_g \right) + q_t \rho c_g, \tag{7.36}$$

$$C_e = S_w \left(c_w - \rho c_g \right) + \rho c_g + c_s, \quad K_e = b_1 \, S_w + b_2, \tag{7.37}$$

where the Péclet numbers for the two regions are expressed as

$$P_{ew} = St^{-1}, \quad P_{eh} = r_\ell^2 \frac{\alpha_{avg}}{\alpha_{he}} St^{-1}, \quad St = \frac{\rho_h L}{\Delta T \, C_{avg}}, \tag{7.38}$$

in which $\alpha_{avg} = K_{avg}/C_{avg}$, $r_\ell = \ell_w/\ell_h$ is the ratio of the initial water to hydrate layer depth, $d_1 = r_\ell^2 K_h/K_{avg}$, $q_t = \sigma r_\ell^{-1} \mathrm{d}s/\mathrm{d}t$, St is the Stefan number and the other parameters have the form:

$$c_w = \frac{n\rho_w \, C_w}{C_{avg}}, \quad c_g = \frac{n\rho_{gb} \, C_g}{C_{avg}}, \quad c_s = \frac{(1-n)\rho_s C_s}{C_{avg}}, \tag{7.39}$$

$$b_1 = \frac{n \, K_w - n \, K_g}{K_{avg}}, \quad b_2 = \frac{n \, K_g + (1-n) \, K_s}{K_{avg}}. \tag{7.40}$$

The thermal constants c_w, c_g and c_s represent the specific heat ratios of the three material components – water, gas and porous medium – respectively to the initial average value of the system. In addition the constants b_1 and b_2 represent the thermal conductivity ratios of the difference between the water and gas to the initial average value of the system and the ratio between a gas to water saturated porous medium. In the special case that the difference between the thermal properties of the gas and water are sufficiently small and the gas density is constant, the variables $\hat{V}_e$, $\hat{C}_e$, and $\hat{K}_e$ will be decoupled from the saturation equation.

Finally the boundary and initial conditions in non-dimensional form are

$$T_w = T_w(0, z_w) = T_{w0}, \qquad T_w(t, 1) = 1, \tag{7.41}$$

$$T_w(s/r_\ell) = T_h(s) = T_D, \tag{7.42}$$

$$T_h = T_h(0, z_h) = 0, \qquad T_h(t, -1) = 0. \tag{7.43}$$

7.4.2 Mass Flux

In the non-dimensional variables the pressure and saturation equations become

$$\begin{aligned} c_t(1 - S_w)\frac{\partial P}{\partial t} = \frac{B_g r_\rho}{r_\mu}\rho\frac{\partial}{\partial z_w}\left[k_{rw}\left(\frac{\partial P}{\partial z} - J_c\frac{\partial f_c}{\partial z} + 1\right)\right] \\ + B_g r_\rho \frac{\partial}{\partial z_w}\left[k_{rg}\rho\left(\frac{\partial P}{\partial z} + r_\rho\rho\right)\right], \end{aligned} \tag{7.44}$$

$$\frac{\partial S_w}{\partial t} + \frac{\partial q_w}{\partial z_w} = 0, \tag{7.45}$$

$$q_w = f_w q_t + h_w B_g(r_\rho\rho - 1) + h_w B_c\frac{\partial f_c}{\partial z_w}, \tag{7.46}$$

where $c_t = \mathrm{d}\rho_g/\mathrm{d}P_g$ is a compressibility factor, $B_g = K\rho_w g/(\mu_g q_{st} n)$ is the ratio of gravitational to viscous forces, $B_c = K\rho_w g\alpha^{-1}/(nq_{st}\ell_w\mu_g)$ is the ratio of capillary to viscous forces, $J_c = B_c/B_g = \alpha^{-1}/(\ell_w)$, is the ratio of capillary to gravitational

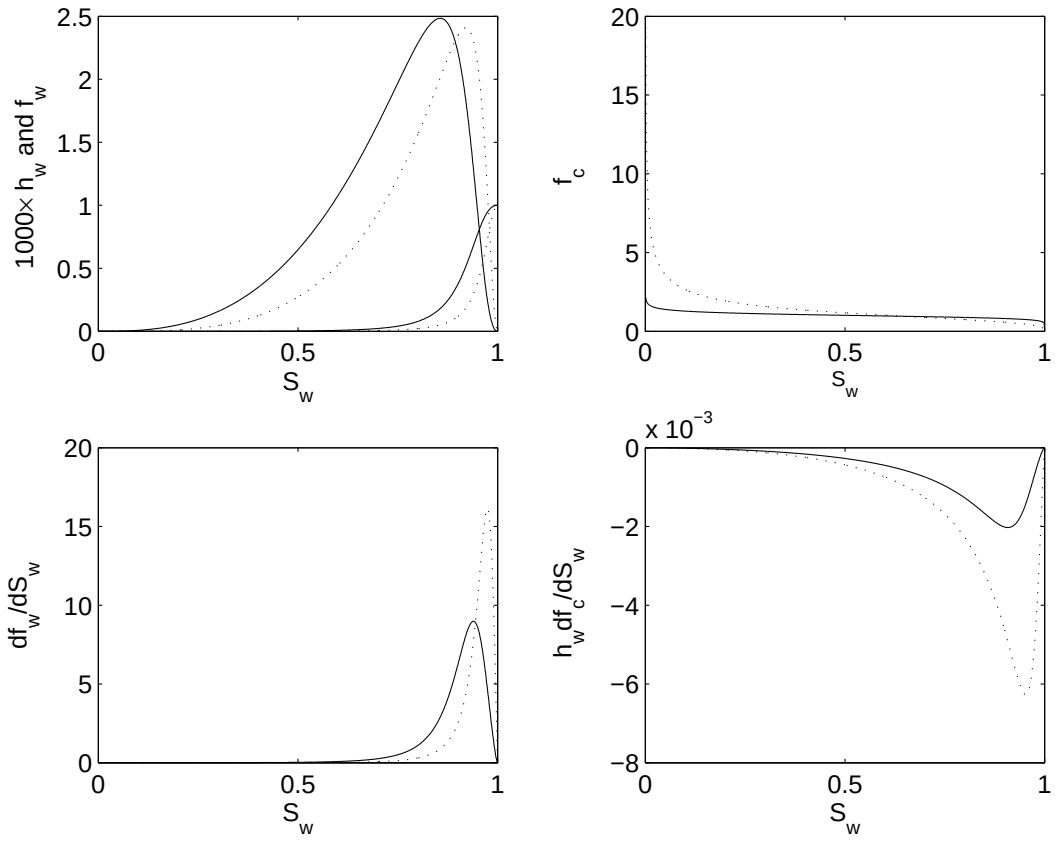

Figure 7.3: Water mobility functions f_w and h_w, capillary pressure f_c, $\mathrm{d}f_w/\mathrm{d}S_w$, and diffusivity $h_w(\mathrm{d}f_c/\mathrm{d}S_w)$ as a function of saturation for $m = .9$ (solid line) and $m = .7$ (dotted line)

forces, $r_\rho = \rho_{gb}/\rho_w$ is a density ratio, $f_w = k_{rw}/(k_{rw} + r_\mu k_{rg})$, $r_\mu = \mu_w/\mu_g$ is the viscosity ratio and $h_w = f_w K_{rg}$. We have plotted the last two mobility functions as well as the capillary pressure, $\mathrm{d}f_w/\mathrm{d}S_w$, and the saturation diffusivity, $h_w(\mathrm{d}f_c/\mathrm{d}S_w)$ against the water saturation for different vales of the fitting parameter m in Figure 7.3. From here on we will assume a constant gas density ($\rho = 1$), which is valid for small pressure changes. This is possible if the flow rates are sufficiently small and the vertical rise height, $\ell_w - s(t)$, of the gas is small.

At the lower boundary we have the following condition

$$q_w(t, s/r_\ell) = \frac{1}{r_\ell}\frac{\mathrm{d}s}{\mathrm{d}t}(S_w - \beta_w), \tag{7.47}$$

which can be combined with (7.46) to obtain an equation that is solely a function of saturation in the following form

$$\frac{1}{r_\ell}\frac{\mathrm{d}s}{\mathrm{d}t}(S_w - \beta_w) = f_w\frac{\sigma}{r_\ell}\frac{\mathrm{d}s}{\mathrm{d}t} + h_w B_g(r_\rho - 1) + h_w B_c\frac{\partial f_c}{\partial z_w}. \tag{7.48}$$

We have assumed a constant gas density and $\sigma/n = 1 - (\rho_{w0} + \rho_{g0}/r_\rho)/\rho_w$.

At the upper boundary we have the following equations

$$q_w = \frac{B_g}{r_\mu}k_{rw}(\chi P_w - 1), \quad q_g = B_g k_{rg}(\chi P_g - r_\rho), \tag{7.49}$$

which can be combined with the definition of capillary pressure and total velocity to obtain the flow rate as a function of saturation in the following form

$$q_w = f_w q_t + B_g h_w(r_\rho - 1) - B_g h_w \chi J_c f_c. \tag{7.50}$$

Dissociation temperature

The dissociation temperature, which we have assumed to be solely a function of pressure, is expressed using the Clausius–Clapeyron equation in non-dimensional form as

$$T_D = \frac{B/\Delta T}{A - \ln\left[\rho_w g \ell_w P_w + P_o\right]} - \frac{T_{D0}}{\Delta T}. \tag{7.51}$$

where the water pressure is used since it is the wetting fluid. The pressure distribution can be obtained from Darcy's law, which can be recast in the form

$$q_w = -\frac{B_g}{r_\mu}k_{rw}\left(\frac{\partial P_w}{\partial z_w} + 1\right), \quad q_g = -B_g k_{rg}\left(\frac{\partial P_g}{\partial z_w} + r_\rho\right), \tag{7.52}$$

where the variables are assumed to be order one quantities. Supposing that we have scaled the equations appropriately, the pressure distribution will be dominated by hydrostatic forces in the case that $B_g \gg 1$. Integrating the above equation in this limit we obtain the hydrostatic pressure distribution, $P_w = 1 - z_w$, which may be

combined with the Clausius–Clapeyron equation to obtain an expression for the dissociation temperature with height in the following form.

$$T_D = \frac{B/\Delta T}{A - \ln\left[\rho_w g \ell_w \left(1 - z_w\right) + P_o\right]} - \frac{T_{D0}}{\Delta T} \tag{7.53}$$

Since we will not look at large changes in the liquid layer height, $\ell_w - s(t)$, and the gravitational number will be large in most geological settings we will take the dissociation temperature to be constant with $T = T_{D0}$.

7.4.3 Fixed Boundary Problem

In this Chapter we fix the position of the moving boundary by using the Landau transformation (Crank, 1984; Furzeland, 1980) defined as

$$x_w = 1 - \frac{2(z_w - 1)}{s/r_\ell - 1}, \qquad x_h = 1 - \frac{2(z_h + 1)}{s + 1}, \tag{7.54}$$

which fixes the moving boundary at $x = -1$. The required derivatives, using the chain rule, are now written as

$$\frac{\partial}{\partial z_w} = \frac{\mathrm{d}x_w}{\mathrm{d}zw}\frac{\partial}{\partial x_w} = \frac{-2}{(s/r_\ell - 1)}\frac{\partial}{\partial x_w}, \tag{7.55}$$

$$\frac{\partial^2}{\partial {z_w}^2} = \left(\frac{\mathrm{d}x_w}{\mathrm{d}z_w}\right)^2 \frac{\partial^2}{\partial x_w^2} = \frac{4}{(s/r_\ell - 1)^2}\frac{\partial^2}{\partial x_w^2}, \tag{7.56}$$

$$\frac{\partial}{\partial t} = \frac{\partial}{\partial t} + \frac{\mathrm{d}x_w}{\mathrm{d}t}\frac{\partial}{\partial x_w} = \frac{\partial}{\partial t} + \frac{\mathrm{d}s}{\mathrm{d}t}\frac{1 - x_w}{(s/r_\ell - 1)r_\ell}\frac{\partial}{\partial x_w}. \tag{7.57}$$

in the liquid layer and similarly for the equations in the hydrate layer. By making this transformation we have essentially displaced the dynamics of the moving interface into the governing equations. The downside of this method is the addition of the extra term in the governing equations, which comes from the time derivative. The benefit is that we don't need to deal with a moving boundary and numerically one that will lie between two grid points.

These equations then take on the following form

$$\frac{\partial T_w}{\partial t} + \left(\frac{(1-x_w)}{c_4\,(s/r_\ell - 1)} \frac{\mathrm{d}s}{\mathrm{d}t} - \frac{2V_e}{C_e(s/r_\ell - 1)} \right) \frac{\partial T_w}{\partial x_w} = \frac{4}{C_e(s/r_\ell - 1)^2 P_{ew}} \frac{\partial}{\partial x_w} \left(K_e \frac{\partial T_w}{\partial x_w} \right), \tag{7.58}$$

$$\frac{\partial T_h}{\partial t} + \frac{\mathrm{d}s}{\mathrm{d}t} \frac{(1-x_h)}{s+1} \frac{\partial T_h}{\partial x_h} = \frac{4}{(s+1)^2\, P_{eh}} \frac{\partial^2 T_h}{\partial {x_h}^2}, \tag{7.59}$$

$$\frac{\mathrm{d}s}{\mathrm{d}t} = \frac{2 r_\ell K_e}{(s/r_\ell - 1)} \frac{\partial T_w}{\partial x_w} - \frac{2\,d_1}{(s+1)} \frac{\partial T_h}{\partial x_h}, \tag{7.60}$$

$$\frac{\partial S_w}{\partial t} + \frac{\mathrm{d}s}{\mathrm{d}t} \frac{1-x_w}{r_\ell\,(s/r_\ell - 1)} \frac{\partial S_w}{\partial x_w} - \frac{2}{(s/r_\ell - 1)} \frac{\partial q_w}{\partial x_w} = 0, \tag{7.61}$$

$$q_w = f_w q_t + h_w B_g\,(r_\rho \rho - 1) - h_w \frac{2B_c}{(s/r_\ell - 1)} \frac{\partial f_c}{\partial x_w}, \tag{7.62}$$

and hold in the fixed domain $(-1, 1)$.

7.5 Reduced models

7.5.1 Large Stefan number problem

With the scaling given in Section 7.4 the Stefan number gives a measure of the degree of separation between the time scales for the evolution of the temperature and saturation. When this number is large the rate of phase change will be small, resulting in a small advective transport of thermal energy. In this case the temperature in the large St limit will be dominated by diffusion in the form

$$\frac{\partial}{\partial z_w} \left(K_e \frac{\partial T_w}{\partial z_w} \right) = 0. \tag{7.63}$$

In the case that the difference in thermal conductivity between the gas an liquid is small or the thermal conductivity of the sediment dominates, we can express $K_e = b_1\, S_e + b_2 \approx b_2$ and the above solution takes on the quasi-linear form

$$T_w = 1 + \frac{1}{1 - r_\ell^{-1} s}\,(z_w - 1)\,. \tag{7.64}$$

For hydrate layers that are initially at the dissociation temperature, and thus will remain so for all time, the speed of the moving boundary, obtained from

the Stefan condition, is determined from the expression

$$\frac{\mathrm{d}s}{\mathrm{d}t} = \frac{r_\ell b_2}{s/r_\ell - 1}. \tag{7.65}$$

This can be integrated to determine the interface position as a function of time:

$$s(t) = r_\ell - r_\ell\sqrt{1 + b_2 t}. \tag{7.66}$$

This relationship shows that the position of the hydrate phase boundary has a square root dependence on time, which is characteristic of a diffusion-dominated mode of heat transport.

Large Viscous Forces

For relatively small permeabilities, $B_c \sim 0$ and $B_g \sim 0$, or large flow rates ($q_t \gg B_g, B_c$) advective forces will dominate and the terms involving gravitational and capillary forces in equation (7.46) can be neglected. The equations in this case can be solved using the method of characteristics, where the advective term in the fixed domain reduce to

$$\frac{\partial S_w}{\partial t} + \left[\frac{\mathrm{d}s}{\mathrm{d}t}\frac{1 - x_w}{r_\ell\,(s/r_\ell - 1)} - \frac{2}{(s/r_\ell - 1)}\frac{\mathrm{d}f_w}{\mathrm{d}S_w}q_t\right]\frac{\partial S_w}{\partial x_w} = 0, \tag{7.67}$$

which has the general form $\mathrm{d}S_w/\mathrm{d}t + u(x_w, t, S_w)\mathrm{d}S_w/\mathrm{d}x_w = 0$. Moving at the characteristic velocity, $\mathrm{d}\,x_w/\mathrm{d}\,t = u$ the saturation is constant and we can solve the ode for the position of the characteristics as

$$x_w(S_w, t) = 1 - 2\sigma\frac{\mathrm{d}f_w}{\mathrm{d}S_w} + \left[\xi + 2\sigma\frac{\mathrm{d}f_w}{\mathrm{d}S_w} - 1\right](1 + 2b_2 t)^{-1/2}, \tag{7.68}$$

where $\xi = x_w(0)$.

Since the sediment is initially water saturated, a shock-separating a mixture of water and gas from water saturated sediment, must form immediately at the moving boundary $x_w(0) = -1$ and propagate downstream. The speed of the

shock can be determined by re-writing equation (7.67) in integral form and taking the limit in which $\mathrm{d}x \to 0$, yielding the following expression

$$\frac{\mathrm{d}X_s}{\mathrm{d}t} = \frac{\left[\frac{\mathrm{d}s}{\mathrm{d}t}\frac{1-x_w}{r_\ell(s/r_\ell - 1)}S_w - 2\frac{f_w q_t}{(s/r_\ell - 1)}\right]}{[S_w]}, \tag{7.69}$$

in terms of the conditions on either side of the shock. Since the shock speed is equal to the water velocity at $x_w = X_s$, $\mathrm{d}X_s/\mathrm{d}t = u$ and we can determine the water saturation behind the shock from

$$\frac{\mathrm{d}f_w}{\mathrm{d}S_w} = \frac{(1-f_w)}{1-S_w}. \tag{7.70}$$

This solution is similar to the well known Buckley–Leverett (Bear, 1991) solution. Here though we have a moving boundary, albeit transformed onto a fixed domain, that generates a flow through the sediment.

7.5.2 Large Capillary Forces

For porous media with low void fractions, such as clay, capillary forces dominate gravitational forces at small length scales. Since in this case the sediment makes up the bulk of the mass, the thermal properties of the medium will be dominated by the solid structure and we can assume that they are constant. In addition if we assume that the specific heat of the gas and liquid are sufficiently similar ($c_1 \sim c_2$) the governing equations reduce to

$$\frac{\partial T}{\partial t} + C_T \frac{\mathrm{d}s}{\mathrm{d}t}\frac{\partial T}{\partial z_w} = \alpha_T \frac{\partial^2 T}{\partial z_w^2} \tag{7.71}$$

$$\frac{\partial S_w}{\partial t} + C_S \frac{\mathrm{d}s}{\mathrm{d}t}\frac{\partial S_w}{\partial z_w} = \frac{\partial}{\partial z_w}\left(\alpha_S \frac{\partial S_w}{\partial z_w}\right), \tag{7.72}$$

$$\frac{\mathrm{d}s}{\mathrm{d}t} = -d_2 \frac{\partial T}{\partial z_w}, \tag{7.73}$$

$$\frac{n}{r_\ell}\frac{\mathrm{d}s}{\mathrm{d}t}(S_{wb} - \beta_w) = f_w q_t - \alpha_s \frac{\mathrm{d}S_w}{\mathrm{d}z_w}, \tag{7.74}$$

where the thermal properties $C_T = c_g\sigma/c_s r_\ell$ and $\alpha_T = b_2/c_s P_{ew}$ are evaluated at the initial concentration and the saturation functions are given as

$$C_S = \frac{\sigma}{r_\ell}\frac{\mathrm{d}f_w}{\mathrm{d}S_w}, \quad \alpha_S = B_c h_w \frac{\mathrm{d}f_c}{\mathrm{d}S_w}. \tag{7.75}$$

The last two conditions equations (7.73) and (7.74) are applied at the moving boundary to determine the interface speed and saturation.

We can simplify the above equations by extending the upper boundary to infinity and applying a uniform initial temperature $T(z_w, 0) = 1$ and saturation $S_w(z_w, 0) = S_i$ within the porous media. In this case we introduce a similarity variable of the form $\eta = z/2\sqrt{\alpha_T t}$ and an assumed interface speed of $s = 2\lambda r_\ell \sqrt{\alpha_T t}$, where λ must be determined as part of the solution. With this new variable the system of equations reduce to the following ODEs:

$$\frac{\mathrm{d}^2 T}{\mathrm{d}\eta^2} = \frac{\mathrm{d}T}{\mathrm{d}\eta}\left(2C_T \lambda r_\ell - 2\eta\right), \tag{7.76}$$

$$\frac{\mathrm{d}}{\mathrm{d}\eta}\left(\frac{\alpha_S}{\alpha_T}\frac{\mathrm{d}S_w}{\mathrm{d}\eta}\right) = \frac{\mathrm{d}S_w}{\mathrm{d}\eta}\left(2C_S \lambda r_\ell - 2\eta\right), \tag{7.77}$$

$$\frac{\mathrm{d}\hat{T}_w}{\mathrm{d}\eta} = -\frac{2\lambda\alpha}{b_2}, \tag{7.78}$$

$$2n\alpha_T \lambda\left(S_w - \beta_w - \frac{f_w \sigma}{n}\right) = -\alpha_s \frac{\mathrm{d}S_w}{\mathrm{d}\eta}. \tag{7.79}$$

Since the temperature equation is decoupled from the saturation equation we can solve for the temperature field exactly in the form

$$T = 1 - \frac{\operatorname{erfc}(\eta - C_T \lambda r_\ell)}{\operatorname{erfc}(\lambda - C_T \lambda r_\ell)}, \tag{7.80}$$

$$\lambda = \frac{b_2}{\alpha_T \sqrt{\pi}} \frac{\exp\left(-(C_T \lambda r_\ell - \lambda)^2\right)}{\operatorname{erfc}(\lambda - C_T \lambda r_\ell)}. \tag{7.81}$$

If the saturation within the sediment only varies by a small amount then we can perform a regular perturbation in the small parameter, $\epsilon = S_i - S_{wb}$, where the boundary conditions have the perturbed values $S_w(\eta = \infty) = S_{wb} + \epsilon$ and $S_w(\eta = \lambda) = S_{wb}$. In this case the series, up to second order, has the form $S_w = S_{wb} + \epsilon S_1(\eta) + \epsilon^2 S_2(\eta)$ and the non-linear saturation functions have the form $\alpha_s = \alpha_0 + \epsilon\alpha_1 + \epsilon^2\alpha_2$ and $C_s = C_0 + \epsilon C_1 + \epsilon^2 C_2$. At first order we have the equation $S_1'' = 2S_1' \alpha_T \left(\lambda r_\ell C_0 - \eta\right)/\alpha_0$, whose solution in terms of error functions as

$$S_1 = 1 - \frac{\operatorname{erfc}\left((\eta - C_0 \lambda r_\ell)\sqrt{\frac{\alpha_T}{\alpha_0}}\right)}{\operatorname{erfc}\left((\lambda - C_0 r_\ell \lambda)\sqrt{\frac{\alpha_T}{\alpha_0}}\right)} \tag{7.82}$$

The condition at the moving boundary at first order will have the form.

$$n\lambda\left(S_{wb}-\beta_w-\frac{f_w(S_{wb})\sigma}{n}\right)= -\frac{\epsilon}{\sqrt{\pi}}\left(\frac{\alpha_0}{\alpha_T}\right)^{1/2}\frac{\exp\left(-\left(\left(C_0\lambda r_\ell-\lambda\right)\sqrt{\frac{\alpha_T}{\alpha_0}}\right)^2\right)}{\operatorname{erfc}\left(\left(\lambda-C_0 r_\ell\lambda\right)\sqrt{\frac{\alpha_T}{\alpha_0}}\right)}, \tag{7.83}$$

which must be solved numerically for the interface saturation S_{wb}.

7.6 Numerical Results

We have solved the set of coupled equations defined in Section 7.4.3 numerically for a fixed domain, using a finite difference discretization with two different methods for the temperature and saturation equations. The temperature equation was solved implicitly using the method of Furzeland (1980) by making guess at the future value of the interface position and correcting this guess iteratively using the Stefan condition. The saturation equation was solved using methods presented in Aziz & Settari (1979) or Peaceman (1977) by first guessing the saturation values at the upper and lower boundaries and then correcting them at each time step using equations (7.48) and (7.50).

The two properties, temperature and saturation, are coupled and must be solved simultaneously. For relatively large Stefan numbers we can separate timescales such that the evolution of the temperature profiles is much faster than the saturation profiles. In this limit the dissociation rate is relatively slow since the ratio of available thermal energy to latent heat is small and the temperature field controlled by diffusion is able to evolve with a quasi-stationary boundary. In our scaling we have defined a timescale with the Stefan number so we are in a long-time limit for the temperature equation, expressed by the large effective diffusivity.

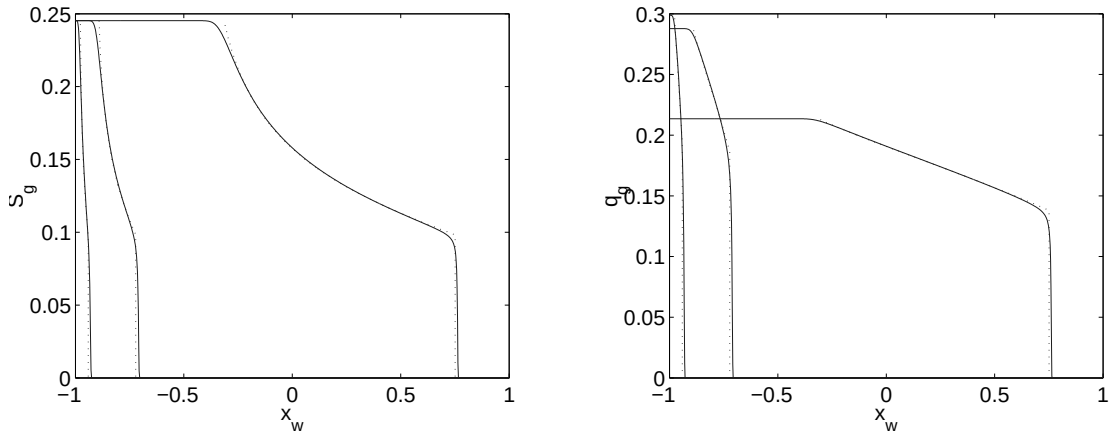

Figure 7.4: Plot of the exact solution (dotted line) to the reduced model presented in section (7.5), using the method of characteristics and numerical solution (solid line). Here $St = 1000$, $m = .9$, $r_\rho = .1$ and the solutions are plotted at $t = .01, .05, .5$.

7.6.1 Comparison with reduced models

We have developed two reduced models, corresponding to a decoupling of the saturation equation from the temperature equation for sediment dominated thermal properties, and simplification of the saturation equation for two different limits. In the first case we assumed a large St limit, which allows the temperature field to be quasi-steady with respect to the saturation and neglected capillary and gravitational forces in comparison to viscous forces. We plotted a representative solution to this reduced model against the numerical solution in Figure 7.4 for different points in time, showing excellent agreement. The capillary and gravitational forces can be very large for $St \gg 1$; none the less this solution gives a good check on the numerical solution.

In the second case we extended the upper boundary to infinity and obtained a similarity solution for the temperature and linearized saturation equation. We plotted a representative solution to the reduced model in Figure 7.5 against the numerical solution. Since we have decoupled the temperature equation from

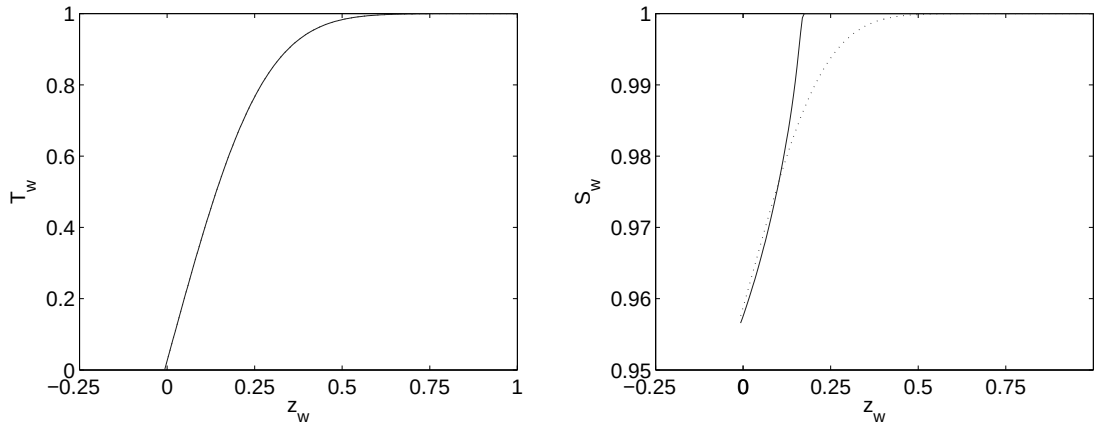

Figure 7.5: Temperature and saturation profiles in the sediment for the reduced model (dotted line) of section (7.5) and the numerical solution (solid line). Here $St = 10$, $m = .9$ and $B_c = 10000$.

the saturation equation and there are no further simplifications, the two solutions for temperature are in excellent agreement as we expected. On the other hand, the saturation equation has been linearized about the interface saturation, which is only valid for very small values of ϵ. For this reason the error associated with reduced model will be smallest near the moving boundary as we can see from Figure 7.5.

7.6.2 Diagnostics

In this section we plot the profiles for temperature, saturation, flow rate and pressure as well as the evolution of the boundary velocities for variations in the four parameter values St, B_c, B_g and r_ρ. The other parameter values, affecting the thermal energy equation, have been fixed to the physically realistic values displayed in Table 7.1. Since we will be looking at relatively large Stefan numbers the dissociation rate will not be very sensitive to changes in the thermal properties of the sediment and we can focus on the parameters appearing in the saturation

Table 7.1: Non-dimensional groups and constants used in the Chapter corresponding to berea sandstone, methane gas, water and methane hydrate.

Parameter	Value	Parameter	Value
d_1	1	c_s	.37
c_w	.79	c_g	.04
b_1	.022	b_2	.98
r_μ	200	r_ℓ	1
A	49.32	B	9459
χ	$> 10^3$	L	$429.66 J/g$
ρ_{wo}	$805.3 \mathrm{Kg/m}^3$	ρ_{go}	$124.7 \mathrm{Kg/m}^3$

equation.

In general the Stefan number will take on a value of approximately $St = 50/\Delta T$ for methane hydrates, with temperature differences no larger than a few degrees, depending on the water depth amongst other things. The capillary and gravitational forces can vary substantially, for different sediment properties. For example berea sandstone ($K = 1 \times 10^{-13} m^2$) will have parameter values of approximately $B_g = 5 \times 10^3 \ell_w / \Delta T$ and $B_c = 5 \times 10^3 / \Delta T$. In addition the parameter r_ρ, which relates the density of gas to the density of water, will vary greatly with pressure according to the ideal gas law.

Effect of the Stefan number

The Stefan number St represents the amount of available thermal energy to the energy required to cause a change in phase from solid to liquid. As one can imagine then, the dissociation rate $\mathrm{d}s/\mathrm{d}t$ is strongly dependent on this number and for constant latent heat represents the amount of thermal forcing in the system. We can write this number as $St = \alpha_{avg}/\ell_w q_{st}$, relating the thermal diffusion velocity to the boundary velocity. Since time is scaled with this parameter and the fluid velocity with q_{st}, it gives an indication of the time scale separation between the saturation and thermal energy equations. For relatively large St, we are looking at

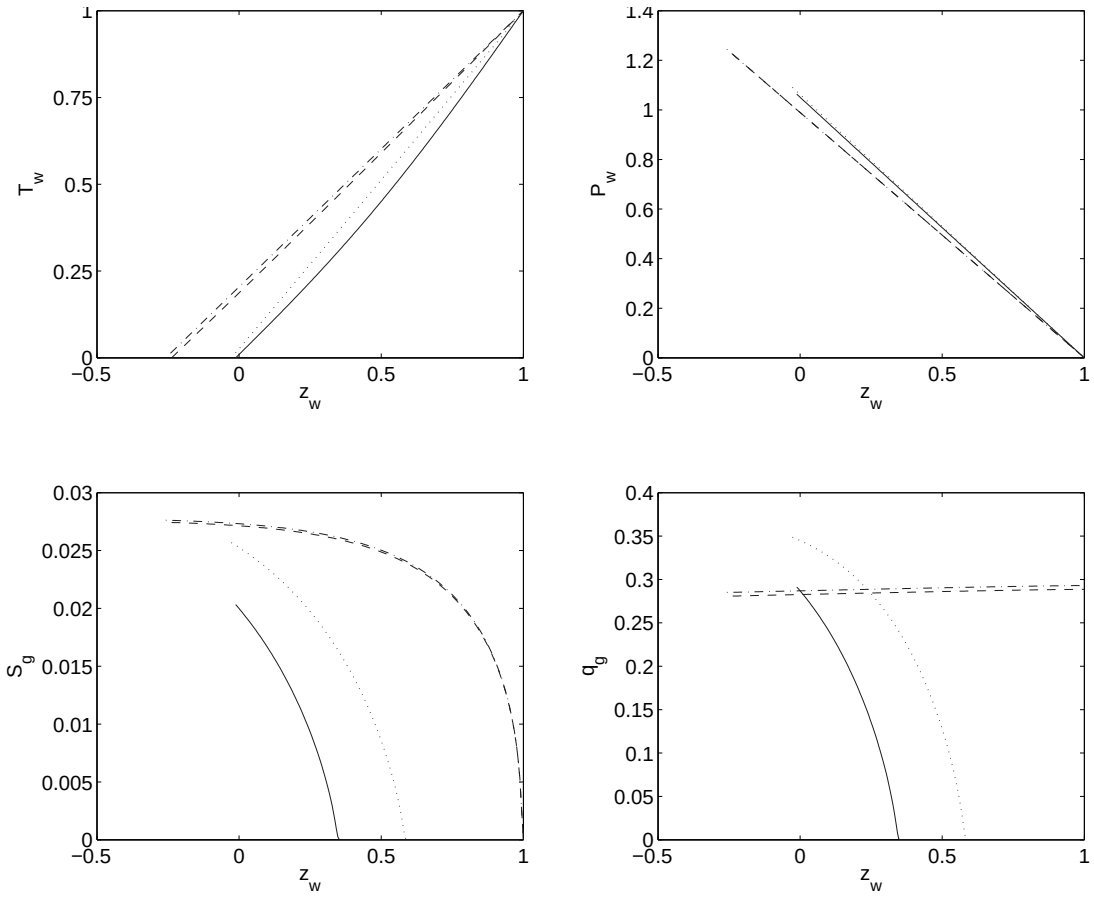

Figure 7.6: Profiles for temperature T_w, water pressure P_w, gas saturation S_g and gas flow rate q_g for $St = 10$ and $t = .03$ (solid line); $St = 10$ and $t = .3$ (dashed line); $St = 100$ and $t = .03$ (dotted line); $St = 100$ and $t = .3$ (dashed-dotted line). Here $B_g = 1000$, $B_c = 10000$, $r_\rho = .1$ and $m = .9$.

the long time behavior of the temperature equation and the temperature profiles as predicted in Section 7.5 and shown in Figure 7.6 are linear and quasi-steady. At early times the temperature will be evolving in time with a diffusion-dominated mode of heat transport but the transport of released gas will not have traveled very far from the moving boundary, leaving the saturation equation relatively unchanged.

In Figure 7.6 we have plotted the profiles for temperature, pressure, gas saturation and gas flow rate for two different values of St and instants in time.

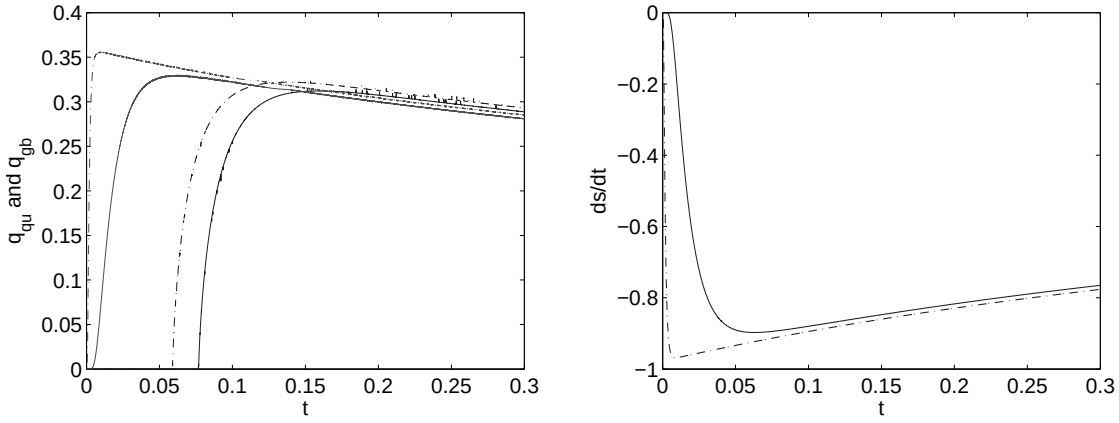

Figure 7.7: Lower boundary gas velocity q_{gb}, upper boundary gas velocity q_{gu} and moving boundary velocity $\mathrm{d}s/\mathrm{d}t$ as a function of time for $St = 10$ (solid line) and 100 (dash-dot line) .Here $B_g = 1000$, $B_c = 10000$, $r_\rho = .1$ and $m = .9$.

In general a small Stefan number will result in a larger boundary velocity due to an increase in the degree of thermal forcing, but since we have scaled time with this parameter the non-dimensional equations experience a decrease in the effective thermal diffusivity. As a result the non-dimensional dissociation rate increases with St and with it the gas flow rate through the sediment. At large times the saturation equation becomes quasi-steady, with small adjustments due to the moving boundary and the flow rate will be almost constant. In addition the pressure distribution in the sediment, as indicated in the upper right hand plot of Figure 7.6 is approximately linear and hydrostatic, due to the relatively large gravitational forces compared to viscous forces, expressed by $B_g \gg 1$.

In Figure 7.7 we have plotted the upper and lower boundary flow rates and moving boundary velocity as a function of time for different values of the Stefan number. When this number is large the temperature diffuses more rapidly, thus increasing the dissociation rate and decreasing the time to quasi-steady state, in which equation (7.64) is valid. As a result the lower boundary flow rate increases, since it is proportional to $\mathrm{d}s/\mathrm{d}t$, and with it the gas breakout time and upper

boundary flow rate. At latter times the dissociation rate is still faster for large values St, due to a faster thermal diffusion towards the moving boundary, which forces the gas flow rate out of the sediment to be larger.

Effect of capillary forces

The capillary number defines a ratio between capillary to viscous forces and tends to dominate when the surface tension is high (low permeability sediments), when the length scale, ℓ_w is small ($B_c \gg B_g$) or for relatively small fluid velocities ($B_c \gg 1$). Capillary forces will act in a similar way to thermal diffusion in that the water will be transported into regions of relatively high gas saturations. Consequently the gas will be forced to diffuse away from the moving boundary, at some velocity that is predicted to increase with the non-dimensional group B_c.

In Figure 7.8 we have plotted the upper and lower gas flow rates as well as the dissociation rate as a function of time and capillary number. The interface velocity $\mathrm{d}s/\mathrm{d}t$ has the same characteristics as that of the previous section due to the relatively large Stefan number and weak coupling of the saturation equation to the temperature equation. Since a larger capillary number tends to diffuse the gas more rapidly into high water saturations the gas reaches the upper boundary sooner than for a smaller value of B_c. In addition the gas flux out of the sediment approaches quasi-steady state on a slower time scale for larger B_c due to the nature of a diffusive dominated flow. In addition, we have plotted the gas saturation and flow rate profiles as a function of B_c and time in Figure 7.8. When the capillary forces are small, gas builds up behind the propagating front and for sufficiently small values will be discontinuous with similarities to the large viscous force model of Section 7.5. When the capillary forces are increased, the diffusive term becomes larger, smoothing out this jump and increasing the speed of the gas front.

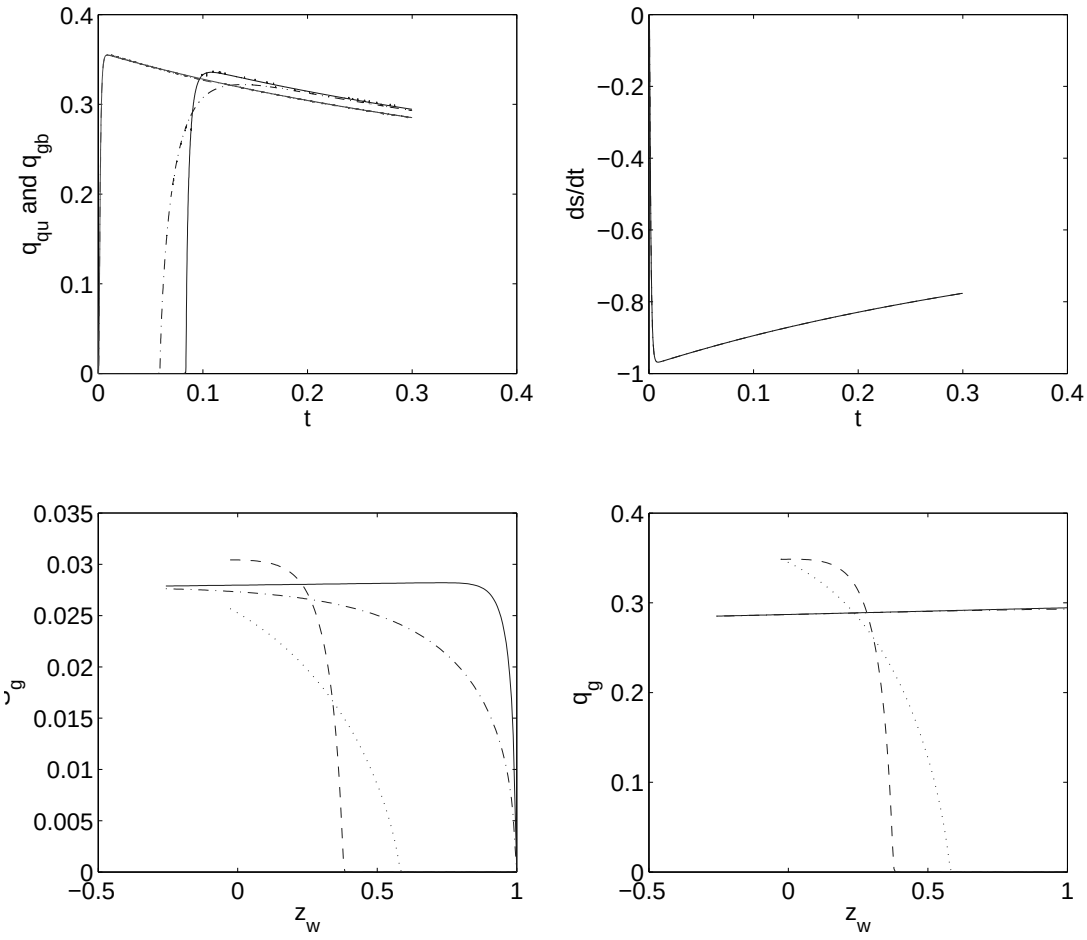

Figure 7.8: Lower boundary gas velocity q_{gb}, upper boundary gas velocity q_{gu} and moving boundary velocity $\mathrm{d}s/\mathrm{d}t$ as a function of time and profiles for gas saturation S_g and gas flow rate q_g for $B_c = 1000$ and $t = .03$ (dashed line); $B_c = 10000$ and $t = .03$ (dotted line); $B_c = 1000$ and $t = .3$ (solid line); $B_c = 10000$ and $t = .3$ (dash-dot line). Here $B_g = 1000$, $St = 100$, $r_\rho = .1$ and $m = .9$.

Effect of gravitational forces

Gravitational forces within a porous media arise as a result of the density difference between the two fluids and tends to force the lighter fluid out of the sediment. The strength of this force can be encompassed in the term $B_g(r_\rho - 1)$, which tends to zero as the density difference decreases or the flow rate becomes large. When the gravitational forces dominate the gas saturation evolves as a result of a shock propagation through the sediment in a similar way to the discussion in Section 7.5. Since the saturation velocity is a decreasing function of water saturation, the gas saturation builds up behind the shock front resulting in the relatively constant values as seen in Figure 7.9. On the other hand, when capillary forces are relatively large, this front becomes smother due to diffusion and we get more curved profiles. At quasi-steady state the gas flow rate has a small vertical gradient that in the absence of capillary forces must coincide with nearly constant saturation values, except near the upper boundary, where the saturation gradient is very large. In addition, smaller values of B_g will result in a larger pressure at the moving boundary due to a relatively larger flow rate through the sediment, but will still look nearly hydrostatic due to $B_g \gg 1$.

We have also plotted the upper and lower boundary velocities in Figure 7.9 as a function of time for different values of B_g. Since stronger gravitational forces will increase the saturation velocity the gas front will reach the upper boundary more quickly and approach a quasi steady state on a smaller time scale. At larger times the gas flow rate is nearly constant, only changing as the boundary recedes, and consequently the upper boundary flow rate will be dominated by the decreasing dissociation rate.

Effect of r_ρ

The parameter r_ρ represents the difference in density between the gas and water and gives a measure of the total velocity in the sediment due to a change in density from hydrate to fluid phases. Since the critical temperature of methane

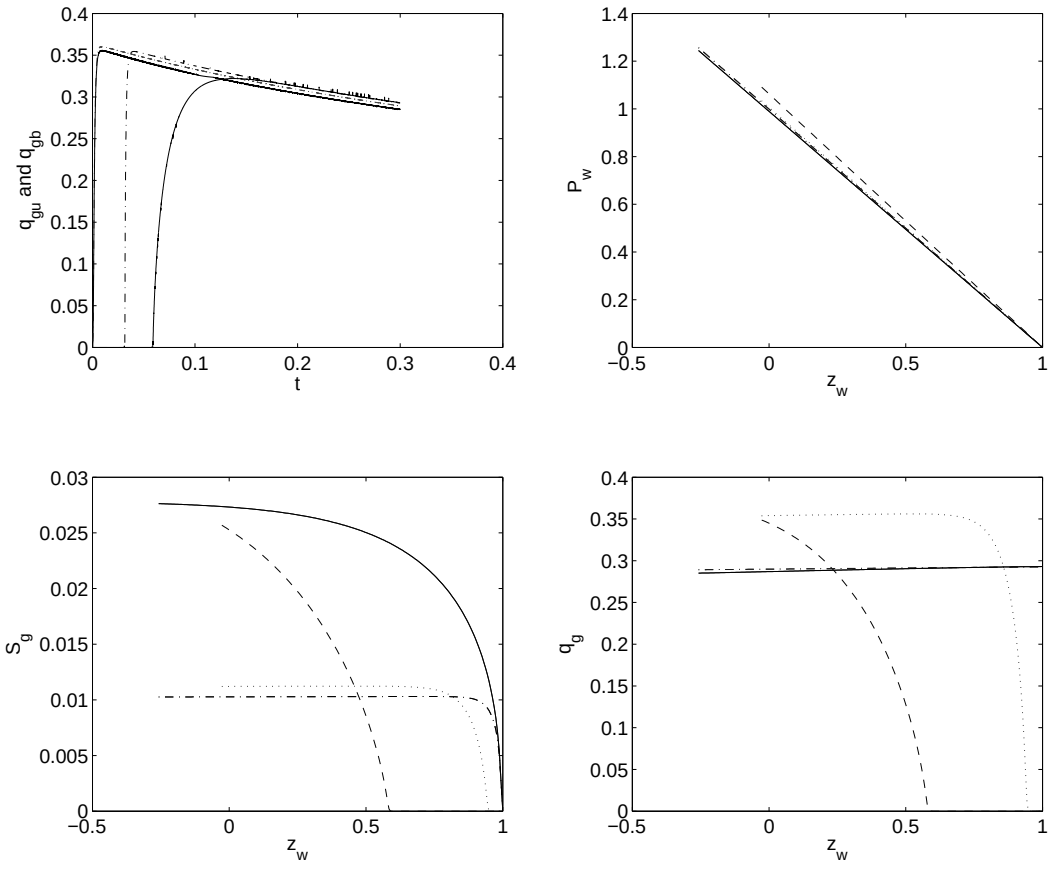

Figure 7.9: Lower boundary gas velocity q_{gb}, upper boundary gas velocity q_{gu} and moving boundary velocity $\mathrm{d}s/\mathrm{d}t$ as a function of time and profiles for water pressure P_w, gas saturation S_g and gas velocity q_g for $B_g = 1000$ and $t = .03$ (dashed line); $B_g = 10000$ and $t = .03$ (dotted line); $B_g = 1000$ and $t = .3$ (solid line); $B_g = 10000$ and $t = .3$ (dash-dot line). Here $B_c = 10000$, $St = 100$, $r_\rho = .1$ and $m = .9$.

is relatively low (less than the freezing point of water) the hydrocarbon will not become a liquid at high pressures, which is the opposite of carbon dioxide, and consequently its density can become comparatively large for deep deposits. When this parameter is small the volume occupied by the gas is larger, which drives the gas saturation up and forces – by mass conservation – the fluid velocities to increase as seen in Figure 7.10. This increase in velocity allows for a faster gas front speed through the sediment and requires a larger pressure gradient, which must come from an increase in moving boundary pressure.

In addition, we have plotted the evolution of the boundary flow rates in Figure 7.10, for two different values of r_ρ. This plot shows larger gas flow rates at the upper and lower boundaries, due to a larger q_t, that result in faster gas breakout times when r_ρ is small.

Volume fluxes

One of the main interests in the development of this model is to investigate the amount of gas released from the seafloor by dissociating gas hydrates. We can gain a better understanding of this by plotting the volume of gas released within a specified time interval defined as

$$V_{gas} = \int_0^{10/St} q_{gu}\,\mathrm{d}t. \tag{7.84}$$

The integral extends to $10/St$ because time scales with the Stefan number and therefore is a better choice physically. We plot contours of the Stefan number against the other three groups, B_c, B_g and r_ρ, discussed in this Chapter in Figure 7.11 and 7.12. Since St is proportional to the inverse of the temperature difference ΔT and in which the fluid velocity scales, the total volume of gas released into the ocean will be strongly related to this number. In fact, as we can see from the figures this is the most important group for our system. The capillary and gravitational forces will also increase the total volume released since they will increase the gas velocity through the sediment. Although, this effect is only expected to be

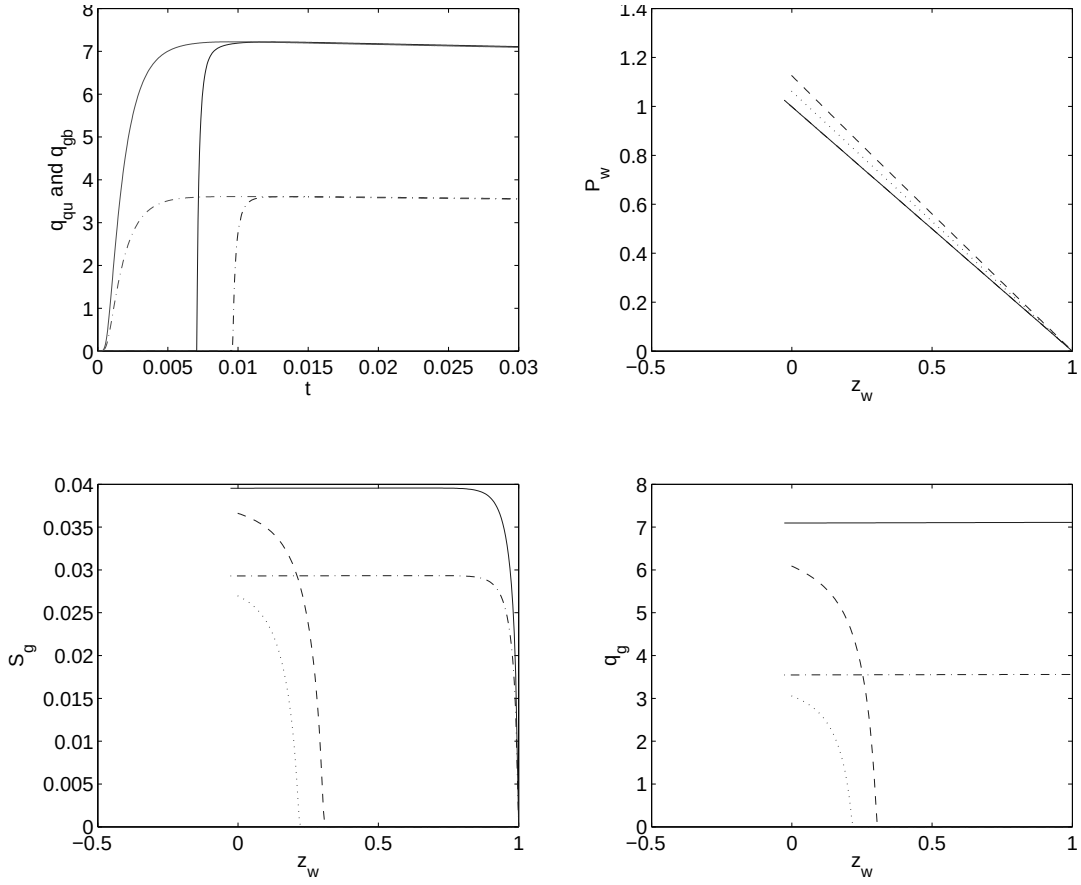

Figure 7.10: Lower boundary gas velocity q_{gb}, upper boundary gas velocity q_{gu} and moving boundary velocity $\mathrm{d}s/\mathrm{d}t$ as a function of time and profiles for water pressure P_w, gas saturation S_g and gas velocity q_g for $r_\rho = .005$ and $t = .003$ (dashed line); $r_\rho = .01$ and $t = .003$ (dotted line); $r_\rho = .005$ and $t = .03$ (solid line); $r_\rho = .01$ and $t = .03$ (dashed-dotted line). Here $B_g = 200$, $B_c = 1000$, $St = 100$ and $m = .9$.

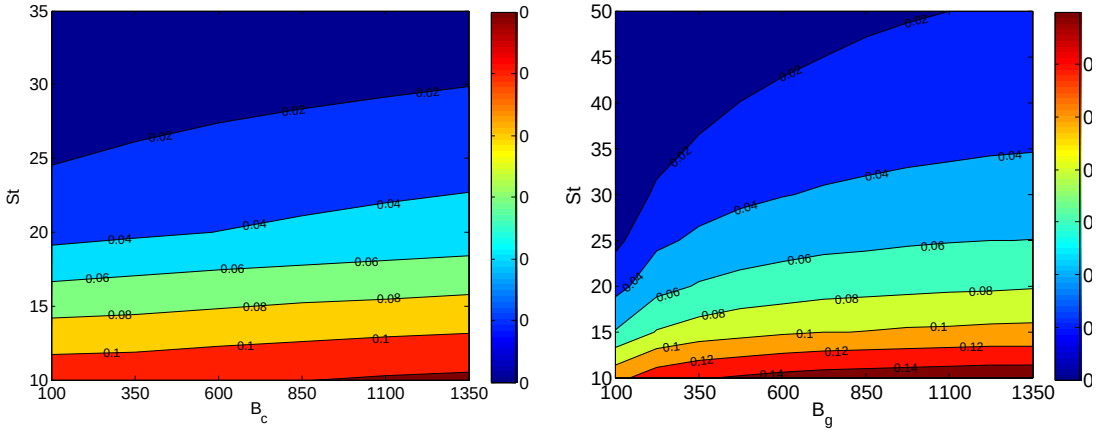

Figure 7.11: Contour plot of equation (7.84) as a function of St and B_c (left) or B_g (right). Here $B_g = 100$ (left only), $B_c = 100$ (right only), $\ell_w = 2$, $m = 0.9$, $r_\ell = \ell_w/2$, $Pe_h = .79/St$, $Pe_w = 1/St$, $b_1 = 0.05$, $b_2 = 0.97$, $c_w = 0.4$, $c_g = .02$, $c_s = 0.6$, $d_1 = 1$, $r_\mu = 300$, $\beta_w = .8$, $\epsilon = 0.5$, $\gamma = 0.5$ and $r_\rho = 0.1$.

important at early times. At steady state the total mass flow rate will be constant in space and equal to the lower boundary gas velocity, which scales with the Stefan number. Furthermore, the density ratio, r_ρ, is a measure of the gas density which decreases with deeper deposits. Since the total mass of methane in the hydrate is constant, a decrease in this ratio will cause the total volume of gas in the sediment to increase. Therefore the volume of gas released will increase with a decrease in the gas density.

7.6.3 Geophysical relevance

In the previous section we discussed some general characteristics of the dissociation problem for different parameter values corresponding to the degree of thermal forcing and sediment properties. In general the structure of *in situ* deposits may vary substantially, depending on their geographic location but here we will discuss some results for the idealized case in which this study applies. To reduce the parameter space we will set $\ell_w = 1\,\mathrm{m}$, $r_\rho = .1$ and use sediment properties corresponding to berea sandstone, which allows us to focus on the effect of

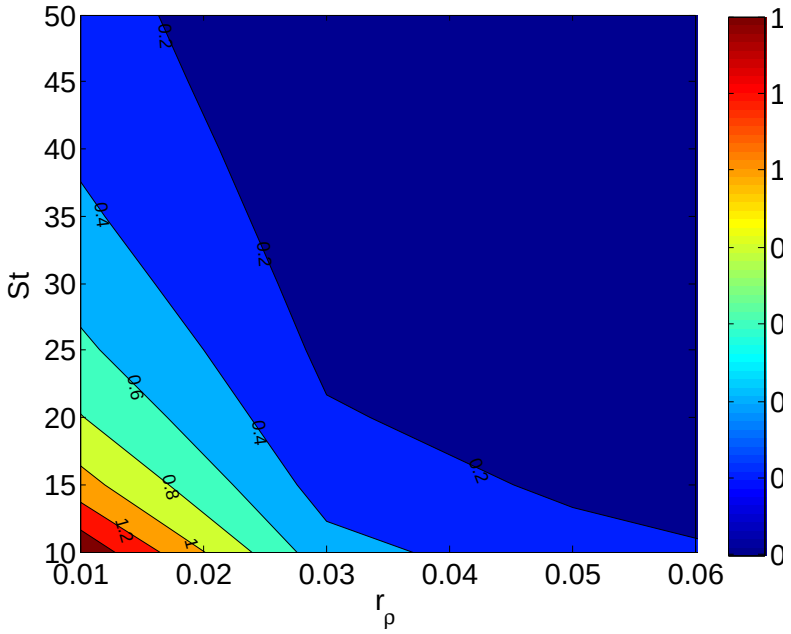

Figure 7.12: Contour plot of equation (7.84) as a function of St and r_ρ. Here $B_g = 100$, $B_c = 100$, $\ell_w = 2$, $m = 0.9$, $r_\ell = \ell_w/2$, $Pe_h = .79/St$, $Pe_w = 1/St$, $b_1 = 0.05$, $b_2 = 0.97$, $c_w = 0.4$, $c_g = .02$, $c_s = 0.6$, $d_1 = 1$, $r_\mu = 300$, $\beta_w = .8$, $\epsilon = 0.5$ and $\gamma = 0.5$

the driving temperature difference ΔT. In this case $q_{st} \approx 5 \times 10^{-8} \Delta T$, which sets the time to $t \approx 2 \times 10^7 \, \hat{t}/\Delta T$ and the filtration rate to $q_g = 5 \times 10^{-8} \Delta T \hat{q}_g$. From the figures in the previous section it would take approximately $.3/\Delta T$ yrs for the gas front to reach the upper boundary and will have a quasi-steady flow rate of $.4 \, A_s \, \Delta T \mathrm{m}^3/\mathrm{yr}$, where A_s is the surface area. For large temperature differences this result indicates that there may be a significant flux of gas entering the ocean water column from dissociating gas hydrates. In reality there may be layers of impermeable rock at some distance above the hydrate layer, which may significantly reduce the gas flow rate as well as a cyclic upper boundary temperature that may promote formation during the cool seasons, further reducing the effective gas flux over geological time scales.

7.7 Conclusion

In this Chapter we have explored gas hydrate dissociation in homogeneous porous media and the gas velocity through the sediment as a function of time for different parameter values. The governing equations corresponding to saturation, temperature and hydrate boundary evolution were solved numerically using a front-fixing scheme and exactly for a few reduced cases. The reduced models were shown to have excellent agreement with the numerical solution in the case of viscous dominated flow, using the method of characteristics, and relatively good agreement for the capillary dominated flow, using a similarity solution to a linearized form of the saturation equation. We plotted the temperature, water pressure, gas saturation and gas flow rate profiles as well as the evolution of the upper, lower and moving boundary velocities as a function of the parameter space St, B_c, B_g and r_ρ. The Stefan number, which is a measure of the thermal forcing in the system, is the dominant factor effecting the dissociation rates of the hydrate and gas velocity throughout the sediment. For small values of St the hydrate will decompose quickly, as a result of a larger degree of thermal forcing, forcing more mass through the sediment and into the ocean. The capillary number relates the importance of capillary forces to viscous forces in the sediment and has the effect of diffusing the gas released at the moving boundary to the upper surface. Therefore larger values of this parameter lead to greater gas fluxes through the sediment and a decrease in gas saturation at the moving boundary due to diffusion. The gravitational number expresses the importance of gravitational forces relative to viscous forces and tends to increase the gas velocity for large values. In addition the density ratio r_ρ determines the volume occupied by the gas at the hydrate interface and increases for deep deposits. For small values of this parameter the gas occupies a larger pore volume, which results in larger gas saturations and flow rates through the sediment. Finally, for deposits that are relatively close to the sea-floor, the volume flux of gas can be substantial for large temperature differences

and surface areas, possibly on the order of grams per year.

8

Dendrite solidification

8.1 Abstract

In this Chapter we solve the steady dendrite problem, growing into a super cooled binary fluid using slender body theory. We consider the full interfacial conditions, including curvature, binary and kinetic-under cooling effects and solve the leading order outer problem using the Wiener-Hopf technique. In the case of a pure liquid we investigate the effect of kinetic under cooling on the interface displacement and compare the results with the similarity solution of Ivantsov (1947). The method is appropriate for slender dendrites and is found to be equivalent to the similarity solution in the small Peclet number limit. The growth rate can be determined uniquely, provided the thickness of the dendrite is known at some position, rather than the radius of curvature. Furthermore we investigate the multi component case and determine the interface position and the growth velocity.

8.2 Introduction

Dendritic solidification has been a topic of considerable interest for many years since it is a phenomenon that is commonly found in many natural and industrial settings (Langer 1980). Provided a fluid is super-cooled (the temperature is below the equilibrium value) and the flux of heat is sufficiently greater than the

surface energy, perturbations of the interface will grow into needle-like structures similar to the diagram in Figure 8.1 (Davis 2001). Since the solid is constantly trying to maintain its relatively warmer equilibrium temperature, the phase boundary grows, releasing latent heat. Therefore the dendrite will increase its thickness and length with time. A single dendrite growing into an under-cooled melt was shown by Ivantsov (1947) to have a parabolic shape in the case of zero surface energy and attachment kinetics. The temperature field and surface shape are given by a similarity solution which yields a family of solutions as a function of growth velocity and radius of curvature at the tip. The similarity solution has been further studied by Horvay and Cahn (1961) and Canright and Davis (1989) in connection with different solidifying shapes.

The similarity solutions are not unique since the radius of curvature must be known (e.g. from experimental data) in order to obtain the growth velocity. This problem can be resolved by introducing curvature effects, since a length scale will be introduced into the problem. Unfortunately, the highly non-linear structure of the boundary conditions makes analytical solutions difficult to obtain in closed form and many investigators have sought to bypass this by solving the problem asymptotically for small surface energy (Xu 1991). In addition, alot of numerical work has been performed on the full problem using various techniques such as level set methods and phase field methods, which yield good agreement with theory and are capable of handling side branching (Kobayashi 1993 and Gibou et. al. 2003).

Furthermore, the formation of dendritic structures is common in binary fluids, such as saltwater systems and metal alloys, which are of interest in environmental settings and may be industrially undesirable (e.g. by weakening materials). In this case mass diffusion may play an important role since the interfacial temperature will be a function of species concentration via the phase diagram. Simple one-dimensional models have been investigated thoroughly by many authors such as Worster (2000) and Davis (2001) and extended to dendrite growth and mushy layers (reactive porous media composed of a dendritic array). Dendritic arrays have

been further analyzed by Spencer and Huppert (1995) who were able to determine the growth rate as a function of dendrite spacing.

In many dendrite solidification problems the structure of the solid may be regarded as relatively thin. Because of the small length scale compared to the extent of the ambient fluid we may attempt to solve the problem asymptotically using slender body theory. This technique has so far not been applied to a dendrite in a way that includes the full set of equations, although it has been used for etching problems (see Kuiken 1984). As a consequence of this technique, the first-order problem with respect to the outer field involves a solid of zero thickness and has a form which is amenable to the Wiener-Hopf technique (Noble 1958). This method is commonly used for the solution of half-plane diffraction problems but has been extended to the propagation of diffusion flames (Wichman and Williams 1983) and chemical etching (Kuiken 1984).

The main disadvantage of the techniques is that we cannot accurately deal with the tip of the dendrite, where the curvature is large and one must resort to a numerical treatment. On the other hand the effects of kinetic under-cooling can be included without much complication. In this Chapter we only consider the two dimensional case although it is possible to extend the method to a three dimensional axisymetric dendrite. Generally, given the appropriate conditions, the dendrite interface will be unstable, leading to the formation of side branches but we will not discuss those here (i.e. we will assume that surface energy dominates and the surface is smooth).

This Chapter is organized up as follows. In section 8.3 we present the model for a dendrite growing into a super-cooled binary melt with a constant velocity. We consider the full interfacial temperature condition, including curvature and kinetic under cooling effects and appropriately non-dimensionalize the equations. In section 8.4, we use slender body theory to replace the unknown boundary position with a line along the length of the dendrite. Furthermore we set up the Wiener-Hopf technique to be solved later. In section 8.5 we investigate the pure

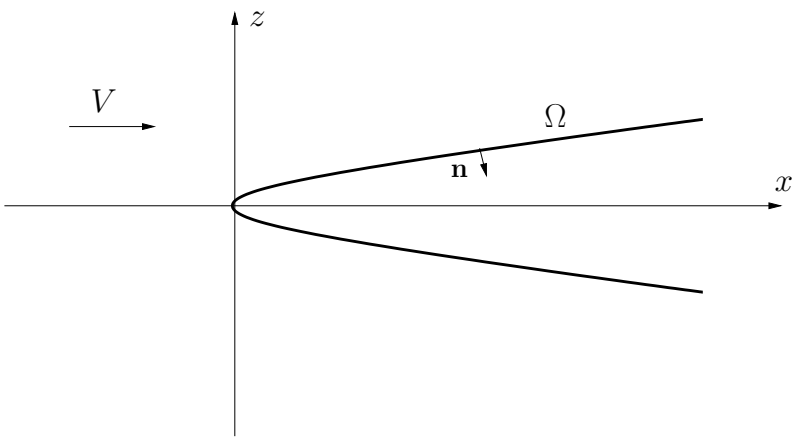

Figure 8.1: Steady state dendrite growing into an under-cooled melt.

liquid case without curvature effects and compare the results with the similarity solution found by Invantsov (1947). In addition, we examine the impact kinetic under cooling has on the interface position. In section 8.6 we solve the problem for a binary fluid and look at the effects of species related parameters such as concentration and diffusion rate. Finally, in section 8.7 we conclude.

8.3 Model description

We look for steady solutions to the dendrite problem shown in Figure 8.1 in the coordinate system moving at the speed V (provided solutions exist). The usual equations describing this problem from Davis (2001) are

$$V\frac{\partial T}{\partial x} = \kappa_\ell \nabla^2 T, \qquad \text{liquid}, \tag{8.1}$$

$$V\frac{\partial T}{\partial x} = \kappa_s \nabla^2 T, \qquad \text{solid}, \tag{8.2}$$

$$V\frac{\partial C}{\partial x} = D\nabla^2 C, \qquad \text{liquid}, \tag{8.3}$$

for temperature T and species concentration, C (note: we have used the Galilean transform $\frac{\partial}{\partial t} = V\frac{\partial}{\partial x}$). These equations represent diffusion with advection, that is an artifact of the moving reference frame. On the boundary Ω, we can use 'pill

box' arguments to express the interfacial jump conditions as

$$\rho_s L V_n = \frac{\kappa_s}{\rho_s C_{Ps}} \mathbf{n} \cdot \nabla T|_s - \frac{\kappa_\ell}{\rho_\ell C_{P\ell}} \mathbf{n} \cdot \nabla T|_\ell, \tag{8.4}$$

$$(C - C_s) V_n = -D \mathbf{n} \cdot \nabla C, \tag{8.5}$$

where κ is the thermal diffusivity, L is the latent heat, C_P is the specific heat, D is the species diffusivity, ρ is the density, C_s is the solid concentration, Ω is the location of the interface, V_n is the normal velocity of the interface and from now on we will assume that the properties are the same for the liquid and solid. The first equation is the Stefan condition and expresses the velocity of the interface in terms of the net rate of heat flux away from the interface. The second equation is the equivalent of the Stefan condition for mass diffusion. Furthermore the interfacial temperature condition is expressed as (Davis 2001)

$$T = T_m \left[1 + \frac{E_s}{L} \nabla \cdot \mathbf{n} \right] + m(C - C_m) - \frac{V_n}{\mu}, \tag{8.6}$$

where E_s is the surface energy per unit area, m, is the liquidus slope, μ is the kinetic coefficient and $\nabla \cdot \mathbf{n}$ is the curvature. This equation is essentially the liquidus curve shown in figure (8.2), modified for kinetic under-cooling and the Gibs-Thompson effect.

We can write the position of the interface for $z > 0$ in parametric form $z = \pm h(x,t)$ and then determine the unit normal to the surface from $n = \nabla(z - h)/|\nabla(z-h)| = (-h_x, 1)/\sqrt{1+h_x^2}$ at the upper surface, where we are pointing out of the solid. The curvature is determined from the divergence of the normal vector $\nabla \cdot \mathbf{n} = h_{xx}/(1+h_x^2)^{3/2}$. We can express the speed of the front normal to itself as $V_n = h_t/\sqrt{1+h_x^2} = V h_x/\sqrt{1+h_x^2}$ for the steady class of problems.

8.3.1 Non-dimensionalization

With reference to the phase diagram in Figure 8.2, the far field temperature and concentration are set to T_∞ and C_∞ respectively. The temperature of the dendrite phase boundary will be larger than T_∞, since the fluid is super-cooled and

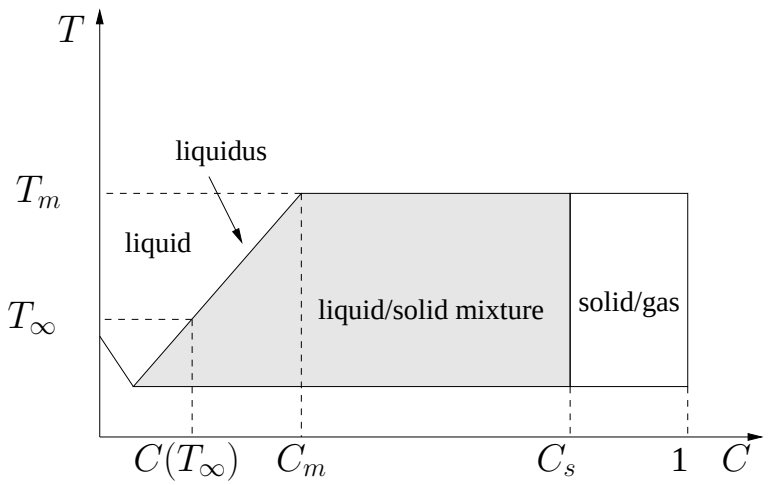

Figure 8.2: Typical phase diagram for a binary mixture of methane gas and water in which gas hydrates (solid ice-like structure) form.

will lie on the liquidus line in the case of zero surface energy and infinite kinetic coefficient. Therefore we non-dimensionalize temperature by $T = T_\infty + \theta\Delta T$ with $\Delta T = T_m - T_\infty$, concentration by $C = C_\infty + \mathscr{C}\Delta C$ with $\Delta C = C_m - C(T_\infty)$, length scales by κ/V and the interface position by $h = \delta y(x)$, where δ is a scale for the thickness of the dendrite and the liquidus slope $m = \Delta T/\Delta C$.

$$\theta_x = \theta_{xx} + \theta_{zz}, \quad \text{liquid/solid}, \tag{8.7}$$

$$\sigma\mathscr{C}_x = \mathscr{C}_{xx} + \mathscr{C}_{zz}, \quad \text{liquid}, \tag{8.8}$$

where $\sigma = \kappa/D$ is the Lewis number. At the interface $z = ay(x)$, we have in the region $z > 0$

$$Say_x = [-ay_x\theta_x + \theta_z]^s_\ell, \tag{8.9}$$

$$(\mathscr{C}_s - \mathscr{C})a\sigma y_x = -ay_x\mathscr{C}_x + \mathscr{C}_z, \tag{8.10}$$

$$\theta - 1 + \mathscr{C}_m = \mathscr{C} + \Gamma\frac{ay_{xx}}{(1 + a^2y_x^2)^{3/2}} - \bar{\mu}\frac{ay_x}{\sqrt{1 + a^2y_x^2}}, \tag{8.11}$$

and a similar set for $z < 0$. Here $\Gamma = E_sT_mV/L\Delta T\kappa$, $\bar{\mu} = V/\mu\Delta T$, $S = L/C_p\Delta T$, $a = \delta V/\kappa$ and the brackets are meant to imply solid minus liquid. In addition, as

will become clearer latter, we differentiate the Stefan condition along the surface as follows

$$\mathbf{t}\cdot\nabla\left(Say_x\right)=\mathbf{t}\cdot\nabla\left(\left[-ay_x\theta_x+\theta_z\right]_\ell^s\right), \tag{8.12}$$

where $\mathbf{t}$ is the tangent vector and $\mathbf{t}\cdot\nabla=(\partial_x, ay_x\partial_z)/\sqrt{1+a^2y_x^2}$.

8.4 Solutions

8.4.1 Long Thin Dendrites

We will assume slender body theory with $a\ll 1$ and expand in the unknown powers of a: $\theta=\theta+a\theta_1...$, $y=y+ay_1+....$ We will set $aS=O(1)$, a large Stefan number limit, but we specify the the size of $\bar{\mu}$ or Γ latter on. In many cases, such as gas hydrates, $\mathscr{C}_S\gg\mathscr{C}$, so we will take this limit in (8.10).

8.4.2 Inner Problem

We re-scale the vertical direction with $z=aZ$ in order to magnify the region surrounding the dendrite. The equations become

$$a^2\theta_x=a^2\theta_{xx}+\theta_{ZZ},\quad \text{liquid/solid}, \tag{8.13}$$

$$Sa^2y_x=\left[-a^2y_x\theta_x+\theta_z\right]_\ell^s,\quad Z=y(x), \tag{8.14}$$

$$\theta-1=\mathscr{C}-\mathscr{C}_m+\Gamma\frac{ay_{xx}}{(1+a^2y_x^2)^{3/2}}-\bar{\mu}\frac{ay_x}{\sqrt{1+a^2y_x^2}} \tag{8.15}$$

To leading order we have in the solid

$$\theta_{ZZ}=0 \tag{8.16}$$

which integrates to a constant that must be equal to zero due to the symmetry condition $\theta_Z(0)=0$. Therefore we can ignore the change in vertical temperature gradient in the solid as well as by x-diffusion. We should note that in our case the solid always has a constant concentration C_s. The problem is now in a form that is solvable by the Wiener-Hopf technique (see Noble 1958), which is the subject of the next section.

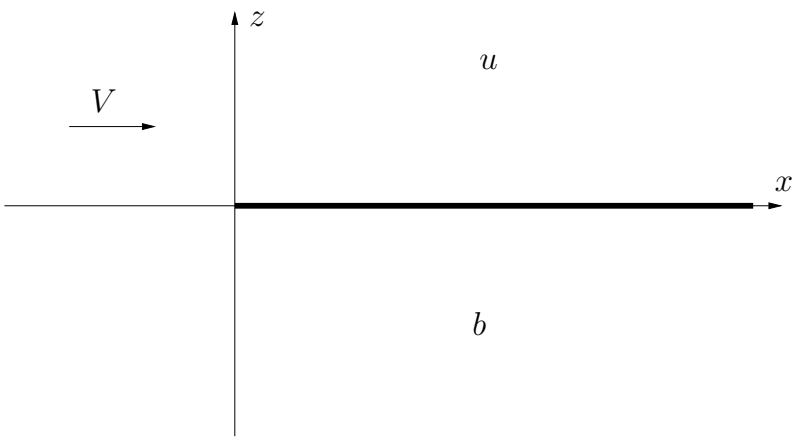

Figure 8.3: Steady-state dendrite growing into an under-cooled melt: outer problem.

8.4.3 Outer Problem:Wiener-Hopf

For the outer problem we have the following equations

$$\theta_x = \theta_{xx} + \theta_{zz}, \qquad z > 0, z < 0, \tag{8.17}$$

$$\sigma\mathscr{C}_x = \mathscr{C}_{xx} + \mathscr{C}_{zz}, \qquad z > 0, z < 0, \tag{8.18}$$

$$Say_x = -\theta_z|_u^b, \qquad z = 0, \tag{8.19}$$

$$Sa\sigma\gamma y_x = -\mathscr{C}_z|_u^b, \qquad z = 0, \tag{8.20}$$

$$\theta - 1 = -\mathscr{C}_m + \mathscr{C} + \alpha\theta_z|_u^b - \beta\theta_{xz}|_u^b, \quad z = 0, \tag{8.21}$$

where $\gamma = \mathscr{C}_S/S$, $\alpha = \bar{\mu}/S$, $\beta = \Gamma/S$, u denotes upper (positive gradient), b denotes bottom (negative gradient) and the dendrite is now a line along the positive x-axis shown in Figure 8.3. Equations (8.19) and (8.20) can be combined to obtain a flux condition

$$\sigma\gamma\theta_z(x,0) = \mathscr{C}_z(x,0). \tag{8.22}$$

We split the upper (denoted u) and lower half (denoted b) of the domain shown in Figure 8.3 as follows

$$\frac{\partial \theta_u}{\partial x} = \frac{\partial^2 \theta_u}{\partial x^2} + \frac{\partial^2 \theta_u}{\partial z^2} \quad -\infty < x < \infty \quad z \geq 0 \tag{8.23}$$

$$\frac{\partial \theta_b}{\partial x} = \frac{\partial^2 \theta_b}{\partial x^2} + \frac{\partial^2 \theta_b}{\partial z^2} \quad -\infty < x < \infty \quad z \leq 0 \tag{8.24}$$

$$\sigma \frac{\partial \mathscr{C}_u}{\partial x} = \frac{\partial^2 \mathscr{C}_u}{\partial x^2} + \frac{\partial^2 \mathscr{C}_u}{\partial z^2} \quad -\infty < x < \infty \quad z \geq 0 \tag{8.25}$$

$$\sigma \frac{\partial \mathscr{C}_b}{\partial x} = \frac{\partial^2 \mathscr{C}_b}{\partial x^2} + \frac{\partial^2 \mathscr{C}_b}{\partial z^2} \quad -\infty < x < \infty \quad z \leq 0 \tag{8.26}$$

with the far field conditions of boundedness

$$(\theta_u, \theta_b, \mathscr{C}_u, \mathscr{C}_b) \to 0 \quad \text{as } z \to \infty \text{ or } x \to -\infty, \tag{8.27}$$

and the intrfacial temperature on the upper and lower side of the dendrite are

$$\theta_u = 1 - \mathscr{C}_m + \mathscr{C} - \alpha \frac{\partial \theta_u}{\partial z} + \beta \frac{\partial^2 \theta_u}{\partial x \partial z}, \tag{8.28}$$

$$\theta_b = 1 - \mathscr{C}_m + \mathscr{C} + \alpha \frac{\partial \theta_b}{\partial z} - \beta \frac{\partial^2 \theta_b}{\partial x \partial z}, \tag{8.29}$$

By taking the Fourier transform in x defined by

$$\hat{\theta}(k, z) = \int_{-\infty}^{\infty} \theta(x, z) \mathrm{e}^{ikx} dx, \tag{8.30}$$

$$\theta(x, z) = \frac{1}{2\pi} \int_{-\infty}^{\infty} \hat{\theta}(k, z) \mathrm{e}^{-ikx} dk, \tag{8.31}$$

we have the following transformed problem

$$\frac{\partial^2 \hat{\theta}_u}{\partial z^2} - \hat{\theta}_u k(k - i) = 0, \qquad \hat{\theta}_u(k, \infty) = 0, \tag{8.32}$$

$$\frac{\partial^2 \hat{\theta}_b}{\partial z^2} - \hat{\theta}_b k(k - i) = 0, \qquad \hat{\theta}_b(k, -\infty) = 0, \tag{8.33}$$

$$\frac{\partial^2 \hat{\mathscr{C}}_u}{\partial z^2} - \hat{\mathscr{C}}_u k(k - \sigma i) = 0, \qquad \hat{\mathscr{C}}_u(k, \infty) = 0, \tag{8.34}$$

$$\frac{\partial^2 \hat{\mathscr{C}}_b}{\partial z^2} - \hat{\mathscr{C}}_b k(k - \sigma i) = 0, \qquad \hat{\mathscr{C}}_b(k, -\infty) = 0, \tag{8.35}$$

with the following equations along the strip, $z = 0$

$$\frac{\partial \hat{\theta}_u^-}{\partial z} = \frac{\partial \hat{\theta}_b^-}{\partial z}, \qquad \hat{\theta}_u^- = \hat{\theta}_b^-, \tag{8.36}$$

$$\frac{\partial \hat{\theta}_u^+}{\partial z} = -\frac{\partial \hat{\theta}_b^+}{\partial z}, \qquad \hat{\theta}_u^+ = \hat{\theta}_b^+, \tag{8.37}$$

$$\frac{\partial \hat{\mathscr{C}}_u^-}{\partial z} = \frac{\partial \hat{\mathscr{C}}_b^-}{\partial z}, \qquad \hat{\mathscr{C}}_u^- = \hat{\mathscr{C}}_b^-, \tag{8.38}$$

$$\frac{\partial \hat{\mathscr{C}}_u^+}{\partial z} = -\frac{\partial \hat{\mathscr{C}}_b^+}{\partial z}, \qquad \hat{\mathscr{C}}_u^+ = \hat{\mathscr{C}}_b^+, \tag{8.39}$$

$$\hat{\theta}_u^+ = \hat{\mathscr{C}}_u^+ - \frac{i(1-\mathscr{C}_m)}{k+i\epsilon} - \frac{\partial \hat{\theta}_u^+}{\partial z}(\alpha + ik\beta) - \beta \frac{\partial \theta_u}{\partial z}\bigg|_{x=0}, \tag{8.40}$$

$$\hat{\theta}_b^+ = \hat{\mathscr{C}}_b^+ - \frac{i(1-\mathscr{C}_m)}{k+i\epsilon} + \frac{\partial \hat{\theta}_b^+}{\partial z}(\alpha + ik\beta) + \beta \frac{\partial \theta_b}{\partial z}\bigg|_{x=0}. \tag{8.41}$$

Here the superscripts $(+)$ and $(-)$ denote functions that are analytic in the upper and lower planes respectively and we have represented 1 by $\mathrm{e}^{-\epsilon x}$ where we take $\epsilon = 0^+$ at some latter point in the analysis. The second condition is a physical result that comes from symmetry. The general solution to the above differential equations is

$$\hat{\theta}_u = C_1 \mathrm{e}^{-z\sqrt{k(k-i)}}, \qquad \hat{\theta}_b = C_2 \mathrm{e}^{z\sqrt{k(k-i)}}. \tag{8.42}$$

$$\hat{\mathscr{C}}_u = C_3 \mathrm{e}^{-z\sqrt{k(k-\sigma i)}}, \qquad \hat{\mathscr{C}}_b = C_4 \mathrm{e}^{z\sqrt{k(k-\sigma i)}}. \tag{8.43}$$

where we have used the boundary conditions at infinity. We cut the k-plane for θ along the imaginary axis from i to $i\infty$ and from 0^- to $-i\infty$ so that $\mathrm{Re}(\sqrt{k(k-1)}) \geq 0$ outside of the cuts. For $\mathscr{C}$ we cut along the imaginary axis from $i\sigma$ to $i\infty$ and from 0^- to $-i\infty$.

The Wiener-Hopf procedure is then to split the conditions at $z = 0$ in terms of plus $(+)$ and minus $(-)$ functions in order to determine the constants

$C_1 - C_4$. We can combine equations (8.40)–(8.42) to get the following

$$\frac{\partial \hat{\theta}_u^+}{\partial z} + \frac{\partial \hat{\theta}_u^-}{\partial z} + \sqrt{k(k-i)}\left(\hat{\mathscr{C}}_u^+ - \mathscr{C}_m\right) = -\sqrt{k(k-i)}\left[-\frac{i}{k+i\epsilon} - \frac{\partial \hat{\theta}_u^+}{\partial z}(\alpha + ik\beta) + \hat{\theta}_u^-\right] + \sqrt{k(k-i)}\beta \left.\frac{\partial \theta_u}{\partial z}\right|_{x=0}, \quad (8.44)$$

$$\frac{\partial \hat{\theta}_b^+}{\partial z} + \frac{\partial \hat{\theta}_b^-}{\partial z} - \sqrt{k(k-i)}\left(\hat{\mathscr{C}}_b^+ - \mathscr{C}_m\right) = \sqrt{k(k-i)}\left[-\frac{i}{k+i\epsilon} + \frac{\partial \hat{\theta}_b^+}{\partial z}(\alpha + ik\beta) + \hat{\theta}_b^-\right] + \sqrt{k(k-i)}\beta \left.\frac{\partial \theta_u}{\partial z}\right|_{x=0}, \quad (8.45)$$

which may be subtracted to get

$$\frac{\partial \hat{\theta}_u^+}{\partial z}\left(1 - \alpha\sqrt{k(k-i)}\right) = \sqrt{k(k-i)}\left(\frac{i(1-\mathscr{C}_m)}{k+i\epsilon} - \hat{\theta}_u^+ - \hat{\mathscr{C}}_u^+\right), \quad (8.46)$$

In addition, by eliminating the constants in equations (8.43), we obtain the following

$$\frac{\partial \hat{\mathscr{C}}_u^+}{\partial z} + \frac{\partial \hat{\mathscr{C}}_u^-}{\partial z} = -\sqrt{k(k-\sigma i)}\left(\hat{\mathscr{C}}_u^+ + \hat{\mathscr{C}}_u^-\right), \quad (8.47)$$

$$\frac{\partial \hat{\mathscr{C}}_b^+}{\partial z} + \frac{\partial \hat{\mathscr{C}}_b^-}{\partial z} = \sqrt{k(k-\sigma i)}\left(\hat{\mathscr{C}}_b^+ + \hat{\mathscr{C}}_b^-\right), \quad (8.48)$$

which may be subtracted and combined with equation (8.22) to obtain

$$-\hat{\mathscr{C}}_u^+ = \frac{\sigma\gamma}{\sqrt{k(k-i)}}\frac{\partial \hat{\theta}_u^+}{\partial z} + \hat{\mathscr{C}}_u^-, \quad (8.49)$$

an expression for the interfacial species concentration. Combining equations (8.46) and (8.49) we have

$$\frac{\partial \hat{\theta}_u^+}{\partial z}\alpha K(k) = -\frac{i(1-\mathscr{C}_m)}{k+i\epsilon} + \hat{\theta}_u^- + \hat{\mathscr{C}}_u^- + \frac{\beta}{2}\left(\frac{\partial \theta_b}{\partial z} - \frac{\partial \theta_u}{\partial z}\right)\Bigg|_{x=0}, \quad (8.50)$$

where

$$K(k) = 1 - \frac{\alpha^{-1}}{\sqrt{k(k-i)}} + \frac{\sigma\gamma/\alpha}{\sqrt{k(k-i\sigma)}} + ik\frac{\Gamma}{\bar{\mu}} = K^+(k)K^-(k), \quad (8.51)$$

The functions K^+ and K^- are analytic in the upper and lower half planes respectively, and may be obtained by inspection or from the general procedure of Noble

(1988). Equation (8.50) can now be re-written, for small surface energy (i.e. $\beta = 0$ and $\Gamma/\bar{\mu} = 0$) as

$$\alpha \frac{\partial \hat{\theta}_u^+}{\partial z} K^+(k) + \left[\frac{(1 - \mathscr{C}_m) i}{K^-(-i\epsilon)(k + i\epsilon)} \right]_+ = \frac{\hat{\theta}_u^- + \hat{\mathscr{C}}_u^-}{K^-(k)} + \left[\frac{-i(1 - \mathscr{C}_m)}{K^-(k)(k + i\epsilon)} + \frac{i(1 - \mathscr{C}_m)}{K^-(-i\epsilon)(k + i\epsilon)} \right]_- = P_L. \tag{8.52}$$

Both sides are functions analytic in the upper (+) and lower half planes (+). As $k \to \infty$ along the positive real axis we assume that the second term goes to zero, which can be verified after we obtain the solution, and therefore from the Louville's theorem $P_L = 0$.

8.5 Pure liquid

For a pure liquid the melting temperature has a constant equilibrium value ($\mathscr{C}_m = 0$) and the solid must also be pure ($\mathscr{C}_s = 0$).

8.5.1 Isothermal solid

In this case equation (8.51) reduces to $K(k)\alpha = -1/\sqrt{k(k-i)} = K^+K^-$ where $K^+ = \alpha^{-1}\sqrt{k}$ and $K^- = -1/\sqrt{k-i}$. Now equation (8.52) may be written as

$$\frac{\partial \hat{\theta}_u^+}{\partial z} \left[\frac{1}{\sqrt{k}} \right]_+ - \left[\frac{i\sqrt{-i\epsilon - i}}{k + i\epsilon} \right]_+ = 0, \tag{8.53}$$

$$\left[\frac{i\sqrt{k-i}}{k + i\epsilon} - \frac{i\sqrt{-i\epsilon - i}}{k + i\epsilon} \right]_- - \hat{\theta}_u^- \left[\sqrt{k-i} \right]_- = 0. \tag{8.54}$$

Now we can combine these equations with equations (8.40) and (8.41) to obtain

$$\frac{\partial \hat{\theta}_u^+}{\partial z} = \frac{\sqrt{1+\epsilon}\,\sqrt{k}\;i\sqrt{-i}}{k+i\epsilon}, \tag{8.55}$$

$$\hat{\theta}_u^- + \hat{\theta}_u^+ = -\frac{i\sqrt{-i}\sqrt{1+\epsilon}}{(k+i\epsilon)\sqrt{k-i}} = C_1, \tag{8.56}$$

which are the temperature and vertical temperature gradient along the phase boundary $z = 0$. With the aid of the inverse transform equation (8.55) can be expressed as

$$\frac{\partial \theta_u}{\partial z} = \frac{\sqrt{1+\epsilon}}{2\pi} \int_{-\infty}^{\infty} \frac{i\sqrt{k}\sqrt{-i}}{k+i\epsilon} \mathrm{e}^{-ikx} \mathrm{d}k, \tag{8.57}$$

For $\epsilon = 0$ we can solve this integral by using a key hole contour with a loop around the brunch cut along the positive real axis to obtain

$$\frac{\partial \theta_u}{\partial z} = \frac{1}{2\pi} \int_0^{\infty} \frac{\mathrm{e}^{-\nu x}}{\sqrt{\nu}} \mathrm{d}\nu = \frac{-1}{\sqrt{\pi x}}, \tag{8.58}$$

where we have made use of the transformation $k = -i\nu$

Combining equations (8.42) and (8.56) and using the inverse transform the temperature in the upper half plane can be expressed as

$$\theta_u = \frac{i\sqrt{-i}\sqrt{1+\epsilon}}{2\pi} \int_{-\infty}^{\infty} \frac{\mathrm{e}^{-\sqrt{k(k-i)}z - ikx}}{(k+i\epsilon)\sqrt{k-i}}\, \mathrm{d}k, \tag{8.59}$$

for the entire liquid domain. With $\epsilon = 0$ this equation can be solved following Wichman and Williams (1982) by introducing the polar coordinates $x = -r\cos(\phi)$, $z = r\sin(\phi)$ $(0 \leq \phi \leq \pi)$, where $r = \sqrt{z^2 + x^2}$ and $\phi = \tan^{-1}(-z/x)$. The solution is

$$\theta_u = \mathrm{erfc}\left(\sqrt{\frac{r-x}{2}}\right), \tag{8.60}$$

and has the expected error function solution from self similarity (Horvay and Cahn 1961).

Results

From the Stefan condition, equation (8.19) we can integrate equation (8.58) to obtain

$$y = \frac{2}{Sa\sqrt{\pi}}\sqrt{x} + c_1, \tag{8.61}$$

where c_1 is determined form the near nose region but for the leading order displacement we can apply the condition $y(0) = 0$ and therefore $c_1 = 0$. This solution is essentially unavoidable since there is no length scale in the system and could be determined from similarity. If we recast this equation in dimensional form we can obtain a family of solutions for the growth rate as a function of the dendrite thickness

$$V = \frac{16\kappa}{S^2\pi}\frac{x}{h^2}. \tag{8.62}$$

Provided we know the ratio x/h^2 from experiments or a numerical solution we can find the velocity V as a function of the thermal diffusivity of the liquid and the Stefan number. Therefore from this expression we can see that the growth velocity increases if heat can be diffused more rapidly or if the temperature gradient is increased. Furthermore we can obtain an expression for the normal velocity in dimensional form as

$$V_n = \frac{4\sqrt{\kappa V}}{S\sqrt{\pi x}}. \tag{8.63}$$

The solution should be compared against the result of Ivantsov (1947), which yields a solution in terms of the experimentally determined radius of curvature of the tip.

Comparison with the similarity solution

We can compare our result with the similarity solution of Ivantsov (1947), in which the interface position is given by (see Horvay and Cahn 1961)

$$y = \frac{2\sqrt{P}}{a}\sqrt{P + x}, \tag{8.64}$$

where $P = VR/2\kappa$ is the Peclet number, R is the radius of curvature at the tip and P is determined form

$$S^{-1} = \sqrt{\pi P}\, \mathrm{e}^{P}\, \mathrm{erfc}(P). \tag{8.65}$$

For large x we can combine equations 8.61 and 8.64 to obtain an expression for P,

$$\sqrt{\pi P} = S^{-1}, \tag{8.66}$$

which is equal to equation 8.65 in the limit of a small Peclet number. Since P decreases with the radius of curvature, our solution is approximately equivalent to the similarity solution for slender dendrites, which is in accordance with our assumption.

8.5.2 Kinetic under-cooling included

Here we solve for the vertical flux along the dendrite surface with the effect of kinetic under-cooling included ($\alpha \neq 0$). In order to do this we first need to obtain the analytic functions K^+ and K^- by using the general splitting technique discussed in Noble (1988)

Splitting

In general the functions analytic in the upper and lower half plane in equation (8.51) are

$$K^-(k) = \exp\left[\frac{1}{2\pi i}\int_{id-\infty}^{id+\infty} \frac{\ln K(\xi)}{k-\xi}\mathrm{d}\xi\right], \tag{8.67}$$

$$K^+(k) = \exp\left[\frac{1}{2\pi i}\int_{ic-\infty}^{ic+\infty} \frac{\ln K(\xi)}{\xi-k}\mathrm{d}\xi\right], \tag{8.68}$$

where $0 < c < \mathrm{Im}(k) < d < i$ and we can imagine a rectangle in the complex plane where the two functions are analytic. We can solve equation (8.68) by closing the contour in the lower half plane with a loop around the cut that extends from 0 to $i\infty$. We do not include the simple pole at $\xi = k$, where it is within the strip

of analycity since it lies outside our contour. With the substitution $\xi = -iu$ and $k = -i\gamma$ we have

$$\ln K^+ = \frac{1}{2\pi i}\int_0^\infty \left[\log\left(1 + i\frac{\alpha^{-1}}{\sqrt{u(u+1)}}\right) - \log\left(1 - i\frac{\alpha^{-1}}{\sqrt{u(u+1)}}\right)\right]\frac{\mathrm{d}u}{u-\gamma}, \tag{8.69}$$

With the well known trigonometric identity $\arctan(z) = [\log(1-iz) - \log(1+iz)]\, i/2$ this integral is

$$\ln K^+ = \frac{1}{\pi}\int_0^\infty \arctan\left[\frac{\alpha^{-1}}{\sqrt{u(u+1)}}\right]\frac{\mathrm{d}u}{u-\gamma}, \tag{8.70}$$

where u represents a purely real variable. By integrating this integral by parts and substituting in the variable $y = \sqrt{u(u+1)}$ we get

$$\ln K^+ + \frac{1}{2}\log(-\gamma) = \frac{\alpha^{-1}}{\pi}\int_0^\infty \frac{\log\left(-1/2 - \gamma + \sqrt{1+4y^2}/2\right)}{y^2 + \alpha^{-2}}\,\mathrm{d}y = f. \tag{8.71}$$

For small α the second term integrates to zero and we are left with the separations found by inspection in section (8.5.1).

Determination of the vertical gradient

From equation (8.52) and the inverse Fourier transform we have

$$\theta_z = \frac{1}{2\pi}\int_{-\infty}^\infty \frac{-i\alpha^{-1}}{K^-(0)}\frac{K^-(k)}{K(k)k}\exp^{-ikx}\,\mathrm{d}k, \tag{8.72}$$

along the interface, where we are using the minus function for reasons that will be apparent latter. If we close the contour in the lower half plane, where $K^-(k)$ is analytic we loop around the branch cut from 0 to $-i\infty$ and express the integral as

$$\theta_z = \frac{-\alpha^{-2}}{\pi K^-(0)}\int_0^\infty \frac{K^-(\gamma)\exp(-\gamma x)}{\sqrt{\gamma(\gamma+1)} + \frac{\alpha^{-2}}{\sqrt{\gamma(\gamma+1)}}}\,\frac{\mathrm{d}\gamma}{\gamma}, \tag{8.73}$$

where γ is purely a real variable. From equation (8.71) and $K = K^-K^+$ we have the following

$$\theta_z = \frac{1}{\pi}\int_0^\infty \frac{\left[i\alpha\sqrt{\gamma(\gamma+1)} - 1\right]}{\alpha^2\gamma^{3/2}(\gamma+1) + \gamma^{1/2}}\,\mathrm{e}^{-\gamma x - f + f_o}\,\mathrm{d}\gamma, \tag{8.74}$$

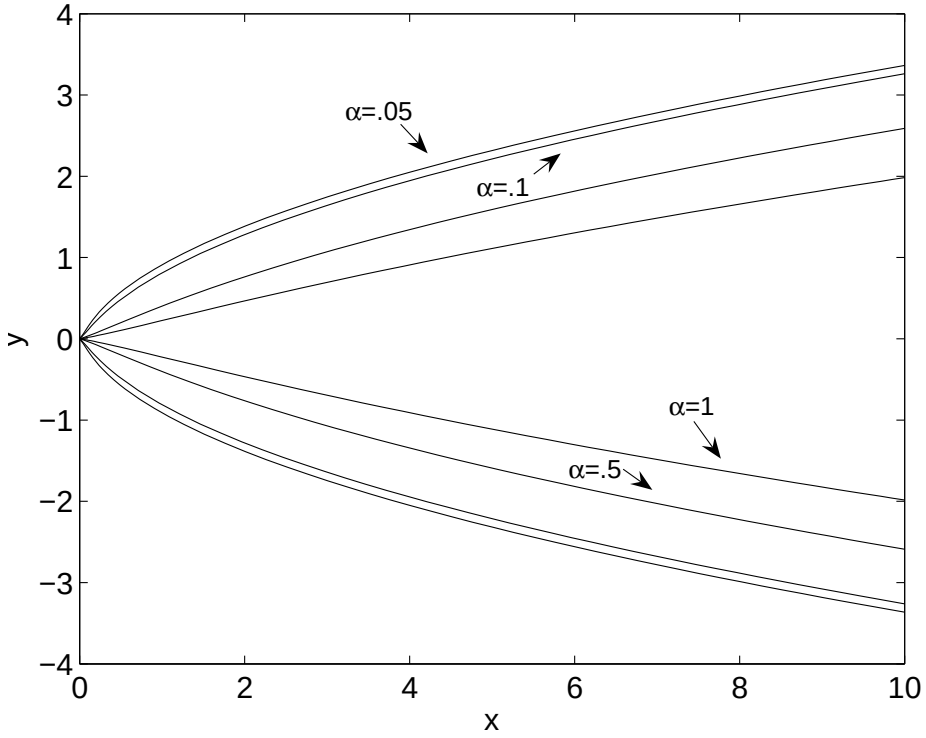

Figure 8.4: Interface position y from equation (8.76) and (8.74) as a function of x for $\alpha = .05, .1, .5, 1$ and with $Sa = 1$.

in which case we take the real part of the integral and f_o is f evaluated at $\gamma = 0$. Note: f_0 is a real number as a function of α and f will in general be complex. We can gain some understanding of the nature of this integral by examining the behavior far from the origin. In this case it can be shown that $-\gamma x >> f_0 - f$ and now we can obtain an asymptotic solution using Watson's Lemma (See Bender and Orszag). By expanding the product multiplying the exponential we have the solution as $x \to \infty$

$$\theta_z = \frac{-1}{\sqrt{\pi x}} + \frac{\alpha^2}{2\sqrt{\pi}\, x^{3/2}} - \frac{3(\alpha^4 - \alpha^2)}{4\sqrt{\pi}\, x^{5/2}} + ... \tag{8.75}$$

From this result we can see that as x increases or α decreases the isothermal solution is obtained.

We have plotted the interface position

$$Say = -\int \theta_z \, \mathrm{d}x + C_1, \tag{8.76}$$

in Figure 8.4 as a function of α, where $y(0) = 0$ for the first order displacement. When the effect of kinetic under-cooling is large the temperature along the interface is depressed, resulting in a slower growth speed. As a result the phase boundary will melt back. It is interesting to not that the parabolic profile is no longer obtained near the nose although for large distance this solution is the same as the isothermal case.

From equation (8.75) we know that the temperature gradient for large x is asymptotically equivalent to the isothermal case since the surface slope decreases in this region. With reference to the Stefan condition, the normal velocity must also be approximately equivalent here. Therefore we can express the growth velocity as

$$V = \frac{16\kappa}{S^2\pi} \frac{1}{x h_x^2}, \tag{8.77}$$

which is independent of the kinetic under-cooling parameter α. With this relationship the velocity has a family of solutions for the surface slope, which could be obtained experimentally.

8.5.3 Vanishing x-diffusion

Since heat is dissipating from the solid into a large body of fluid that lies above and below the x-axis, we expect vertical diffusion to dominate diffusion in the horizontal direction, except near the nose. Neglecting this term the equations reduce to

$$\theta_x = \theta_{zz}, \quad z > 0, \quad z < 0, \tag{8.78}$$

$$Say_x = -\theta_z, \quad z = 0, \tag{8.79}$$

$$\theta = 1 - \alpha\theta_z, \quad z = 0. \tag{8.80}$$

The boundary conditions in this case are

$$\theta(0,z)=0, \tag{8.81}$$

$$\theta(x,\infty)=0, \tag{8.82}$$

where the first condition arises from the solution in the region $x<0$. The set of equations can be solved by Laplace-transforms defined as

$$\hat{\theta}(s,z)=\int_0^\infty \theta(x,z)(e)^{-sx}dx, \tag{8.83}$$

$$\theta(x,z)=\frac{1}{2\pi i}\int_{c-i\infty}^{c+i\infty}\hat{\theta}(s,z)\mathrm{e}^{sx}ds. \tag{8.84}$$

The transformed equations are

$$\hat{\theta}_{zz}=s\hat{\theta}, \tag{8.85}$$

$$\hat{\theta}(s,\infty)=0, \tag{8.86}$$

$$\hat{\theta}(s,0)=\frac{1}{s}-\alpha\hat{\theta_z}, \tag{8.87}$$

with the solution

$$\hat{\theta}=\frac{\mathrm{e}^{-\sqrt{s}z}}{s\left(1-\alpha\sqrt{s}\right)}, \tag{8.88}$$

$$\theta=\frac{1}{2\pi i}\int_{c-i\infty}^{c+i\infty}\frac{\mathrm{e}^{-\sqrt{s}z}}{s\left(1-\alpha\sqrt{s}\right)}\mathrm{e}^{sx}ds. \tag{8.89}$$

Differentiating equation (8.89) with respect to z, we have the following reduced equation along the interface

$$\theta_z(0,x)=-\frac{1}{2\pi i}\int_{c-i\infty}^{c+i\infty}\frac{\mathrm{e}^{sx}}{\sqrt{s}}\,\mathrm{d}s-\frac{\alpha}{2\pi i}\int_{c-i\infty}^{c+i\infty}\frac{\mathrm{e}^{sx}}{1-\alpha\sqrt{s}}\,\mathrm{d}s, \tag{8.90}$$

where we have used a partial fraction expansion and the linearity property of the inverse Laplace transform. The first integral can be evaluated by deforming the contour around the left half plane with a loop around the branch point at $s=0$ and the negative real axis. For the second integral we can use the same contour, where the pole at $s=1/\alpha^2$ an be neglected since it lies outside the contour. Therefore

$$\begin{aligned}\theta_z(0,x)=&-\frac{1}{\sqrt{\pi x}}+\frac{\alpha^2}{\pi}\int_0^\infty \mathrm{e}^{-rx}\frac{\sqrt{r}}{1+\alpha^2 r}\mathrm{d}r=\\ &-\frac{1}{\sqrt{\pi x}}+\frac{1}{8\sqrt{\pi x}}\mathrm{e}^{x/2\alpha^2}D_{-2}\left(\frac{\sqrt{2x}}{\alpha}\right),\end{aligned} \tag{8.91}$$

where D_{-2} is the parabolic cylinder function defined as (see Abromowitz and Stegun)

$$D_{-2}(p) = \mathrm{e}^{p^2/4}\sqrt{\frac{\pi}{2}}\left[\sqrt{\frac{\pi}{2}}\mathrm{e}^{-p^2/2} - p\,\mathrm{erfc}\left(\frac{p}{\sqrt{2}}\right)\right]. \tag{8.92}$$

We have the solution as $x \to \infty$

$$\theta_z = \frac{-1}{\sqrt{\pi x}} + \frac{\alpha^2}{2\sqrt{\pi}\,x^{3/2}} - \frac{3\alpha^4}{4\sqrt{\pi}\,x^{5/2}} + ... \tag{8.93}$$

We can determine the temperature profiles by manipulating equation (8.89) as follows

$$\theta + \alpha\theta_z = \frac{1}{2\pi i}\int_{c-i\infty}^{c+i\infty}\frac{\mathrm{e}^{sx-\sqrt{s}z}}{s}\mathrm{d}s. \tag{8.94}$$

The contour integral can be completed by deforming the contour onto the left half plane with a loop around the branch cut along the negative real line and a pole at the origin. The resultant first order ode is

$$\theta + \alpha\theta_z = \mathrm{erfc}\left(\frac{z}{2\sqrt{x}}\right). \tag{8.95}$$

This can be solved using an integrating factor $(\mathrm{e}^{z/\alpha}/\alpha)$ to obtain

$$\theta = \mathrm{erfc}\left(\frac{z}{2\sqrt{x}}\right) + \mathrm{e}^{x/\alpha^2 - z/\alpha}\left[\mathrm{erf}\left(\frac{z}{2\sqrt{x}} - \frac{\sqrt{x}}{\alpha}\right) + \mathrm{erf}\left(\frac{\sqrt{x}}{\alpha}\right)\right] - \alpha\theta_z(0,x). \tag{8.96}$$

In Figure 8.5 we have plotted the vertical temperature gradient θ_z from the Wiener-Hopf formulation equation (8.74), the asymptotic solution for large x equation (8.75) and the solution for vanishing x-diffusion equation (8.91). As we expect none of the solutions are equivalent near $x = 0$ since we expect horizontal diffusion to be important in this area.

8.6 Binary substance

Here we retain all the terms related to species such as $\mathscr{C}_m$, σ, γ, and etc. and solve for the flux, temperature and concentration using the same techniques

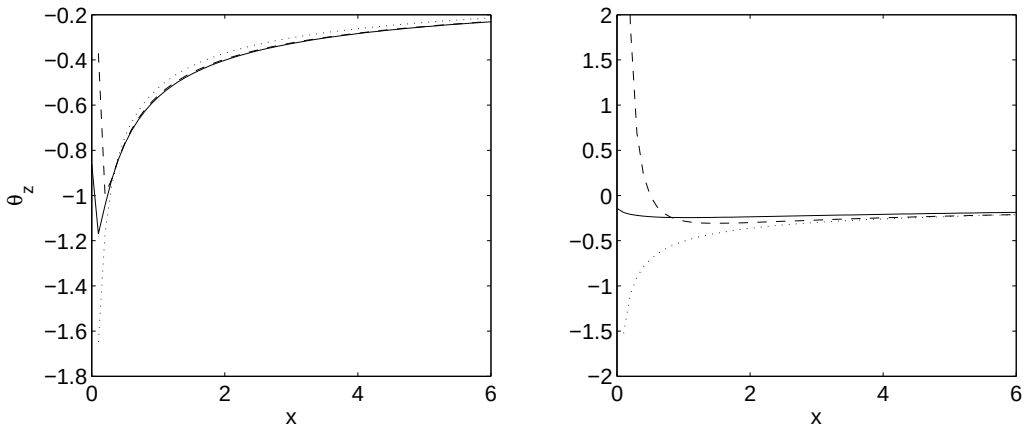

Figure 8.5: θ_z as a function of x for $\alpha = .1$ (left) and $\alpha = 1$ (right) for equation 8.74 (solid line), equation 8.91 (dotted line) and equation 8.75 (dashed line).

as the previous section on a pure liquid. To be consistent we take $\Gamma/\bar{\mu} \ll 1$ so that curvature effects can be ignored although this will not be the case near the tip, where the slope $y_x \gg 1$.

8.6.1 Wiener-Hopf

For the zero kinetic under-cooling case ($\alpha = 0$) the shape will be controlled by the rate of diffusion of heat relative to solute. The (+) and minus (−) functions are $K^+ = \alpha^{-1}\sqrt{k}$ and $K^- = \sigma\gamma/\sqrt{k - i\sigma} - 1/\sqrt{k - i}$ respectively. On using equation (8.52) and the inverse transform with $\epsilon = 0$, we have the following integral

$$\frac{\partial \theta_u}{\partial z} = -\mathscr{B}\sqrt{i}\,\frac{1}{2\pi}\int_{-\infty}^{\infty} \frac{\mathrm{e}^{-ikx}}{\sqrt{k}}\mathrm{d}k, \tag{8.97}$$

where k is still an imaginary number and $\mathscr{B} = (1 - \mathscr{C}_m)/(1 - \sigma^{1/2}\gamma)$. The solution is of the same form as the pure case:

$$\frac{\partial \theta_u}{\partial z} = \frac{2\mathscr{B}}{\sqrt{\pi x}}, \tag{8.98}$$

Furthermore, the species flux is given by

$$\frac{\partial \mathscr{C}_u}{\partial z} = \frac{2\mathscr{B}\sigma\gamma}{\sqrt{\pi x}}. \tag{8.99}$$

From this equation the normal velocity and interface position as a function of x are given from equation (8.19) to be

$$Say_x = \frac{2\mathscr{B}}{\sqrt{\pi x}}, \tag{8.100}$$

$$Say = 4\mathscr{B}\frac{x^{1/2}}{\sqrt{\pi}}. \tag{8.101}$$

From this we can express the growth rate as

$$V = V_{iso}\mathscr{B}^2 = \frac{16\kappa(1-\mathscr{C}_m)^2}{\pi(S-\mathscr{C}_s\sigma^{1/2})^2}\frac{x}{h^2}, \tag{8.102}$$

where V_{iso} is the velocity for the isothermal case and x is dimensional. The important result here is that although the profile is parabolic it will have a thickness that is dependent on the chemical properties. For a fixed temperature scale and variable far field concentration, the largest velocity will occur when $C_\infty = C_m$, the maximum concentration. Alternatively no growth is possible if $C_\infty = C(T_\infty)$, the liquidus concentration since there would be no flux of mass to the interface. Furthermore, the growth velocity increases when the Stefan number decreases for the usual reasons and when $\mathscr{C}_s$ decreases; hydrate concentration is small relative to the concentration scale.

In the limit of a large Lewis number (i.e. the species diffusion is infinite), the concentration field will be approximately constant and the velocity reduces to the isothermal case, provided $\mathscr{C}_m = 0$. On the other hand in the limit of a small Lewis number the velocity is approximately

$$V = \frac{16D(1-\mathscr{C}_m)^2}{\pi\mathscr{C}_s^2}\frac{x}{h^2}, \tag{8.103}$$

in which the velocity scales with mass diffusion and the parameter concentration $\mathscr{C}_s$. This result is equivalent to the planar growth of a binary fluid discussed by Worster (2000) in that $\mathscr{C}_s$ replaces S when species diffusion is small. Generally this is the case for many fluids (salt, gas hydrate, etc.) since $\sigma \approx 100$.

8.6.2 Vanishing x-diffusion

This problem is similar to the pure case but another equation is required to account for the transport of solute concentration. We have the following equations

$$\theta_x = \theta_{zz}, \quad \sigma \mathscr{C}_x = \mathscr{C}_{zz}, \tag{8.104}$$

and on the interface we have

$$\theta = 1 - \mathscr{C}_m + \mathscr{C} - \alpha\theta_z, \tag{8.105}$$

$$\sigma\gamma\theta_z = \mathscr{C}_z, \qquad Say_x = -\theta_z, \tag{8.106}$$

with the far field conditions $\theta(x,\infty) = \mathscr{C}(x,\infty) = 0$ and the far left conditions $\theta(0,z) = \mathscr{C}(0,z) = 0$. Invoking the Laplace transform and applying the boundary conditions we have

$$\theta = \mathscr{B}\frac{1}{2\pi i}\int_{c-i\infty}^{c+\mathrm{i}\infty} \frac{\mathrm{e}^{sx-\sqrt{s}z}}{s(1-\sqrt{s}\hat{\alpha})}\mathrm{d}s, \tag{8.107}$$

$$\mathscr{C} = \mathscr{B}\sigma^{1/2}\gamma\frac{1}{2\pi i}\int_{c-i\infty}^{c+\mathrm{i}\infty} \frac{\mathrm{e}^{sx-\sqrt{s\sigma}z}\,\mathrm{d}s}{s(1-\sqrt{s}\hat{\alpha})}, \tag{8.108}$$

after using the inverse Laplace transform and $\hat{\alpha} = \alpha/(1-\sigma^{1/2}\gamma)$. The temperature equation has the same form as for the pure liquid case and will have the same solution for the temperature as equation (8.91) and (8.96) with the modified form of the kinetic under-cooling term $\hat{\alpha}$. It is interesting to note that the effect of kinetic under-cooling is now scaled with the Lewis number and the parameter γ. The temperature gradient at the phase boundary therefore is

$$\begin{aligned}\theta_z(0,x) = -\frac{\mathscr{B}}{\sqrt{\pi x}} + \mathscr{B}\frac{\hat{\alpha}^2}{\pi}\int_0^\infty \mathrm{e}^{-rx}\frac{\sqrt{r}}{1+\hat{\alpha}^2 r}\mathrm{d}r = \\ -\frac{\mathscr{B}}{\sqrt{\pi x}} + \mathscr{B}\frac{1}{8\sqrt{\pi x}}\mathrm{e}^{x/2\hat{\alpha}^2}D_{-2}\left(\frac{\sqrt{2x}}{\hat{\alpha}}\right).\end{aligned} \tag{8.109}$$

In many cases such as the growth of snowflakes, gas hydrates and sea ice the kinetic coefficient $\mu \ll 1$ and does not become important unless for very large

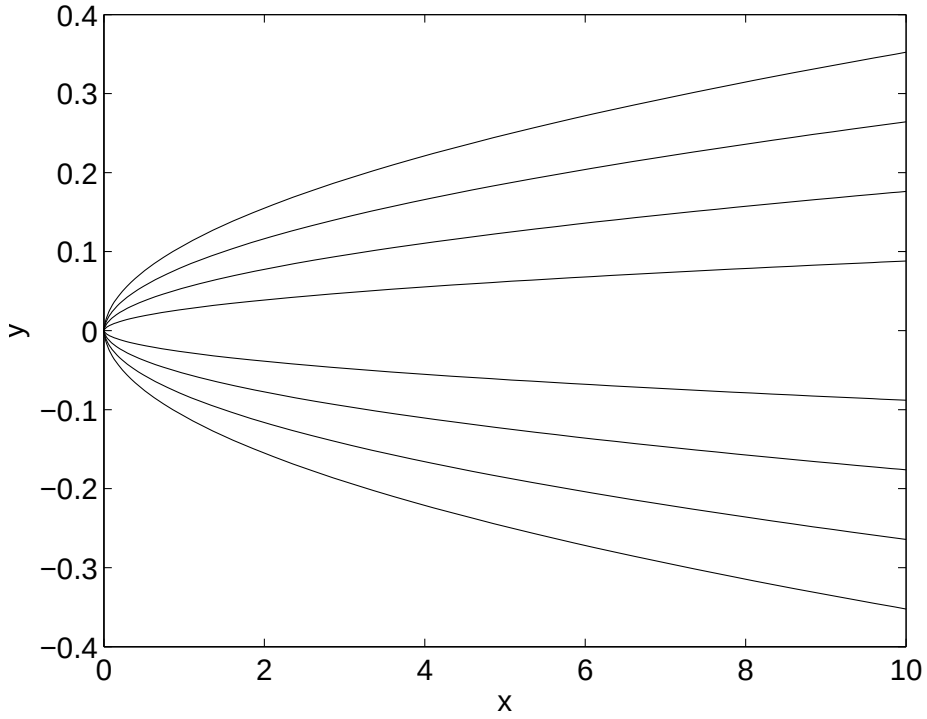

Figure 8.6: Interface position y from equation (8.76) and (8.109) as a function of x for $\mathscr{B} = .025, .05, .075, .1$ corresponding to thicker profiles respectively and with $Sa = 1$ and $\hat{\alpha} = 0$.

growth rates. In addition, for binary solidification the kinetic coefficient is scaled with the Lewis number, which is very small in the applications mentioned above and therefore has the effect of reducing the effect of under-cooling even further. In figure (8.6) we have plotted the interface position as a function of the concentration of the far field temperature difference $\mathscr{B} \propto \mathscr{C}_m$. As mentioned previously, as the concentration C_∞ decreases below the equilibrium value, corresponding to the local temperature the growth decreases and we obtain the slimmer profiles shown in figure (8.6).

8.7 Conclusion

In this Chapter we have investigated the steady dendrite problem for a binary liquid using slender body theory in order to determine the interface position to leading order. The essence of this method is to expand the temperature and interface position about an appropriate length scale for the thickness and solve the outer problem. Under this assumption the equations are amenable to the Wiener-Hopf technique, which is a complex variables method that is useful for split boundary problems. In the case of a pure liquid we were able to verify the interface profile found by the similarity solution of Ivantsov (1947) for an isothermal solid. Furthermore we extended the model to include the effect of kinetic under cooling and found that the profile is no longer parabolic but has a reduced thickness near the nose region. In addition we investigated the binary liquid problem and found that the interface retains its parabolic structure although it may have a thinner shape depending on the far-field concentration relative to its liquidus value and diffusion relative to heat.

9

Summary and Conclusions

9.1 Chemically reacting plumes

Plumes are the most common form of large Reynolds number convection in the atmosphere and are frequently encountered within occupied spaces (Linden, 2000). Previous studies have not considered the effect of chemical reactions in the classical plume models of Morton et al. (1956), although there are important applications as discussed in the introduction of this thesis. In our studies we analytically, numerically and experimentally investigated the plume dynamics associated with a second order non-reversible reaction between the source and entrained ambient fluid. The projects can essentially be broken up into two distinct studies: passive reactions in filling boxes and exothermic/endothermic reactions in unbounded ambients.

9.1.1 Plumes in ventilated spaces with passive reactions

In this case we examine the evolution of species concentration within a ventilated room as a fundamental study for contaminate removal in occupied spaces. We assume that the reaction is passive, such that the plume dynamics do not couple with the chemistry since the heat of reaction is negligible. Clearly the evolution of the chemical species depends on the reaction rate, the initial concen-

trations, the shape of the room and the plume dynamics. However in general, we can break the species evolution into three distinct phases. Initially, as the source fluid flows into the room, the mean concentration of the input chemical increases due to the inflow, with some loss due to the reaction with the initial room species. After a finite time, the layer of fluid contaminated by the inflow reaches the opening to the exterior at the base of the room. During an ensuing intermediate phase, the rate of increase in the concentration of the input chemical then drops, due to the extra sink for the input chemical of the outflow through the opening. During this intermediate stage, the concentration of the input chemical continues to rise, but at a reduced rate due to the reaction with the fluid in the room. Ultimately, all the fluid (and hence the chemical) that was originally in the room is lost, both through reaction and outflow through the opening. Finally, the room approaches steady state in a few filling box time scales, in which the space in completely filled with source fluid.

In relation to contaminate transport, if a hazardous chemical enters a room from a plume source this species will rise to the ceiling before descending into the occupied zone. Therefore, people must be evacuated before the first arrival time of circulated plume fluid as predicted by Caulfield and Woods (2002). Although for large reaction rates or a small initial plume species relative to ambient species this time will be extended significantly. Alternatively, if the room is initially contaminated, then a plume will be more efficient at extracting this chemical since the concentration of the contaminant will always be larger near the vent. In addition, for large reaction rates and relatively small ambient species concentrations, this contaminant will be extracted at faster time scales. Furthermore, if the product species is hazardous, a window of time will exist in which the contaminant is at a sufficiently high concentration (assuming the chemical is hazardous at high concentrations) but will decrease for weak reaction rates and relatively small source concentrations.

9.1.2 Plumes in infinite spaces with exothermic/endothermic reactions

In this study we developed a model for a turbulent plume in an unbounded ambient, taking into account a general exothermic or endothermic chemical reaction. In many cases, such as pyrophoric materials in air and the dilution of sulfuric acid in water, the chemical reactions can be highly exothermic; therefore we used the non-Boussinesq formulation. The problem was essentially separated into two groups: unstratified and stratified ambients. In this first case we were able to obtain an exact solution for large heats of reaction, in which the volume flux scales with $z^{2/5}$ rather than the $z^{3/5}$ scaling associated with no reaction. Furthermore, we quantified the deviation from pure plume behavior as a function of the release/absorption of heat and the reaction rate. In the case of an exothermic reaction, the plume was shown to behave more plume like, since the buoyancy force increases relative to momentum. On the other hand an endothermic reaction yields the opposite behavior although for large amounts of heat absorption the plume will become a fountain and spread horizontally into the environment.

In the second case, we examined the effect of reaction rate, heat of reaction and ambient species stratification on the maximum rise height of the plume moving through a linear density field. The most important finding, was that the maximum rise height of the plume may decrease with reaction rate for an exothermic reaction. This is due to a larger entrainment rate near the source, where the density and reaction rate are strongest.

9.1.3 Future directions

Evaporative cooling

With the growing demand in energy required in the near future, especially in the developing world, it is becoming increasingly important to offset this growth with more energy efficient and sustainable technologies. Since many industrialized countries spend a significant amount of their energy budget on ventilation systems,

which are relatively inefficient compared with hybrid natural ventilation systems in certain geographical regions, this is an area in which many improvements may be possible. One possible technology is evaporative cooling, in which dry air is mixed with water droplets and forced into an occupied space where the water changes phase from liquid to vapor. Latent heat is absorbed, thus cooling the surrounding air. This technology is very popular in hot dry climates such as the U.S. Southwest and the Middle East, since the cooling efficiency can be very large and operational costs relatively low in comparison with air conditioners. Evaporative cooling has been used for years in cooling towers to cool circulated water (Fisenko et al. 2004). A major drawback is the increased humidity of the cooled air which may accelerate the corrosion of electronic or other equipment and create an uncomfortable environment in comparison with dry air. Therefore, a complete understanding of the cooling rate and transport of moisture in ventilated spaces is necessary, especially if this scheme is to be integrated into a natural ventilation framework.

The fundamental fluid dynamical aspect of this problem is the distribution of water droplets with variable size and concentration within a turbulent plume. As the plume naturally entrains ambient fluid, the water droplets evaporate provided the air is sufficiently dry in order to maintain the equilibrium vapor concentration. In doing so latent heat is absorbed, thus increasing the density of the fluid and coupling to the plume dynamics through the buoyancy force. Clearly this process will increase the humidity as well as cool the air and an understanding of the most efficient control strategies are critical, in order to employ it most effectively in an air conditioning design.

Batch reactors

Often materials with a specific structure or composition are manufactured using continuous batch reactors, where fluid is injected into a well mixed space and a product chemical is extracted from the bulk fluid. Under normal circumstances

the reaction is passive and the reactants see a homogeneous environment, where the properties of the system can be described by simple equations that depend on the inlet flow rates and reaction mechanisms (see Aris 1969). When the reaction has an exothermic step, the homogeneity may break down with convection dominating the external mixing for large temperature differences (Campbell et al. 2007). This process has the potential to behave like a turbulent plume, especially for large vessels with fluid injected from the bottom. Clearly, the mixing process, especially for unmixed reactors, needs to be well understood so that the manufacturing process is as efficient as possible.

9.2 Gas hydrates

Methane gas hydrates are contained within the ocean seafloor in extremely large quantities. Unlike ice, which generally requires cold temperatures to exist, hydrates, in addition, need to be near a source of methane. Because of this they are always in a transitory state at sufficiently large times scales, forming and decomposing in response to the transport of heat, salt and dissolved methane gas. In this study we have sought to examine how gas hydrates melt, dissolve and dissociate in a fundamental sense, using equations that are as simple as possible. In general we considered a homogeneous, rigid matrix that is separated into two sections: a layer of hydrate mixture in the lower layer and a layer of water and sediment on top. By conserving heat, species, mass and momentum we were able to quantify the movement of this interface as a function of appropriate physical conditions. Due to the complex phase diagram associated with methane hydrates, the problem can be broken up into two parts: melting/dissolving and dissociation.

In the first case the local fluid temperature is less than the three phase boundary and the hydrate release s dissolved gas upon decomposition. For pure hydrate layers ($S_h = 1$), the velocity of the retreating interface scales with the rate of species diffusion and therefore will depend on the concentration difference

in the system. Essentially, if the water temperature increases or the dissolved methane concentration decreases the decomposition rate will be faster. Moreover, we examined the effect of an arbitrary hydrate saturation in the lower layer. This had faster interface velocities, since the amount of heat required to be remove at this boundary is comparatively smaller.

In the second case, the local fluid temperature is above the three phase boundary, causing the hydrate to dissociate into water and gas. Compared to the previous model, dissociation is more complicated because there is a multi-phase flow through the upper porous layer. Nonetheless we can still use Darcy's Law for the flow field with appropriate empirical relationships for the permeability and capillary pressure. This scenario is possible if the overlying water column temperature increases (by global warming, seafloor lifting, etc.) or if the pressure decreases (by a decrease in sea level, seafloor lifting, etc.). We developed a simple model assuming pure hydrate saturation, constant densities, and a homogeneous porous matrix, in order to understand physically the mechanisms involved in the problem. These assumptions, though limiting, are most likely obtainable for sediments with cold vents, such as those found near Vancouver Island. Here the hydrate layer can be found meters below the seafloor and the saturations can be larger than eighty percent. Generally, for gas hydrate dissociation, the controlling parameter is the Stefan number as this relates the amount of sensible heat to latent heat in the system. Therefore, if this number decreases (e.g. the water temperature increases relative to the three phase temperature) the hydrate dissociation increases, causing the flux of gas into the water column to increase as well.

9.2.1 Mass flux rates

In Chapter 7 we described a simple theoretical method for gas hydrate dissociation but we did not explore the influence of specific deposits. Here we relate the results to two test cases associated with regions of high hydrate saturations (such as off Vancouver island). We assume the methane deposits are within a few

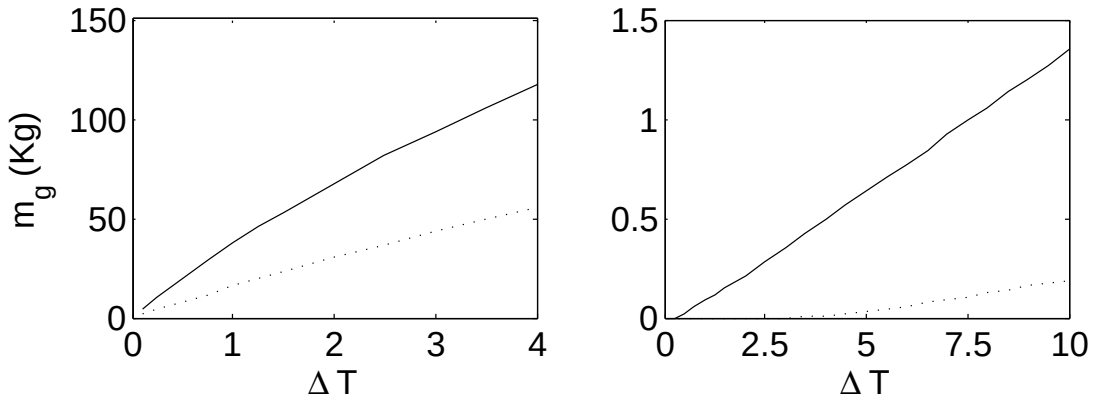

Figure 9.1: Total mass (in kilograms) of methane gas leaving the seafloor per unit area in one year as a function of the temperature scale ΔT and liquid layer depth $\ell_w = 1$ meter (left) and 4 meters (right). The results are based on the model developed in Chapter 7. We have used properties for sandstone (solid line) and clay (dotted line), assuming that the thickness of the hydrate layer is double the liquid layer.

meters below the seafloor and the porous medium is homogeneous, with appropriate thermal and dynamic properties corresponding to sandstone and clay. In Figure 9.1 we show the total mass of methane gas, m_g, (per unit area) leaving the sea floor in one year as a function of the temperature difference ΔT (boundary minus equilibrium temperature) and hydrate deposit depth ℓ_w. As we expect, m_g increases with the temperature difference and for shallower deposits. Generally, we expect the gas flow rate to be largest for sandstone, in the large Stefan number case, where diffusion dominates because the average thermal diffusivity is larger than clay.

Typically the temperature difference will be no larger than a few degrees and we can see from Figure 9.1 that the total mass entering the ocean water column is relatively large.

9.2.2 Experimental work

When we first starting working on this project we were interested in performing some experiments to help us understand what was going on and to compare with our model. We started setting up the experiments with come colleagues in the chemistry department at UCI using isobutane as the hydrate former. The main advantage of this hydrocarbon in comparison to methane is its very low formation pressure (near 1 atm and $\approx 1.7^{\circ}C$). Eventually we abandoned the experiments for several reasons, mainly concerning the ability to accurately control the temperature.

Furthermore, although the experiments may be appropriate for the model presented in Chapter 7, they cannot be compared to *in situ* deposits. The main problem is that in general the length scales in the ocean are much larger than in the laboratory and we cannot get dynamic similarity (gravitational forces dominate for deep deposits but capillary forces dominate for shallow hydrate layers). Therefore, the experiments would be of little interest to geologists or other investigators interested in the dissociation of hydrates.

9.2.3 Future directions

Variable hydrate saturations

In most cases the hydrate saturation is not pure and the model presented in Chapter 7 will not apply. The main issue is due to the hydrate bearing region decomposing internally and thus absorbing latent heat, rejecting methane gas (either dissolved or is gas form) and diluting the solute concentration. In Chapter 5 we developed the basic model for this situation, which will serve as a starting point for an appropriate study. The main source of uncertainty, involves an appropriate condition for the hydrate mixture/water interface, which in the small Lewis number limit implies $S_h = 0$. Therefore in this limit no gas flux can occur. It may be possible to overcome this by considering the inner problem but so far this has

not been done.

9.3 Dendrite solidification

Dendrites are a common occurrence generally appearing with multiple structures such as snowflakes, sea ice, metal castings and etc. and are important for many reasons including ocean convection, material strength and many more. In Chapter 8 we examined a simple case involving a single dendrite growing into a super-cooled binary fluid. We used slender body theory, which is appropriate for small Peclet numbers as determined from similarity theory. The dendrite surface position was found to be parabolic but when kinetic effects were included the interface position took on a new form with a thinner profile. In addition, the effect of a binary fluid is to reduce the growth rate since mass diffusion is slower than heat and therefore dominates the interfacial velocity.

9.3.1 Future directions

Near Nose Region

The analysis presented in Chapter 8 will not apply near the tip of the dendrite since the scaling associated with slender body theory breaks down in regions with large curvature. In this case we need to deal with the full non-linear interfacial conditions, which we can do by rescaling the length with $(x, z) = a(\xi, \eta)$

$$a\theta_\xi = \theta_{\xi\xi} + \theta_{\eta\eta}, \qquad \eta < y(\xi), \tag{9.1}$$

$$y_\xi = [y_\xi \theta_\xi - \theta_\eta]^s_\ell, \qquad \eta = y(\xi), \tag{9.2}$$

$$\theta = 1 + \frac{\Gamma}{a}\frac{y_{\xi\xi}}{(1+y_\xi^2)^{3/2}} - \bar{\mu}\frac{y_\xi}{\sqrt{1+y_\xi^2}}. \tag{9.3}$$

For small a the temperature field in the liquid and solid to leading order may be approximated as Laplace's equation

$$\theta_{\xi\xi} + \theta_{\eta\eta} = 0 \qquad \eta < y(\xi). \tag{9.4}$$

Due to the complicated nature of the interfacial conditions, a closed form solution may not be possible although the equations can be solved numerically using boundary element methods. This solution essentially corresponds to the inner solution and will need to be matched to the outer solution obtained in Chapter 8 in order to find the growth rate. Of course for zero surface energy and infinite kinetics the solution is given by the similarity solution. Thus following Horvay and Cahn (1961) the interface position is

$$h = 2\sqrt{P}\sqrt{x}, \qquad S^{-1} = \sqrt{\pi P}, \tag{9.5}$$

where P is the Peclet number. It would be interesting to solve the equations for the surface energy and kinetic effects included, which we will complete in due time.

Bibliography

Ablowitz, Mark J. & Fokas, Athanassios S. 2003 *Complex Variables: Introduction and applications*. Cambridge University Press.

Abramowitz, Milton & Stegun, Irene A. 1964 *Handbook of Mathematical Functions with Formulas, Graphs, and Mathematical Tables*, ninth dover printing, tenth gpo printing edn. New York: Dover.

Ahmadi, G., Ji, C. & Smith, D. H. 2004 Numerical solution for natural gas production from methane hydrate dissociation. *J. Petrol. Sci. Eng.* **41**, 269–285.

Aris, Rutherford 1969 *Elementary Chemical Reactor Analysis*. Prentice-Hall, Inc,.

Asaeda, T. & Imberger, J. 1993 Structure of bubble plumes in linearly stratified environments. *J. Fluid Mech.* **249**, 35–57.

Aziz, K. & Settari, A. 1979 *Petroleum Reservoir Simulation*. New York, NY: Academic Press.

Baines, W. D. & Turner, J. S. 1969 Turbulent buoyant convection from a source in a confined region. *J. Fluid Mech.* **37**, 51–80.

Bear, Jacob 1991 *Introduction to Modeling of Transport Phenomena in Porous Media*. 101 Philip Dr. Norwell, MA 02061: Kluwer Academic Publishers.

Bender, Carl M. & Orszag, Steven A. 1999 *Advanced Mathematical Methods for Scientists and Engineers: Asymptotic Methods and perturbation theory*. Springer.

Bhat, G.S. & Narashima, R. 1996 A volumetrically heated jet: large-eddy structure and entrainment characteristics. *J. Fluid Mech.* **325**, 303–330.

Bloomfield, L. & Kerr, R. C. 2000 A theoretical model of a turbulent fountain. *J. Fluid Mech.* **424**, 197–216.

Brasseur, Guy & Granier, Claire 1992 Mount pinatubo aerosols, chlorofluorocarbons, and ozone depletion. *Science* **257**, 1239–1243.

Brewer, Peter G., Peltzera, Edward T., Friedericha, Gernot, Ayab, Izuo & Yamaneb, Kenji 2000 Experiments on the ocean sequestration of fossil fuel co2: ph measurements and hydrate formation. *Marine Chemistry* **72**, 83–93.

Buffett, B.A. 2000 Clathrate hydrates. *Annu. Rev. Earth Planet. Sci.* **28**, 477–507.

Campbell, A.N., Cardoso, S.S.S. & Hayhurst, A.N. 2007 A comparison of measured temperatures with those calculated numerically and analytically for an exothermic chemical reaction inside a spherical batch reactor with natural convection. *Chemical Engineering Science* **62**, 3068 – 3082.

Canright, D. & Davis, S.H. 1989 Similarity solutions for phase-change problems. *Metallurgical Transactions A* **20A**, 225–235.

Cardoso, S. S. S. & Woods, A. W. 1993 Mixing by a turbulent plume in a confined stratified region. *J. Fluid Mech.* **250**, 277–305.

Carlotti, Pierre & Hunt, R. Gary R. 2005 Analytical solutions for turbulent non-boussinesq plumes. *J. Fluid Mech.* **538**, 343–359.

Carslaw, H. S. & Jaeger, J. C. 2001 *Conduction of Heat in Solids*. 1946: Oxford science publications.

Caulfield, C. C. P. & Woods, A. W. 1995 Plumes with non-monotonic mixing behaviour. *Geophys. Astrophys. Fluid Dyn.* **79**, 173–199.

Caulfield, C. P. & Woods, A. W. 1998 Turbulent gravitational convection from a point source in a non-uniformly stratified environment. *J. Fluid Mech.* **360**, 229–248.

Caulfield, C. P. & Woods, A. W. 2002 The mixing in a room by a localized finite-mass-flux source of buoyancy. *J. Fluid Mech.* **471**, 33–50.

Clarke, J.F. & McChesney, M. 1964 *The Dynamics of Real Gases*. Butterworth.

Conroy, Devin T., Llewellyn Smith, Stefan G. & Caulfield, C. P. 2005 Evolution of a chemically reacting plume in a ventilated room. *J. Fluid Mech.* **537**, 221–253.

Cooper, P. & Linden, P. F. 1996 Natural ventilation of an enclosure containing two buoyancy sources. *J. Fluid Mech.* **311**, 153–176.

Crank, John 1984 *Free and Moving Boundary Problems*. Oxford University Press.

Davis, S.H. 2001 *Theory of Solidification*. Cambridge University Press.

Dickens, Gerald R. 1999 The blast in the past. *Nature* **401**, 752–755.

Dillon, W.P. & Max, M.D. 2003 *Natural Gas Hydrate in Oceanic and Permafrost Environments*. Springer.

Esposito, S.J. & Thomson, N.R. 1999 Two-phase flow and transport in a single fracture-porous medium system. *Journal of Contaminant Hydrology* **37**, 319–341.

Fisenko, S.P., Brin, A.A. & Petruchik, A.I. 2004 Evaporative cooling of water in a mechanical draft cooling tower. *International Journal of Heat and Mass Transfer* **47**, 165–177.

Furzeland, R.M. 1980 A comparative study of numerical methods for moving boundary problems. *J. Inst. Maths Applics* **26**, 411–429.

Genuchten, M. Th. Van 1996 A consistent approach for applying numerical boundary conditions for multiphase subsurface flow. *J. of Contaminant Hydrology* **23**, 157–184.

Germeles, A. E. 1975 Forced plumes and mixing of liquids in tanks. *J. Fluid Mech.* **71**, 601–623.

Gibou, Frdric, Fedkiw, Ronald, Caflisch, Russel & Osher, Stanley 2003 A level set approach for the numerical simulation of dendritic growth. *Journal of Scientific Computing* **19**, 183–199.

Gill, A.E. 1982 *Atmosphere and Ocean Dynamics*. New York: Academic Press.

Handa, Y. Paul 1990 Effect of hydrostatic pressure and salinity on the stability of gas hydrate. *J. Phys. Chem.* **94**, 2652–2657.

Holder, G. D. 1984 The potential of natural gas hydrates as an energy source. *Ann. Rev. Energy* **9**, 427–445.

Horvay, G. & Cahn, J.W. 1961 Dendritic and spheroidal growth. *Acta Metallurgica* **9**, 695–705.

Hunt, G.R. & Kaye, N. B. 2005 Lazy plumes. *J. Fluid Mech.* **533**, 329–338.

Hunt, G. R., Cooper, P. & Linden, P. F. 2001 Thermal stratification produced by plumes and jets in enclosed spaces. *Building Environ.* **36**, 871–882.

Hunt, G. R. & Kaye, N. G. 2001 Virtual origin correction for lazy turbulent plumes. *J. Fluid Mech.* **435**, 377–396.

Ivantsov, G.P. 1947 Temperature field around spherical, cylindrical, and needle shaped crystals which grow in supercooled melt. *Dokl. Akad, Nauk SSSR* **558**, 567–569.

Kamath, V.A. & Holder, G.D. 1987 Dissociation heat transfer characteristics of methane hydrates. *AIChE Journal* **33**, 347–350.

Kobayashi, Ryo 1993 Modeling and numerical simulations of dendritic crystal growth. *Physica D* **63**, 410–423.

Kuiken, H.K. 1984 Etching: a two dimensional mathematical approach. *Proc. R. Soc. Lond. A* **392**, 199–225.

Kvenvolden, Keith A. 1993 Gas hydrates-geological perspective and global change. *Rev. of Geophysics* **31**, 173–187.

Kvenvolden, K. A., Ginsburg, G. D. & Soloviev, V. A. 1993 Worldwide distribution of sub aquatic gas hydrates. *Geo-Marine Letters* **13**, 32–40.

Langer, J. S. 1980 Instabilities and pattern formation in crystal growth. *Reviews of modern physics* **52**, 1–30.

Linden, P.F. 2000 *Convection in the Environment. In Perspectives in Fluid Dynamics (*ed. G.K. Batchelor, H.K. Moffatt & M.G. Worster), pp. 289–345. Cambridge University Press.

Linden, P. F., Lane-Serff, G. F. & Smeed, D. A. 1990 Emptying filling boxes: the fluid mechanics of natural ventilation. *J. Fluid Mech.* **212**, 309–335.

Liu, Xiaoli & Flemings, Peter B. 2007 Dynamic multiphase flow model of hydrate formation in marine sediments. *Journal of Geophysical Research* **112**, 1–23.

Lu, Hailong, Moudrakovski, Igor, Riedel, Michael, Spence, George, Dutrisac, Regent, Ripmeester, John, Wright, Fred & Dallimore, Scott 2005 Occurrence and structural characterization of gas hydrates associated with a cold vent field, offshore vancouver island. *Journal of Geophysical Research* **110**.

MacDonald, Gordon J. 1990 Role of methane clathrates in past and future climates. *Climate Change* **16**, 247–281.

McDougall, T. J. 1978 Bubble plumes in stratified environments. *J. Fluid Mech.* **85**, 655–672.

Morton, B. R., Taylor, G. I. & Turner, J. S. 1956 Turbulent gravitational convection from maintained and instantaneous sources. *Proc. R. Soc. Lond.* A **234**, 1–23.

Noble, B. 1988 *Methods Based on the Wiener-Hopf Technique for the Solution of Partial Differential Equations*. American Mathematical Society.

Patnaik, Pradyot 1999 *A Comprehensive Guide to the Hazardous Properties of Chemical Substances*, 2nd edn. Wiley.

Peaceman, Donald W. 1977 *Fundamentals of numerical reservoir simulation*. Elsevier Scientific Publishing Company.

Rempel, A.W. & Buffett, B.A. 1997 Formation and accumulation of gas hydrate in porous media. *J. Geo. Phys. Res.* **102**, 10151–10164.

Ricou, F. P. & Spalding, D.B. 1961 Measurements of entrainment by axisymmetrical turbulent jets. *J. Fluid Mech.* **11**, 21–32.

Riedel, Michael, Novosel, Ivana, Spence, George D., Hyndman, Roy D., Chapman, Ross N., Solem, Richard C. & Lewis, Trevor 2006 Geophysical and geochemical signatures associated with gas hydraterelated venting in the northern cascadia margin. *GSA Bulletin* **118**, 23–28.

Rooney, G. G. & Linden, P.F. 1996 Similarity considerations for nonboussinesq plumes in an unstratified environment. *J. Fluid Mech.* **318**, 237–250.

Sassen, Roger, Joye, Samantha, Sweet, Stephen T., DeFreitas, Debra A., Milkov, Alexei V. & MacDonald, Ian R. 1999 Thermogenic gas hydrates and hydrocarbon gases in complex chemosynthetic communities, gulf of mexico continental slope. *Organic Geochemistry* **30**, 485–497.

Scase, M. M., Caulfield, C. P. & Dalziel, S. B. 2006 Boussinesq plumes and jets with decreasing source strengths in stratified environments. *J. Fluid Mech.* **563**, 463–472.

Selim, M.S. & Sloan, E.D. 1989 Heat and mass transfer during the dissociation of hydrates in porous media. *AIChE Journal* **35**, 1049–1052.

Sloan, E.D. 2003 Fundamental principles and applications of natural gas hydrates. *Nature* **426**, 353–359.

Sloan, E. D. 1990 *Clathrate Hydrates of Natural Gas*. 270 Madison Avenue, New York, New York 10016: Marcel Dekker, Inc.

Socolofsky, Scott A. 2001 *P.h.D Thesis: Laboratory Experiments of Multiphase Plumes in Stratification and Crossflow*. Massachusetts Institute of Technology.

Spencer, Brian J. & Huppert, Herbert E. 1995 Steady-state solutions for an array of strongly-interacting needle crystals in the limit of small under cooling. *Journal of crystal growth* **148**, 305–323.

Stefan, J. 1891 Über die theone der eisbildung inbesondere über die eisbildung im polarmeere. *Ann. Physik und Chemie* **42**, 269–296.

Stern, L., Kirby, S.H., Durham, W.B., Circone, S., Waite, W.F. & edited by Michael D. Max 2003 *Natural Gas Hydrate in Oceanic and Permafrost Environments*. Springer.

Tieszen, Sheldon R 2001 On the fluid mechanics of fires. *Annu. Rev. Fluid Mech.* **33**, 67–92.

Tsypkin, G.G. 2001 Mathematical model for dissociation of gas hydrates coexisting with gas in strata. *Doklady Physics* **46**, 806–809.

Tunnicliffe, V. 1992 Hydrothermal-vent communities of the deep sea. *American Scientist* **80**, 336–349.

Turner, J. S. 1973 *Buoyancy Effects in Fluids*. London, England: Cambridge University Press.

Wichman, I.S. & Williams, F.A. 1983 A simplified model of flame spread in an opposed flow along a flat surface of a semi-infinite solid. *Combustion Science and Technology* **32**, 91–123.

Williams, Forman A. 1985 *Combustion Theory*. Benjamin/Cummings Publishing Company.

Woods, A.W. 1992 Melting and dissolving. *J. Fluid Mech.* **239**, 429–448.

Woods, A.W. 1995 The dynamics of explosive volcanic eruptions. *Rev. Geophys.* **33**, 495–530.

Woods, A.W. 1997 A note on non-boussinesq plumes in an incompressible stratified environment. *J. Fluid Mech.* **345**, 347–356.

Woods, A. W. & Caulfield, C.-C. P. 1992 A laboratory study of explosive volcanic reactions. *J. Geophys. Res.* **97**, 6699–6712.

Woods, A. W., Caulfield, C. P. & Phillips, J. C. 2003 Blocked natural ventilation: the effect of source mass flux. *J. Fluid Mech.* **495**, 119–133.

Worster, M.G. 2000 *Solidification of Fluids In Perspectives in Fluid Dynamics a Collective Introduction to Current Research. Edited by G.K. Batchelor, H.K. Moffatt and M.G. Worster.*. Cambridge University Press.

Worster, M. G. & Huppert, H. E. 1993 Time-dependent density profiles in a filling box. *J. Fluid Mech.* **132**, 457–466.

Wu, Y.S., Forsyth, P.A. & Jiang, H. 1996 A consistent approach for applying numerical boundary conditions for multiphase subsurface flow. *J. of Contaminant Hydrology* **23**, 157–184.

Xu, Jian-Jun 1991 Interfacial wave theory of solidification: Dendrite pattern formation and selection of growth velocity. *Physical Review A* **43**, 930–947.

Xu, W. & Ruppel, C. 1999 Predicting the occurrence, distribution, and evolution of methane gas hydrate in porous marine sediments. *J. Geo. Res.* **104**, 5081–5095.

Yousif, M.H., Li, P.M., Selim, M.S. & Sloan, E.D. 1990 Depressurization of natural gas hydrates in berea sandstone cores. *J. of Inclusion and Molecular Recognition in Chemistry* **8**, 71–88.

Zheng, L., Yapa, P.D. & Chen, F. 2002 A model for simulating deep water oil and gas blowouts-part 1: Theory and model formulation. *J. Hyd. Res.* **41**, 339–351.